Bulletin 55
(Part 2 of 3 Parts)

THE SHOCK AND VIBRATION BULLETIN

Part 2
Dynamic Testing, Flight Vehicle Dynamics, Seismic Loads and Fluid-Structure Interaction

JUNE 1985

A Publication of
THE SHOCK AND VIBRATION INFORMATION CENTER
Naval Research Laboratory, Washington, D.C.

Office of
The Under Secretary of Defense
for Research and Engineering

SYMPOSIUM MANAGEMENT

THE SHOCK AND VIBRATION INFORMATION CENTER

J. Gordan Showalter, Acting Director

Rudolph H. Volin

Jessica Hileman

Elizabeth A. McLaughlin

Mary K. Gobbett

Bulletin Production

Publications Branch, Technical Information Division,
Naval Research Laboratory

Bulletin 55
(Part 2 of 3 Parts)

THE SHOCK AND VIBRATION BULLETIN

JUNE 1985

A Publication of
THE SHOCK AND VIBRATION INFORMATION CENTER
Naval Research Laboratory, Washington, D.C.

The 55th Symposium on Shock and Vibration was held in Dayton, Ohio, October 22-24, 1984. The Aeronautical Systems Division, Wright-Patterson Air Force Base, Ohio, was the host.

Office of
The Under Secretary of Defense
for Research and Engineering

CONTENTS

PAPERS APPEARING IN PART 2

Damping Practices

Damping and Isolation

SESSION CHAIRMEN AND COCHAIRMEN

Date	Session Title	Chairmen	CoChairmen
Tuesday, 23 October, A.M.	Opening Session	Mr. Jerome Pearson, Air Force Wright Aeronautical Laboratories, Wright-Patterson Air Force Base, OH	Dr. J. Gordan Showalter, The Shock & Vibration Information Center, Naval Research Laboratory, Washington, DC
Tuesday, 23 October, P.M.	Dynamic Testing	Mr. Edwin M. Rzepka, Naval Surface Weapons Center, Silver Spring, MD	Mr. Frederick Anderson, U.S. Army Missile Command, Redstone Arsenal, AL
Tuesday, 23 October, P.M.	Fluid-Structure Interaction	Mr. Arthur D. Carlson, Naval Underwater Systems Center, New London, CT	Dr. Y. S. Shin, Naval Post Graduate School, Monterey, CA
Wednesday, 24 October, A.M.	Plenary A	Mr. Henry Caruso, Westinghouse Electric Corporation, Baltimore, MD	
Wednesday, 24 October, A.M.	Flight Vehicle Dynamics	Mr. Joseph J. Popolo, Grumman Aerospace Corporation, Bethpage, NY	Mrs. Phyllis Bolds Air Force Wright Aeronautical Laboratories, Wright-Patterson Air Force Base, OH
Wednesday, 24 October, A.M.	Damping and Isolation	Dr. John P. Henderson, Air Force Wright Aeronautical Laboratories, Wright-Patterson Air Force Base, OH	Dr. David I. G. Jones, Air Force Wright Aeronautical Laboratories, Wright-Patterson Air Force Base, OH
Wednesday, 24 October, P.M.	Seismic Loads	Mr. James P. Ballard, U.S. Army Engineer Waterways Experiment Station, Vicksburg, MS	Mr. Donald Bettge, Federal Emergency Management Agency, Washington, DC
Wednesday, 24 October, P.M.	Damping Practices	Dr. Lynn C. Rogers, Air Force Wright Aeronautical Laboratories, Wright-Patterson Air Force Base, OH	Mr. Michael Parin, Anatrol Corporation, Cincinnati, OH
Thursday, 25 October, A.M.	Plenary B	Dr. Ronald L. Eshleman, Vibration Institute, Clarendon Hills, IL	

Thursday, 25 October, A.M.	Machinery Dynamics	Dr. Ronald L. Eshleman, Vibration Institute Clarendon Hills, IL	Mr. Robert Leon, Liberty Technology Center, Inc. Conshohocken, PA
Thursday, 25 October, A.M.	System Identification	Dr. H. Joseph Weaver, Lawrence Livermore Laboratory, Livermore, CA	Dr. David Brown University of Cincinnati, Cincinnati, OH
Thursday, 25 October, P.M.	Structural Analysis	Mr. Tommy L. Dobson, 6585 Test Group, Holloman, Air Force Base, NM	
Thursday, 25 October, P.M.	Short Discussion Topics	Mr. James Bair, Aeronautical Systems Division, Wright-Patterson Air Force Base, OH	

TRIAXIAL VIBRATION SYSTEM

W. Douglas Everett and Thomas M. Helfrich
Pacific Missile Test Center
Point Mugu, California

During the reliability tests of external stores the Pacific Missile Test Center has been successful in reproducing the in-service vibration experienced by the store when carried on a high performance jet aircraft. A combination of acoustic and mechanical excitation provides the appropriate vibration magnitude and spectrum. One of the advantages of using acoustic energy has been the simulation of the vibrational state simultaneously in three axes. In attempting to increase our test capability to include stores carried on helicopters and other low speed platforms and to maintain a triaxial vibration capability, the Pacific Missile Test Center is developing a test facility that will test a 500 pound store in the 0 to 500 Hertz frequency range with a stroke of 2 inches double amplitude. A review of existing low frequency triaxial vibration equipment was conducted, a preliminary design was completed, and individual component and initial developemental model tests were concluded. This paper presents a description of the device, an overview of the effort to date, an analytical investigation of the motion, and an evaluation test plan that has been developed for a thorough evaluation of the device.

INTRODUCTION

The majority of environmental and reliability vibrational test programs subject the test item to vibrational motion in a succession of tests in one or two independent axes to achieve final results in three directions. Various objections are made against this test procedure. First, sequential testing in three axes is not valid for use in reliability tests and the generation of Mean-Time-Between-Failure (MTBF) data because of the uncertainty in the effective duration. Second, a three-by-one directional test also necessitates periodically discontinuing the test to reorient the item with the next axis. This process is time consuming because the time to correctly reorient the item and to adjust and reposition the data sensors can often be greater than the length of the time for the test itself. Hence, running a one directional test three times with different test setups can consume more than three times as much time, personnel, and facilities when compared to a test run without interruption in the three directions simultaneously. Third, a test using three axes of simultaneous vibration can produce realistic operational stresses which increases the validity of the test.

In response to these objectives and potential improvements, a triaxial shaker system capable of vibration in three simultaneous independent axes has been developed. This system can provide reliability data, a realistic reproduction of the in-service vibration environment, and potentially reduce test costs.

PREVIOUS SYSTEMS

Various systems have been developed to reproduce in-service three-dimensional vibrational levels in the test laboratory. To duplicate the three-dimensional state, a system must be capable of providing an uncoupled excitation to three independent axes simultaneously. A fault common to many such systems is cross-axial transmission where a purely uniaxial vibration imparts a percentage of its motion, which can be greater than 100 percent to the other two, presumed independent, directions. Most desirable is the minimum percentage of motion imparted and this is greatly dependent on the system design. Another problem generic to these systems is the difficulty in providing fixed rotational degrees of freedom. In either case, if the degrees of freedom increase from the three translational degrees of freedom test baseline, the system may be rendered inappropriate for vibrational tests. Thus, the method and design employed to input and maintain independent translational motion is the critical factor to achieve acceptable results.

One of the earliest systems built specifically to reproduce triaxial motion was evaluated at White Sands Missile Range (WSMR), New Mexico, in the early 1960's. It consisted of a solid aluminum cube, 0.13 meters edge length, driven in three perpendicular axes by a plate mounted on the end of each drive rod. The drive plate and block were interfaced through a gravity fed, viscously stabilized oil film which permitted perpendicular

displacements. At low frequencies, the oil film transmitted well. However, at higher frequencies, decoupling and separation of the drive plate and block would occur. Although this design had no provision for attaching a test object without causing severe moments, and was thus incapable of supporting a test program, it did provide some insight into the relevant problems of triaxial vibration.

Later designs reflected more complex, and more capable, approaches. One of these, a system built by Wyle Laboratories, Alabama, was also evaluated at WSMR. Comprised of a 0.4 meter square table with input rods connecting below the table and at two adjacent corners, the system used circular steel flexures mounted between the drive rods and exciter tubes. Another frame and flexure tube set isolated the table from rotation. Though performance was greatly improved over the earlier oil film method, a severe resonance at 150 Hertz and greater than 100 percent distortion at certain frequencies severely reduced this system's potential.

A system developed in 1975 by WSMR represented a substantial improvement over earlier attempts to induce triaxial vibration. Electrodynamic shakers arranged in a conventional gravitational orientation provided excitation to a rectangular test platform. In the x-y plane, three preloaded spherical couplings (2x, 1y) transmitted horizontal motion to the table, while vertical excitation was maintained through nine journal bearing posts and passing through a lower plate fixed to the support structure. These posts are their corresponding bearings fixed the vertical motion. To allow for horizontal translation of the upper test platform, which attaches to the horizontal shakers, cutouts were made through the lower plate and post where the upper plate bolts to the shaker, thus providing 0.0271 meters of horizontal movement.

Evaluation of this system at WSMR showed that vertical cross-axis motion because of a horizontal input was less than 50 percent. However, cross-axis motion because of a vertical input was much larger. Random excitation tests showed that the bare table could possibly be equalized to within 2 decibels, excluding three points in the frequency range. Reproduction of actual ground transportation spectral levels for a structural dummy Chaparral missile revealed a close matching of the experimental power spectral density (PSD) to the required envelope at almost all points. In summary, this system proved effective in that it reproduced triaxial vibration. However, certain limitations, including a resonance below 500 Hertz and the fact that only the centermost section of the table was coherent through 2 kilohertz, reduced the effectiveness of this system.

A recently developed system, using a method similar to the early oil film system, is under construction by Wyle Laboratories, Alabama, and will be evaluated at the Harry Diamond Laboratory, Maryland. In this system, three shakers drive a rectangular test platform. Translational motion of the platform is achieved through the use of a hydrostatic bearings, which provide a high stiffness connection, and a mechanical linkage to provide the necessary preload. The opposite ends of the rods hinge so that no bearing forces are developed and rotation is constrained by another set of bearings. The system is expected to be capable of accelerating 100 pounds to 40g, a maximum frequency of 2000 Hertz, and equalization to within 2 decibels across the platform. A computerized controller provides 3 independent inputs. A full evaluation is currently underway.

Additional multiaxial vibration testing systems that have been developed are for seismic and stress screen systems. The first reproduces seismic ground motion for earthquake simulation. The second is used to ensure product acceptance during subsequent reliability tests. Each system is particularly suited for its designed purpose. Hence, there exist self-imposed limits either in frequency range or test load capability.

In the case of earthquake simulation, the system is purposely designed for a maximum frequency range from 50 to 100 Hertz. This limit is commonly considered to be the upper bound for seismic ground motion which may influence man-made structures. Wyle Laboratories, Alabama, operates a large, 36,000 pound triaxial simulator of this type using a system of torque tubes to minimize the rotational modes and hence, the cross-coupling of motion. The systems frequency limit

is 100 Hertz. It has been in operation since 1982.

The Sopemea aerospace test facility, France, also possesses a triaxial seismic simulator. While capable of loads up to 2000 kilograms (4500 pounds) and independent acceleration levels in the vertical and horizontal directions of 6.5g, the upper frequency limit is only 50 Hertz. Conversion of either of these systems to increase the operating frequency range to 500 Hertz would be impractical. First, any resonant behavior of the system was purposely pushed above the maximum limit of 50 to 100 Hertz by design and thus may occur in the 500 Hertz range. Second, the increasing probability of cross-axis motion transmission at the higher frequencies may require extreme modifications to the original systems to produce the desired results.

The Santa Barbara Research Center, California, has developed a triaxial stress screen system to perform a temperature and vibration screen of parts and workmanship of missile electrical components to ensure lot acceptance. Driven by five oscillating pneumatic hammers, the system provides three directional acceleration, (characterized more as impulse response than steady state vibration), although this varies by more than 20 percent across the test platform. (In the stress screen scheme this variance is inconsequential since actual reproduction is not the goal.) The frequency range is 2 kilohertz. The limitation exists in the size and weight of the test item. In this case, the system was designed for small electrical components. Conversion of this system to accommodate larger test items for reliability testing would require that accurate PSD reproduction be possible. Also, extensive experimentation would be needed to obtain the proper smear of the hammer excitation to achieve the required vibration levels. Because this must be done individually for each different test item, the system's flexibility would dramatically decrease.

CURRENT SYSTEM

The triaxial system shown in figure 1 consists of four major elements. First, the test platform or platen, constructed of magnesium, provides a rigid base for mounting a test item. Hemispherical in shape and with 12 inch radius, the curved underside is machined flat at three mutually perpendicular points to allow for attachment to the rod bundles. These attachment points are oriented such that the axial directions of the shakers comprise the upper edges of a triangular pyramid. Hence, the actuator force vectors coincide with the center of the table mounting surface. This orientation yields a compact design and provides for easy attachment of the actuator to the reaction mass. This also permits the test item to cantilever over the edge of the platen without interference because all hardware is located beneath the test table. The magnesium alloy, SAE no. 51, provides sufficient stiffness to prevent deformation of the table in the test frequency range. It weighs approximately 80.3 kilograms (177 pounds).

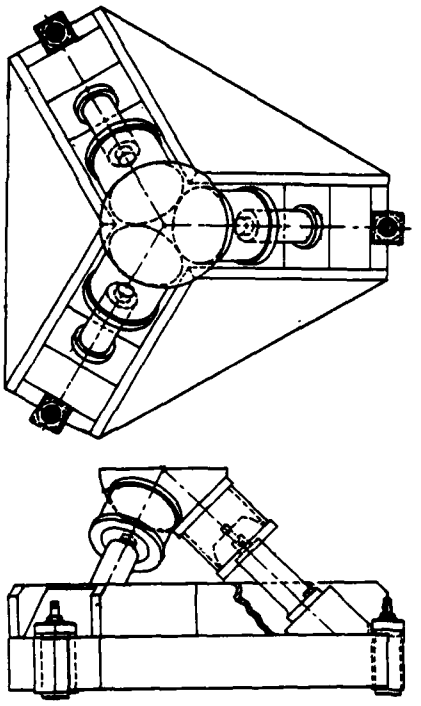

Figure 1. Two View Sketch of Triaxial Shaker Assembly.

Second, the base, constructed of numerous 10-inch carbon steel plates configured to a 1.85 meter (6.1 foot) equilateral triangular box, uses two-inch thick stiffener plates to locate and orient the actuators. It also acts as a reaction mass and isolates the rest of the laboratory from the vibration generated by the shakers.

Third, the shakers are part of an existing laboratory hydraulic system manufactured by Shore Western (SW) Mfg., California. The system includes a hydraulic power supply and actuators designed to apply single axis vibration to a large test platform. Each of the shakers is capable of an output vibrational force of 5000 pounds, a stroke of 3 inches double amplitude, and an operating frequency range of 2 to 500 Hertz. Control is accomplished through a SW Mfg. SC -3000 B servocontroller, an Exact Electronics, Oregon, Model 350 precision low frequency generator, and two Exact Model 344 variable phase generators. The variable phase generators enable reproduction of any net force vector by the correct selection of the force level and phase difference for each actuator. Random vibration is also available in the control system when supplemented by existing laboratory equipment, but control algorithms have not been worked out.

Lastly, the flexible drive rod bundles, positioned between the platen and the actuators, are the critical and unique component of the system. Proper triaxial motion requires that the drive rods be very stiff in the axial and rotational modes, yet be compliant in transverse displacement. This is achieved by a large set of slender drive rods in a cylindrical bundle which can deliver the shaker thrust even though partially bent. The rods are spring steel stock, 1/16 inch in diameter, with a 10 inch free length and are rigidly fixed at each end.

Five thousand of these rods are bundled in the form of a cylinder 13 inches in diameter, 10 inches long, and with a wall thickness of 1/2 inch. The upper rod bundle ring is designed to bolt directly to the platen. The lower ring is threaded for attachment to a special adapting flange, manufactured from 6061 Aluminum Alloy, which threads to the lower rod bundle ring and is lightly press fitted to the shaker ram. The original adapter, constructed of magnesium, did not have the strength required to resist the moments developed during transverse displacement of the rod bundle. The threaded flange design allows for mounting of the rod bundle/platen assembly to another shaker system simply by the manufacture of a different flange adapted to that shaker's mounting design.

Initial operation of this system showed that the flexible drive rods worked better than originally expected. The table transmitted well at 400 Hertz and the rod bundles tolerated transverse displacements of up to 2 inches. However, as mentioned above, the rod bundle adapter flange began to deform where it is press fitted to the shaker ram due to the inadequate strength of the magnesium. Thus, the system was disassembled for the remanufacture of this part before any quantitative evaluation test results could be obtained.

As described, the system should be capable of accelerating the bare table to 44g vertically and 36.5g horizontally. Other performance parameters shall be found experimentally as described later in this paper.

For comparison, table 1 provides a summary of frequency, acceleration, actuator type, and design method for the various triaxial systems discussed in this paper.

ANALYSIS

For several reasons a theoretical investigation of the current system was initiated. First, a basic understanding of the dynamic behavior the system was clearly needed to further develop the system and plan evaluation tests. Of particular interest were the natural frequencies and the deflection cases of the rod bundles. Secondly, by calculating the unforced homogeneous case, the natural frequencies could be predicted and resonance problems within the test frequency range anticipated. Third, an analysis baseline was required for comparison with any future alterations in the system in order to determine their overall effect.

The investigation consisted of the following:

1. Model development, in which the essential properties of the system and its responses are captured but avoiding an extremely detailed account of all the influences on the system.

TABLE 1. TRIAXIAL SYSTEM SUMMARY

SYSTEM	FREQ. RANGE (HERTZ)	ACCELERATION (g)	ACTUATOR TYPE	METHOD
OIL FILM	LOW	VERY LOW	ELECTRODYNAMIC	GRAVITY FED OIL FILM
WYLE	2000	SMALL	ELECTRODYNAMIC	FLEXURE TUBES COUPLINGS
WSMR	2000	12 VERTICAL	ELECTRODYNAMIC	J. BEARINGS & COUPLINGS
SOPEMEA	50	13 VERTICAL 6.5 HORIZ.	HYDRAULIC	HINGED ACT'RS & COUPLINGS
WYLE SEISMIC	100	4.5 (3000 LBS)	PNEUMATIC	TORQUE TUBES
WYLE		40.(HORIZONTAL)	ELECTRODYNAMIC	HYDROSTATIC
HDL	2000	25.(VERTICAL) 53.(RESULTANT)		BEARINGS & ROTATIONAL
PMTC	500	44 VERTICAL 36.5 HORIZ.	HYDRAULIC	FLEXIBLE ROD BUNDLES

2. A theoretical development of equations from the model and calculation of those solutions which are readily available without consuming large amounts of time or computational facilities.

3. Lastly, use the solutions to predict potential problems in the design, mostly resonance related, and to propose system alterations to correct them.

This was not meant to be an engineering analysis, but rather a preliminary look to predict resonance within the operating frequency range.

MODELING

Three modes of the shaker motion were evaluated in terms of natural frequency. Two of them correspond to displacement of the platen and one of the hydraulic rams along the axis of the ram as shown in figure 2. The other corresponds to rotation of the platen about the axis of one of the rams are shown in figure 3. These are not actually normal modes of the system but under certain conditions, which will be defined later, are approximations to the three lowest normal modes (actually the nine lowest since by symmetry each one is three-fold degenerate). Since first order errors in mode shape produce only second order errors in frequencies this kind of rough approximation is considered adequate background for a test program.

The simplifying conditions assumed are of three kinds. First, it is assumed that a test item is mounted on the platen so that the mass and mass-moments-of-inertia of the platen-plus-test-item are the same as those of a magnesium sphere having the same radius as the platen. This assumption avoids all inertial cross-coupling terms among motions along the actuator axes and rotations. The hypothetical test items weighs about 225 lbs.

Second it is assumed, as an approximation, that the elastic cross-coupling terms are zero. For example it is assumed that shearing of a rod bundle, as in figure 2, does not produce a torque on the platen. This, along with the first assumption about the test mass, is implicit in the assumption that the simple motions shown in figures 2 and 3 are normal mode shapes.

Third, the hydraulic system is modeled as a simple elastic spring. This neglects viscous effects in the oil and the operation of the servo-valve.

Within the simplifying assumptions, the model has only seven

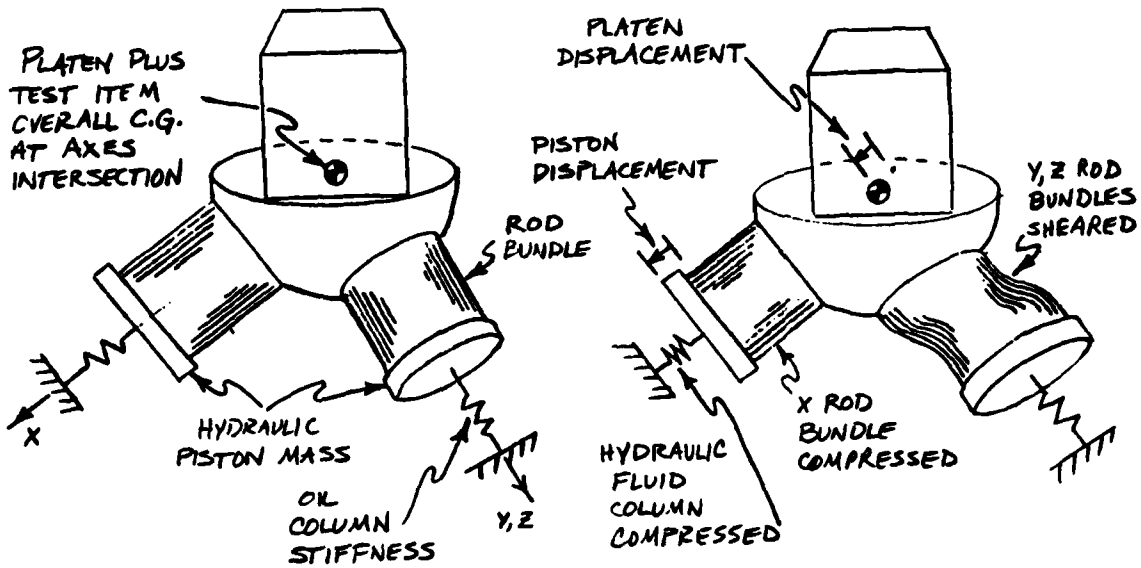

Figure 2. Shaker Translational Deflection.

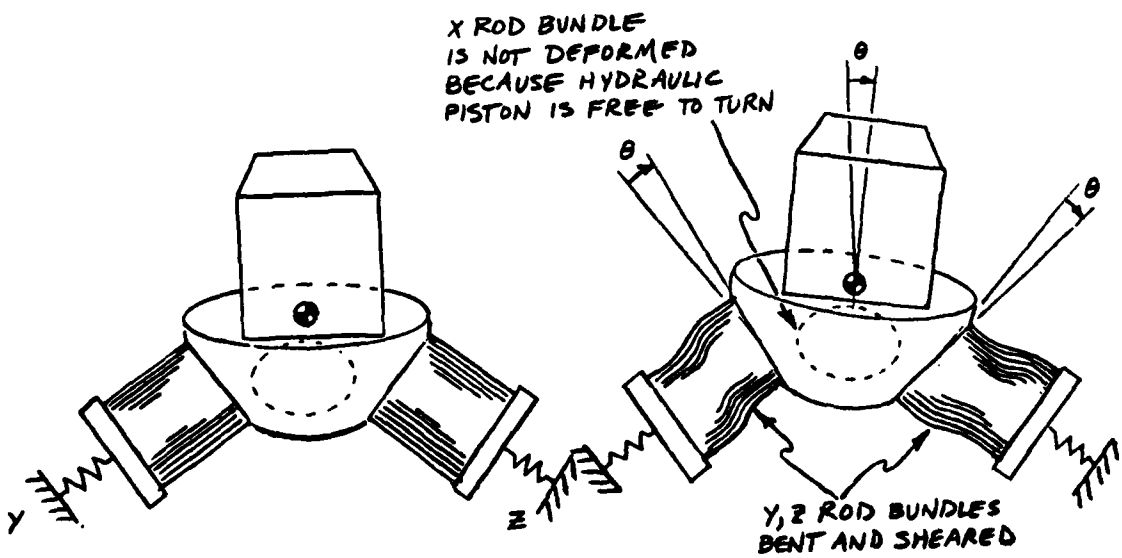

Figure 3. Shaker Rotational Deflection.

parameters, four stiffnesses and three inertias. Only the values and a brief description will be given here; for more detail see the appendix. The stiffness are:

$K_c = 22.1 \times 10^7$ lb/ft, the compressive stiffness of a rod bundle parallel to the rods.

$K_s = 6.64 \times 10^3$ lb/ft, the shearing stiffness of a rod bundle.

$K_h = 8.56 \times 10^6$ lb/ft, the stiffness of a hydraulic actuator due to the compressibility of the oil.

$K_\theta = 30.8 \times 10^6$ ft lb/rad, the angular stiffness of a rod bundle; i.e., the resistance to tipping the place of the platen end of a bundle while holding the actuator end fixed.

The three inertias are:

M = 14.13 slg, the mass of the platen plus its hypothetical test item.

M = 0.93 slg, the mass of a hydraulic actuators central rod and piston plus the spider holding the rods.

$I = 5.65$ slg ft^2, the moment of inertia of the platen-plus-test-item about its center of mass; it is assumed to have spherical symmetry so it is the same about all axes.

From these parameter values the natural frequency of the three lowest modes (nine counting symmetries) can be calculated.

Because the parameters have disparate magnitudes the calculations are particularly simple. First, consider the lowest translational mode. Because $K_c >> K_s$ & K_h the two masses may be regarded as moving together as a unit. Because $K_h >> K_s$ the latter can be neglected completely. So the natural frequency is:

$$F_1 = \left(\frac{1}{2\pi} \quad \frac{K_h}{M+m} \right)^{\frac{1}{2}}$$

$$= 120 \text{ Hz}$$

The other translational mode of the model corresponds to the platen and the ram moving out of phase instead of together. Because $K_c >> K_h$ & K_s the latter two can both be ignored and the system treated as two masses joined by a spring. The natural frequency is

$$F_2 = \frac{1}{2\pi} \left[\frac{K_c (M+m)}{M\,m} \right]^{\frac{1}{2}}$$

$$= 1790 \text{ Hz}$$

The third mode of the model is the rotational one. It's natural frequency is

$$F_0 = \frac{1}{2\pi} \left(\frac{2K_\theta}{I} \right)^{\frac{1}{2}}$$

$$= 526 \text{ Hz}$$

Only the lowest frequency, F_1, is within the intended operating range of the triaxial shaker (0-500 Hz). It is primarily due to the compliance of the hydraulic oil and has nothing to do with the shaker design. If this prediction is correct it may be necessary to change to electrodynamic shakers to achieve the desired performance.

INITIAL TEST RESULTS

As of the date of this publication, selected initial tests from the test matrix in table 2 have been performed. These tests include the following:

1. Sine sweep in each actuator axis with empty table; 1.8g level.

2. Sine sweep in one actuator axis with empty table; 10g level.

3. Sine sweep in one lateral direction with loaded table; 10g level.

4. Three-dimensional simultaneous random vibration control of a missile/launcher combination; captive flight buffet levels.

In the following pages, these test setups are described, and test data is presented and discussed.

In addition to other transducers placed in various locations on the shaker table, a triaxial accelerometer was used for vibration control in each test run and was oriented to correspond to the actuator axes or with conventional gravitational axes, depending on the direction of vibration control for each run. Positioning of the triaxial accelerometer is identified under each

test setup description. Vibration control computers supplied the actuator drive signals in a closed loop fashion for each test run. Test data was recorded on magnetic tape for each run and included response data from the triaxial accelerometer axes, servo drive signal, and irig B timing.

The sine sweep runs at 1.8g with single actuators were conducted to determine frequency response of the actuator/rod bundle combination, cross axis response due to single actuator input, moment resistance of the shaker table, and uniformity of response characteristics among the three rod bundles. The triaxial accelerometer was oriented in the table center with its axes corresponding to the actuator axes x, y and z. The accelerometer of the triaxial group which corresponded to the actuator direction under test served as the control accelerometer for each sweep. A logarithmic sweep of 10 minute duration was conducted for each actuator direction at 1.8g, with a 6 Hz starting frequency. Data was reduced to acceleration vs frequency plots for each accelerometer, and servo drive signal was plotted as voltage vs frequency.

Figure 4 presents unfiltered acceleration vs frequency plots for each actuator direction for the sine sweep with actuator 1. Data from the sweeps with actuators 2 and 3 is not presented due to its extreme similarity to data from actuator 1. Figure 4 shows that the 1.8g level was maintained in actuator axis 1 throughout most of the frequency range up to 400 Hz. The filtered-data (not shown) did not contain the amplitude fluctuations between 20 and 40 Hz apparent in the unfiltered plots. A significant portion of the cross axis data fall below 0.5g, 75% below the 1.8g in-axis levels. The peaks in both cross-axis plots from 65 to 100 Hz and 300 to 400 Hz closely approach the 1.8g in-axis level. This effect is currently under investigation. Examination of the drive signal for this run (figure 5) shows that maximum drive level was required of the controller above 400 Hz. This effect is thought to be due to force limitations in the hydraulic actuator. The sine sweep was aborted at 440 Hz as a result of below-tolerance response levels.

A sine sweep at 10g was conducted in-axis with a single actuator for comparison of table response characteristics between low and high level inputs. The 10g run also included the objectives of the lower level sweep and an identical equipment setup. A logarithmic sweep of 10 minute duration was conducted with actuator 1, controlling in-axis response to 10g's with a starting frequency of 15 Hz for an initial displacement of one inch.

Figure 6 contains unfiltered in-axis and cross axis acceleration vs frequency plots from the triaxial accelerometer at the table center, and figure 7 shows the servo drive signal for this run.

The in-axis response data in figure 6 maintains a level of over 10g from 15 to approximately 230 Hz. Again, the filtered data showed a constant 10g response throughout most of this frequency range. The two cross-axis response plots are nearly identical, with levels 77% below in-axis response from 15 to 58 Hz, and 40% below in-axis levels above to 70 Hz. Cross axis reached in-axis levels from 58 to 70 Hz. This effect is similar to that for the 1.8g run and is not fully explainable at present. Figure 7 shows that maximum drive was required above 150 Hz. Below tolerance in-axis response was reached at 230 Hz where the sweep was aborted, again due to actuator force limitations. Comparing drive signals for the 1.8 and 10g levels, it is clear that a non-linear relationship exists between drive signal voltage and in-axis table response.

The sine sweep runs in conventional axis directions (vertical and both lateral) are intended to test the capability of the system to provide vibration excitation in directions corresponding to normal test package orientation as well as to examine the items studied in the single-axis sine sweeps. Figure 8 defines the X, Y, and Z directions in the gravitational reference frame with respect to the shaker table. To achieve table response in any of the conventional X, Y, or Z directions, all actuators must be driven to provide appropriate displacement components in the actuator XYZ coordinate system. To operate in the X, Y, and Z directions simultaneously, three vibration control computers are used and their drive signals are split and conditioned through a special network to transform them into the required actuator signals.

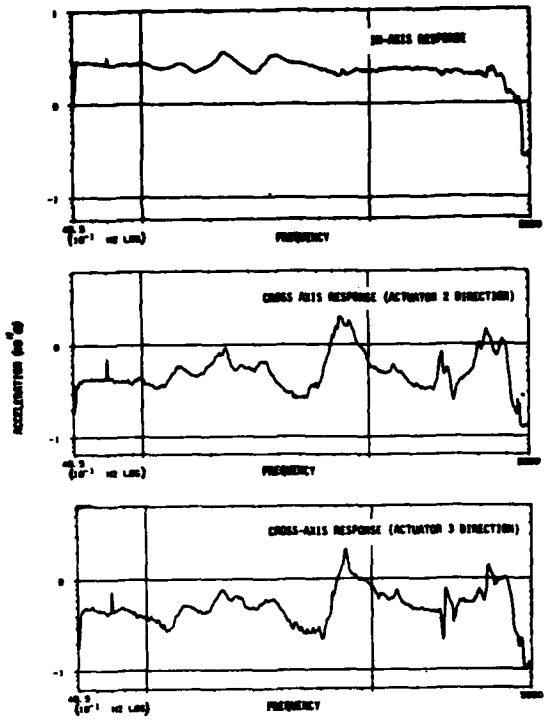

FIGURE 4. ACCELERATION VS FREQUENCY PLOTS
1.8 G SINE SWEEP IN ACTUATOR AXIS

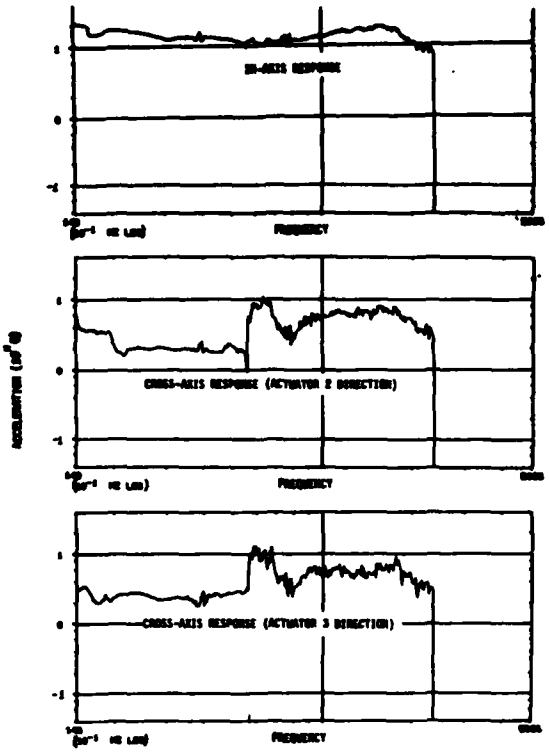

FIGURE 6. ACCELERATION VS FREQUENCY PLOTS
10 G SINE SWEEP IN ACTUATOR AXIS

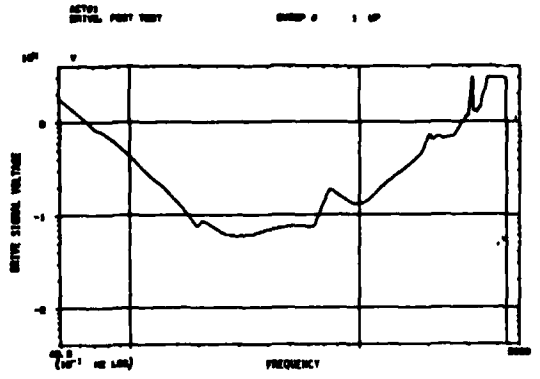

FIGURE 5. DRIVE SIGNAL
1.8 G. SINE SWEEP IN ACTUATOR AXIS

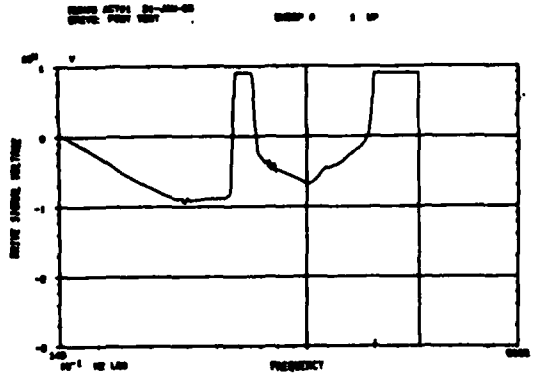

FIGURE 7. DRIVE SIGNAL
10 G SINE SWEEP IN ACTUATOR AXIS

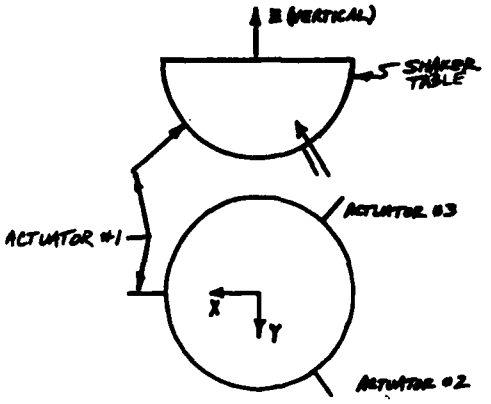

Figure 8. X,Y,Z Gravitational Coordinate Definition

As an initial test, a loaded table condition with excitation in the Y direction was chosen for a sine sweep study. A 184 lb block of steel with dimensions 8" x 9" x 9" was bolted to the shaker table with its center of gravity located 4 inches vertically from the table surface and centered laterally. The triaxial accelerometer was fixed to the top of the steel block and oriented with the X, Y, and Z axes. A logarithmic sweep of ten minute duration was run in the Y direction starting at 15 Hz for a maximum peak displacement of one inch. Data reduction was similar to the other sine sweep runs.

Figure 9 shows unfiltered acceleration vs frequency plots for the triaxial accelerometer. Cross axis response levels in the vertical (Z) direction are roughly 60% below the in-axis response from 15 to 45 Hz, and an average of 40% below the 10g in-axis level at frequencies above 64 Hz. From 45 to 64 Hz, vertical cross axis levels reach 10g. Lateral cross axis (X) levels reach the in-axis level over much of the frequency range. These effects will require further investigation. The drive signal required for this lateral axis sweep (figure 10) displays the same characteristics found in earlier sweeps. Maximum drive occurs at 120 Hz, and the sweep was aborted at approximately 240 Hz.

Three axes random vibration testing was conducted to determine the capability of the shaker system to accurately reproduce a random vibration environment in three axes simultaneously. For this test a realistic test item and setup was desired. The AIM-9L "SIDEWINDER" missile was chosen as a test specimen. The missile basic characteristics are length, 9.5 feet, diameter, 5 inches and weight, 190 pounds. High level buffet vibration response data was available from captive flight studies of another SIDEWINDER missile (reference 8) wherein triaxial vibration data had been collected from the guidance and control section bulkhead of the missile and presented as power spectral density (PSD) plots corresponding to the longitudinal, lateral, and vertical axes of the missile.

For the shaker test, the missile was mounted to a SIDEWINDER launcher which was bolted to an adapter block. The adapter block was bolted to the shaker head so that the center of gravity (CG) of the load was approximately centered over the CG of the shaker table. The control triaxial accelerometer was bonded to the missiles gas bottle cavity at essentially the same location as for the captive flight measurements.

The PSD's presented in reference (8) were re-defined in terms of break points (PSD vs frequency) and entered into three vibration control computers which were assigned to control response in the X, Y, or Z direction. Each channel from the triaxial accelerometer was fed back to the computer assigned to control response in that direction. During the test, accelerometer response and irig B timing was recorded. Data was taken at the full response level upon equalization of the controllers.

Figure 11 displays 3 PSD plots taken from the triaxial control accelerometer response signal. Also shown are the desired responses as defined for each X, Y, and Z direction. With the exception of the vertical response PSD, a reasonably good match was obtained between desired and achieved levels.

The result obtained here is a significant achievement, particularly in consideration of the inherent difficulty of control due to test item complexity and the fact that the flight data used for control purposes was envelope of data taken from the vibration response of a different

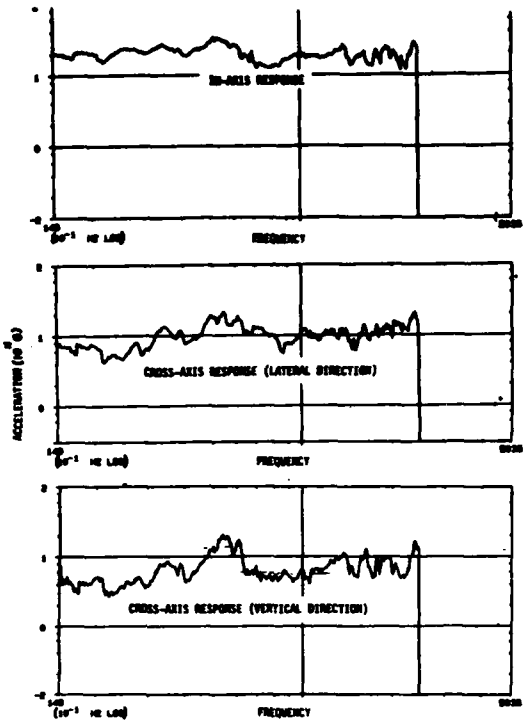

FIGURE 9. ACCELERATION VS FREQUENCY PLOTS
10 G LATERAL SINE SWEEP

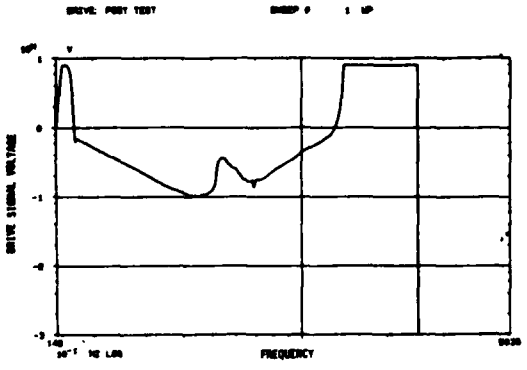

FIGURE 10. DRIVE SIGNAL
10 G. LATERAL SINE SWEEP

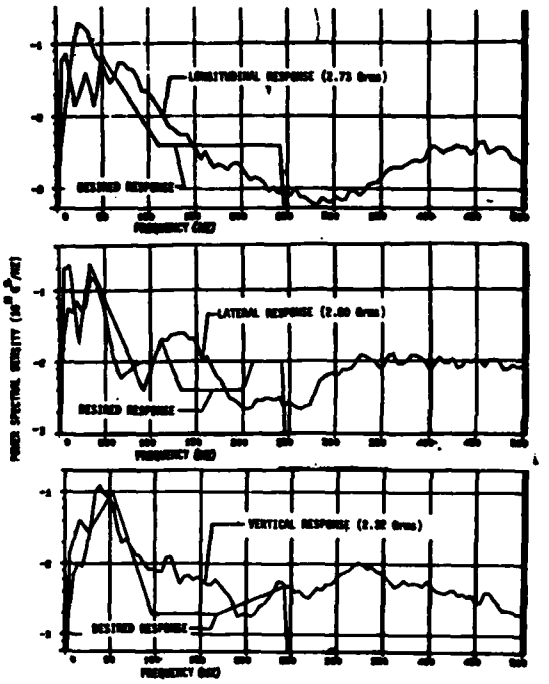

FIGURE 11. POWER SPECTRAL DENSITY PLOTS
3-DIMENSIONAL RANDOM VIBRATION TEST

SIDEWINDER missile. The simultaneous use of three vibration controllers in conjunction with the three dimensional shaker assembly has now been proven quite feasible.

These initial test results provide some insight into the behavior of the triaxial shaker system. The rather high cross-axis response seen in certain frequency bands in the sine sweep data need to be explained and eliminated if possible. Additional simultaneous-three-dimensional vibration testing will be carried out with various test items to better define the advantages and limitations of the present triaxial vibration system.

RECOMMENDATIONS

A recommendation is made for the evaluation of the current triaxial system to determine its applicability for environmental and reliability vibration test programs. The following evaluation tests are proposed:

1. Actuator Frequency Response

   Examine frequency response and moment resistance at maximum and 10 percent of maximum levels using sine wave input.

2. Directional Response (X, Y, Z gravitational).

   Examine frequency response and moment resistance at maximum and 10 percent of maximum levels using sine wave input to demonstrate purity of convential axis testing.

3. Random Vibration Response. Explore random vibration reproduction for possible use in test programs.

4. Experimental Test Comparison. Validation of test vibration reproduction in three axes by comparison of PSD's for a particular test component and prove reduced resource requirements.

   Table 2 illustrates the load condition, frequency range, and acceleration levels for the tests listed above.

TABLE 2. TRIAXIAL SYSTEM TESTS

AXIS DIRECTION	EMPTY MAX g 2-500 hz	200#X50#' MAX g 2-500 hz	200#X50#' 10% g 2-500 hz	100#X15#' MAX g RANDOM	100#X15#' 10% g RANDOM	COMPONENT FLIGHT VIB
ACTUATOR no. 1	X	X				
ACTUATOR no. 2	X	X				
ACTUATOR no. 3	X	X	X	X	X	
VERTICAL	X	X				
LATITUDE	X	X				
LONGITUDE	X	X	X	X	X	
3-D TRIAXIAL						X

REFERENCES

1. Elements of Vibration Analysis, L. Meirovitch, McGraw Hill Inc., 1975, Chapter 3.

2. Classical Mechanics, H. Goldstein, Addison-Wesley Publ. Co., 1950, Chapter 1.

3. "A Three Dimensional Vibration System", F.M. Edgington, Shock and Vibration Bulletin 46, August 1976. Part 3, pages 15-26.

4. Elementary Differential Equations, W.E. Boyce and R.C. DiPrima, J. Wiley & Sons, Inc., 1977, Chapter 3.

5. "Seismic Testing/Seismic Simulators", Sopemea-Aeronautical and Space Industry Laboratories, Villacoublay Cedex, France. Technical Note No. 654, 1982.

6. "Six Degree of Freedom Vibration Stress Screening", G.K. Hobbs and R. Mercado, Proceedings of the Institute of Environmental Sciences, May 1-3 1984, pages 280-288.

7. Directory of Services, Wyle Laboratories, Norco, CA. 1984, page 31.

8. "Results of the F/A-18/AIM-9L Captive Flight Test Program (Wing Tip Station) and Vibration Compatibility Assessment", J.D. Grimsley, NWC Technical Memorandum 5010, March 1983.

APPENDIX

Calculation of model parameters.

Stiffnesses

Compressive stiffness of a rod bundle is just the stiffness of one rod times the number in a bundle.

$$K_c = N \frac{Ea}{\ell}$$

Each rod is 1/16 inches in diameter and made of steel, so:

$$= 6000 \frac{10^7 \text{ lb/in}^2 (1/16 \text{ in})^2 \pi/4}{10 \text{ in}}$$

$$= 1.84 \times 10^7 \text{ lb/in}$$

$$= 22.1 \times 10^7 \text{ lb/ft}$$

Shear stiffness of a bundle is just the stiffness of one rod times the number in a bundle. For a single rod the formula may be found in any text covering beam design

$$K_s = N \frac{12 E I}{\ell^3}$$

Here I is the second-moment of cross-sectional area of a single rod. Since the rods are circular

$$I = a \frac{d^2}{16} = 0.757 \times 10^{-6} \text{in}^4$$

Substituting yields

$$K_s = 6000 \frac{12 \times 10^7 \text{ lb/in}^2 \times 7.57 \times 10^{-7} \text{in}^4}{8 \times 10^3 \text{ in}^3}$$

$$= 553 \text{ lb/in}$$

$$= 6.64 \times 10^3 \text{ lb/ft}$$

The angular stiffness of the rod bundle comes primarily from the stretching of the rods on one side and the compression on the other. The stiffness is most easily evaluated by treating the whole bundle as a circular tube whose wall cross-section has area Na. When the platen rotates through angle θ about, say the x-axis actuator, one edge of the z-axis rod bundle is depressed by rθ (where r is the radius of the bundle) and the other edge is extended by the same amount. The bundle is also sheared, as shown in figure 2, but this contributes relatively little to the restoring moment.

The linear variation of strain from one side of the bundle to the other is the same as that in a bent beam so the restoring moment is given by:

$$M = \frac{I_B \sigma}{r}$$

where I_B is the second-moment of area of the bundle cross-section and σ is the stress in the outermost part of the bundle. The latter may be calculated as the stress in a rod at the edge of the bundle times the rod area per unit bundle area.

$$\sigma = \frac{E r \theta}{\ell} \frac{Na}{\pi (r_2^2 - r_1^2)}$$

where r_2 and r_1 are the outer and inner radii of the bundle (6.625 in and 6.063 in).

The cross-section moment is given by:

$$I_B = \pi (r_2^2 - r_1^2) \frac{(r_2^2 + r_1^2)}{4}$$

On substituting into the moment equation the stiffness (moment per unit angle) is found to be

$$K_\theta = \frac{M}{\theta} = \frac{(r_2^2 + r_1^2) E Na}{4}$$

$$= 37.1 \times 10^7 \text{ in lb/rad}$$

$$= 30.8 \times 10^6 \text{ ft lb/rad}$$

The hydraulic stiffness is given by

$$K_h = 2 \frac{BP}{(s/2)}$$

where B = bulk oil modules, 2.5×10^6 lb/in^2

P = piston area, 2.5 in^2

S = stroke, 3.5 in

The value is

$$K_h = 0.712 \times 10^6 \text{ lb/in}$$

$$= 8.856 \times 10^6 \text{ lb/ft}$$

The three inertias are simpler to calculate. The platen-plus-test-item mass is just (by hypothesis) the mass of a magnesium sphere with a one foot radius

$$M = \frac{4}{3} \pi r^3 P$$

$$= \frac{4}{3} \pi (108.7 \text{ lb/ft}^3)$$

$$= 455 \text{ lb}$$

$$= 14.13 \text{ slg}$$

The moment of inertia is given by

$$I = M \frac{2}{5} r^2 = 5.56 \text{ slg ft}^2$$

The hydraulic ram weight is 26 lb (manufacturers' data) and the aluminum spider adds about 4 lbs, so

$$M = 30 \text{ lb} = 0.93 \text{ slg}$$

DISCUSSION

Mr. Hinckley (Boeing Aerospace Company): How are the rod bundles attached to the adapter flange?

Mr. Helfrich: They are stacked up; they are almost press-fitted. Then we use a very high strength epoxy glue.

Mr. Hinckley: Are they attached as a bundle?

Mr. Helfrich: You jam the rods down into the adapting flange as tight as you can get them. You jam as many rods as you can get in the area machined out of a flange.

Mr. Hinckley: Do the rods just go around the outside edge, or are they a solid bundle?

Mr. Helfrich: No. The outside edge is a cylinder. The wall thickness is about a half inch around the cylinder. We jammed as many rods as we possibly could, and then we used a high strength epoxy to fill in the spaces.

Mr. Volin (Shock and Vibration Information Center): Were the natural frequencies predicted with any type of a payload on the table?

Mr. Helfrich: No. It was with an empty table.

Mr. Volin: How much effect will a payload have on the natural frequencies you predicted?

Mr. Helfrich: We don't know because we really don't have that much experience with it with it running. We don't expect them to come down too much more because the plate and the mass are rather large to begin with; they weigh almost 200 pounds. By adding another 200-pound object, with the high stiffness of the rods, we wouldn't expect the natural frequencies to come down by 100 or 200 Hz or anything like that.

Mr. Volin: It seems if the payload is highly reactive, it might act as a dynamic absorber, and it might make substantial differences in the natural frequencies.

Mr. Helfrich: That is a possibility. We did a very quick analysis which took us about a week and a half. We wanted to see if we would run into any natural frequencies on the way, like for a first start-up kind of thing, when we started to run it.

Mr. Anderson (Rosemount, Inc.): If you were to use a machine like this for high speed aircraft, requiring higher frequencies, what would have to be changed in your design?

Mr. Helfrich: We would have to go back and look at the stiffness of the rod bundles and possibly change the platen mass somewhat. That is really what the natural frequencies depend on. The way it is set up now, it has quite a few degrees of freedom. So it is hard to limit the degrees of freedom, and therefore, to control some of the natural frequencies. I really don't know what we would do if we had to go to 2 kHz.

Mr. Anderson: So, you think there might be some real design limitations in going too much higher in frequency?

Mr. Helfrich: There may be. You may need some very strange modifications. We really haven't looked into that.

Mr. Thomas (Grumman Aerospace): How did you arrive at the configuration? Did you try any other types of configurations?

Mr. Helfrich: You mean the use of rods?

Mr. Thomas: Yes. The use of rods themselves.

Mr. Helfrich: I think that came about because we wanted it to flex in several directions. The cylinders have a lot of strength, and they are very stiff in bending. If we just used a rectangular plate that was solid with rods, it would flex, but by using a cylinder, it is much stiffer. So, that was the motivation to go to a cylinder. Then, we inverted it upside down, rather than off the side, because that way we can hang some missile packages on it and not interfere with the rod bundles.

INITIAL DESIGN AND TESTING OF A UNIQUE HIGH FREQUENCY FATIGUE TEST SYSTEM

David I.G. Jones
Materials Laboratory (AFWAL/MLLN)
Wright-Patterson AFB, Ohio 45433

The development of a high-frequency resonant fatigue test system for investigating crack initiation and propagation behavior in test specimens under combined low cycle (LCF) and high cycle (HCF) loading is described. The system offers significant advantages in low cost and simplicity. The paper describes initial dynamic response predictions for the prototype system, and comparisons with experimental measurements. Plans for improvement and implementation of the system are briefly discussed.

INTRODUCTION

The High Cycle/Low Cycle (HCF/LCF) Problem

Materials used in rotating components of jet engines are subjected to unusually severe environmental conditions during their operational life times. In particular, rotating components such as disks and blades are sometimes subjected to combined high temperature excursions, high "steady" stresses from centrifugal loads and significant high frequency "dynamic" stresses from resonant vibration response, so that a typical component might experience cycles of temperature and stress as illustrated in Figure 1. The resulting thermal-mechanical cycling of the component material can lead to initiation and propagation of cracks at voids, defects or scratches. The crack initiation and propagation characteristics of materials used in jet engine components vary widely, according to whether the material is ductile or not, and depend on temperature, low cycle stress (steady), high cycle stress, frequency, dwell time, local atmospheric conditions and many other parameters. Test methods to obtain such data vary widely, but generally do not deliver realistic operational conditions to the specimen. In particular, few material test systems can independently control low cycle and high cycle loads, even in accordance with simplified thermal-mechanical cycles, over a wide frequency range, and most test systems are limited to a high cycle frequency of at most a few hundred hertz. For example, most servo-hydraulic systems can combine low cycle loads with high cycle loads at frequencies up to about 40 Hz. A few electromechanical systems can operate at frequencies up to 500 Hz, and sometimes more when using system resonances. None of these systems are simple or low cost, however, and a need exists for a test system which is simple, low cost, and operates at very high frequencies with high deliverable tensile loads.

Current Test Approaches [1-6]

Figure 2 illustrates one approach to inducing combined high frequency/low cycle loads in a test specimen [1]. The low cycle load is provided by a pneumatic system. The shaker table is free to operate at any selected frequency and with any current input (within equipment limits) and hence provide the high frequency load. The high frequency load amplitude is limited at very high frequencies by the mass of the shaker table and attached specimen and grip so that, even with a large shaker, very limited HCF load capability is available above 1000 Hz. Figure 3 illustrates some possible ways of introducing high frequency HCF loads into a specimen. In the free-free system, the specimen acts as one of the springs joining the free masses and the first non-rigid body mode can be excited at the frequency $\omega_f = \sqrt{2k/m}$, where k is the net stiffness joining the two masses. In the clamped-free

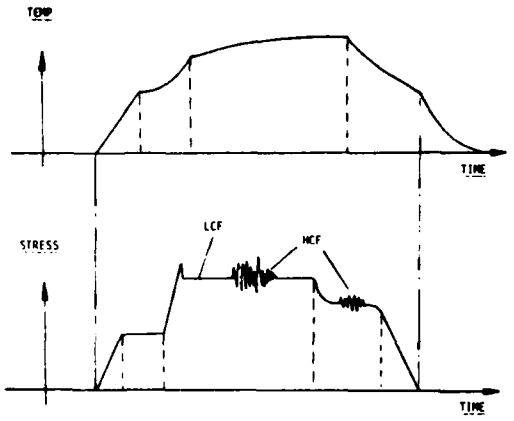

Figure 1. Idealized Thermal-Mechanical Cycle

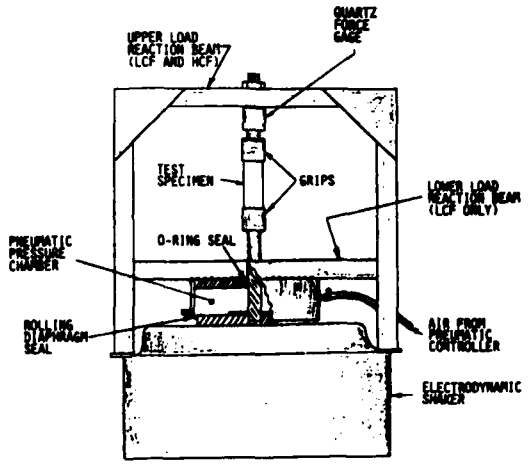

Figure 2. A High Frequency HCF/LCF Test System (Goodman [1])

system, resonance occurs for the one-degree of freedom system at a frequency $\omega_r = \sqrt{k/m}$. These idealized concepts have been used in some limited instances to study crack initiation at very high frequencies. However, it is difficult to produce satisfactory test arrangements, because the mass(es) must be supported and the frequency of the system changes as the crack grows in the specimen. Table 1 summarizes some of the advantages and disadvantages of existing test systems.

Requirements for a High Frequency HCF/LCF Test System

A low cost high frequency HCF/LCF test system must meet certain criteria in order to be viable, including (a) The system must operate at a resonance so that the resulting magnification of HCF loads minimizes the high frequency excitation forces required, (b) The damping in the mode of vibration used must be very low so that the magnification can be as high as possible, i.e. the system must be supported at anti-nodal points; all sources of damping, such as joints and interfaces, must be minimized, (c) The means of applying the LCF load must be structurally uncomplicated and effective, (d) The system must be very stiff, so that the resonant frequency of the system does not change significantly as the crack in the specimen propagates during a test, and (e) introducing and removing the specimens should be simple and positive. Other conditions will probably emerge over time, but the above conditions are enough to be getting on with. Not many concepts can be found to meet all or most of these conditions.

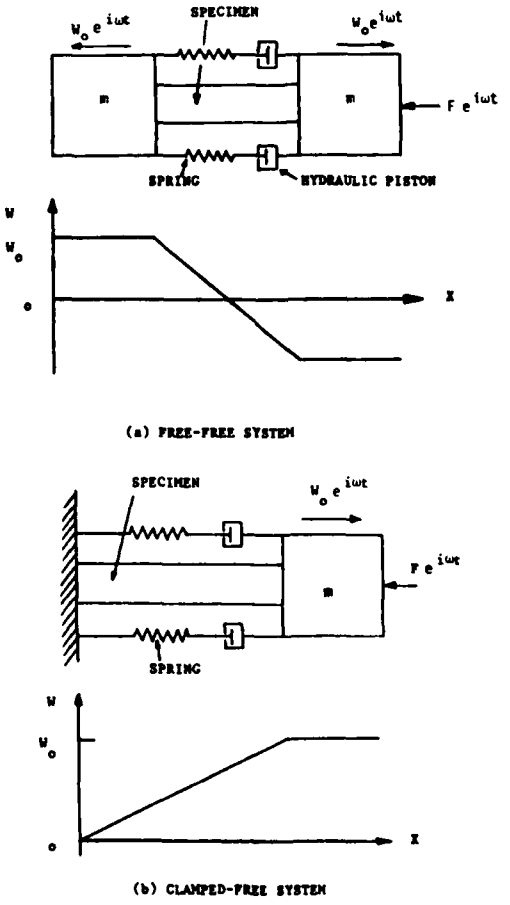

Figure 3. Some very high frequency HCF/LCF Concepts

TABLE 1. CURRENT APPROACHES

SYSTEM	FREQUENCY RANGE	ADVANTAGES	DISADVANTAGES
Most Current Servo Hydraulic Systems	0 to 30 Hz	• Well established technology	No high frequency capabilities
Instron (M0121) [3]	0 to 600 Hz	• Commercially available system	• Expensive • Care needed to avoid poor dynamic stress distribution in specimen
Goodman Shaker [1]	0 to 1000 Hz	• Modification of existing equipment	• Relatively low cost • Limited load capability at high frequency
Ultrasonic Systems (Longitudinal stress waves)	10,000-100,000 Hz	• Only present approach to very high frequency	• Nonuniform stress field in specimen • Frequency changes as crack grows

Proposed New Test System

Figure 4 illustrates the concept for a new resonant system which may meet the above criteria [7]. The resonance in which the system is excited by the driving force at point 5 is the two-nodal diameter mode, for which the lines AA and BB are nodal planes. The supports at points 2 are therefore placed at nodal points. The low damping ensures that enough magnification can be achieved at resonance to satisfy conditions (a) and (b). If the thickness, width, and diameter of the ring are selected properly, the stiffness of the ring can be made much greater than that of the specimen (preferably at least 10 times), so that crack propagation in the specimen does not change the resonant frequency to an excessive degree, thereby satisfying condition (d). The hydraulically loaded piston, if designed properly, can apply the LCF load in a direct manner, with adequate control and without significant modification to the designed system dynamics. The HCF loading at point 5 can be provided by an electrodynamic shaker.

PROTOTYPE SYSTEM DESIGN AND ANALYSIS

Prediction of Frequencies and Modes

The basic concept of this test system is that of a cylindrical shell vibrating in its low order modes, sketched in Figure 5. The N = 2, M = 0 mode is particularly suitable for this application, since the two points corresponding to the ends of the specimen vibrate at maximum amplitude and the nodal diameters at the ±45 degree positions are very suitable as support positions. Initial analytical prediction of the natural frequencies of the system without specimen was accomplished using a particular set of shell equations developed by Miller [8]. The resonant frequency f_N, corresponding to the order N of the mode (for M = 0), is given by the approximate expression:

$$f_N = \frac{\omega_N}{2\pi} = \frac{1}{2\pi}\sqrt{\frac{E\,H^2N^2(1-N^2)^2}{12\,\rho\,R^4(1-\nu^2)\,(1+N^2)}} \qquad (1)$$

with f_N in Hz and E, H, ρ and R in any consistent system of units. Note that N = 0 and N = 1 give f_N = 0, corresponding to rigid body modes. One restriction on the use of equation (1) is that the parameter $\beta = H^2/12R^2$ be small, though specific limits are difficult to define, so that the application of equation (1) to very thick shells will involve some error.

Prediction of Forced Response

In the thin shell theory used by Miller, the two dimensional mode shapes for M = 0 and N = 2, 3 and 4 are assumed to be of the form:

$$\Phi_N = \mathrm{Sin}\,(N\theta) \qquad (2)$$

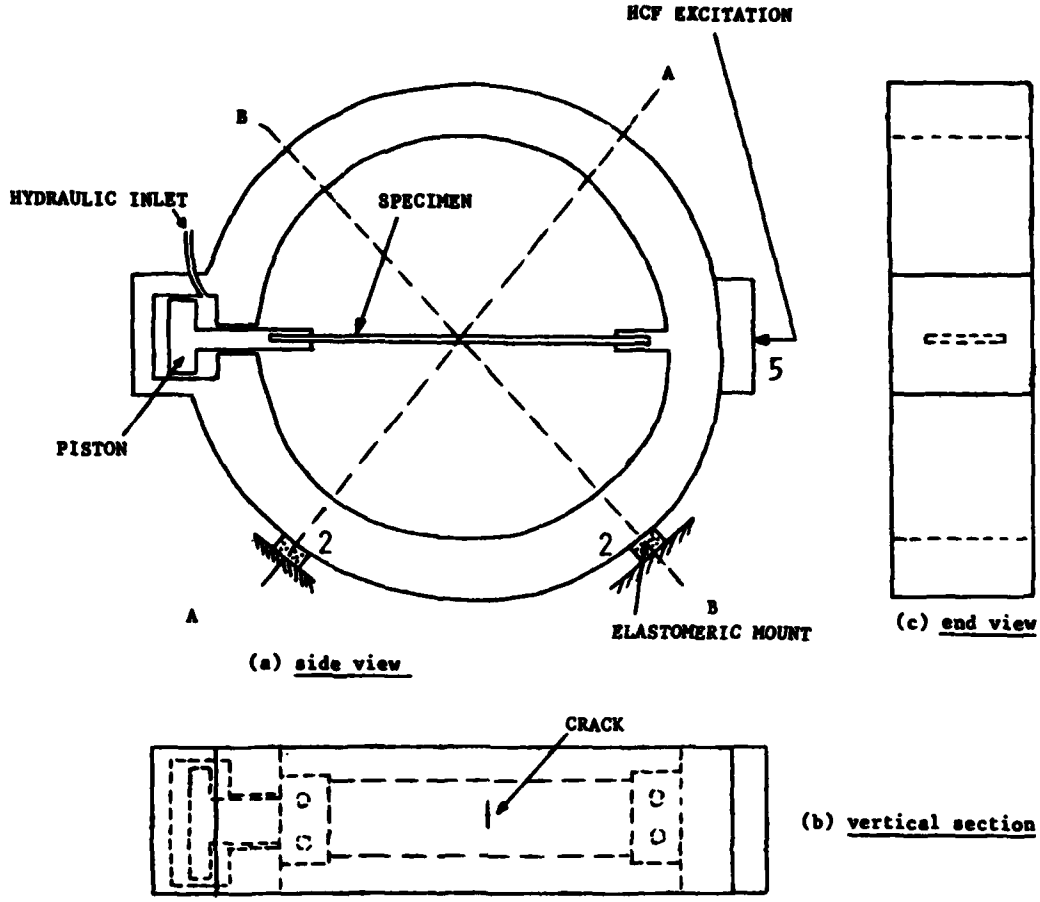

Figure 4. Proposed high frequency HCF/LCF System (Project Theta)

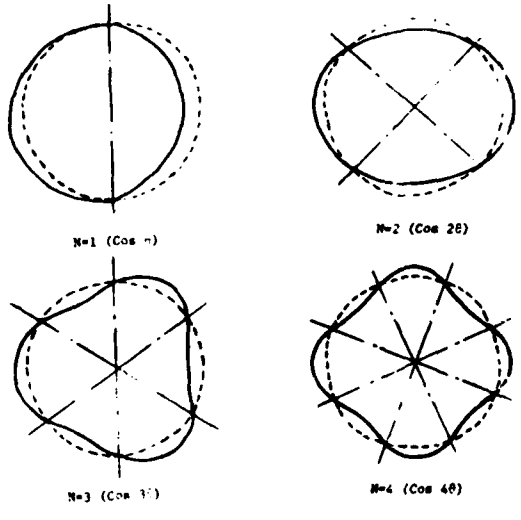

Figure 5. Typical two-dimensional modes of circular cylinder

the coordinate system being r in the radial direction, z in the axial direction and θ in the tangential direction. If it is assumed that, in the modes of interest, deformations in the z direction and along the axis of the shell are small, then the equation of motion will involve only the radial displacement W and may be written in the form:

$$\psi W(\theta, z) + \rho bH \frac{\partial^2 W(\theta, z)}{\partial t^2} = F(\theta, z) \quad (3)$$

where ψ is a complicated operator in the space variables (θ,z) which depends on the specific shell equations used. However, given the mode shapes and resonant frequencies from equations (1) and (2), we may use the homogenous form of equation (3) to give the relationship:

$$\psi \Phi_N(\theta, z) = \rho bH \omega_N^2 \Phi_N(\theta, z) \quad (4)$$

This, along with the orthogonality properties of the modes, enables us to predict the forced response. If a discrete line force $F\delta(R\theta - R\theta_1)e^{i\omega t}$ is applied along the line $\theta = \theta_1$, then (3) becomes:

$$\psi W(\theta, z) - \rho bH\omega^2 W(\theta, z) = F\delta(R\theta - R\theta_1) \qquad (5)$$

which is solved by using the series representation of $W(\theta, z)$:

$$W(\theta, z) = \sum_{N=1}^{\infty} W_N \Phi_N(\theta, z) \qquad (6)$$

Substituting (6) into (5), factoring by $\Phi_m(\theta,z)$, and integrating over the area gives:

$$W_N \rho bH (\omega^2_N - \omega^2) \int_0^{2\pi R} \mathrm{Sin}^2(N\theta)\, Rd\theta =$$

$$= F \int_0^{2\pi R} \delta(R\theta - R\theta_1)\, \mathrm{Sin}(N\theta)\, Rd\theta$$

$$\therefore \quad W_N = \frac{F \Phi_N(\theta_1)}{\pi\rho HR(\omega_N^2 - \omega^2)} \qquad (7)$$

Since $m = 2\pi\rho HR$ is the mass per unit width of the cylinder, the receptance α_{12} is:

$$\alpha_{12} = \frac{W(\theta_2)}{F(\theta_1)} = \sum_{N=1}^{\infty} \frac{\Phi_N(\theta_2)\,\Phi_N(\theta_1)}{(m/2)(\omega_N^2 - \omega^2)} \qquad (8)$$

Equation (8) gives the complete response of the system to a line force at any station θ_1. If, as must happen in practice, a small amount of damping exists, we must replace ω^2_N in equation (8) by $\omega^2_N(1 + i\eta_N)$, where η_N is the modal loss factor, so that:

$$\alpha_{12} = \sum_{N=1}^{\infty} \frac{\Phi_N(\theta_2)\,\Phi_N(\theta_1)}{(m/2)\left[\omega_N^2(1+i\eta_N) - \omega^2\right]} \qquad (9)$$

For the $N = 2$ mode, $\Phi_2(0) = \Phi_2(\pi) = 1$ so that, at the specimen extremities, the net peak excursion at resonance is:

$$\Delta W = W(0) + W(\pi) = \frac{2F}{(m/2)\omega_2^2\,\eta_2} \qquad (10)$$

Equation (10) allows one to calculate the value of the driving force F needed to generate a specific excursion ΔW for given modal mass (m/2), resonant frequency ω_2 and modal loss factor η_2. Specifically:

$$F = \frac{1}{4} m \omega_2^2 \eta_2 \Delta W \qquad (11)$$

In order to keep F as low as possible, one must reduce the modal loss factor η_2 since the effective modal stiffness $k_2 = m\omega_2^2/4$ should not be reduced beyond the point where it is at least ten times the specimen stiffness ($k_s = EA/L$). If the stiffness is determined in a static loading test, where a force F is applied at both ends of a diameter, the displacement ΔW is equal to $4F/(m/2)\omega_2^2\,\eta_2$, not the value given in equation (10), so that the effective static stiffness is $k_2/2$. For a steel ring of 8 inches outer diameter, 5 inches inner diameter, 4 inches width, for example, m is about 36.8 Lb., and $k_2 = 1.25 \times 10^7$ Lb./in. For a specimen 0.09 inches thick, 1.5 inches wide and 4 inches long, $k_s = 1.01 \times 10^6$ Lb./in. If the maximum HCF stress in the specimen is σ_{max}, then $\sigma_{max} = E_s \Delta W_{max}/L$. Therefore, equation (11) gives the value of F needed:

$$F = k_2 \eta_2 L\sigma_{max} / E_s \qquad (12)$$

For $k_2 = 1.25 \times 10^7$ Lb./in, $\eta_2 = 0.005$, $L = 4$ in., $\sigma_{max} = 10^4$ Lb./in^2, $E_s = E = 3 \times 10^7$ Lb./in^2, then $F = 83.3$ Lb. and $\Delta W = 0.00133$ in. These numbers indicate that it is feasible to obtain the loads and displacements desired.

First Prototype Configuration

Dimensions were sought to give a frequency f_2 of about 3 KHz, well above any frequency achieved previously, and a stiffness ten times that of the specimen. The geometry selected was a steel ring of outer diameter 8 inches, inner diameter 5 inches, width 4 inches as illustrated in Figure 6. The frequency f_2 was predicted through equation (1) to be 3648.3 Hz. Figures 7 to 9 show the specific test configuration for Prototype I. The ring is supported by two rubber pads ("isomode") at the 45 degree stations, corresponding to the node lines in the N = 2 mode. The specimen was held by two machined grips which were passed through slots cut in the ring and then bolted in place. The

tension in the specimen was set to correspond to a torque of about 300 in-Lb applied through the two bolts A and B in Figure 6. Figure 7 shows two observation ports that were cut into the ring to allow examination of the specimen during a fatigue test. These, unfortunately, introduced excessive non-symmetry into the system and will be eliminated in later prototypes.

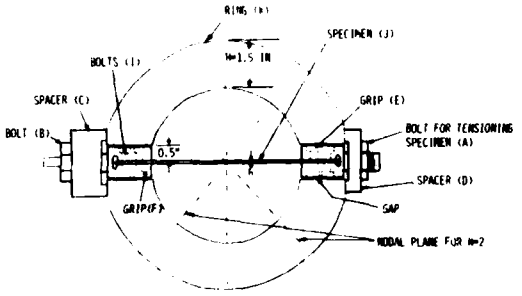

Figure 6. Prototype 1 Geometry (Project Theta)

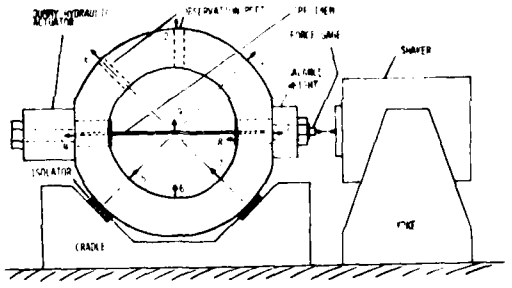

Figure 7. Loading and excitation for Prototype 1

Figure 8. Test system for Prototype 1

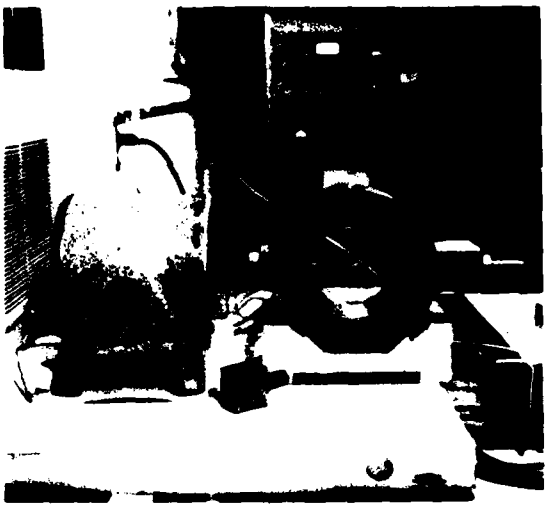

Figure 9. Test system for Prototype 1

DYNAMIC TESTING OF FIRST PROTOTYPE SYSTEM

Measurement of Receptances and Mode Shapes Without Specimen

The system was excited by a small electrodynamic shaker as illustrated in Figure 7. The force was measured at the excitation point by a force gage and the acceleration response was picked up by a miniature accelerometer placed successively at various points on the ring. The points were identified by a set of number pairs (i,j), the first set i defining the plane of excitation (in the plane of the ring), the plane i = 0 being the face at which the system was excited, the plane i = 1 being the mid-plane and the plane i = 2 the opposite face. The second set of numbers j represented the angular position, counting counter clockwise from the point of excitation. Typical compliance spectra, measured by a digital sine-sweep test system [9], are illustrated in Figure 10 for the ring having no test specimen. The N = 2 mode is clearly seen, and occurred at a frequency of about 2850 Hz, lower than predicted, partly because of the observation ports cut in the ring.

Mode shapes were measured by setting the excitation frequency at each peak in turn, and

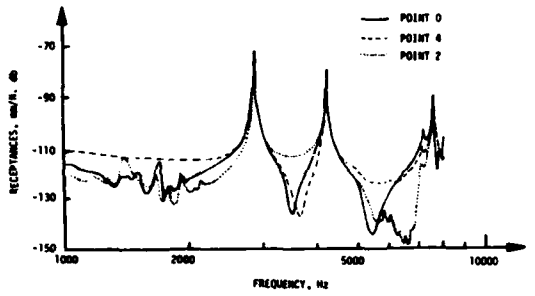

Figure 10. Measured receptance versus frequency plot (excitation at 00, no specimen)

moving the accelerometer around the ring, measuring successive amplitudes and phases between force and response. By this means, the N = 2 mode was observed as a twin mode at 2849 Hz and 2973 Hz, the two branches being at about 45 degrees to the other, and having slightly different frequencies because of the slight asymmetry of the system. Major modes observed are illustrated in Figures 11-15.

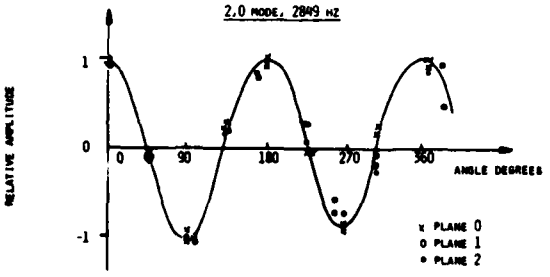

Figure 11. Mode shape at 2849 Hz (2,0 mode, no specimen)

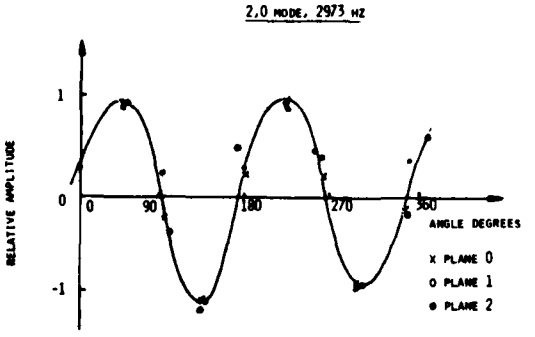

Figure 12. Mode shape at 2973 Hz (2,0 mode, no specimen)

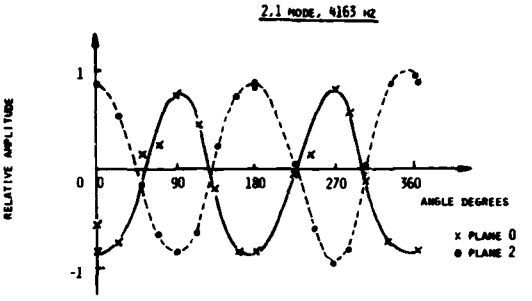

Figure 13. Mode shape at 4163 Hz (2,1 mode, no specimen)

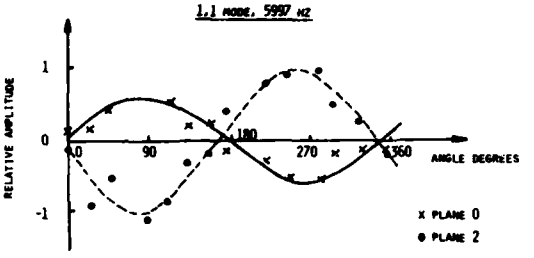

Figure 14. Mode shape at 5997 Hz (1,1 mode, no specimen)

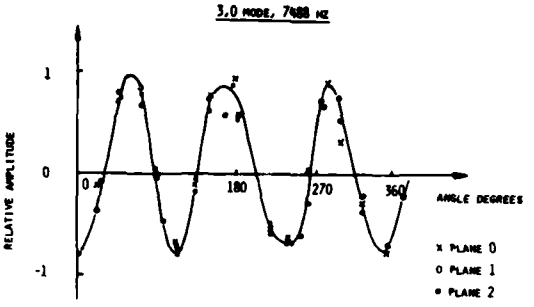

Figure 15. Mode shape at 7488 Hz (3,0 mode, no specimen)

Figure 16 gives the measured force spectrum, as measured by the force gage for a fixed shaker input current. It is seen that the force is high up to about 1800 Hz, but drops rapidly thereafter, being down by about 20 db at the frequency of the N = 2 mode. The dropoff after 1800 Hz is due primarily to the force needed to accelerate the shaker table.

Measurement of Receptances and Mode Shapes with Specimen in Place

Modal tests were now conducted for a

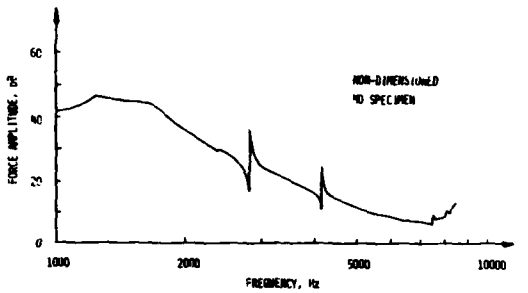

Figure 16. Measured force spectrum versus frequency (excitation at 00, no specimen)

specimen 2 inches wide by 0.093 inches thick by 5 inches long. The tension in the specimen was set manually to correspond to a torque of about 300 in-lb at the bolts. Typical measured response spectra are illustrated in Figure 17. It is seen that many peaks arise for which motion of the system differs greatly from those observed without the specimen, but the major peak near 2500 Hz corresponds to the N = 2 mode and is well-behaved. Point 8 is at one end of the specimen while point 9 is measured at the center of the specimen as illustrated in Figure 7. Figure 18 illustrates the N = 2 mode with the specimen in place. Note that some bending of the specimen occurs, caused by the slight asymmetry of the system.

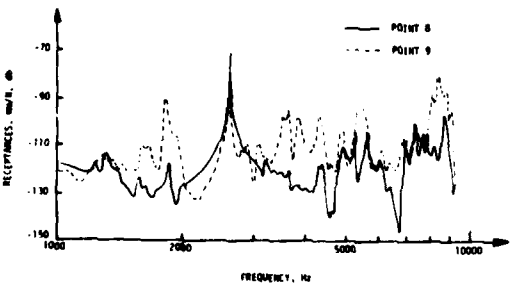

Figure 17. Plot of receptance versus frequency (excitation at 00, with specimen)

Measured Performance for Prototype 1

When the modal tests had been completed, the shaker input was increased to the maximum level attainable at the resonance frequency f_2 = 2500 Hz. The maximum acceleration measured at each end of the specimen was observed to be about 180 g's.

$$\therefore \Delta W = \frac{180 \times 2 \times 386}{(2\pi \times 2500)^2} = 5.61 \times 10^{-4} \text{ in.}$$

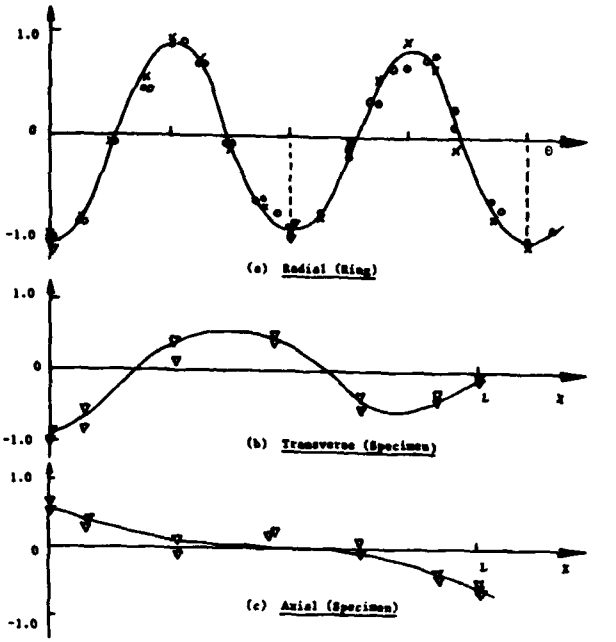

Figure 18. Mode shape at 2497 Hz (1,0 mode, with specimen)

For η_2 = 0.005 (giving a magnification of about 200) and m = 36.8 Lb., the driving force amplitude is calculated from equation (11) to be:

$$F = \frac{1 \times 36.8}{4 \times 386} \times (2\pi \times 2500)^2 \times 5.61 \times 10^{-4} \times 0.005$$

$$= 16.56 \text{ Lb}$$

This is about 10 db below the nominal maximum force of 50 Lb., and agrees quite well with Figure 16 at 2500 Hz. The estimated maximum stress in the specimen is:

$$\sigma_{max} = E_s \Delta W/L = 3 \times 10^7 \times 5.61 \times 10^{-4}/5$$

$$= 3365 \text{ Lb/in}^2$$

This is well below the maximum desired HCF stress, but it is clear that higher levels can be achieved by reducing the loss factor η_2, possibly to 0.002, increasing the driving force F, possibly to 30 Lb, by means of a larger shaker, reducing the length L, perhaps to 3 inches, and decreasing the width of the specimen. With all of these changes, σ_{max} could increase to about 15000 Lb./in².

Finally, the maximum transverse acceleration of the specimen was about 180

g's. This means that the transverse displacement of the specimen at 2500 Hz was about 2.80×10^{-4} in. The maximum bending stress in the specimen is given by:

$$\sigma_b = 3 \times 10^7 \times \frac{0.093}{2} \times \frac{\pi^2}{(5/2)^2} \times 2.80 \times 10^{-4}$$

$$= 617 \text{ Lb/in}^2$$

This is small compared with the HCF stress of 3365 Lb/in^2, mainly because the specimen was thin. The elimination of the asymmetry of the system should reduce this bending stress considerably.

DESIGN OF SECOND PROTOTYPE

A new design was developed to correct several of the undesirable features of the first prototype, including the orientation of the specimen, which in turn necessitated the observation ports. The new design has the specimen aligned in the plane of the ring, so that observation and heating of the specimen from the side will be possible. The basic form of this prototype is illustrated in Figure 19, and it is under construction at the time of writing.

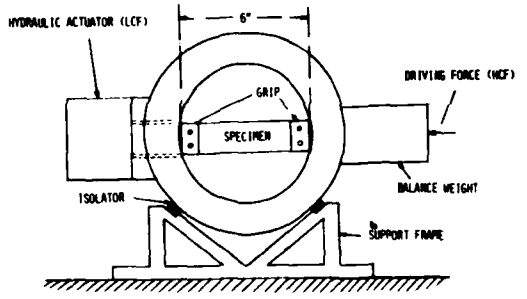

Figure 19. Proposed Geometry of Prototype 2

DISCUSSION AND CONCLUSIONS

The work conducted so far has established the feasibility of designing and manufacturing a high frequency HCF/LCF test machine to operate in the frequency range 2-5 KHz and apply HCF loads up to 10K Lb./in^2 and LCF loads up to 100 K Lb./in^2. The basic mechanical form of the system has been fixed, although details of size, specimen grip arrangements, hydraulic loading actuator, etc., have still to be optimized. The development of the control software to apply the HCF and the LCF loads in a programmed sequence, and to ensure that appropriate loads and temperatures are applied during the course of a test, as a crack grows, is not the subject of this paper. It is anticipated that several systems of this type will eventually be built, to conduct high frequency HCF/LCF tests on current and future advanced aerospace materials.

REFERENCES

1. R. C. Goodman and A. M. Brown, "High Frequency Fatigue of Turbine Blade Material", AFWAL-TR-82-4151, October 1982. (0-1000Hz+).

2. B. E. Powell and I. Henderson, "The Conjoint Action of High and Low Cycle Fatigue", AFWAL-TR-83-4119, Materials Laboratory, Air Force Wright Aeronautical Laboratories, November 1983.

3. Instron Major - Minor Cycling System (M0121 - Serial #). Company Literature, 1983 (0-600 Hz).

4. MTI/LAB Servo Hydraulic Vibration System (300 Hz and 2000 Hz systems), Company Literature, Latham NY, 1983. (0-2000 Hz).

5. MTS Servo Hydraulic Test Systems, Company Literature, 1983 (0-300 Hz).

6. ISI - Ling Dynamic Test Systems, Company Literature (0-180 Hz).

7. D.I.G. Jones, "Very High Frequency High/Low Cycle Fatigue Test Machine", Air Force Invention No 15,666, AF/JACPD, Wright-Patterson AFB, Ohio, 18 April 1983.

8. P. R. Miller, "Free Vibrations of a Stiffened Cylindrical Shell", ARC Report No. 19,338, L.A. 22, Aeronautical Research Council (UK), May 1957.

9. D. K. Rao, "Measurement of Dynamic Characteristics of a Structure using Programmed Sine Sweep Test", Proc. 3rd International Modal Analysis Conference, Orlando FL, January 28-31, 1985.

ACKNOWLEDGEMENTS

The concept of the subject high frequency HCF/LCF test system, discussed in this paper, was conceived in its essential form by the author, based on well known principles and practices in mechanics. Needless to say, however, the development, evaluation, refinement, manufacture and exploitation of the concept is a team effort. Particular aspects of the development program will be published by the individuals involved at the proper time. In the meantime, the author would like to express his appreciation to at least some of the individuals and organizations involved; including Conor Johnson and his colleagues at CSA Engineering, Palo Alto CA for preliminary Finite Element

Analysis, A. D. Nashif of Anatrol Corporation, Cincinnati OH, and T. Lagnese, AFWAL/MLTC, Dayton OH for the early modal tests, Dr D. K. Rao of the Indian Institute of Technology (currently an NRC Fellow at the Materials Laboratory) for developing software for digital sine-sweep testing of the prototype system and for control of HCF/LCF tests, R. C. Goodman of University of Dayton Research Institute, Dayton OH for assistance with some detail design and with application of strain gages for stress measurement, D. Koester of University of Dayton Research Institute, for detail design of the hydraulic actuator and second prototype, and R. Fields-Payne, R. Lemaster, and K. Draper for timely and efficient preparation of the manuscript.

NOMENCLATURE

b	breadth of ring
E	Young's modulus of ring material
E_s	Young's modulus of specimen material
F	amplitude of exciting force
f_N	resonant frequency of symmetric mode having N nodal diameters, Hz
H	thickness of ring
i	$\sqrt{-1}$
k_N	modal stiffness of N nodal diameter mode
k_s	specimen stiffness (longitudinal)
L	length of specimen
m	mass of ring
N	number of nodal diameters
t	time
W	radial response displacement amplitude
W_N	Nth component of modal expansion of W
z	station along axis of disk
β	nondimensional parameter $(H^2/12R^2)$
ΔW	relative HCF excursion of specimen across ring diameter
Φ_N	mode shape having N nodal diameters
ν	Poisson's ratio of ring material
ρ	density of ring material
σ_{max}	maximum HCF stress amplitude in specimen
σ_b	maximum bending stress in specimen
θ	Angular station around ring, measured anticlockwise from horizontal plane at point of excitation
ψ	Operator in space variables
ω_N	natural frequency of N nodal diameter mode (radians per second)
ω	circular frequency

INVESTIGATION OF MODES, FREQUENCIES AND FORCED RESPONSE OF A HIGH FREQUENCY FATIGUE TEST SYSTEM

Dantam K. Rao
David I. G. Jones
Air Force Materials Laboratory (AFWAL/MLLN)
Wright-Patterson AFB, OH 45433

A low cost, resonance based Fatigue Test System Prototype, designed for studying the crack-growth rates of turbine or disc blade materials under the combined action of a High Cycle Fatigue Load (HCF) and Low Cycle Fatigue Load (LCF), has been fabricated by the Materials Laboratory. This paper presents theoretical and experimental analysis of dynamic characteristics of this prototype structure. The theoretical investigation of natural frequencies and modes is carried out by the Finite Element Method using planar and solid elements available in NASTRAN. The experimental tests are conducted using a micro-computer based system STEPSINE (which plots the Frequency Response Function in real time), with the HCF/LCF machine excited by Stepped Sine excitation. Accelerance response of the structure is also measured by a commercial dual channel FFT analyzer. The natural frequencies calculated by the Finite Element Model are compared with experimental values measured by the STEPSINE system and FFT Analyzer. Factors affecting the accuracy and quality of the dynamic characteristics obtained by using these three methods are discussed.

1. INTRODUCTION

It is well known that critical components of aircraft jet engines, such as turbine blades and discs, are subjected to severe thermomechanical stresses. The complex static and dynamic loads on these key components can initiate a crack, or accelerate the growth of a pre-existing crack, affecting the total life of the jet engine. One major objective of current studies in the Materials Laboratory is to evaluate and judge the "resistance" of turbine blade or disc materials to crack initiation or crack-growth, and investigation into as how this resistance is affected by the High Cycle and Low Cycle (HCF/LCF) Fatigue loads.

The thermo-mechanical loads acting on the blade or disc can be broadly classified into three groups, viz.

(1) Low Cycle Centrifugal Forces due to rotation,
(2) High Cycle Dynamic Forces due to pulsating gas flows,
(3) Thermal Loads due to high temperatures of engine

All these real world loads on blades or discs are so complex that it is nearly impossible to simulate them exactly in the Laboratory. Hence, most of the HCF/LCF fatigue machines developed so far attempt to approximately simulate these real world load conditions by applying Laboratory-generatable and controllable loads on a blade material specimen.

A typical HCF/LCF Fatigue test machine essentially centers around a turbine disc or blade material test specimen, which is usually rectangular or hour-glass in shape. This specimen is rigidly gripped on both edges by two relatively stiff, accurately slotted rectangular grip blocks, and HCF/LCF loads are applied by electro-hydraulic or electro-pneumatic systems. Fig. 1 displays schematically the HCF/LCF load cycle applied to a test specimen. It shows that the load cycle consists of a Low Frequency Load (called Major Cycle) which simulates the centrifugal forces, with a superposed High Frequency Load (called Minor Cycle) which simulates the dynamic loads on the turbine blades. The specimen is further immersed in a thermal bath for controlled simulation of the operating temperatures of jet engine.

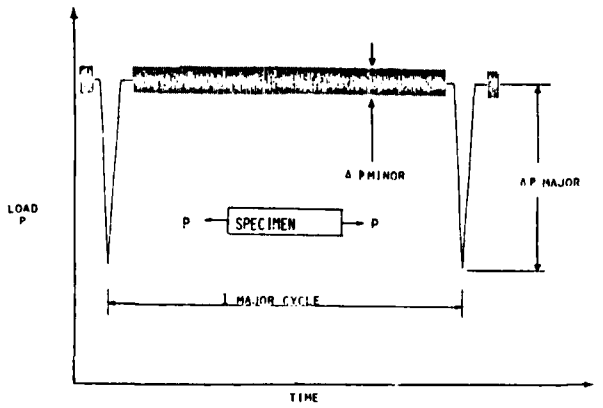

Fig. 1. Major/Minor Cycle Load Wave Form used for High Cycle Fatigue of Turbine Blade Material Program

Although these three characteristic loading requirements (HCF, LCF and thermal) for the blade Fatigue test machine are well known, their physical realization is beset with some difficulties. One of the major difficulty concerns with simultaneous application of low and high frequency loads. The technology for applying low frequency load is already well-developed, its end-product being a Tensile/Compression Test Machine. A different technology for applying dynamic loads also exists, its end-product being a electrodynamic or electro-hydraulic shaker. Obviously, combined HCF/LCF loading involves the marriage of these two widely different technologies. A few HCF/LCF test machines have been developed based on this concept, and are described in some detail in Refs [1] and [2]. All these HCF/LCF machines apply the LCF load (Major Cycle) to the specimen using an electro-hydraulic or electro-pneumatic system. They apply the HCF (Minor Cycle) load by using an electro-magnetic or electro-dynamic shaker system. THe HCF load generated by the shaker is transmitted only to the specimen, and not to the LCF loading system, by using properly designed isolators.

Such a design of HCF/LCF test machine has a built-in limitation on the performance envelope for the following reason. The excitation force f applied by the shaker on the specimen is

$$f = f_o - \omega^2 m x \qquad (1)$$

where

f_o = rated force output by the shaker

ω = frequency of excitation

m = mass of moving parts of shaker armature

x = vibration displacement of shaker armature

Thus, at low frequencies, the inertia force required to vibrate the moving parts of the shaker armature is low, and hence most of the shaker generated force is transmitted to the structure. However, as the frequency increases, more and more of the shaker-generated force f_o will be spent in vibrating its armature, and hence lesser force will be available to vibrate the structure. For example, a typical HCF/LCF machine, whose development and construction is documented in [1], can generate a dynamic stress of 8500 psi at 200 Hz in a 8 x 2 x .09 inch specimen. This applied dynamic stress reduces to 2000 psi at 1000 Hz and further to 500 psi at 2000 Hz. Thus it is clear that these machines cannot be used to test the turbine blade or disc material specimen at frequencies higher than about 1000 Hz.

Since dynamic stresses of up to 30000 psi at frequencies of up to 7000 Hz are not uncommon in aircraft jet engine blade components, it is thus imperative to explore alternative ways of generating HCF loads at higher frequencies. The principle of resonance, by which a structure can be made to vibrate severely at its resonance frequency by using a relatively small dynamic force, seems to be an attractive proposition. This principle forms the basis for the design of a new HCF/LCF machine developed by Jones [3]. Details of design calculations and development work regarding translation of this concept to a testable prototype are reported in Ref. [3]. As described in [3], this new HCF/LCF test system is based on the principle that, if a specimen is gripped inside a ring and the ring is vibrated in an elliptic mode such that the specimen ends are at the anti-nodes, pulsating forces are generated in the specimen due to resonance of the ring. The fabricated prototype of this HCF/LCF fatigue test machine forms the basis for comparison of theoretical and experimental results concerning natural frequencies, mode shapes, loss factors and frequency response which are reported in this paper.

2. DESCRIPTION OF HCF/LCF TEST MACHINE PROTOTYPE

Fig. 2 shows schmetically the principal hardware involved in the first prototype of the resonance-based HCF/LCF test machine. The cylindrical resonating ring shown in this figure has an inside diameter of 5 inches, outside diameter of 8 inches and width of 4 inches. A 6 in. long, 2 in. wide, .09 in. thick specimen, which is to be tested, is bolted between two rigid slotted end-grips and the entire assembly of specimen and grips is clamped to the ring along its horizontal diameter by means of external bolts and nuts as shown in Fig. 2.

The entire assembly of the ring, specimen and grips is placed on isolators supported by a

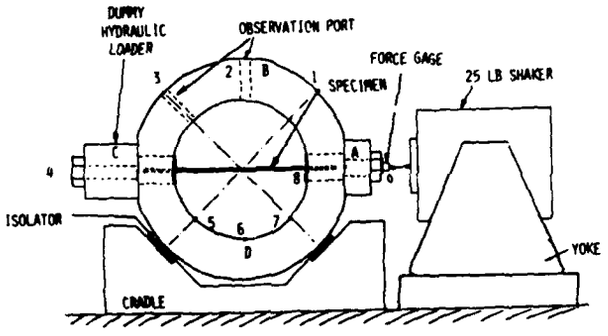

Fig. 2. Loading and Excitation for Prototype HCF/LCF test machine

heavy cradle. Observation ports are provided on the top of the ring to measure the growth of crack in the centre of the specimen. The Minor cycle Load is applied by resonating the ring in its elliptic mode using a horizontal shaker coupled to one end of the grip; the Major Cycle Load is proposed to be applied through a hydraulic device not shown in Fig. 2. As already explained, the design objective of this machine is to generate a 30000 psi stress in the specimen at a high frequency of 2000-5000 Hz when the ring is resonated in the 2 nodal diameter mode. Simple calculations show that, in order to generate 30000 psi in the specimen, its ends must vibrate with an amplitude of 2 mils at the design HCF frequency. This paper reports the theoretical and experimental investigations conducted on this HCF/LCF test machine, and compares resulting natural frequencies, modes and frequency response functions using three different techniques, viz, the FEM, an measurement system called STEPSINE and an FFT analyzer.

3. FINITE ELEMENT ANALYSIS

Even though the structure of the HCF/LCF machine shown in Fig. 2 appears simple and amicable to modelling by the Finite Element Method, actual development of an "acceptable" FEM model (which will predict natural frequencies and modes that are comparable to experimentally measured values) has turned out to be a not-so-easy task.

One of the first Finite Element Model that has been developed using MSC NASTRAN, shown in Fig. 3, simulates the ring by 8 solid HEXA elements around the circumference and two layers of elements along the 4 in. width of the ring. The specimen is modeled by 32 quadratic plate elements QUAD4 and TRIA3, whereas the grips are simulated by solid HEXA elements. Detailed description of this model and consequent results are reported in [4]. This model calculated a natural frequency of 4164 Hz for 2-nodal diameter mode, whereas the

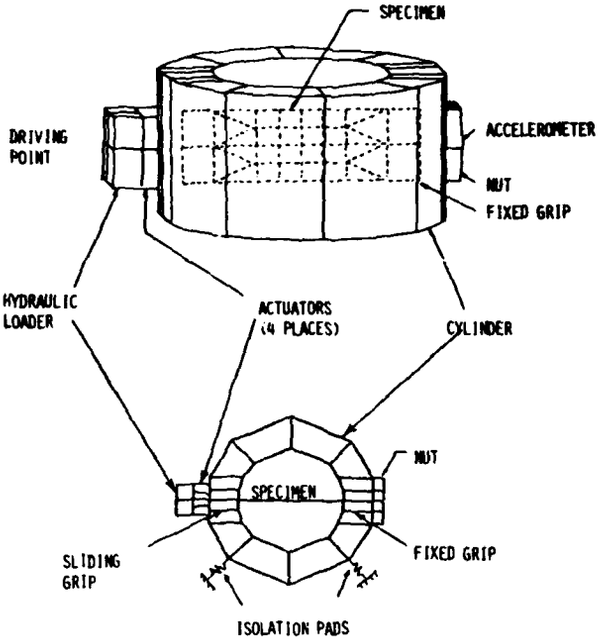

Fig. 3. A Coarse Solid Element FEM Model analysed in [4]. Calculated Freq. = 4164 Hz. Measured Freq. = 2585 Hz

measured value was around 2585 Hz. This the large difference between Finite Element and experimental frequencies was due to a number of factors. Firstly, it is realized that the size of the ring, especially its diameter to the thickness ratio of 8/3, is such that the assumed deformation pattern built into the element shape functions may not satisfactorily simulate the actual deformation, since it does not vibrate like a pure membrane (as in a thin ring structure). This brings into forefront the classical difficulty in the FEM analysis, namely that the deformation pattern calculated by any FEM model is as good as the assumed deformation pattern built into the elements, and it is tough for the plate-like elements HEXA to simulate the thick shell-like behavior of the ring. Another major factor which influenced the accuracy of the FEM model is the number of elements used in simulating the ring, which dominates the deformation pattern. Keeping in view these two factors, following few paragraphs outline some numerical experiments conducted while developing an "acceptable" FEM model.

Planar models. A conceptually simple planar model of ring and specimen is shown in Fig. 4. According to this model, the ring is simulated by 12 quadratic elements QDMEM2 of NASTRAN which allows for inplane extensions only, and each element covers an arc of 30 deg. The specimen is modeled by 10 rod elements which permit only axial extension and compression. The specimen and ring are rigidly connected at

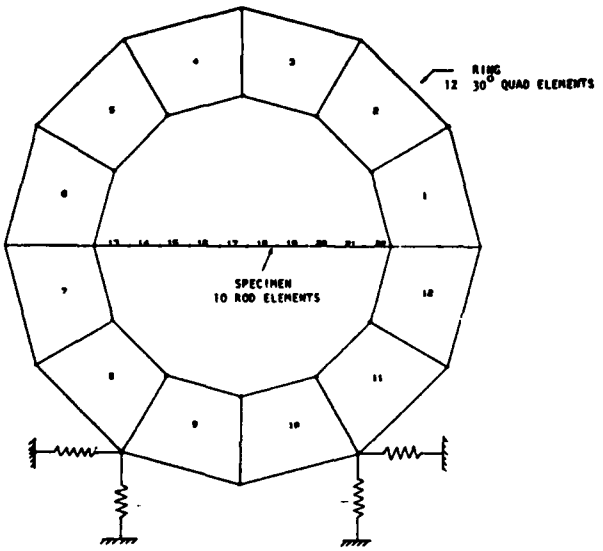

Fig. 4. Simple planar element FEM Model. Calculated Freq = 4981 Hz and 10381 Hz. Measured Freq. = 2585 Hz

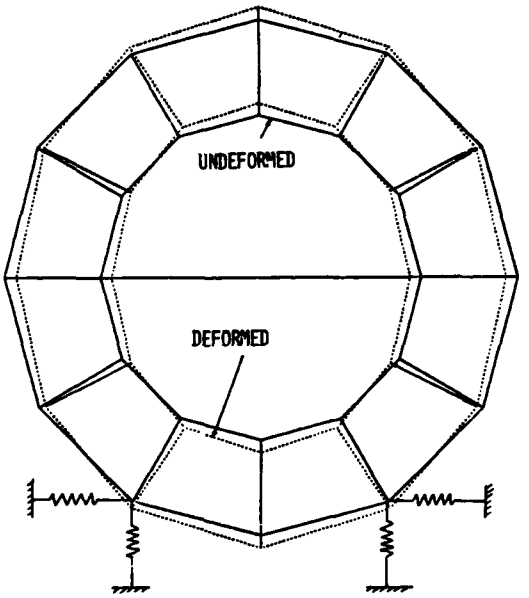

Fig. 5. Mode Shape at 4981 Hz for the FEM model shown in Figure 4

the ends so that continuity of displacements is maintained. The isolators are modeled by springs which have identical stiffness in horizontal and vertical direction. This simple model has predicted natural frequencies of 4984 Hz and 10381 Hz, and a typical mode shape is shown in Fig. 5. The large difference between measured resonance frequency of 2585 Hz and calculated value of 4984 Hz is partly due to the type of element used and partly due to the number of elements used. This difference is reduced gradually by an iterative process of modal refinement, wherein different types of elements and different number of elements are tried in constructing alternative Finite Element Models.

Fig. 6 shows the results of this model refinement on the convergence of the natural frequencies toward the measured values for the ring alone resting on isolators. This figure shows that, as finer elements are used, better correlation is obtained between FEM and measure values. For satisfactory prediction of natural frequencies, it is clear from this Figure that the element arc should subtend an angle of less than 5 deg. Even with this finer elements, there was an 18% difference between the FEM and measured values, viz. 3326 Hz vs. 2820 Hz. This error was due to differences between the prototype and its FEM model. The prototype has two observations holes in the thickness dimension which could not be accommodated in the planar model; it also has massive specimen grips which reduced its natural frequency.

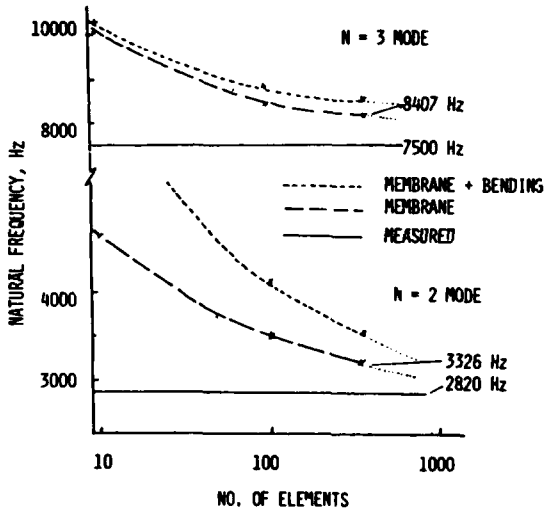

Fig. 6. Effect of Number and Type of Elements on the Convergence of Natural Frequencies

Solid models. The earlier conclusion that 5 deg. elements are needed to construct an acceptable FEM model of the ring explains the discrepancy between natural frequencies calculated from 45 deg. solid model shown in Fig. 3 and measured values. A better three dimensional FEM model of a free ring, which uses isoparametric elements that subdivide the ring into finer 10 deg. solid elements

circumferentially, 2 layers radially and 3 layers along the thickness, is shown in Fig. 7. It was developed using MSC NASTRAN. This model calculated frequencies of 2982 Hz and 8430 Hz (and some others) which are fairly close to the measured values of 2840 Hz and 7500 Hz. The ever-present error is probably due to the presence of isolators in the prototype, whereas the FEM model of Fig. 7 deals with a ring which is free on all sides.

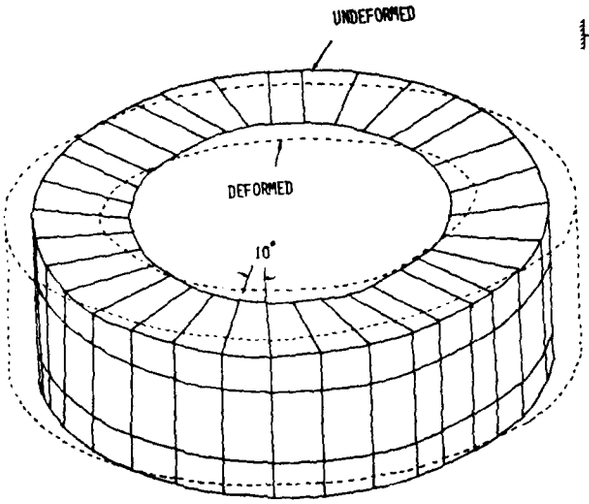

Fig. 7. Refined Solid Element Model. Calculated Freq. = 2981 Hz Measured Freq. = 2820 Hz

Fig. 8 shows an acceptable FEM model of the HCF/LCF ring. It uses 5 deg. elements, and yielded natural frequencies of 2940 Hz and 8020 Hz that are closer to the measured values of 2840 Hz and 7500 Hz. The continued difference is due to the fact that the FEM model has not provided for the observation and grip holes present in the prototype.

Having devised an acceptable FEM model which calculates the natural frequencies fairly close to the measured values, the next logical step could be to use it to compare calculated and measured frequency response. However, one critical factor which affects the frequency response around resonance, which is of major interest in the design of the HCF/LCF machine, is the damping of the entire system. There are wide and varied mechanisms of damping built into the system, such as material damping, friction and interface slip. Since, at present, it is difficult to introduce all these mechanisms into any FEM model, a better way is to rely more on experimentally measured Frequency Response Function (FRF) than use the FEM results. Next few sections describe some relevant details of the measurement technique used and present some of the measured Frequency Response Functions.

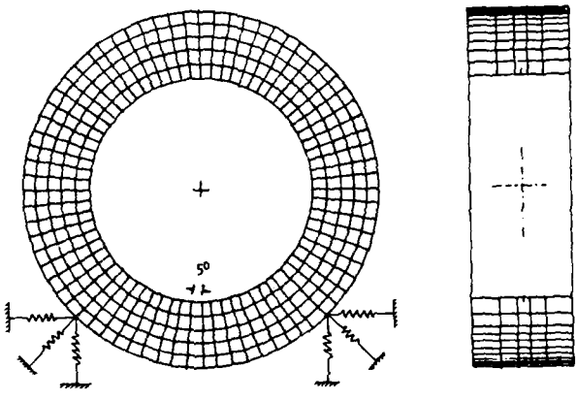

Fig. 8. Acceptable FEM Model of the Ring using solid elements

4. "STEPSINE" FREQUENCY RESPONSE MEASUREMENT TECHNIQUE

Till the mid-seventies, the Frequency Response Functions (FRF), such as Compliance, Mobility, Accelerance or Dynamic Stiffness were measured mostly by continuous Sine-Sweep based Analog Systems, or large mainframe computer based digital systems along with instrumentation taperecorders. Rapid developments of microcomputers have lead to significant changes in the FRF measurement techniques, and dedicated microcomputer-based dual channel FFT analyzers have gained wide popularity recently. Fast FRF measurement by FFT analyzers is not without penalty, however, as considerable care must be exercised to control the large number of parameters which affect the accuracy, such as aliasing, windowing, sampling, averaging and frequency resolution. These problems result in a large spread in the accelerance response measured by different FFT analyzers, such as that shown in Fig. 9. Similar large spread in the FRF plots measured by FFT techniques has been reported by Ewins [5] in his analysis of Round Robin Survey Results in Europe.

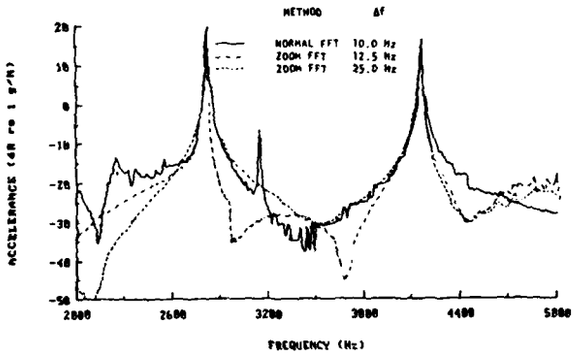

Fig. 9. Large spread in FRF measurements by FFT Analyzers

To avoid these problems, a different system, called STEPSINE system [6], which uses a shaker to excite the structure at a single frequency and plots the FRF as the frequency is varied in specified steps, is utilized for majority of the FRF measurements presented herein.

Fig. 10 shows schematically the hardware needed by the STEPSINE system measure FRF. This system is centered around the desktop computer IBM CS 9000 which has majority of the cost/performance features of the popular IBM PC computer, but is built around a more powerful 16/32 bit MC 68000 microprocessor. This computer acts as the system controller. The driving software STEPSINE has three broad subdivisions: the preprocessor, processor and postprocessor. The user can input data through the pre-processor. The processor part then drives the excitation system and measures the force and response of the structure. It also plots the Frequency Response Function on the screen in real time as the test progresses. A post processor allows the user to perform system identification in real time. This STEPSINE system has a frequency range of 1 μHz to 1 MHz with a frequency resolution of 1 μHz. It can be used with various shakers and transducers; their selection depends partly on size of the structure and partly on the availability. Details of the STEPSINE system and comparison of its performance with dual channel FFT analyzers with and without zoom facility appear elsewhere [6].

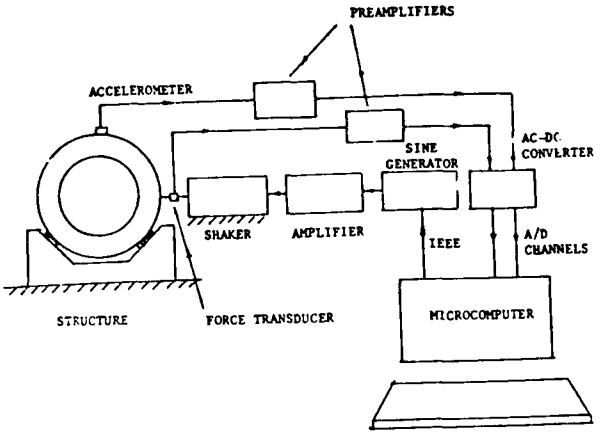

Fig. 10. Schematic of Frequency Response Measurement Set-up for the STEPSINE system

5. COMPLIANCE RESPONSE OF HCF/LCF RING

Fig. 11 shows typical compliance measurements at 4 salient points of the HCF/LCF ring, viz. the horizontal points A, C corresponding to the ends of specimen, and B, D corresponding to top and bottom positions of the ring as shown in Fig. 2. The FRF plots shown in Fig. 11 cover the range of 1000-10000 Hz with a frequency resolution of 20 Hz. This is the resolution that can be obtained by a typical dual channel FFT analyzer with time series block size N = 1024 and maximum frequency set to 10000 Hz.

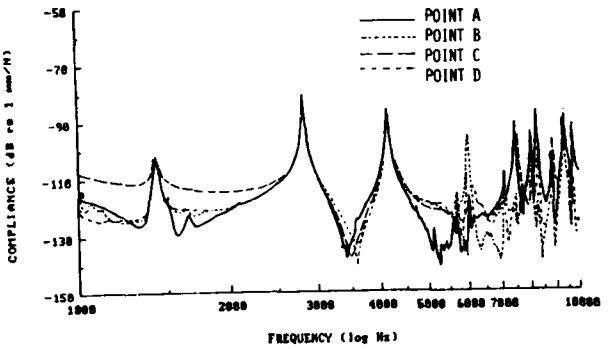

Fig. 11. Typical Compliance Plots of HCF/LCF Ring at 4 points. Frequency Resolution = 20 Hz.

STEPSINE system has also the facility to display, from the same set of FRF measurements, the plots of exciting force, response and various FRFs such as compliances, mobility etc. Fig. 12 displays typical excitation force, response, and resulting compliance, stiffness and accelerance plots. Fig. 12(a) and (b) show the measured force and acceleration response at point D of the structure. The force is seen to pass through a minimum at the resonance frequency. This peculiarity of "kinks" in measured forces at resonance frequencies is explained by analysis of three degree model of the combined structure, force transducer and shaker armature system shown in Fig. 13.

The matrix equation governing the displacements of the ring, force transducer and shaker armature is

$$\begin{bmatrix} (-m_1\omega^2+k_1+k) & -k & 0 \\ -k & (-m_2\omega^2+k+k_2) & -k_2 \\ 0 & -k_2 & (-m_3\omega^2+k_2+k_3) \end{bmatrix} \begin{bmatrix} X_1 \\ X_2 \\ X_3 \end{bmatrix} = \begin{bmatrix} 0 \\ 0 \\ f_o \end{bmatrix} \quad (2)$$

The displacements of the ring and force transducer are, hence,

$$x_1 = k\,k_2\,f_o/\Delta \quad (3)$$

$$x_2 = (-m_1\omega^2 + k_1 + k)k_3 f_o/\Delta$$

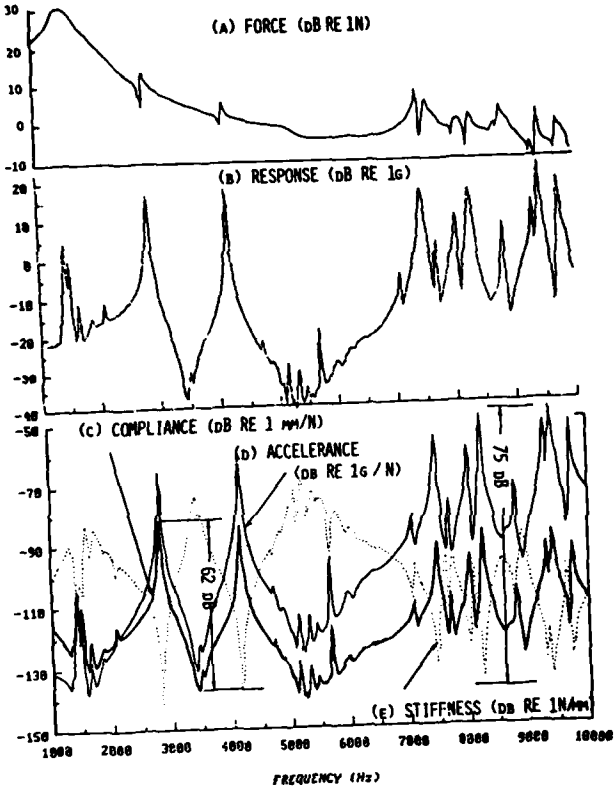

Fig. 12. Compliance and Accelerance Plots showing Different Dynamic Ranges

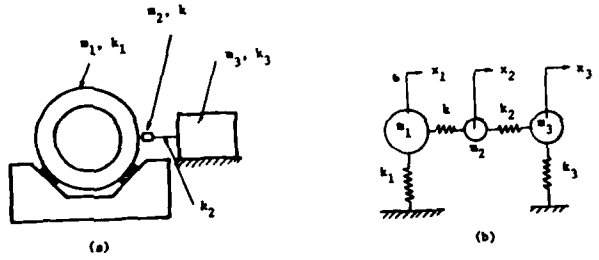

Fig. 13. Three Degree Model of the Structural Measurement System. (a) Structure, and (b) Model

where Δ denotes the determinant of transfer matrix. From these displacements, the force f as seen by the force transducer, and the measured compliance of ring are given by

$$f = k(x_2 - x_1) = k\,k_2(k_1 - m_1\omega^2)f_o/\Delta \qquad (4)$$

$$\alpha_{11} = x_1/f = 1/(k_1 - m_1\omega^2) \qquad (5)$$

Equation (5) makes it clear that measured α_{11} is independent of the measurement chain, as it should be. Further, equation (4) shows that the measured force f crosses zero when $k_1 = m_1 \cdot \omega^2$ i.e., at structural resonance frequency. In reality, since the computer plots only the absolute value of the force transducer output, this zero crossing is replaced by a minimum, such as the one seen in Fig. 12.

One key parameter of considerable interest is the dynamic range of the entire measurement set-up from the structure to the FRF plot. It is defined as the difference between the Highest Peak and the Lowest Valley in the FRF plot. Although one expects that the dynamic range to be independent of the FRF variable selected, Fig. 12(c) and (d) show that higher dynamic range can be obtained by using accelerance as the FRF variable instead of compliance. Thus, selection of proper FRF variable for display does influence the dynamic range of total system.

When a structure, like the HCF/LCF ring, is excited by a shaker, it is usual to associate the term "resonance frequency" as that frequency where the observed response shows a relative local maximum. However, the excitation force delivered by the shaker to these structure may not remain constant in the resonance zone. This lead to two apparently different "resonance frequencies", one corresponding to the peak of compliance plot (2816.6Hz), and another corresponding to peak of response plot (2827.5Hz), as shown in Fig 14. Of these, the "resonance frequency" of 2816.6 Hz is the true resonance frequency since it measures the ratio of response and excitation.

The measured compliance response of 2820 Hz is used to compare the mode shape with calculated mode shape from FEM as shown in Fig 15. This Figure shows that, whereas the calculated mode is symmetric at top and bottom portions of the ring, according to measurements, the bottom half of ring vibrates with less amplitude than the top half. Additional details of mode shapes measured by a technique called "Modal Imaging Process" are given in Ref. [7].

6. "SEEK RESONANCE" METHOD

A coarse resolution of 20 Hz was used to plot the FRFs in Fig. 11, and hence resonance frequencies from it are accurate to ± 20 Hz. Since using high resolution (as done in Fig. 12) increases the measurement time enormously, a "Seek Resonance" facility was incorporated into the STEPSINE system by which the user can increase the resolution of the measured FRF data only around identified resonance frequencies. This method consists of moving the digital cursor to a selected resonance point (e.g. 2820) on the FRF plot, and initiating the "Seek Resonance" Facility by pressing a key on the computer keyboard. The microcomputer then automatically measures

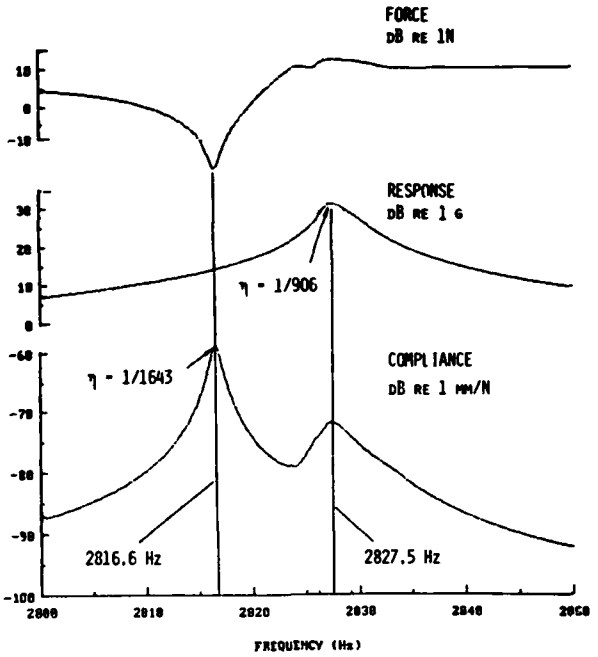

Fig. 14. Different "Resonance Frequencies" shown by Compliance and Response plots

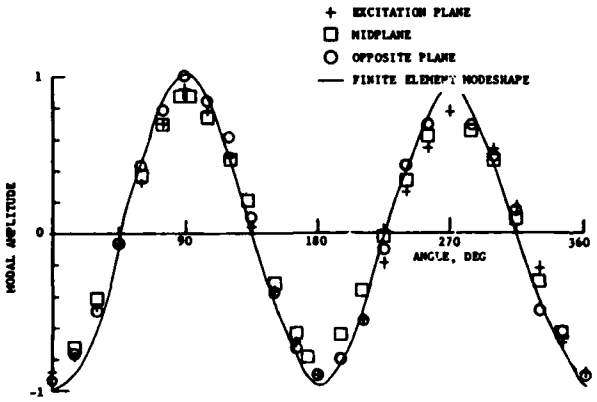

Fig. 15. Measured Mode Shape of the HCF/LCF Ring compared to the FEM-Calculated Mode Shape

the frequency response data around the resonance with finer resolution, plots it, and finds the resonance frequencies, compliance and loss factor by locating the peak and the half-power points. This "Seek Resonance" method differs from the widely used zoom facility in two important respects which improve the confidence in FRF measured: (1) It sets automatically the frequency range of finer measurement to the half-power bandwidth, and (2) it uses measured frequency response over this bandwidth to find the resonance frequencies and loss factors instead of using curve-fitted data.

Fig. 16 shows typical compliance plot of point D of the HCF/LCF ring using this "Seek Resonance" method. It shows that the "Seek Resonance" method increases the accuracy for measured compliance at resonance by as much as 5 to 20 dB. Thus, this Figure makes it clear that the compliance plot, if measured with resolution of 20 Hz, (which is typical regular FFT analyzers) may be in error by as much as 20 dB at the resonance points.

An alternative popular method of increasing the accuracy of FRF measurement is to zoom on the frequency range which contains the resonance frequency. In this method, the user selects the center frequency (which usually is identical to the resonance frequency) and a

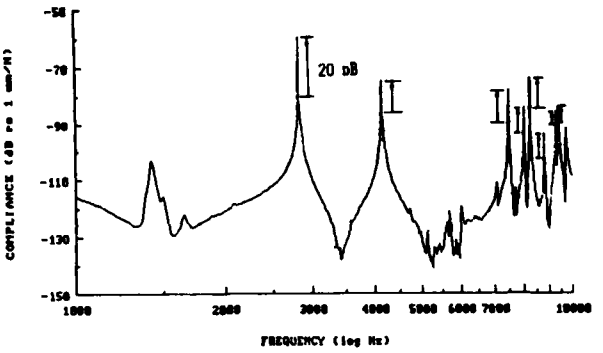

Fig. 16. Improved Accuracy of Compliance at Resonance obtained by "Seek Resonance" Method.

bandwidth around it, and performs the FRF measurement in this narrower frequency range which results in higher frequency resolution. Fig. 17 compares the FRF measurement in the zoom range of 2800-2850 Hz with a resolution of 2 Hz with that obtained by the SEEK RESONANCE method. This figure shows that zoom range yields an improved compliance (at resonance) of -67.8 dB, but the SEEK RESONANCE method sharpens the peak further by 9.3 dB to -58.51 dB.

Preceding discussion leads to the conclusion that the selection of right frequency resolution and the right FRF variable influence its accuracy. To investigate the affect of frequency resolution on the frequencies and loss factors of the HCF/LCF ring, a series of measurements are undertaken with resolution varying from .02 Hz to 20 Hz. Fig. 18 shows how the resonance frequencies

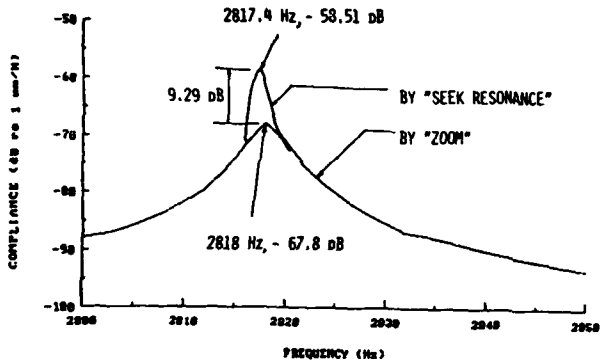

Fig. 17. Comparison of Compliance measured by Zoom Technique and Seek Resonance Technique

and loss factors converge as the frequency resolution is reduced from 20 Hz to 0.02 Hz. This figure shows that the coarser resolution of 20 Hz measured the resonance frequency to a good accuracy of 0.12%. However, the measured loss factor changed from 1/1799 to 1/193 for mode 1 and from 1/684 to 1/134 for mode 2 as resolution is decreased form 0.05 Hz to 20 Hz. This leads to the conclusion that, while the use of 20 Hz resolution (available with typical with FFT) could have measured the resonance frequency with good accuracy, it could lead to loss factor estimate which can be off by a scale factor as high as 10.

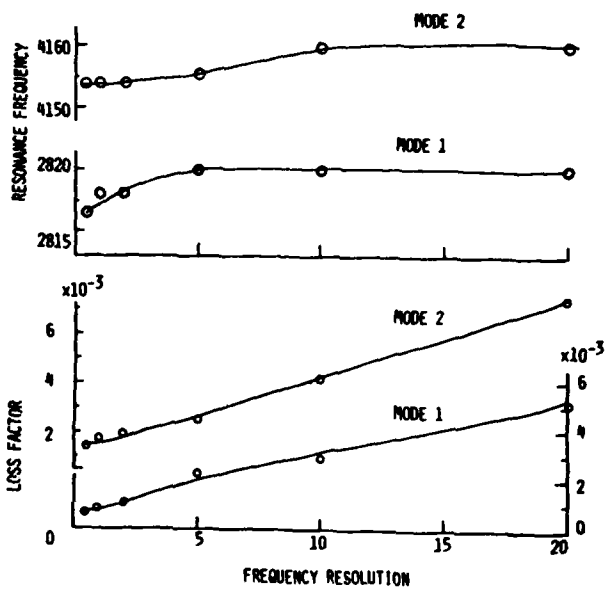

Fig. 18. Variation of Resonance Frequencies and Loss Factors with Frequency Resolution

7. IDENTIFICATION OF MODAL PARAMETERS

The compliance plots, such as those in Fig 11, form the basis of identification of modal parameters such as resonance frequencies, modes and modal loss factor. Current modal analysis techniques [8] - [11] depend heavily on efficient curve fitting algorithms to extract modal parameters from these FRFs. However, as shown above, the calculated loss factor can be undependable if curve fitting algorithms are used on FRF data with coarse frequency resolution. This situation is illustrated below for the HCF/LCF ring data.

Table 1 below presents the resonance frequencies, compliance and loss factors obtained at point D by using the STEPSINE system with a frequency resolution of 20 Hz. This data shows that the two nodal diameter resonance frequency is 2820 Hz and the loss factor at this frequency is 1/178.

TABLE 1. Resonance Frequencies of HCF/LCF Ring Measured with resolution of 20 Hz.

Sl No Factor	Resonance Freq. Hz	Compliance dBre 1 mm/N	Loss Factor
1	2820	-81.00	1/178
2	4160	-85.62	1/1391
3	6000	-97.92	1/156
4	7100	-107.61	1/190
5	7480	-113.85	1/279
6	8040	-104.84	1/287
7	8260	-99.74	1/372
8	8820	-100.56	1/231
9	9320	-90.56	1/418
10	9440	-98.40	1/300

The STEPSINE system has also a facility by which it can generate a table of measured modal parameters after using the "Seek Resonance" method to improve the accuracy. Such computer-generated table is shown in Fig 19. Comparing these results with those of Table 1 (which are those obtained without the Seek Resonance Facility), it is clear that substantial inaccuracies can creep in the measured loss factors if they are based on FRF data with too coarse a resolution.

SL NO.	RESON FREQ (Hz)	COMPLIANCE (dB re 1 mm/N)	MODAL LOSS FACTOR
1	2817.00	-60.95	1/ 1643
2	4151.00	-73.13	1/ 952
3	5992.00	-89.10	1/ 873
4	7088.00	-91.25	1/ 1781
5	7483.00	-105.00	1/ 868
6	8028.00	-93.94	1/ 1082
7	8258.00	-87.03	1/ 2043
8	8507.00	-91.04	1/ 1037
9	9313.00	-85.25	1/ 880
10	9421.00	-93.79	1/ 420

Fig. 19. Computer Printout of System Parameters for HCF/LCF Ring at Point D

The normal Manual Method of measurement of loss factor by the half-power point method usually consists of tuning the structure to resonance frequency f_r where the response shows a peak, finding half-power points f_1 and f_2, and calculating loss factor by

$$\eta = \frac{f_1 - f_2}{f_r} \qquad (6)$$

However, as discussed earlier, Fig. 14 shows that the "resonance frequency" of response plot can be different from that shown by the compliance plot. THe loss factor measured from the response plot is 1/906, whereas that measured from compliance plot is 1/1643. Hence it is clear that, for this structure, loss factor measured from the response plot is not a true indication of the structural loss factor.

8. FREQUENCY RESPONSE OF RING WITH SPECIMEN

In order to estimate how introduction of a test specimen and grips affect the resonance frequencies and damping, a 2 in. wide test specimen was inserted into the ring along with the grips, and the entire HCF/LCF test machine is excited by the shaker along the axis of the specimen. The "Seek Resonance" method was employed to measure accurately the resonance frequencies and modal loss factors in the 1000-10000 Hz frequency range. Fig. 20 shows typical compliance plot at point A of the ring, whereas Fig. 21 displays the table of resonance frequencies, compliance and loss factors produced by the "Seek Resonance" method. Comparison of these with Figs. 16 and 18 show that the resonance frequency of interest, viz 2817 Hz decreased to 2585 Hz with grips and specimen in place. This is due to the fact that, even though the specimen stiffens the structure, the massive grips overcorrected the increase in the stiffness. Fig. 21 shows that the loss factor at the two-nodal diameter mode of interest increased from 1/1643 to 1/891 with the specimen inserted in its place. Thus we conclude that damping of the structure has been doubled when the specimen is inserted, and this is due to dissipation of energy in relative motion between the grip and the ring mating surfaces.

Fig. 22 shows the compliance of the structure at the centre of the specimen in the lateral direction. This figure shows that there is an additional frequency of 1836 Hz at which the specimen can resonate.

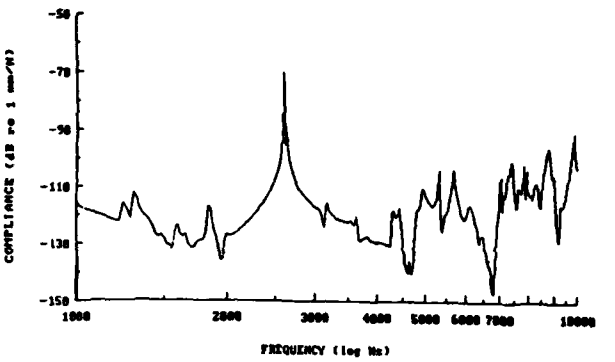

Fig. 20. Typical Compliance Plot of the HCF/LCF Test Machine with Specimen, with "Seek Resonance" Method

SL NO.	RESON FREQ (Hz)	COMPLIANCE (dB re 1 mm/N)	MODAL LOSS FACTOR
1	2585.15	-70.87	1/ 891
2	5312.43	-103.72	1/ 252
3	5458.06	-103.41	1/ 88
4	7052.22	-104.19	1/ 155
5	7391.20	-100.66	1/ 77
6	7831.37	-101.68	1/ 320
7	7937.27	-103.78	1/ 458
8	8772.18	-95.89	1/ 61
9	9830.45	-91.73	1/ 123

Fig. 21. Computer Printout of System Parameters for HCF/LCF Ring with Specimen at Point A

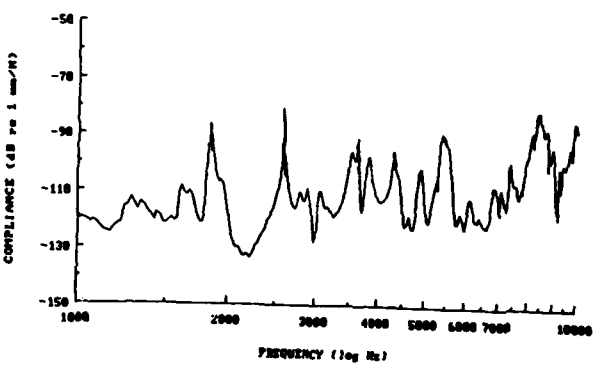

Fig. 22. Compliance Plot at the Center of Specimen showing an additional Resonance Frequency at 1836 Hz

9. COMPARISON FO THEORETICAL AND EXPERIMENTAL RESULTS

Details of theoretical and experimental techniques for determining the dynamic characteristics of the HCF/LCF ring structure have been presented in the preceding paragraphs. Fig. 15 has already presented a comparison of theoretical and measured mode shapes at for 2 nodal diameter mode. Tables 2 and 3 below compare the theoretical and measured natural frequencies of the HCF/LCF ring structure with and without the specimen.

Table 2. Comparison of measured and calculated natural frequencies of the HCF/LCF ring without specimen

STEPSINE	FFT	CALCULATED
2817	2820	2868, 2982
3489	3150	3391
4151	4161	3979
5992	4980	5942
7083	7160	7113
7483	7720	-
8028, 8258	8580	8430
8807	9140	8912

Table 3. Comparison of measured and calculated natural frequencies of the HCF/LCF ring with the specimen

STEPSINE	FFT	CALCULATED [4]
2585	2520	-
3201	3300	3840
5312	4380	4165
5658	5000, 5160	4761, 5433
7052	7160	-
7391	7640	-
7831	7740	7756
7937	8100	7961

These tables show that, while the FEM model is able to predict major frequencies of interest, it has also generated additional frequencies which could not be found in measurement. The converse is also true, viz. some of the measured frequencies could not be found in the FEM calculated frequencies. This discrepancy is possibly due to the fact that boundary conditions of the prototype could not be exactly simulated in the FEM model (especially, the way in which the specimen and the grips are connected to the ring). In addition, the observation ports present in the prototype disturb the symmetry, resulting in skewing of some mode shapes and corresponding natural frequencies.

10. CONCLUSIONS

This paper has analyzed the dynamic characteristics of HCF/LCF fatigue test machine that has been designed and fabricated in the Materials Laboratory. Investigation of response and compliance plots around the major resonance frequency showed that the loss factor measured by using the half-power point method on response plot can be erroneous. Analysis of the measured compliance plots show that the operating frequency at which HCF Load can be generated using the resonance principle is 2820 Hz. Insertion of a specimen and grips into the resonating ring reduces this frequency to 2585 Hz, and doubles the damping at this frequency. It is concluded that future designs must evolve a gripping mechanism which will not introduce additional damping, and the grips must be so light that they do not reduce this HCF frequency.

ACKNOWLEDGEMENTS

The work reported in this paper has been performed at the Air Force Materials Laboratory under a grant from National Research Council. The authors are indebted to Dr Ching-U Ip, of TRW for FEM result presented in Fig. 7. They also appreciate the considerable care and diligence of Karen Draper and Roxanne Lemaster in preparing the manuscript of this paper.

REFERENCES

1. R.C. Goodman, and A.M. Brown, "High Frequency Fatigue of Turbine Blade Material", Report No. AFWAL-TR-82-4151, Air Force Wright Aeronautical Laboratories, 1982.

2. B.E. Powell and I. Henderson, "The Conjoint Action of High and Low Cycle Fatigue," Report No. AFWAL-TR-83-4119, Air Force Wright Aeronautical Laboratories, 1983.

3. D.I.G. Jones, "Initial Design and Evaluation of a Unique High Frequency Fatigue Test System," Shock and Vibration Bulletin, No. 55, 1985.

4. CAE Engineering Report, "Finite Element Analysis of HCF/LCF Test Machine," Report No. 83-11-02 to Universal Energy Systems, Dayton, Nov. 1983.

5. D.J. Ewins, "State-of-the-Art Assessment of Mobility Measurement - a Summary of European Results," Shock and Vibration Bulletin, No. 51, Part 1, pp. 15-35, 1981.

6. D.K. Rao and D.I.G. Jones, "Measurement of Dynamic Characteristics of a Structure Using Programmed Sine Step Test," in Proc. 3rd International Modal Analysis Conference, Orlando, FL, Vol. I, pp. 338-345, 1985.

7. D.K. Rao, "Interactive Modal Imaging Process for Vibrating Structures" to appear in Journal of Vibration, Acoustics, Stress and Reliability in Design, Trans. ASME. 1985/86.

8. A.L. Klosterman, "On the Experimental Determination and Use of Modal Representation of Dynamic Characteristics," Ph.D Thesis, University of Cincinnati, 1971.

9. H.G.H. Goyder, "Methods and Application of Structural Modeling from Measured Structural Frequency Response Data," J. Sound Vib., Vol. 68, No. 2, pp. 209-230, 1980.

10. J. Allemang, "Experimental Modal Analysis Bibliography," Proc. 1st Int. Modal Analysis Conf., Orlando, FL, pp. 714-726, 1982.

11. D.I.G. Jones and A. Muszynska, "Damping Measurement by Dynamic Stiffness Method," Proc. Vibration Damping Workshop, Flight Dynamics Laboratory, AFWAL Report, 1984.

DATA ANALYSIS TECHNIQUES TO SUPPORT STRUCTURAL MODELING

J. W. Jeter and P. H. Merritt
Albuquerque Engineering Center
Hughes Aircraft Company
Albuquerque, New Mexico 87119

Finite element structural analysis of a complex system is generally restricted by the size of a structural model which can be realistically included in a computer analysis. Furthermore, practical problems are often lacking a definitive representation of the significant input for the model. This paper describes the use of coherence analysis to attack both the problem of model complexity and the problem of input definition. The techniques utilized for simple and multiple coherence analysis are described, examples are presented, and the effects of the techniques on a practical analysis are discussed. The procedure has advantages which are applicable to most large scale applications of finite element modeling techniques.

INTRODUCTION

The development of Fourier Transform techniques for digital computers has resulted in significant improvement of the tools available to the data processing community. Processing algorithms now exist which can provide experimenters greater insight into the meaning of their results [1 and 2]. An important application has been in the area of source identification for linear systems. Multiple input sources that may be independent or dependent for a given system can be identified, and the existence and significance of unidentified sources can be determined. These techniques can also have a significant influence in the structural modeling arena. Complex structural systems require complex models for which a balance between efficiency and accuracy is needed. Coherence analysis techniques can influence both of these concerns. It is possible, through the application of these techniques to appropriate experimental data, (a) to determine whether input to a model is sufficiently specified so that the output is reasonably accurate and (b) to minimize the number of inputs required to produce good output. The latter has important consequences in analysis techniques such as component mode synthesis where reduction of degrees of freedom is a primary factor in bringing computer costs down to an acceptable level. If driving functions are shown to be superfluous, the corresponding degrees of freedom are candidates for elimination.

APPROACH

A fundamental concept in structural modeling is that by specifying the input to the model, the output can be calculated. The assumption that it is possible to specify the input is often subject to question. The accurate determination of the energy paths that stimulate a complex structure is a difficult task. Consider a large piece of equipment that is mounted in an airplane. The inputs may typically consist of 3 angular and 3 linear motions and perhaps acoustics. If the equipment spans a significant distance on the floor, the floor modes may apply

different inputs to different sections of the equipment. If cables or braces are attached to the equipment they may also act as paths to couple input excitations.

Consider the approach typically used to evaluate a numerical model. Measurements are made at some selected locations to specify inputs and outputs of the item under test. These measured output data are compared with the mathematical model outputs after the model is driven using the measured input data. If the results agree to within some limits, the model is used to extend some aspect of structural performance. This can be very risky if the engineer does not assure himself that the outputs were truly a function of the measured inputs.

A better technique to verify the dependency of data is coherence analysis. The basic idea of coherence analysis is that correlated data maintains a phase relationship. Consider the simple system shown in Figure 1. Depending on the magnitude of the noise input it may or may not be possible to describe y(t) by specifying x(t). By transformation into the frequency domain via the Fourier transform it is possible to utilize some very powerful analysis techniques to analyze the relationships between y(t) and x(t). The coherence function is specified as follows,

$$\gamma_{xy}^2 = \frac{G_{xy}^2}{G_{xx} G_{yy}} \qquad (1)$$

where:

γ_{XY}^2 = the coherence function between X and Y.

G_{XY} = the cross-spectrum between X and Y.

G_{XX} = the auto spectrum of X.

G_{YY} = the auto spectrum of Y.

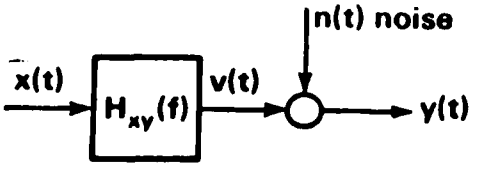

Figure 1. Simple Input/Output System

In this paper capital letters will be used for frequency domain quantities and small letters for time domain quantities. Each of the above spectrums is defined as the expected value of the Fourier transform operation. The averaging of many single transforms is necessary to build statistical confidence. The numerator, G_{xy}, must be averaged as a complex operation prior to using its magnitude. In fact, that is the key to understanding the coherence function. The cross-spectrum can be considered as a vector quantity. If this vector always remains fixed in orientation, the expected value of the numerator of equation (1) will converge to a value that is equal to the product of the auto spectrums in the denominator. The coherence function will approach unity and this states that x(t) accounts for y(t). However if y(t) comes primarily from the noise input, then the cross-spectrum, G_{xy}, will not stay fixed in orientation and the expected value of G_{xy} will converge to zero. Therefore for uncorrelated data, the coherence function approaches zero.

The basic idea of coherence analysis can be extended to more complex problems. Consider Figure 2 where two inputs cause the output. If $x_1(t)$ and $x_2(t)$ are completely independent inputs, then the output is simply the summation of the two inputs. If the noise is zero, it can easily be shown that,

$$\gamma_{1y}^2 + \gamma_{2y}^2 = 1 \qquad (2)$$

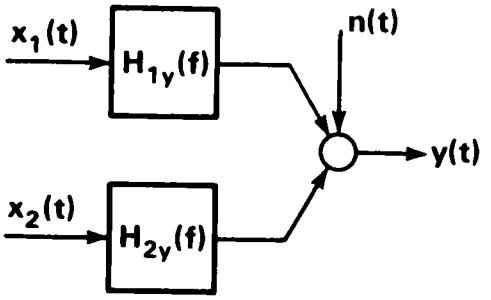

Figure 2. A Two Input - One Output System

The problem is more complex when $x_1(t)$ and $x_2(t)$ are correlated. In this case the summation of the two simple coherences would yield a value greater than one when no noise was present. Therefore a new approach is needed. The procedures specified by Dr. Julius Bendat [2] have been followed in this paper. The approach is to (1) order the inputs such that the first input is defined to be the primary input, (2)

remove all the correlated effects between x_1 and x_2 from x_2, and (3) analyze the problem as two independent inputs. This general approach can be systematically extended to any number of inputs. Some new terminology is required to write the equations. The term $G_{22.1}$ means the auto spectrum of x_2 with all the effects of x_1 removed. The notation $G_{yy:21}$ means the auto spectrum of y based on x_2 and x_1. The procedure starts by defining L_{12} as,

$$L_{12} = G_{12}/G_{11} \tag{3}$$

This transfer function relates the correlated parts of the two inputs. Next calculate $G_{22.1}$ as,

$$G_{22.1} = G_{22} - L_{12}\, G_{21} \tag{4}$$

where G_{21} is the complex conjugate of G_{12}.

This removes all correlated effects between x_1 and x_2 from x_2. Next calculate a transfer function between input x_1 and the output,

$$L_{1Y} = G_{1Y}/G_{11} \tag{5}$$

Notice that L_{1Y} is not equivalent to H_{1Y} in Figure 2; it includes correlated effects that couple through the H_{2Y} path. These effects can be visualized by drawing the block diagram as shown in Figure 3. Next,

$$G_{2Y.1} = G_{2Y} - L_{1Y}G_{21} \tag{6}$$

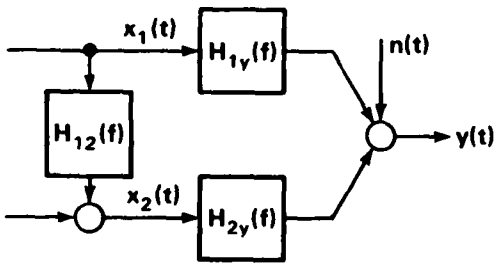

Figure 3. A Two Input - One Output System with Related Inputs

This is the cross spectrum between x_2 and y with all the effects of x_1 removed. Next,

$$L_{2Y} = G_{2Y.1}/G_{22.1} \tag{7}$$

This is the transfer function from the conditioned second input to the output.

Now the effects of x_1 can be removed from the output,

$$G_{YY.1} = G_{YY} - L_{1Y}G_{Y1} \tag{8}$$

The noise that is uncorrelated with either input can be found by,

$$G_{YY.21} = G_{YY.1} - L_{2Y}G_{Y2.1} \tag{9}$$

Now by utilizing the above derived signals the problem can be envisioned as two independent and uncorrelated inputs as shown in Figure 4.

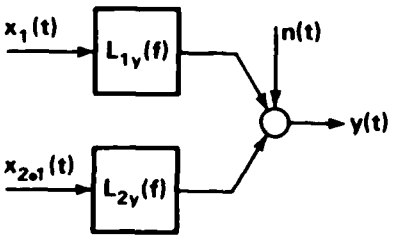

Figure 4. A Two Input - One Output System Decomposed into Independent Inputs

Now coherence functions can be written for the uncorrelated system,

$$\gamma^2_{1y} = \frac{|G_{1y}|^2}{G_{11}\,G_{yy}} \tag{10}$$

$$\gamma^2_{2y.1} = \frac{|G_{2y.1}|^2}{G_{22.1}\,G_{yy.1}} \tag{11}$$

$$\gamma^2_{y:21} = 1 - \frac{G_{yy.21}}{G_{yy}} \tag{12}$$

where the last coherence function is called the multiple coherence function.

The output is now attributed to the uncorrelated inputs,

$$G_{y:1} = \gamma^2_{1y}G_{yy} = \frac{|G_{1y}|^2}{G_{11}} \tag{13}$$

$$G_{y:2.1} = \gamma^2_{2y.1}G_{yy.1} = \frac{|G_{2y.1}|^2}{G_{22.1}} \tag{14}$$

The total output can now be envisioned as a sum of 3 independent terms,

$$G_{YY} = G_{Y:1} + G_{Y:2.1} + G_{YY.21} \tag{15}$$

This approach is a recursive approach that can be extended to as many inputs as necessary for a particular system [2]. The data obtained from equations

10 through 12 and from 9, 13, and 14 have proven to be most useful for graphically displaying the data, as will be shown in the next section. By displaying the partial coherence functions on one plot it is possible to see which inputs are dominant. The second useful composite plot is the display of all the terms in equation (15), which shows the power contributed by each input and its relative importance.

APPLICATION

The system shown in Figures 5 and 6 represents a portion of an aircraft mounted structure which is loaded primarily by the vibration of the aircraft and other portions of the structure. Inputs for this portion of the structure are defined by accelerometer triads located near its base; outputs are accelerometer readings taken on the component box structure and on the mirror at a distance from the base. One of the input triads is located on a stiff, massive slab structure; the other input triad is mounted on an extension to the slab, is called the "tab", which is less stiff as shown in Figure 6. The component of interest straddles the two segments. A coherence analysis is to be used to determine whether the input sufficiently describes the output and whether any input has an insignificant influence on the output.

The first step of the data analysis process is an examination of the time histories of the input and output to insure that the signals have no linear trends, offsets or obvious distortions. These effects impede the data analysis process and are removed from the data prior to coherence analysis.

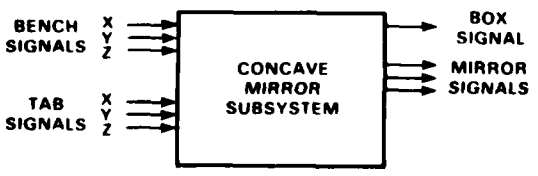

Figure 5. Bench Optical Component Model

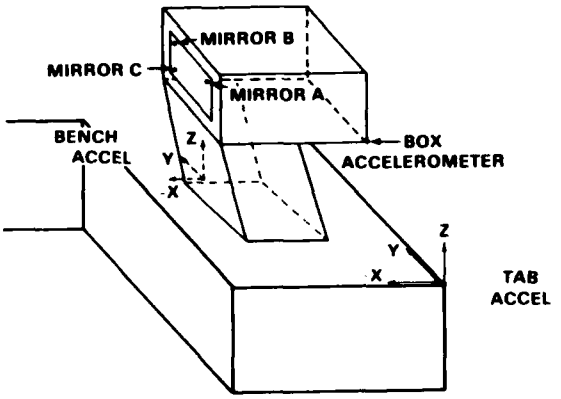

Figure 6. Accelerometer Locations

Autospectra of the input and output are then examined to determine significant resonances. Insight into the structural behavior can often be extracted from the data at this stage. For example, consider the autospectra for the inputs to this structure shown in Figure 7. Note all accelerations are in gravities (G's). The peak in the spectral density at 800 Hz for the y and z accelerometers on the tab is consistent with a localized bending motion for the tab portion of the structure. Now consider Figure 8, which shows the autospectra of the output. All output accelerometers are oriented in the x direction. The accelerometer on the mirror indicates a resonance at about 800 Hz while the accelerometer at the box does not. This would lead one to suspect that bending of the tab somehow couples into the mirror without influencing the box. This behavior will be scrutinized further. The presence of a 20 Hz resonance in all of the autospectra is indicative of a rigid body mode.

The next step in the data analysis process is the development of simple coherences between the inputs to determine the degree of interdependence of these signals. Coherences of zero indicate independent data. Coherences of unity indicate a linear relationship between the inputs. This may mean that one input can be dropped or may mean that the model must be driven with correlated inputs. Coherences between zero and unity are inconclusive at this point - multiple signal analysis is necessary to complete the evaluation of this data. Simple coherences for the accelerometers on the tab are shown in Figure 9 and can be used as an example. Although all three signals had high

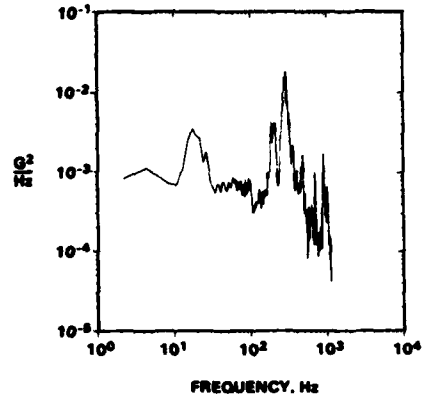

(x direction)

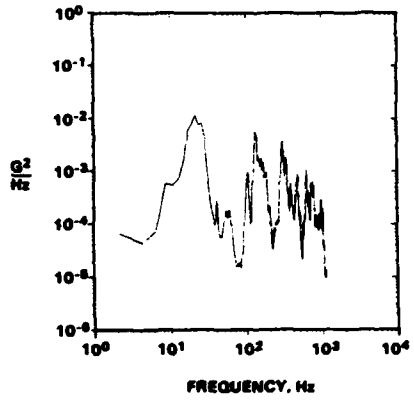

(y direction)

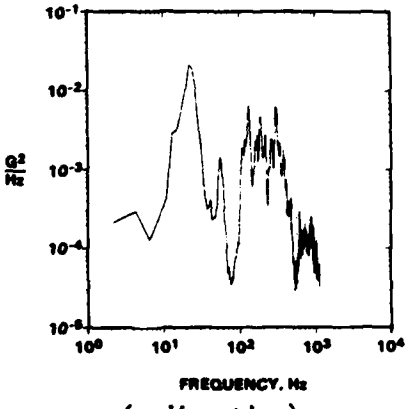

(z direction)

Figure 7(a). Autospectra of Bench Accelerations

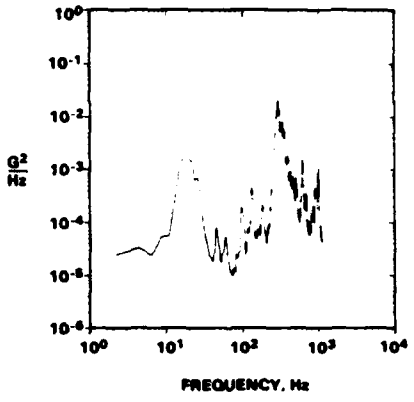

(x direction)

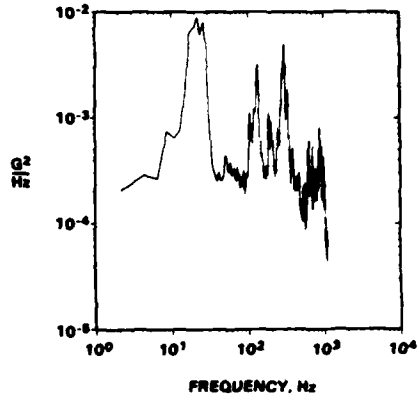

(y direction)

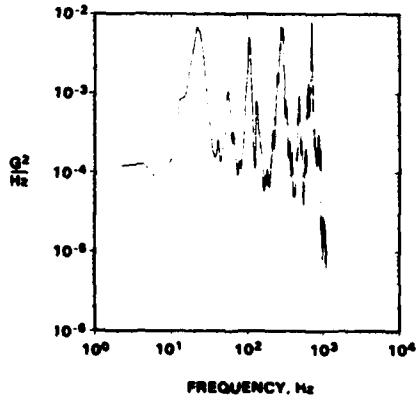

(z direction)

Figure 7(b). Autospectra of Tab Accelerations

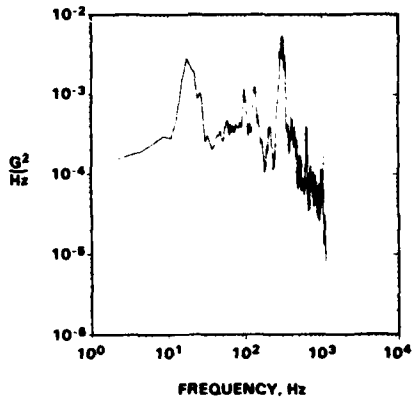

(a) Box output

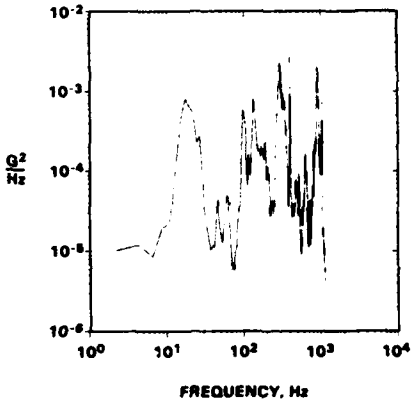

(b) Mirror output

Figure 8. Autospectra of Box and Mirror Outputs

input at 20 Hz, high coherence is present at that frequency only for the x and y accelerometers. Apparently the z motion of the tab has a different source than the x and y motion. On the other hand, the high coherence between the y and z signals at 800 Hz is consistent with the hypothesis of a bending motion for the tab.

The analysis indicates multiple signal analysis is needed to further evaluate the input signals. Simple coherences are used to determine dominant signals. It is desirable to lump mutual characteristics with the signals which most strongly affect output. To do otherwise would exaggerate the significance of the weaker signal. The relative influence of the input signals can be determined by developing simple coherences between each input and the

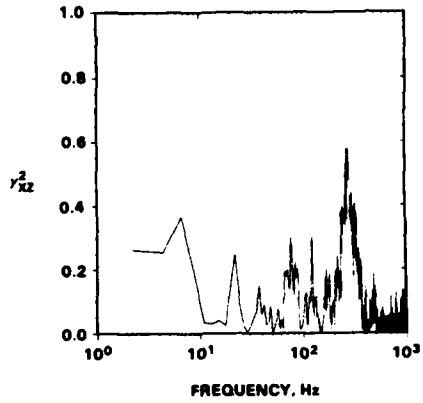

(a) Coherence between x and z accelerations

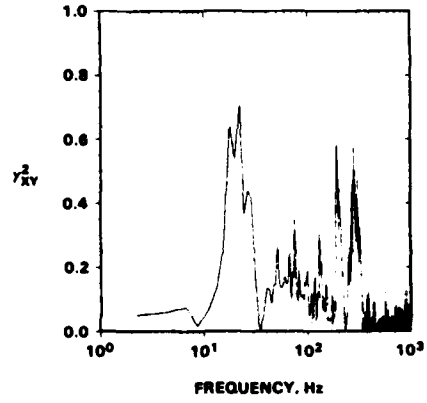

(b) Coherence between x and y accelerations

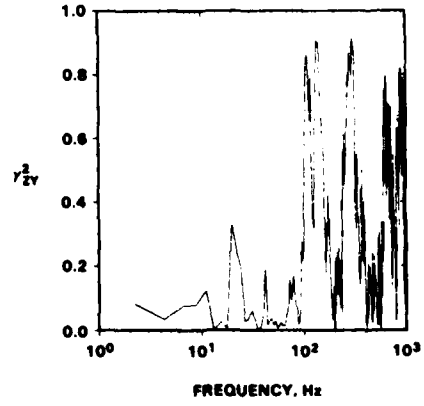

(c) Coherence between y and z accelerations

Figure 9. Simple Coherences Between Tab Accelerations

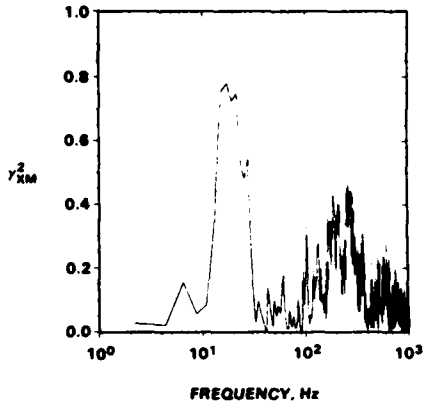

(a) Coherence between tab-x and mirror accelerations

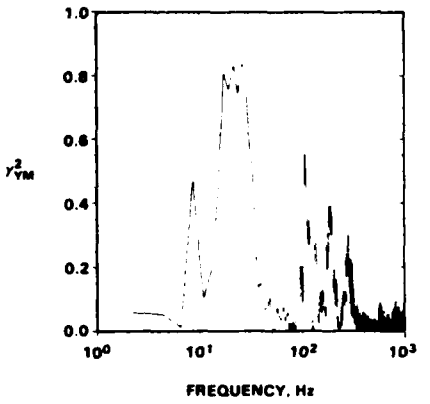

(b) Coherence between tab-y and mirror accelerations

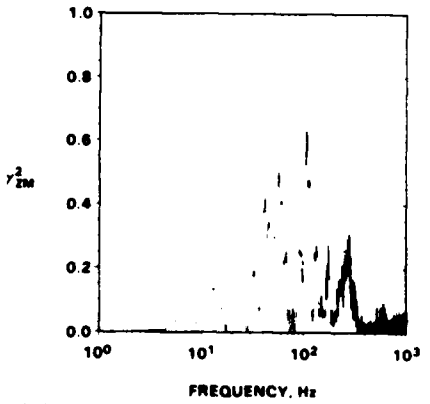

(c) Coherence between tab-z and mirror accelerations

Figure 10. Simple Coherence Between Tab Acceleration Components and Mirror Acceleration

output. The signals are then ordered according to relative strength for the partial coherence analysis. A second reason for developing simple coherences between input and output is evident in Figure 10 which shows the coherence between the signals at the bench tab and the signals at the mirror. Although the bench tab and the mirror both displayed resonances at approximately 800 Hz, the coherence between these signals is poor at that frequency, indicating independent sources at the respective locations. One may begin to question the impact of tab motion on the mirror behavior.

The results of the simple coherence analysis make exclusion of the tab signals a consideration. An indication of the consequences of this step can be found by considering the partial and multiple coherences of the bench signals with respect to the output. These coherences are shown in Figures 11 and 12, where the box accelerometer signal is used as the output. The signals in the y and z direction are seen to be insignificant when characteristics in common with the x signal are removed. The multiple coherence of the three inputs to the output, however, is rather poor. Noise, which in this case includes the tab motion, dominates the output.

The partial and multiple coherences were redone with input from the tab included. Results are displayed in Figure 13. The y and z signals from the tab were seen to have a significant influence at higher frequencies. Their inclusion results in a conspicuous improvement in the multiple coherence.

The partial/multiple coherence analysis provides information on frequency ranges where a causal relationship may exist between input and output. Whether this relationship results in significant influence on the output can best be determined using conditioned spectral density functions which give the autospectrum of the output when the linear effects of one or more input signals have been removed. The partial coherences can be used with the conditioned spectral density functions to get the total contribution to the output attributable to all of the input signals considered. This total is called the coherent output power. The difference between this spectrum and the total output spectrum is a measure of the noise contribution to the total output spectrum. Figures 14 and 15 summarize the coherent output power analysis for the output signals at the

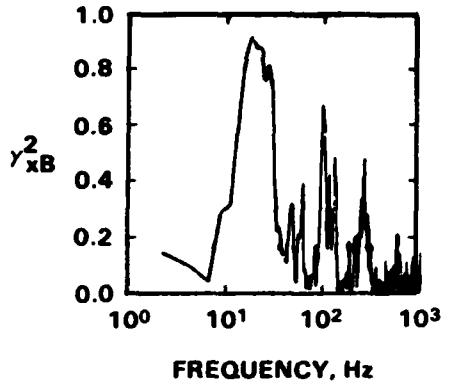

(a) Coherence between bench x and box acceleration

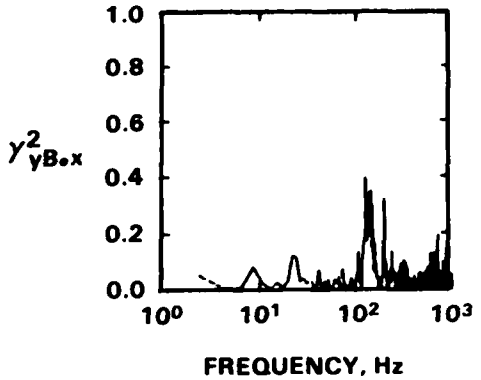

(b) Partial coherence between bench y and box acceleration (effects of x removed)

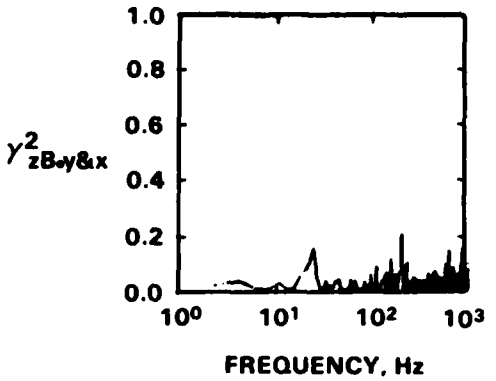

(c) Partial coherence between bench z and box acceleration (effects of x and y removed)

Figure 11. Partial Coherences Between Bench Accelerations and the Box Acceleration

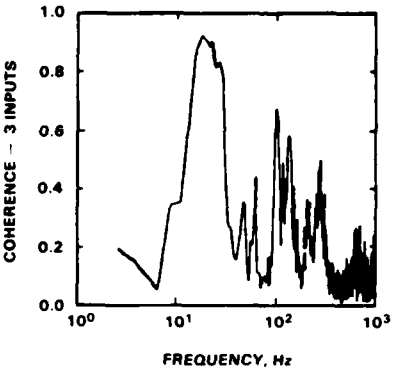

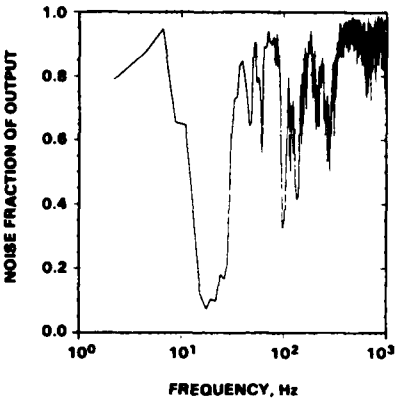

Figure 12. Multiple Coherence of Bench Accelerations to Box Motion

box and at the mirror face, respectively. The noise contribution at the box is flat, indicative of an uncorrelated noise source. The noise contribution for the mirror has more character, implying additional sources may be influencing the output signal. It is of interest to note that the noise contribution is dominant at 800 Hz.

The results of this analysis, along with engineering judgement, provide the analyst with guidance in the tasks of elimination of superfluous input and determination of adequacy of input sources. The actions taken are obviously problem dependent.

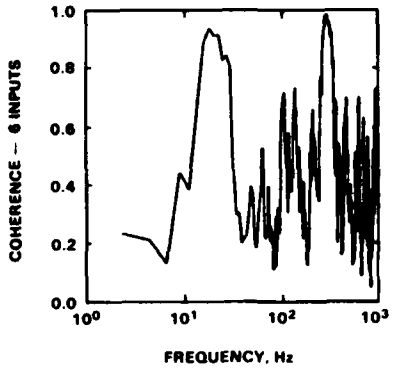

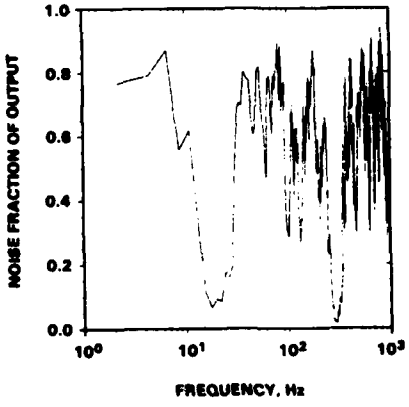

Figure 13. Multiple Coherence of Bench and Tab Accelerations to Mirror Motion

CONCLUSIONS

Simple and multiple coherence analysis techniques have been demonstrated to be powerful tools for use in development of a finite element structural analysis. This approach has several very useful attributes for the structural analyst.

1) The approach permits complex coupled systems to be decomposed into simpler independent inputs.
2) The analyst can order the inputs based on physical insight and data reduction results.
3) The composite coherence plot permits an overall visual display of the cause and effect relationship between the data.

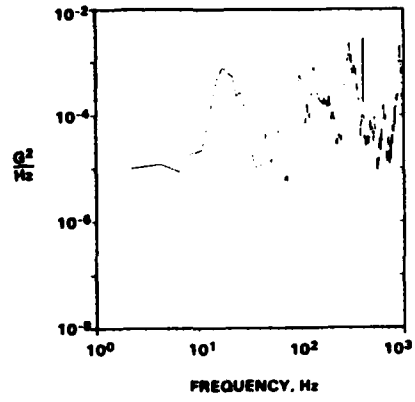

(a) Spectrum of box acceleration

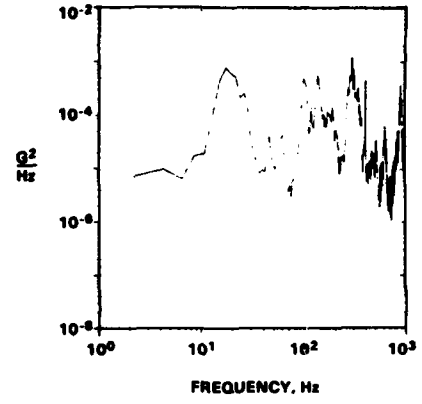

(b) Contribution to box acceleration from six inputs

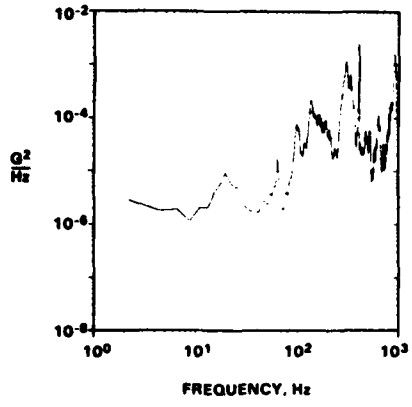

(c) Noise contribution to box acceleration with respect to six inputs

Figure 14. Coherent Output for Box Motion

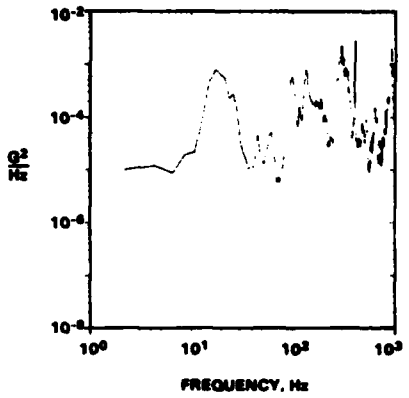

(a) Spectrum of mirror acceleration

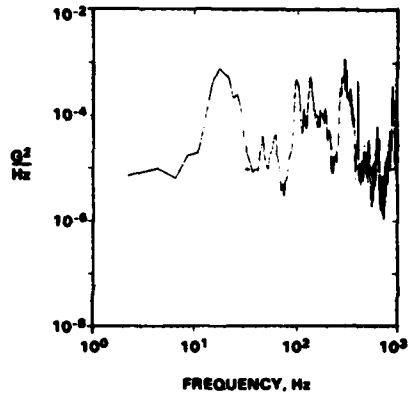

(b) Contribution to mirror acceleration from six inputs

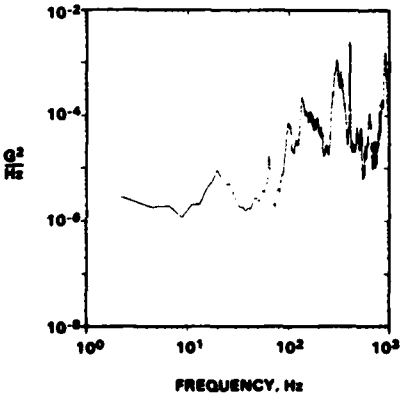

(c) Noise contribution to mirror acceleration with respect to six inputs

Figure 15. Coherent Output for Mirror Motion

4) The composite power spectrum plot permits a separation of the inputs and permits attributing the effects to the correct source.
5) If a significant input has been omitted the noise spectrum will show a dynamic signature which indicates the unmeasured input.

The consequence of this information is important insight to be directed towards model simplification and source identification.

ACKNOWLEDGEMENTS

This effort was sponsored by the Air Force Weapons Laboratory under contract F29601-83-C-0042.

REFERENCES

1. Merritt, P. H. and Bardwell, K. E., "Noise and Signal Identification Using Redundant Instrumentation," ISA Conference, Denver, Colorado, May 1984.

2. Bendat, Julius and Piersol, Allan, Engineering Applications of Correlation and Spectral Analysis, John Wiley and Sons, 1980.

3. Bendat, Julius. "Source Identification Using Partial Coherence Functions", unpublished memo, December 1982. Under contract to Air Force Weapons Laboratory, Kirtland AFB, NM.

DISCUSSION

Mr. Hammond (Southampton University): As I understand it, you said because you had three inputs, and because you conditioned the second and the third inputs with respect to the first input, the conditioned spectrum was small. You concluded it was not necessary to have the second and the third inputs in your NASTRAN model.

Mr. Merritt: If you have to eliminate them, it would go that way.

Mr. Hammond: Are inputs two and three correlated with input one?

Mr. Merritt: Yes.

Mr. Hammond: But in any general input to a particular physical device, inputs one, two and three may be uncorrelated; in that case, all three inputs should be included. You are reflecting the fact that the correlation between the inputs is not necessarily the transmission path between the inputs and the final response.

Mr. Merritt: There are many aspects to your question. First of all, if the inputs were uncorrelated, you have a simple problem; everything will add up. You have a nice, well-defined problem. But, you are asking how do you throw one away when you blamed everything on input number one. That can be very tricky. You get into path identification in that case. We looked at the simple coherences between each input and the ouput first. By that simple coherence we ranked our inputs. It should be, though, that if you blame everything on input number one, indeed it should carry the correlated parts that come through inputs two and three. When you use Bendat's notation, and if you use the L transfer function instead of the H transfer function, indeed, that L transfer function is not a simple path from the input to the output. It could be a combination of many paths.

Mr. Hammond: As long as you have identified the correct path that includes the effective transmission so that it can get from there to there, then it is okay.

Mr. Merritt: Yes. But, it may not be as simple as you think when you first start.

Ultra-High-Velocity Impacts Utilizing a Rocket Sled and an Explosively Accelerated Flyer Plate

R. A. Benham, W. R. Kampfe
Sandia National Laboratories

Well-controlled impacts of reentry vehicle nose tips with relatively thick targets at controlled inclination and at velocities above 14,000 fps can now be obtained using a newly developed testing method. The instrumented nose tip is mounted on a rocket sled and is accelerated to a velocity of more than 6000 fps. An explosively accelerated flyer plate (target) is driven toward the sled, at the proper angular orientation, at velocities of more than 8000 fps. Impact of the target and nose tip occurs at the combined velocities. Precise timing is required to produce the desired impact conditions and impact diagnostic information as well as output from the onboard instrumentation system. This method has been demonstrated in two experiments, with total test costs a fraction of that of the only other alternative—a rocket flight test.

Introduction

New contact fuze systems for reentry vehicle warheads must be tested at impact velocities higher than generally available from existing laboratory test methods. In the past, fuze systems have been tested on rocket sleds at velocities up to about 8990 fps[1] and, using explosively accelerated flyer plates, to velocities up to about 12,000[2] fps. Higher velocities have only been obtained using rocket flight tests.

A test method has been developed which combines the rocket sled and explosive flyer plate systems and which may produce impact velocities of up to 20,000 fps. The flyer plate can be made to rotate end-over-end to produce impact at any angle between 0 and 65 degrees (angle between the target surface normal and nose tip axis)[3]. The instrumented reentry vehicle nose tip is mounted on the rocket sled while the explosive flyer plate system is positioned at the end of the sled track. As the rocket sled approaches the end of the track, a sled-activated trigger pulse initiates an explosive to drive the plate into the nose tip, thus providing impact at the combined velocities. The electrical signal from the nose tip occurs when cutter wings (bars) on the sled make electrical contact with screen boxes mounted along side of the track. The screen boxes are connected to recorders for storing the impact output signal. The screen box data collection technique, the rocket sled, and explosive system (each developed earlier) are here combined to obtain the high-velocity impacts required.

This paper describes results of a test in which a sled-mounted, instrumented reentry vehicle nose tip traveling at 6230 fps was impacted by an aluminum target (3.083 inches thick, 11.6 inches in diameter), oriented at 27°, and traveling at 8326 fps. Flash x-ray shadowgraphs, high-speed motion pictures and impact transducer output all indicated excellent performance of the test technique at 14,556 fps.

Rocket Sled System

The rocket sled design and screen box data transmission system used for these experiments were developed in 1978 and are described in detail in other documents[1]. The rocket sled is a monorail configuration consisting of a Javelin IIC rocket motor with steel top-vented shoes attached to the front and back of the rocket motor. An aluminum fairing cone with a carbon nose tip containing the contact fuze was attached to the front shoe assembly. Figure 1 shows the rocket sled system at the impact location (note: 1 mile of track behind the sled). Twin pylons connected the front mounting ring to the shoe and contained holes for routing the signal line from the contact fuze sensor to the cutter bars mounted on each side of the front shoe (Figure 2).

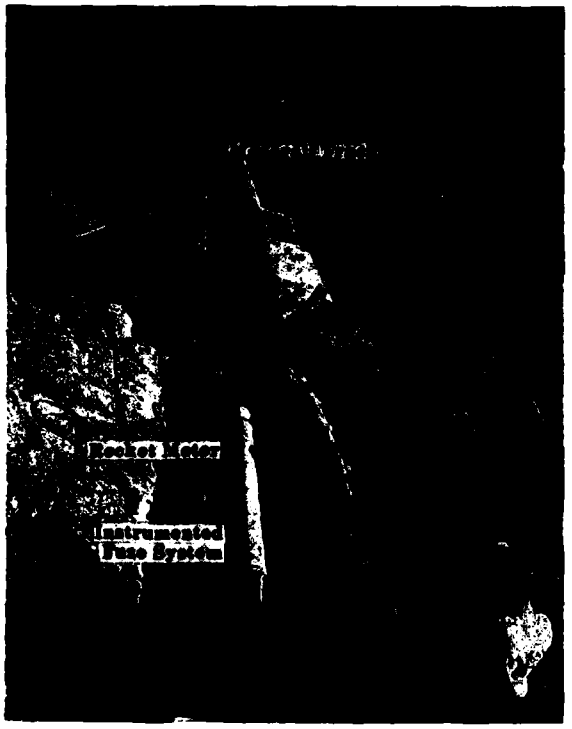

Figure 1. Rocket Sled at the Impact Location

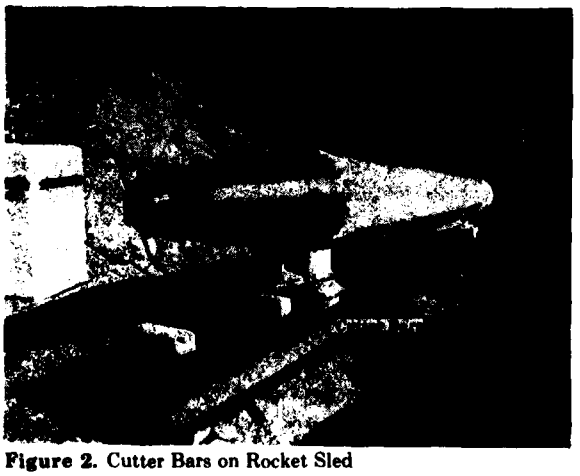

Figure 2. Cutter Bars on Rocket Sled

Two sets of screen boxes were attached to each side of the rail in the region of expected impact. The sled-mounted cutter bars cut through the screen boxes, completing electrical connection from the contact sensor to the recorders (see Figure 3). The impact was designed to occur while the cutter bars were contacting the screen boxes. The screen boxes consisted of 4-inch aluminum channel with copper screen stretched across the open channel. The screen was then pre-cut down the middle, and the horizontal copper wires were removed 1 inch on either side of the cut. The first set of screen boxes (30 inches long) bled off any residual charge that may have built up on the cutter bars during the sled run. The second set of screen boxes (60 inches long), positioned less than a cutter-bar length beyond the shorting boxes, was connected to the recorders for data gathering—see Figure 4. The positioning of the data screen boxes required that, even with maximum timing errors, the sled cutter bars would still be engaged during impact to monitor the sensor output.

Figure 3. Cutter Box

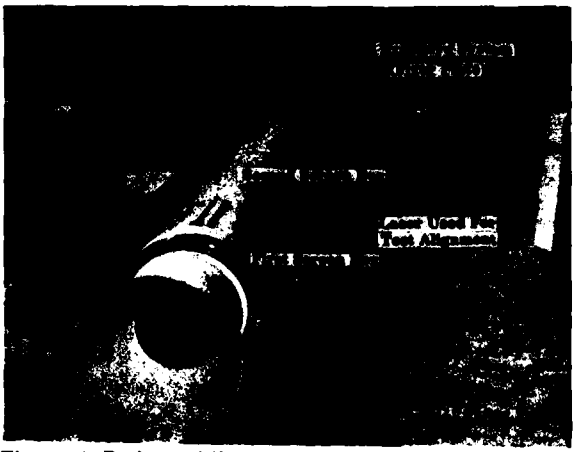

Figure 4. Rocket and Explosive Flyer Plate System

The Javelin IIC rocket motor, developed for sled testing, has the following characteristics:

Burn time	1.76 sec
Thrust	31,560 lb
Impulse	55,540 lb-sec
Loaded Weight	338 lb
Specific Impulse	242.8 sec

The total sled weight of 404 pounds was distributed as follows:

Front and rear shoe assemblies with cutter bars	45 lbs
Fairing cone and carbon nose tip with contact sensor	21 lbs
Rocket motor	338 lbs

These parameters indicate that a sled velocity of 6200 fps could be obtained for a 5000-foot length of track.

The sled trajectory was monitored using a Sandia Laboratories-developed Laser Tracker[4]. This tracker is capable of tracking a rocket sled traveling 6000 fps.

Break wires were used for determining sled velocity, as well as for triggering the flyer plate explosive system. The velocity break wires were placed 10, 30 and 50 feet from the planned impact location.

Explosive Flyer Plate System

The explosive system for this test consisted of 250 pounds of Composition C-4 explosive packed into a composite lead/steel barrel which weighed 4000 pounds. This explosive barrel system acted to propel a flyer plate (the impact target) to impact the sled-mounted test item. Figure 5 shows a sketch of the explosive system seen in Figure 4. The flyer plate (thickness) was varied across a diameter so that the different flyer thickness led to different local velocities, thus generating the end-over-end rotation of the plate at a rate of 470 radians per second. The flyer plate geometry (thickness), along with barrel tamping and explosive and cushion properties, was used to predict flyer plate initial velocity of 8900 fps. The velocity and the rotation rate determine the angular rotation per unit length of trajectory. This rotation value allows calculation of the location of the explosive system to give impact at the desired angle. A previous shock and vibration paper details the flyer plate design calculations[3]. Calculations to account for reduced velocity caused by air drag were applied to determine the expected impact velocity of 8875 fps. This particular flyer plate design had never been used before; therefore, predictions were expected to be only within 5% of the predicted value[3]. (The actual velocity was 6.2% lower than expected.)

Flash x-ray exposures of the flyer plate prior to impact have typically been used to measure flyer plate condition, velocity, and orientation. This data allows determination of flyer plate/test item contact within ± 1 μs and has been extremely reliable. Three exposures were used for diagnostics of this test. The film was placed in protective cassettes to insure no film damage during the test. The setup of this system is detailed in a later section.

The site for this test was located about one-half mile from other test facilities and, therefore, a significant effort was made to contain the damaging effects of the explosive system (shrapnel and blast overpressure) within a radius of less than 2300 feet. A 6-foot thick overburden of dirt was piled above the explosive charge to reduce the trajectories of the parts of the barrel as it disassembled during flyer plate launch*. The dirt barrier was also extended around and above the flash x-ray tube heads to prevent hardware damage. Figure 6 shows the barriers for this test.

*Methods have earlier been developed for predicting shrapnel size and velocity along with methods of estimating the effect of the dirt barrier on trajectory. These methods were used to calculate the safe range for this test.

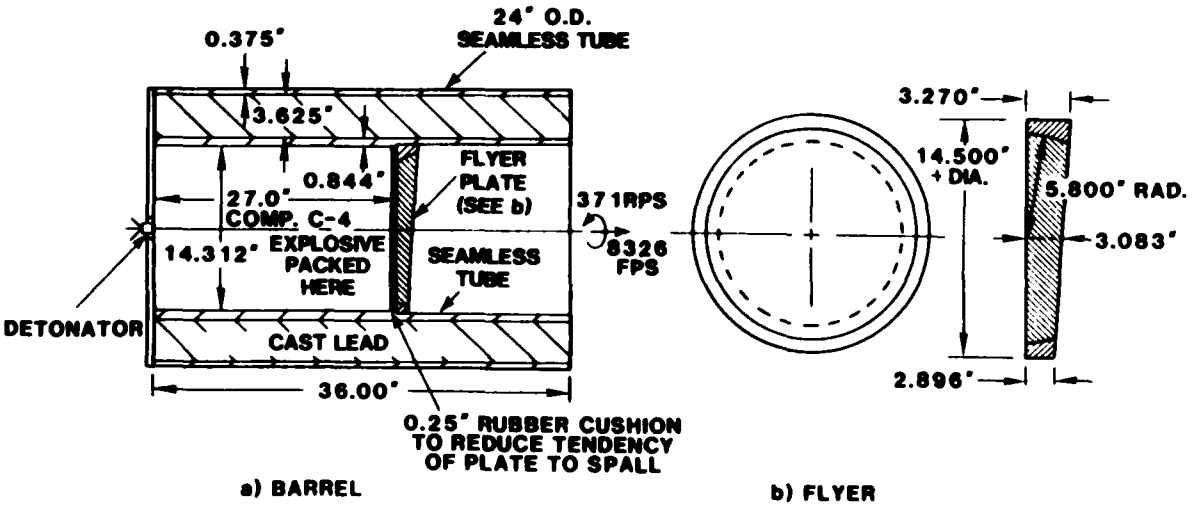

Figure 5. Explosive Barrel and Flyer System

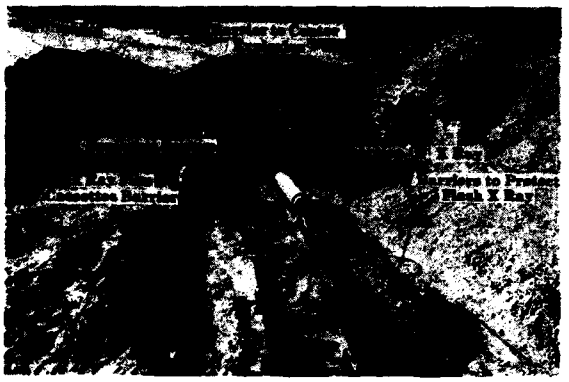

Figure 6. Barriers to Contain Explosion and Protect X-Ray System

Combined Systems Setup

Figure 7 shows a plan view of the test setup. The flyer plate/nose tip impact was planned to occur directly above the end of the track extension. A 22-foot section of rail was welded to the end of the permanent track so that any impact damage would not occur on the permanent portion of the track. The prime x-ray film was set up so that the nose tip position should have been in the middle of the film at impact time. The two other x-ray cassettes were in positions 20 and 40 inches closer to the explosive system. The Explosive System Triggering break wire on the track was positioned so that the flyer, if traveling at the calculated rotation rate and velocity, would have rotated 40° at the time of impact. The flyer was calculated to travel 154″ in 1576 μs to impact. The sled velocity, multiplied by the flyer plate travel time, determined the placement of this break wire on the track (131.6 inches from the end of the track). The break wire signal activated a high-voltage fire set which then initiated the explosive charge and also started delay timers for the x-ray pulsers so that the pulses would occur when the flyer was between each of the x-ray tube heads and the corresponding film cassettes.

Time tolerance was extremely important for these tests. Figure 8 shows possible error sources and the effect of these errors on obtaining data through the screen boxes, as well as diagnostic x-ray data.

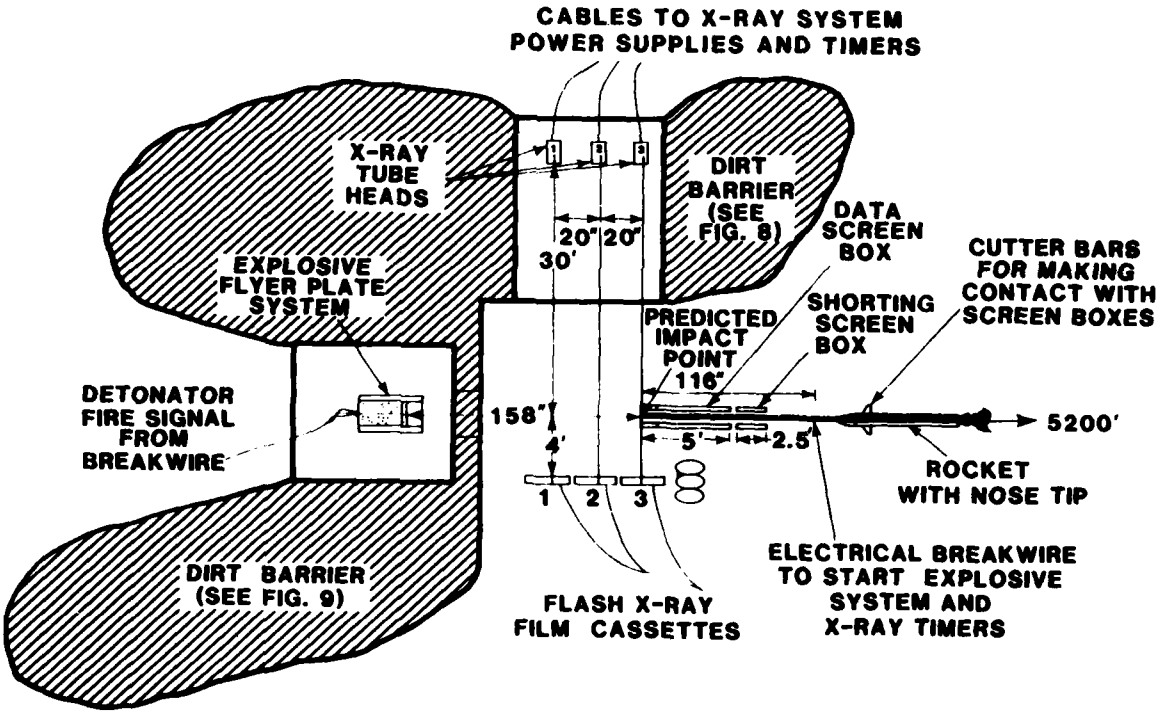

Figure 7. Plan View of Test Set-Up

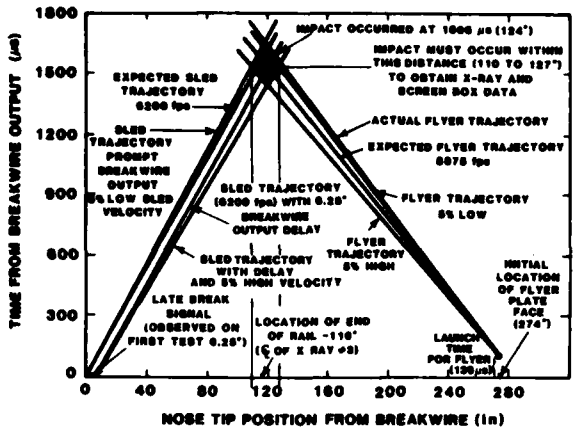

Figure 8. Effect of Velocity Errors on Impact Condition and Diagnostics

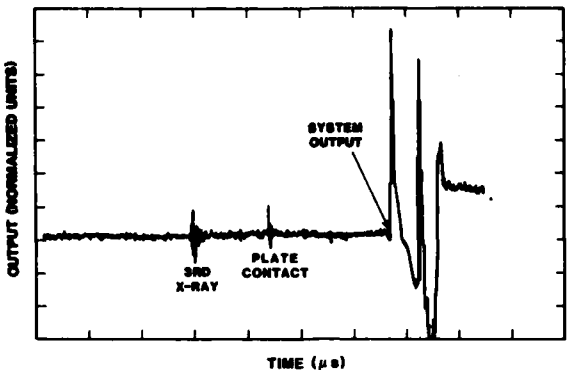

Figure 10. Impact Fuze Output Through Screen Box

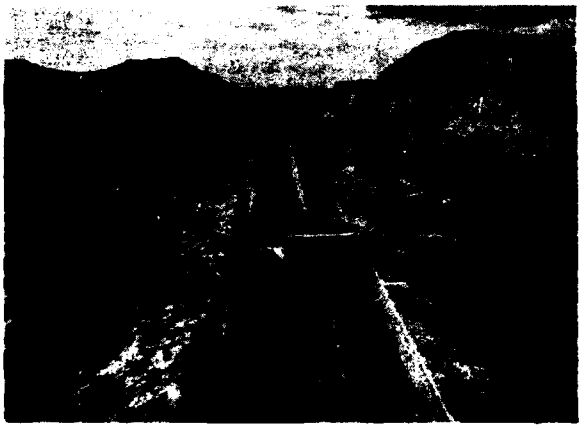

Figure 11. Impact Region After Test

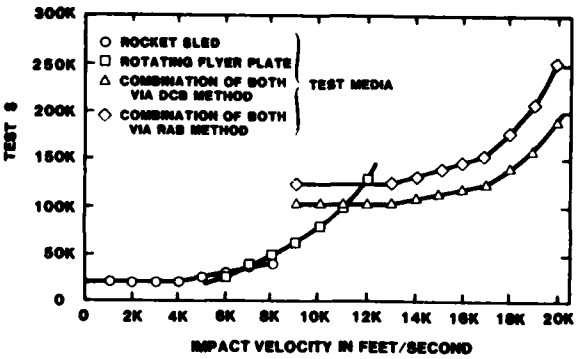

Figure 12. Single Model Impact Fuze Test Costs vs Test Media

Test Results

The experiment was conducted successfully. The Explosive System Triggering break wire properly functioned, starting the x-ray time delay generators and initiating the explosive system. The sled-mounted nose tip and flyer plate impacted 1606 μs after the break wire signal, approximately 30 μsec later than expected. Figure 9 is a tracing of the x-ray exposure of the plate just prior to impact. The closure velocity was 14,556 fps (6230 fps from sled and 8326 fps from the flyer plate); the plate at impact time had rotated only 27°, versus the 40° expected.† Figure 10 shows the data from the fuze system through the screen boxes. The timing events and x-ray exposures were all consistent, giving good confidence in impact time measurements. A delay of 90 μs from the sled break wire contact to actual HE initiation signal output was oversved on this test. Compensations from a previous test reduced the effect of this error. Figure 11 shows the test site after the test (compare with Figure 6).

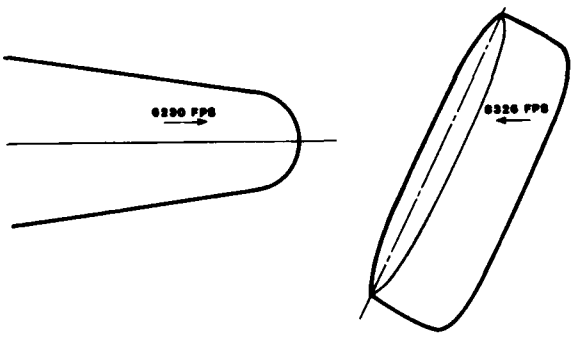

Figure 9. X-Ray Exposure Prior to Impact

†The difference in rotation was found to be caused by a ground effect, since the flyer plate trajectory was close to the ground. This effect can be eliminated in the future.

Conclusions

A combined rocket sled/explosive flyer plate test technique has been developed which will produce impacts in the 10 to 20,000-feet-per-second range. System timing worked as predicted except for the delay from break wire touch to circuit open (90 μs). This delay may be accounted

for in future setups or an alternate signal method, such as breaking a laser beam, should allow more positive timing for insuring diagnostic data recovery. Target velocity and thickness can be adjusted to obtain desired impact conditions. Explosive systems of 1000 pounds are feasible at the Sandia sled facility. The cost for this test was less then $100 K—dollars. System performance and cost information is summarized in correspondence on file at SNLA[5].

References

[1]D. L. Preston, "The Transmission of High Frequency Data From Rocket Sleds Through Screen Boxes," Sandia Laboratories Report SAND76-0067 Aug. 1976.

[2]F. H. Mathews and B. W. Duggin, "Barrel-Tamped, Explosively Propelled Plates for Oblique Impact Experiments," Shock and Vibration Bulletin, No. 46, Pt. 2, Aug. 1976, pp 145-154.

[3]R. A. Benham, "Terminal Velocity and Rotation Rate of a Flyer Plate Propelled by a Tube Confined Explosive Charge," Shock and Vibration Bulletin, No. 49, Pt. 2, Sept. 1979, pp 193-201.

[4]K. C. Bauhs, "Instruction Manual for Sandia's Laser Tracker," Sandia Laboratories Report SAND80-2049 June 1981.

[5]Letter From: G. E. Clark, 2362, To: D. C. Bickel, 7535 and R. A. Benham, 7533, Subject: Test Costs for "High Velocity" Impact Tests Dated April 17, 1984 Sandia National Laboratories.

WATER IMPACT TESTING OF A FILAMENT WOUND CASE

A. A. Schmidt and D. A. Kross
NASA/Marshall Space Flight Center
Huntsville, Alabama

and

R. T. Keefe
Chrysler Corporation
New Orleans, Louisiana

A lightweight Filament Wound Case (FWC) Solid Rocket Booster (SRB) is being developed by NASA to increase the payload capability of the Space Shuttle. As with the steel boosters, the current plan is to recover the FWC SRB's after they impact the ocean at 65 to 85 ft/sec. As the boosters enter the ocean (nozzle first) the water moves away from the vehicle creating a cavity, which then collapses on the vehicle, and results in a significant loading event. To understand this loading event, tests were conducted on a quarter scale FWC model to measure cavity collapse pressure distributions, deflected shape and the effects of end conditions and pressure scaling.

INTRODUCTION

A lightweight Filament Wound Case (FWC) Solid Rocket Booster (SRB) is being developed by NASA to increase the payload capability of the Space Shuttle. As with the steel boosters, the current plan is to recover the FWC SRB by decelerating them via deployment of parachutes and then impacting the ocean tail first at 65 to 85 ft/sec. A major design consideration for the FWC SRB aft structural region is the water impact cavity collapse loading, depicted in Fig. 1. Flight experience gained from steel motor cases indicate that the high energy cavity collapse loadings cause significant structural dynamic responses. With the FWC, this problem is compounded because little is known about composite structure response to this unsymmetric dynamic loading.

A joint analytical/test program was initiated to determine the loading and structural dynamic responses. This program included an 8.5% rigid model water impact test, which was completed in June 1983, for determining rigid body loads as a function of impact conditions. Results from the 8.5% model were used to generate preliminary design loads.

The second water impact test series, which is the subject of this paper, addressed the structural dynamic response of an actual filament wound cylinder subjected to cavity collapse loads. These tests were conducted in the Hydroballistics Facility at Naval Surface Weapons Center, White Oak, MD. Objectives of the tests were to 1) determine the cavity collapse dynamic pressure loading environment, 2) evaluate the structural dynamic response of the scale model FWC, 3) assess the effect of joint flexibility on response, 4) evaluate the effect of adding stiffener rings, and 5) investigate atmospheric pressure scaling effects on applied pressures, cavity shape and cavity closure dynamics. Test results will be combined with analytical investigations at a later date to predict full scale loads and responses.

MODEL DESCRIPTION

The test article shown in Fig. 2 was a quarter scale model of the aft segment area of the booster. The model weighed approximately 2,000 lbs. and

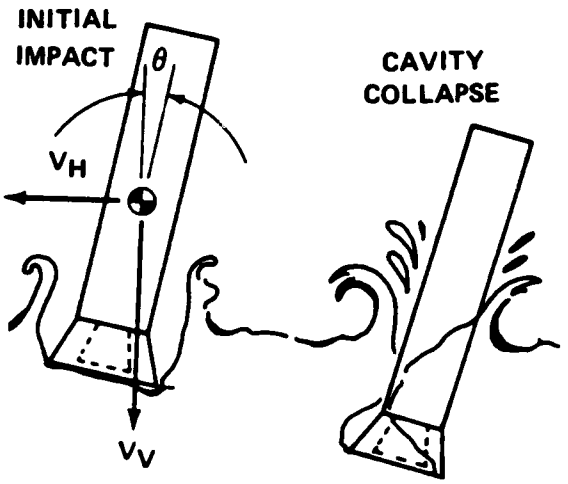

Fig. 1 - Cavity Collapse Loading

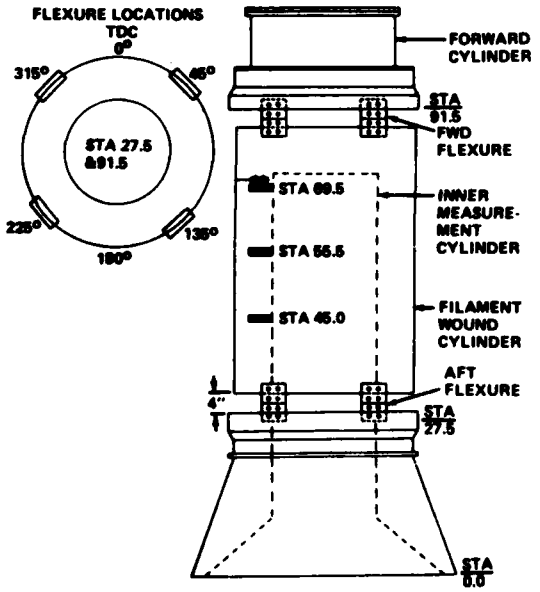

Fig. 2 - Test Article

each of its four major elements were connected with mechanical fasteners. These four major elements were, 1) the aft skirt, 2) inner measurement cylinder, 3) FWC segment and, 4) forward cylinder.

The aft skirt was constructed of mild steel and represented flight geometry in a general sense only, since the aft skirt was meant to serve as a cavity generator and provide structural attachment between the FWC and the inner measurement cylinder. The inner measurement cylinder was used as a rigid mounting base for the relative deflection (of the case) and rigid body accelerometers. A filament wound graphite-epoxy cylinder of quarter scale thickness and diameter represented the FWC. As shown in Table 1 it was composed of eleven alternating layers of helical and hoop windings. The helical wind angle was 29° and there were a total of eight helical lamina (four pairs of ±29°) and three 90° (hoop) lamina. This composite cylinder did not have flight type scaled pinned joints but, instead, was simply attached with 40 equally spaced bolts at each end. The forward cylinder served as a structural closeout of the forward end of the model.

TABLE 1

Filament Wound Cylinder

LAYER NUMBER	THICKNESS (INCHES)	ANGLE OF PLY (DEGREES)
1	0.0236	29.0
2	0.0236	– 29.0
3	0.0273	90.0
4	0.0236	29.0
5	0.0236	– 29.0
6	0.0273	90.0
7	0.0236	– 29.0
8	0.0236	29.0
9	0.0273	90.0
10	0.0236	– 29.0
11	0.0236	29.0

TOTAL THICKNESS = 0.271 INCHES
LENGTH OF CYLINDER = 56 INCHES
DIAMETER = 36 INCHES
WEIGHT = 95 LB.
LAMINATE PROPERTIES
AXIAL 7.2×10^6 PSI
HOOP 6.2×10^6 PSI
G_{XY} 2.6×10^6 PSI
V_{XY} 0.34

The four major structural elements were augmented with additional hardware, as required to meet various run peculiar objectives. This hardware

included a flow restricter, forward and aft flexures, and case stiffener rings. Table 2 defines the various configurations tested.

TABLE 2

Configuration Tested

CONFIG NUMBER	AFT SKIRT, INNER CYL, FWC SEGMENT AND FWD CYL.	FLOW RESTRICTOR	FWD & AFT FLEXURES	STIFFENER RINGS
I	YES	NO	NO	NO
II	YES	YES	NO	NO
III	YES	YES	YES (TYPE A)	NO
IV	YES	NO	YES (TYPE B)	NO
V	YES	NO	YES (TYPE B)	YES (3)

A flow restrictor was used on selected tests to decelerate the model quicker, causing the cavity to collapse lower on the case. Flexures were added at each end of the FWC to increase its flexibility. Type A flexures were used at the forward interface for configurations III, IV and V, and at the aft interface in configuration III. Stiffer Type B flexures were used at the aft interface for configurations IV and V.

It was important to test with stiffener rings on the case, but to wind them on, as on the full scale, was impractical from cost and schedule standpoints. Aluminum stiffener rings used for configuration V, were the most practical way to represent full scale stiffener rings. These rings, shown in Fig. 3, were mounted using an adhesive and tensioned by tightening the bolts holding each two-piece ring together.

Instrumentation Program

Model instrumentation consisted of 18 deflection, 22 pressure, 16 acceleration, and 40 strain transducers. Deflection measurements were made using Schaevitz Model 2002XSD which was specially modified to fit geometric constraints imposed by the model. Pressures were measured with PCB Piezotronics high frequency Model H113 A22 pressure transducers. These transducers were mounted in fiberglass impregnated nylon which in turn mounted in the composite case. Composite case and inner cylinder accelerations were measured with PCB Model H302-A04 quartz accelerometers. Tangential and axial strains of the composite cylinder were measured using Dentronics strain gage Model AP2316N C6ETS with a 10 mils thick Kapton backing.

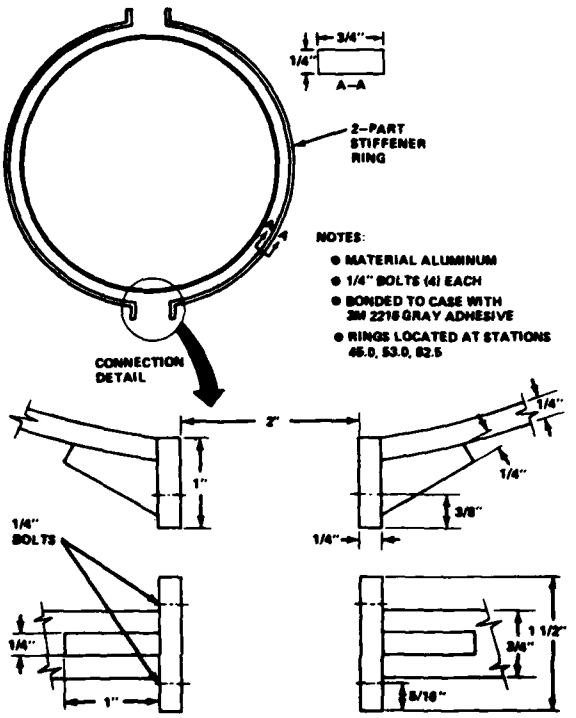

Fig. 3 - Stiffener Ring Geometry

The deflection measurements were located at model axial stations 45.0, 55.5, and 69.5 at circumferential positions of zero and 180 degrees. In addition, at the lower two axial stations, deflection measurements were located every 30 degrees around from -90 to +90 degrees. Note that the zero degree location (lee side) is the area of maximum cavity collapse pressure. The pressure measurements were similarly concentrated on the model lee side to obtain the detailed localized distribution. Four accelerometers were mounted on the relatively stiff inner measurement cylinder to obtain rigid body accelerations. The remaining 12 accelerometers were located on the FWC to measure radial case responses. Strain gages were located on the inner and outer surfaces of the FWC in the axial and tangential direction, every 90 degrees circumferentially, at two axial positions. In addition, strain gages were located on the mid and aft stiffener rings.

The data acquisition and recording system was capable of recording signals from 0 to 10 KHZ. Measurements were recorded direct IRIG wideband at 30 IPS. Seventy-eight channels were recorded on each run and time code was recorded on every fourteenth tape recorder channel. Before further processing the data were filtered at 5 KHZ and digitized at 10,000 samples/second.

High speed (~ 250 frames/sec.) motion picture coverage, with split water image, was provided in the pitch and yaw planes. Above water documentary (~ 24 frames/sec.) photographic coverage was also provided. In addition, above water video coverage was used for quick-look evaluation purposes.

Test Conditions

Table 3 lists test conditions for all drops. Pertinent scaling is discussed in reference 1.

TABLE 3

Test Conditions

RUN NO.	VERTICAL VELOCITY V (FT/SEC)	IMPACT ANGLE θ (DEG)	TANK PRESSURE P_∞ (PSIA)	STRUCT. CONFIG.
1	32.5	0	14.7	I
2	32.5	0	3.7	I
3	32.5	10.25	3.7	I
4	32.5	5.75	3.7	II
5	37.5	5.75	3.7	II
6	37.5	5.75	1.2	II
7	37.5	0	3.7	II
8	42.5	0	3.7	II
9	42.5	5.75	3.7	II
10	42.5	3.5	3.7	II
11	37.5	3.5	3.7	II
12	32.5	0	14.7	III
13	32.5	0	8.2	III
14	32.5	0	3.7	III
15	32.5	0	3.7	IV
16	32.5	5.5	3.7	IV
17	32.5	3.5	3.7	IV
18	37.5	3.5	3.7	IV
19	37.5	3.5	3.7	IV
20	37.5	6.25	3.7	IV
21	42.5	3.75	3.7	IV
22	42.5	6.5	3.7	IV
23	37.5	3.5	3.7	V
24	37.5	6.0	3.7	V
25	42.5	3.5	3.7	V
26	32.5	3.5	3.7	V

Using Froude scaling relationships, model impact velocities correspond to full scale values of 65 to 85 ft/sec. Also, 3.7 psia tank air pressure relates to one atmosphere full scale.

Since the main purpose of Run 1 was to check out the instrumentation, recording system and model, the tank pressure was ambient. The majority of the remaining tests were performed at 3.7 psia.

Data from runs one through three revealed that the cavity was collapsing too high on the model. A flow restrictor was placed at the base of the inner measurement cylinder to increase the model rigid body deceleration, and thereby lower the point of cavity collapse. This geometry, denoted as configuration II, was used in runs 4 through 14. For run 6, the tank pressure was lowered to 1.2 psia to further examine pressure scaling effects.

To increase the radial deflection of the composite cylinder, type A flexures were added at each end of the composite cylinder. This was configuration III, and was used in runs 12 through 14. The aft flexures experienced a permanent yield on run 14, so, stiffer type B flexures were used at the aft interface for the completion of testing.

Configuration V was identical to configuration IV, except for the addition of three stiffener rings. These rings simulated the cavity collapse rings planned for the full scale Filament Wound Case.

Test Results Summary

Figure 4 shows that peak measured cavity collapse pressures were not a distinct function of model configuration. Maximum radial deflections for the various model configurations are shown in Fig. 5. Configuration III experienced the maximum deflections since the least stiff flexures were used. The effect of impact velocity on peak cavity collapse is illustrated in Fig. 6. Peak cavity collapse pressures dropped approximately 40% by reducing the impact velocity 10 ft/sec. This effect is not as readily observable for the radial displacement shown in Fig. 7. Maximum displacements, however, are affected by impact angle, as shown in Fig. 8.

The effect of tank air pressure on the peak cavity collapse pressures and associated radial deflections is shown in Figures 9 and 10, respectively. Time histories of typical cavity

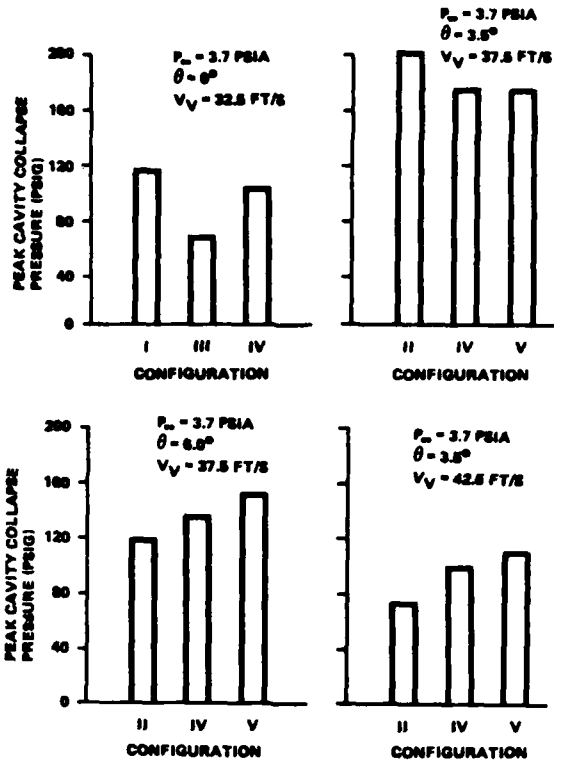

Fig. 4 - Peak Cavity Collapse Pressure (PSIG) for Different Configurations

collapse pressures and displacements are given in Figures 11 and 12 for different tank pressures. Although the pressure peaks on the time histories are of a similar magnitude, the area under the pressure-time trace (impulse) is greater for the lower tank air pressure. Similarly, the displacement is significantly increased as the tank pressure is lowered, as noted in figure 12.

Pressure traces in Fig. 11 behave erratically. Specifically, the pressure before the peak positive amplitude dips below ambient, which is not physically possible. As the pressure approaches ambient, cavitation should occur. Ambient should be the lowest pressure physically possible.

The pressure transducers were mounted in a nylon insert which, in turn, was screwed into a tapped hole in the FWC. The purpose of the nylon insert was to isolate the transducer from the case. Subsequent modal testing with the pressure transducers installed revealed that the output signal was influenced by the local case strain.

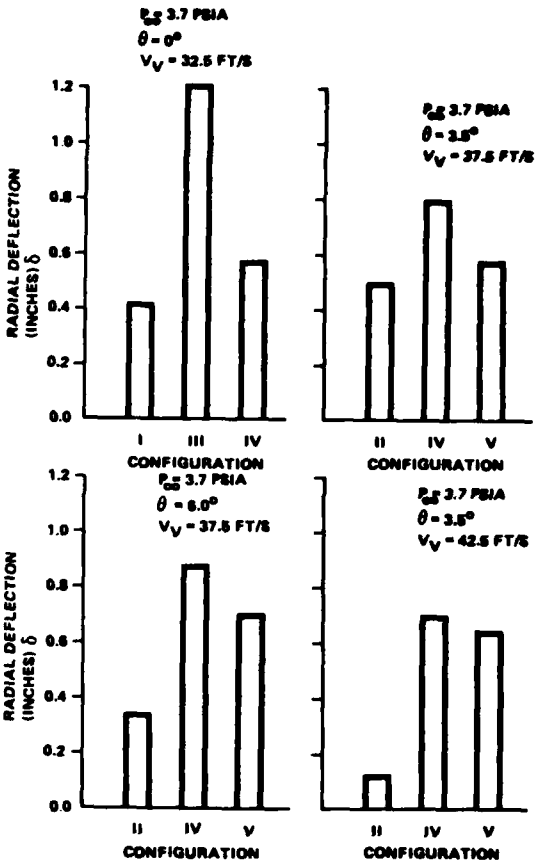

Fig. 5 - Radial Deflection (in.) for Different Configurations

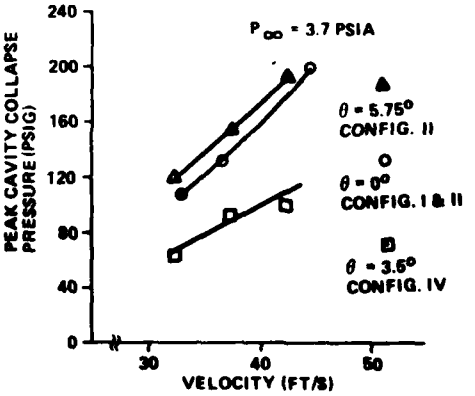

Fig. 6 - Peak Cavity Collapse Pressure (PSIG) as a Function of Velocity (Ft/S)

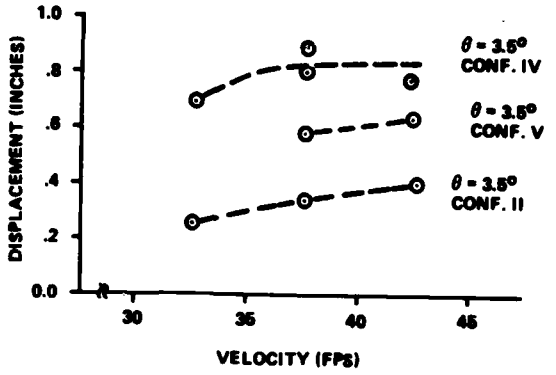

Fig. 7 - Radial Displacement (inches) as a Function of Velocity (Ft/S) (degrees)

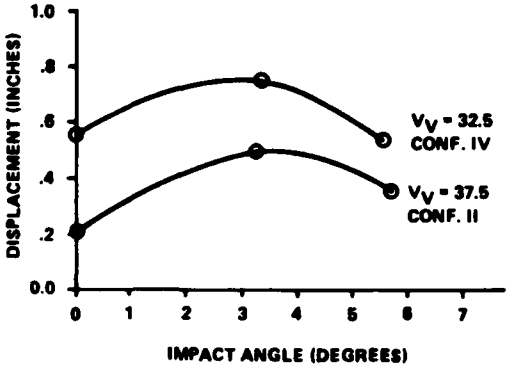

Fig. 8 - Radial Displacement (inches) as a Function of Impact Angle (degrees)

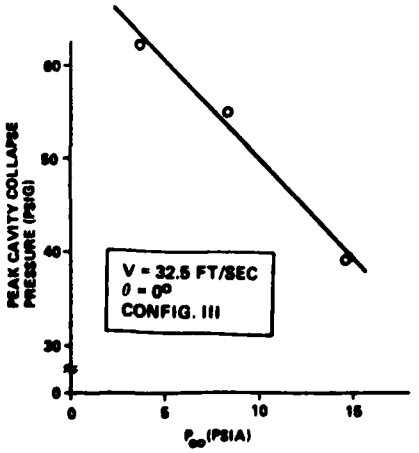

Fig. 9 - Peak Cavity Collapse Pressure (PSIG) as a Function of Tank Pressure (PSIA)

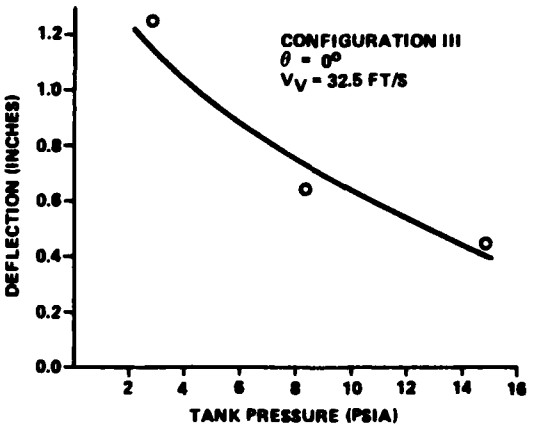

Fig. 10 - Deflection (inches) as a Function of Tank Pressure (PSIA)

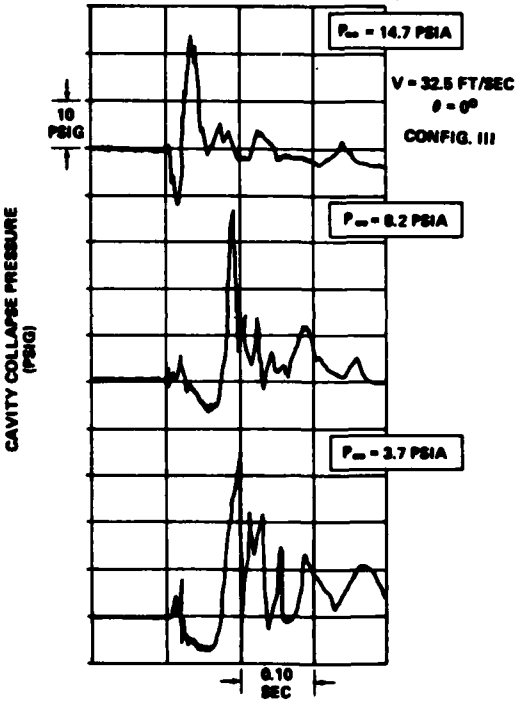

Fig. 11 - Cavity Collapse Pressures - Effect of Tank Pressure

Attempts to correct the pressure data were inconsistent, due, in part, to the sensitivity of the precise installation as well as the local FWC strain. Therefore, pressure results should be considered trend indicators only.

The effect of end condition stiffness on the FWC response is shown in Fig. 13. The peak radial displacement is nearly three times larger when the less stiff flexures were used.

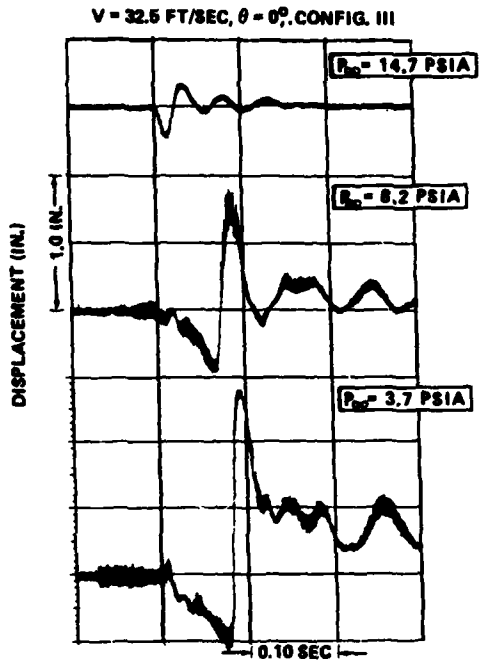

Fig. 12 - Radial Displacement - Effect of Tank Pressure

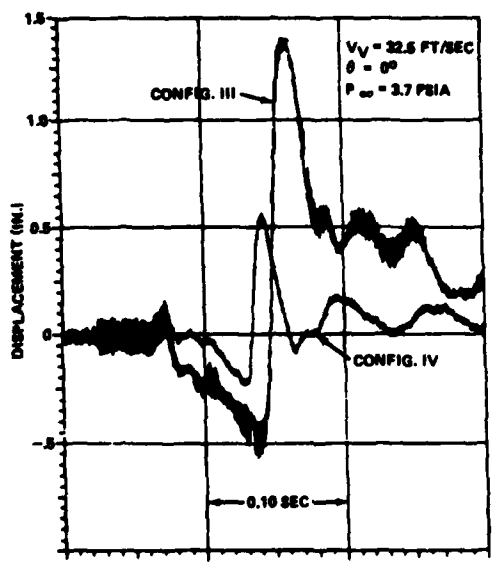

Fig. 13 - Radial Displacement - Effect of End Conditions

The typical axial and circumferential pressure distributions are presented in Figures 14 and 15, respectively.

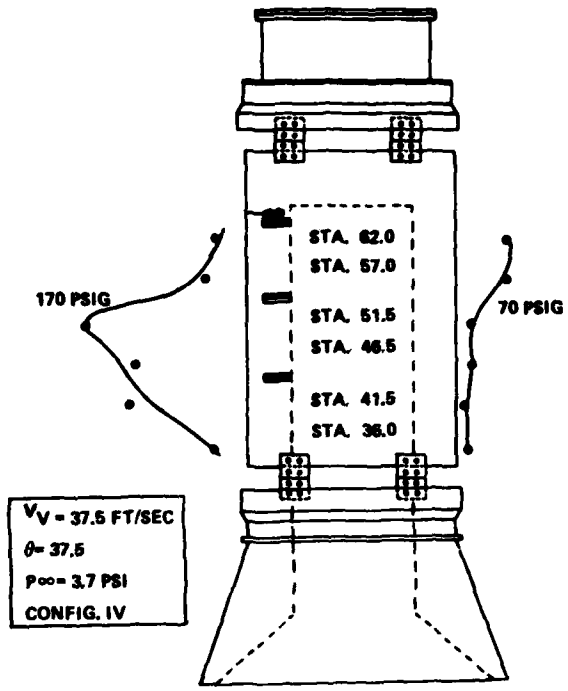

Fig. 14 - Axial Pressure Distribution

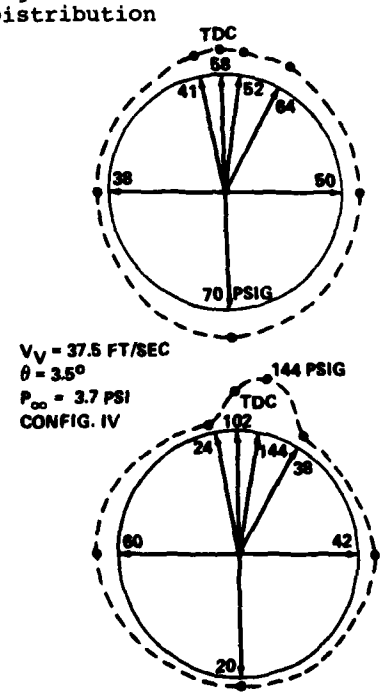

Fig. 15 - Circumferential Pressure Distribution

Note that the maximum pressure is of a localized nature circumferentially, and, to a lesser extent, axially. Fig. 16 illustrates that peak pressures measured along the case occur simultaneously. The corresponding distributions of deflection at the time of cavity collapse is shown in Figures 17 and 18. This distribution of radial displacement indicates a shell bending "lima bean" shape. The tangential strain gage measurements located on the inner and outer case surfaces near the point of maximum deflection are given in Fig. 19. Again, significant bending is noted from these measurements.

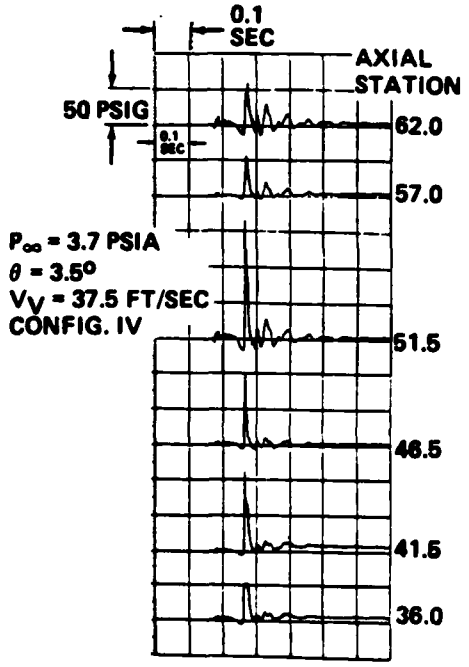

Fig. 16 - Axial Pressure Distribution Time Histories

The effect of stiffener rings on pressure, displacement, and case strain is shown in Figures 20 through 22. The pressure time history is similar except for a very narrow spike which peaks over 200 psig for the configuration without rings. The maximum displacement was reduced by approximately 15 percent when the stiffener rings were included. The maximum measured strains, however, were similar for both configurations. The strains measured on the stiffener ring at locations approximately 30 degrees from the maximum displacement radial location are shown in Fig. 23. The strain signatures are very similar for case and stiffener

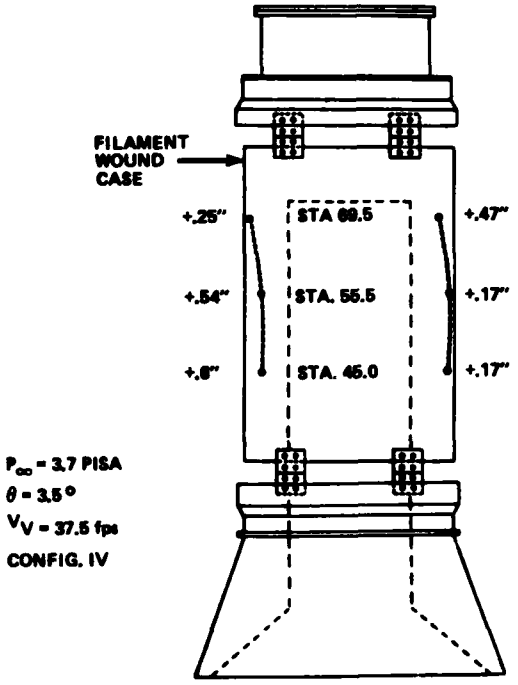

Fig. 17 - Radial Displacement at Cavity Collapse

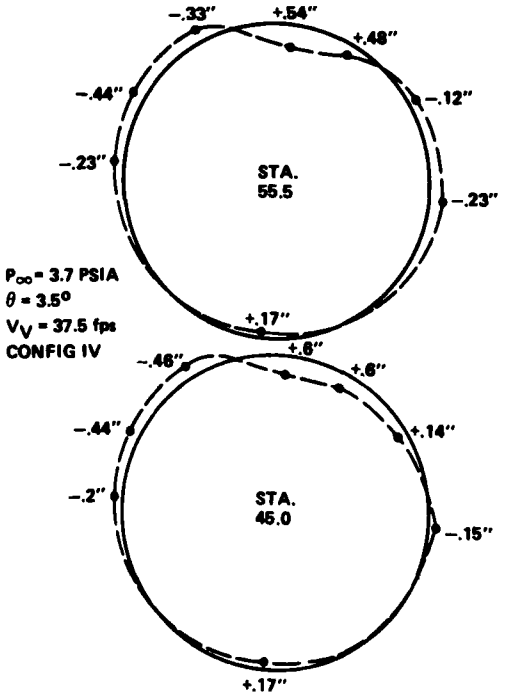

Fig. 18 - Radial Displacements at Cavity Collapse

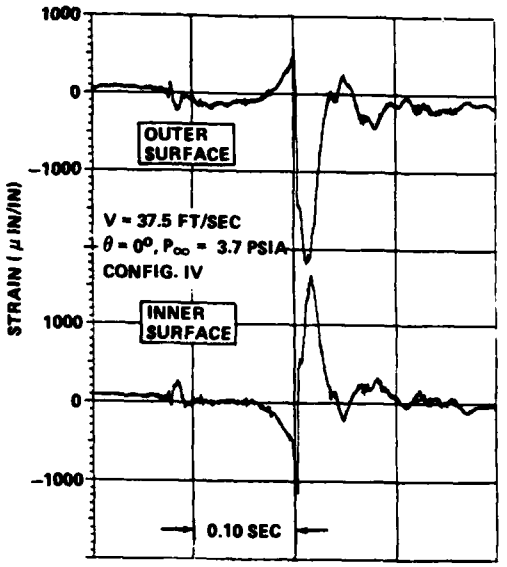

Fig. 19 - Case Tangential Strain

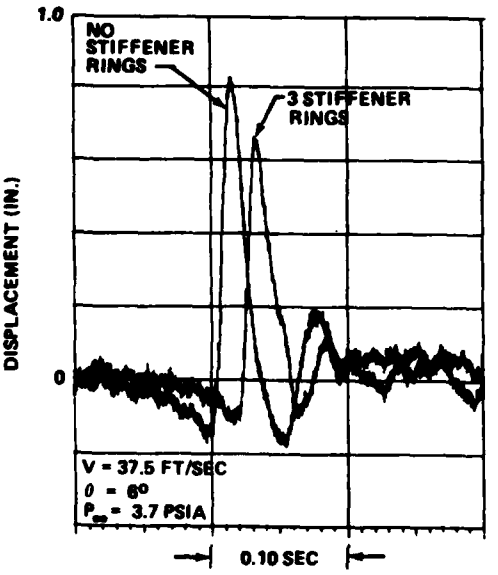

Fig. 21 - Radial Displacements with and without Stiffener Rings

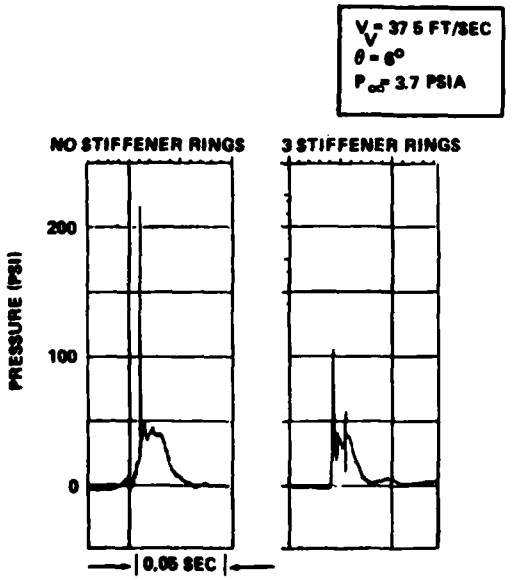

Fig. 20 - Cavity Collapse Pressures with and without Stiffener Rings

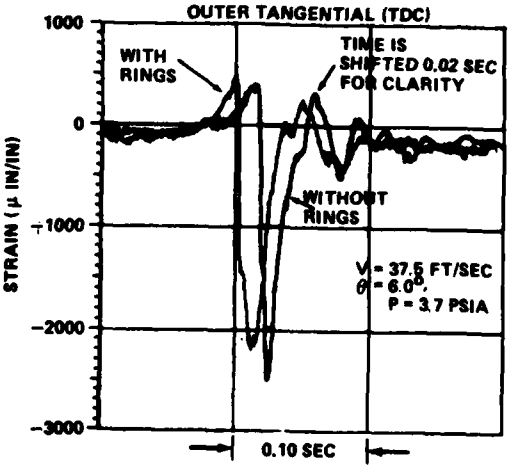

Fig. 22 - Effect of Stiffener Rings on Case Strains

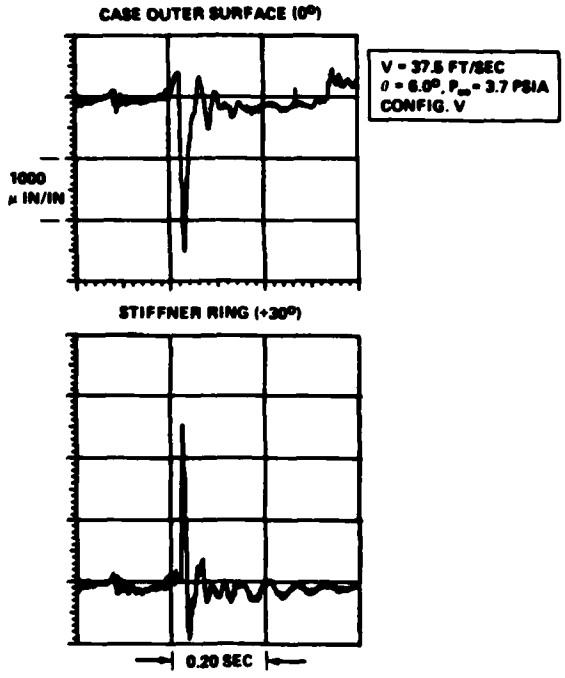

Fig. 23 - Case and Stiffener Ring Tangential Strains

ring for about three cycles; following this, the ring evidently debonds, as evidenced by the different signatures. A post test inspection revealed this debond.

Summary and Conclusions

A total of 26 water impact test were conducted using a quarter-scale FWC model to evaluate cavity collapse loading and associated structural dynamic response. Vertical impact velocities, angle and tank ambient pressure were varied to examine their effects on cavity collapse loading. The influence of structural joint flexibilities and stiffener rings were investigated. Pressure, displacement, acceleration, and strain data were recorded and additional analyses are underway. Significant trends have been identified and the following conclusions may be drawn from the results given above:

a. A reduction in peak cavity collapse pressure of up to 40 percent can be achieved by reducing the scale model impact velocity by approximately 20 percent. This effect is not as readily observable relative to the maximum radial deflections that were measured.

b. Atmospheric pressure scaling has a profound effect on the peak cavity collapse pressures as well as the maximum deflections. Measured peak pressures were doubled and deflections increased ~ five times when the tank air pressure was reduced from 14.7 psia to 3.7 psia.

c. End condition flexibility of the FWC composite cylinder did not have a major effect on the measured peak pressures. The impulse, however, did increase with increasing flexibility as did the maximum deflections. This implies that structural/water interaction needs to be addressed on the full scale FWC.

d. The cavity collapse pressure distribution, at the time of maximum load, is of a highly peaked localized nature. In addition, the maximum values appear to occur simultaneously.

e. The deflection pattern at the time of cavity collapse has a shell bending "lima bean" shape.

f. The addition of stiffener rings reduced the maximum deflection by approximately 15 percent.

g. Debond of the stiffener rings did occur and, at this time, represents a significant concern for the full scale FWC.

REFERENCES

1) R. Madden, H. A. Wright, D. A. Kross, "Scaling of Water Impact Data for Space Shuttle Solid Rocket Booster," Shock and Vibration Bulletin, Vol. 44, No. 3, pp. 165-175, August 1974.

DISCUSSION

Mr. Whang (David Taylor Naval Ship R&D Center): Were the pressure gages for the cavity pressure measurements right on the outer surface of the cylinder?

Mr. Schmidt: The pressure transducers were screwed into a fiberglass impregnated nylon molding, which was then screwed into the filament wound case. The pressure head was very slightly recessed from the surface; there was an RTV over that surface.

Mr. Whang: Were the pressures that you measured the interface pressures at various points on the outer skin?

Mr. Schmidt: Yes.

Mr. Whang: Do you have any hypotheses on what the scaling problems might be, or are you just searching for some scaling problems in going from the quarter scale to full scale? When you say quarter scale, is that just linear scaling?

Mr. Schmidt: It is linear scaling on geometry.

Mr. Whang: Was there some reason to doubt that certain scaling laws would work?

Mr. Schmidt: In any test you can only scale just so many things. This case had full scale properties for the elastic moduli, but I believe the pressure should scale linearly.

FLIGHT VEHICLE DYNAMICS

AIRWORTHINESS FLIGHT TEST PROGRAM OF AN AIRCRAFT EQUIPMENT FAIRING

V.R. MILLER
FLIGHT DYNAMICS LABORATORY
AF WRIGHT AERONAUTICAL LABORATORIES
WRIGHT-PATTERSON AFB, OH

and

T.P. SEVERYN
DIRECTORATE OF FLIGHT TEST ENGINEERING
4950th TEST WING
WRIGHT-PATTERSON AFB, OH

This paper contains the results of an airworthiness flight test program of an aircraft equipment fairing. The objective of the tests was to insure the airworthiness of the aircraft with the installed fairing. The tests were conducted to determine the structural integrity of the modifications and their effects on the aircraft handling qualities. The tests were extended to allow more detailed data acquisition and analysis due to the problems encountered with flow separation, aerodynamic buffeting and noise-induced fatigue. The test indicated that the airspeed envelope of the aircraft be restricted while the fairing was installed, and that structural modifications to portions of the aircraft be made. Rigid inspection requirements were levied after each flight to detect any structural damage.

INTRODUCTION

A diamond-shaped fiberglass fairing was designed, fabricated, and mounted on the underside of an Air Force transport. The shape and size of the fairing was such that a turbulent flow environment was anticipated behind the fairing which could interact with the aircraft structure. If the flow environment was too severe, intense fluctuating pressures would occur which could result in fatigue cracks in the aircraft outer skin and/or backup structure. As a result, an aerodynamic evaluation was performed to demonstrate the structural integrity and airworthiness of the modifications. A series of test missions were flown in two phases to accomplish this (Ref. 1).

TEST ITEM AND INSTALLATION

A testbed transport aircraft was used for the test missions. The test item was a diamond-shaped fairing mounted on the centerline lower fuselage as depicted in Figure 1. The fairing extended 152.4 cm (60 in.) along the centerline, and from butt line (BL) 26 left to 26 right, and 39.37 cm (15.5 in.) below the aircraft. The forward faces each contained six ram-air inlet slots 7.37 by 2.54 cm (2.9 by 1.0 in.) and the right rear face contained four ram-air exit slots, two 15.88 by 3.18 cm (6.25 by 1.25 in.) and two 17.78 by 2.54 cm (7.0 by 1.0 in.). In addition, the right forward face contained a radome aperture approximately 52.07 by 16.76 cm (20.5 by 6.6 in.) in size. All of the ram-air slots and the radome aperture were fitted with aluminum closeout panels during testing in the ferry configuration.

INSTRUMENTATION AND TEST EQUIPMENT

Phase 1

The initial test instrumentation consisted of pressure microphones and accelerometers. Yarn tufting attached to the fairing and aircraft skin allowed flow investigation using 16mm motion pictures and still photographs. The transducers consisted of Gulton Industries Model MVA2400 1/4" microphones and Vibrametrics Model M1000 accelerometers. The microphones were either flush mounted on the aircraft skin behind the fairing or mounted inside of the fairing. The microphones contained a vibration compensating system which cancelled any output due to microphone vibration. The

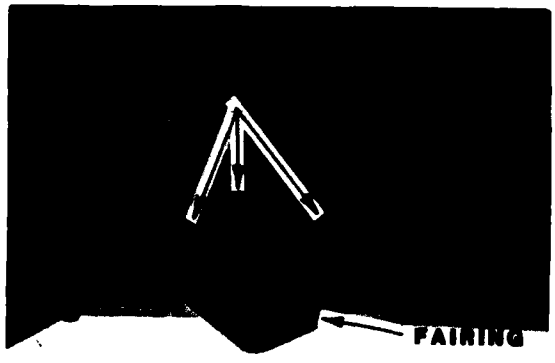

FIG. 1 FAIRING INSTALLATION - RAM-AIR COVERS ON

accelerometers were of extremely small size and mass, weighing less than 2 grams, and did not change the dynamic response of the structure to which they were mounted. They were bonded on the interior of the fairing surface, the antenna mounting plate, and the aircraft skin 144.8 cm (57 in.) behind the fairing, using Eastman 910 adhesive. Cabling was used to carry the transducer output signals to amplifiers, whose outputs were recorded on a Leach Model MTR3200 tape recorder. In addition to the tranducer signals, channels were available for a time code generator and a PAM commutator signal sampling the amplifier gain levels. An edge track was used for voice recording in-flight. The yarn tufting was attached to the fuselage and fairing skins prior to the test flights and photographed in-flight to allow analysis of the flow patterns around and over the fairing.

Phase 2

Following the initial test flights and data reduction, the existing system was converted and an additional system installed to record signals from an array of twenty-four pressure microphones aft of the fairing. Figure 2 includes the locations of the pressure microphones installed for the second phase. In addition, an inertial navigation system (INS) was installed in the test aircraft for Phase 2 to determine sideslip angle in-flight.

TEST CONDITIONS

All testing was accomplished at Wright-Patterson AFB, Ohio. Eight sorties were required to complete the aerodynamic evaluation of the modified aircraft. In addition, T-38, F-4, and T-37 aircraft were utilized as photo and safety chase during the tests.

Phase 1

The first flight of Phase 1 testing was conducted with the fairing ram-air covers installed (ferry configuration). Flight conditions included steady sideslips in clean (gear and flaps up), approach (gear down, flaps 50%) and gear down - flaps up configurations, and clean approach to stall buffet tests. Speeds ranged from 150 to 325 knots indicated airspeed (KIAS).

The second flight was again conducted in the ferry configuration and completed the unfinished profile of Flight 1. Test conditions included:

a. Clean level turns to 1.5 and 2.0g.

b. Gear down level acceleration and decelerations from 180 to 300 KIAS.

c. Clean level acceleration and deceleration from 180 to 325 to 180 KIAS.

d. Clean steady sideslips.

e. Clean high speed descent at 0.88 Mach/350 KIAS.

The third flight was conducted with the fairing ram-air covers removed (test configuration). Test conditions included:

a. Steady sideslips in clean and approach configurations.

b. Clean level turns to 1.5 and 2.0g.

c. Level accelerations and decelerations from 180 to 300 to 180 KIAS in both clean and gear down configurations.

d. Clean approach to stall buffet.

The fourth flight repeated test points from flight two necessitated by a partial instrumentation failure.

Phase 2

The Phase 2 testing was conducted with the beefed up skin behind the fairing. The fifth flight, in the test configuration, included test conditions of:

a. Stable speeds in increasing increments in both clean and gear down configurations.

b. Clean steady sideslips.

c. Level deceleration in both clean and gear down configurations from 300 to 200 KIAS.

The sixth flight was conducted with the fairing and equipment removed (baseline configuration) in order to obtain baseline noise data on the aircraft, repeating the flight five profile.

The seventh flight conducted in the ferry configuration, included:

a. Stable speeds in increasing increments in both clean and gear down configurations.

b. Clean steady sideslips.

c. Level decelerations from 325 to 200 KIAS clean, and from 300 to 200 KIAS gear down.

d. Clean penetration descent at 285 KIAS.

Prior to and after Phase 2 flight non-destructive evaluations (NDE) were made of the aircraft structures using portable x-ray equipment to detect any fatigue cracks.

Phase 3

Phase 3 consisted of one flight with the fairing equipment operational to verify the ram-air cooling adequacy. No acoustic or vibration data were obtained.

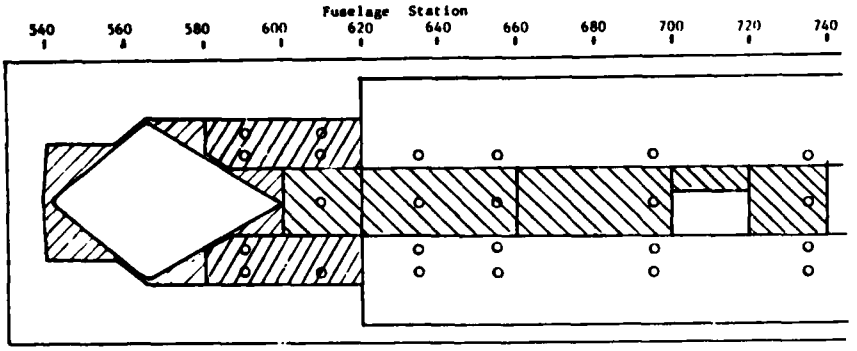

	FS	BL		FS	BL		FS	BL
1	735	L26	9	655	L26	17	610	L26
2	735	L16	10	655	L16	18	610	0
3	735	0	11	655	0	19	610	R16
4	735	R16	12	655	R16	20	610	R26
5	695	L26	13	635	L26	21	590	L26
6	695	L16	14	635	L16	22	590	L16
7	695	0	15	635	0	23	590	R16
8	695	R16	16	635	R16	24	590	R26

Doubler .090 in
Panels .125 in

FIG. 2 STRENGTHENED SKIN/PANEL AREAS AND PHASE 2 MICROPHONES

DATA REDUCTION AND ANALYSIS

Phase 1

The pressure microphone and accelerometer tapes were processed after each flight. The recorded microphone data were processed and computer plots generated of frequency (Hz) versus sound pressure level (dB). Accelerometer data were also processed by computer and plots were generated of frequency versus power spectral density (g^2/Hz). Reference 2 provides extensive explanation of the reduction techniques and equipment used.

Phase 2

As was previously done, the pressure microphone data tapes were delivered for processing after each flight, and plots generated for analysis. Baseline noise data were collected with the fairing and equipment removed which provided the basis for determining noise directly due to the fairing installation. Reference 3 contains detailed analyses of the acoustic data collected during Phase 2.

TEST RESULTS AND DISCUSSION

The fairing installation was demonstrated to be structurally sound to 2.0g and to 315 knots equivalent airspeed (KEAS)/0.88 Mach, however, problems related to the installation did develop. On the first flight, aerodynamic buffeting from separated airflow around the fairing was severe enough to be felt in the cabin at 240 KIAS upon takeoff climbout. The aircraft test crews indicated that the cabin noise levels were substantially higher than normal. The buffeting increased in intensity with airspeed and was judged too severe to continue beyond 325 KIAS and 15000 feet pressure altitude (PA). Figure 3 presents the accelerometer and pressure microphone data for this high speed condition where peak power spectral density (PSD) values correlate with the peak decibel readings. Both data show marked rises near 90 Hz, the peak frequency predicted by Karman vortex analysis. This indicates that most of the vibration was due to the noise generated by the separated flow.

Flight 2 completed the first profile including the high altitude test points. While climbing, the chase aircraft pilot reported that he thought something had separated from the test aircraft. When cleared in for a closer inspection though, nothing unusual was noted. The mission was then completed without further incident. Upon postflight inspection, it was discovered that an antenna panel immediately behind the fairing was indeed missing. Since the antenna was not required for any test operations, the missing panel was replaced by an aluminum close-out panel which was securely fastened.

The third flight was conducted in the test configuration with airspeed limited to 300 KEAS due to the previously discovered problems. No noticeable changes in noise level were evident versus the covers-on-flight. Post-flight inspection of the fuselage revealed a cracked hinge on a centerline panel just aft of the antenna close-out panel. The hinge was replaced for Flight 4, which repeated the test point of Flight 2, whose data were lost due to an instrumentation failure. Postflight inspection revealed the same hinge had cracked during this 1.7 hour flight. Subsequently, sonic fatigue life calculations were made. The

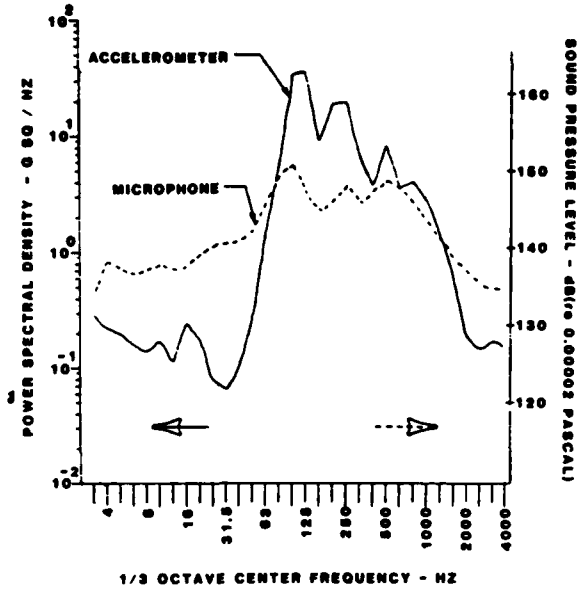

FIG. 3 ACCELEROMETER AND MICROPHONE SPECTRA AT 325 KIAS AND 15000 FEET PA

sonic fatigue evaluation consisted of establishing the acoustic load on the structure, determining the modal frequency of the fundamental mode of vibration, estimating the maximum root mean square (RMS) stress response of the structure, and determining the life of the structure from a suitable random amplitude RMS fatigue stress and life relationship (S-N curve).

The acoustic environment used in this evaluation was based on the data obtained from the microphones located in the vicinity behind the fairing. The frequency spectra from these microphones were used to establish the spectra levels (1 Hz bandwidth) of the acoustic load. Since small changes in frequency affected the spectrum level in some regions, a median value over a 50-300 Hz frequency range was used to establish the acoustic level. Based upon personal experience, the spectrum levels were reduced by 3 dB since the fluctuating pressures produced by separated flow are weakly correlated.

The structural response is based on Miles' single degree-of-freedom model, which assumes that only the fundamental mode exhibits significant response. The fundamental mode response frequency depends on the boundary conditions selected. Exact solutions for all edges clamped and all edges simply supported were used to determine the upper and lower bounds for the natural frequency estimate. Empirical data from typical aircraft riveted structure has shown that the fundamental frequency generally occurs one-half way between these two theoretical cases. The fundamental mode response frequency for a flat plate ($R=\infty$) with all edges simply supported, f_{11}, is given by (Ref. 4):

$$f_{11}^2 = \frac{\pi^2 E h^2 (b/a + a/b)^2}{48 \rho a^2 b^2 (1 - \nu^2)} \quad Hz^2 \qquad (1)$$

where
- a = length of plate (short side)
- b = length of plate (long side)
- E = Young's modulus of plate
- h = plate thickness
- ρ = mass per unit volume
- ν = Poisson's ratio

The fundamental mode response frequency for a flat plate ($R=\infty$) with all edges clamped, f_{11}', is given by (Ref. 4):

$$f_{11}'^2 = \frac{14.05 E h^2 [3.307((b/a)^2+(a/b)^2)+2]}{4\pi^2 \rho a^2 b^2} \quad Hz^2 \qquad (2)$$

The next step was to determine the maximum RMS stress response of the panel. Various charts and equations are available to estimate the dynamic stress at the center of the long side of a flat rectangular plate, $\bar{\sigma}_s$. An expression for different materials from Ref. 4 is shown below:

$$\bar{\sigma}_s = \frac{1.62 \times 10^{-4} (E/\rho)^{0.25} a^{-0.5} b^{1.75} S_p(f_{11})}{h^{1.75} \zeta^{0.56} [3(b/a)^2+3(a/b)^2+2]^{0.84}} \quad psi \qquad (3)$$

where $S_p(f_{11})$ = excitation power spectral density at the fundamental frequency (psi^2/Hz)
ζ = damping ratio

The last step was to determine the life of the panels. Random amplitude RMS reverse bending fatigue stress versus life relationships (S-N curves) for the panel materials are needed for this analysis. Reference 4 contains the necessary S-N curves. The cycles to failure or N for the appropriate stresses were obtained from the reverse bending S-N curves. The time to failure was determined by dividing the cycles to failure by the average frequency of the fundamental mode. The results of the fatigue analysis for three representative panel sizes are summarized in Table 1. The design life of the fairing must be known to place the estimated fatigue lives into perspective. The average time for each flight segment must also be known as well as the factor of safety. A 400 hour life was estimated for the fairing missions. Therefore, sonic failure problems would be expected for the aircraft structure behind the fairing where

TABLE 1 SUMMARY OF STRESS AND FATIGUE LIFE ESTIMATES (REF. 2)

CONDITION	PANEL SIZES					
	18x20x.051 Inch		10x10x.040 Inch		10x32x.040 Inch	
	Stress (PSI)	Life (Hrs)	Stress (PSI)	Life (Hrs)	Stress (PSI)	Life (Hrs)
15000 MSL						
250 KIAS	1100	-	2500	795	3100	224
300 KIAS	2900	797	5000	16	6000	5.2
320 KIAS	2600	950	6000	5.6	8000	2.6
35000 MSL						
250 KIAS	1200	-	2900	556	3700	74.7
275 KIAS	1900	-	3900	119	4600	22.4
300 KIAS	2400	797	5000	15.9	6900	2.6

life estimates were much less than 400 hours. Two of the panels shown in Table 1 would be expected to encounter fatigue problems.

Various solutions which would increase the sonic fatigue life of the affected areas were available. Aerodynamic fixes in the form of fairing extension, splitter wedges, or redesign a different fairing which is aerodynamically tapered would suffice. Structural changes in the form of additional skin together with the necessary backup structure would also provide a sufficient fix. A new design or fairing extension would provide the cleanest aerodynamic fix while a structural modification would adequately "beef up" the affected regions but not aerodynamically address the turbulent flow problem.

After considering all aspects of the test program, it was determined that the aircraft skin and panels behind the fairing would be strengthened to withstand the aerodynamic buffeting induced by the fairing. Accordingly, 0.228 cm (0.090 in.) doublers were added on both sides of the fairing from Fuselage Station (FS) 580 to 620, and the centerline panels were replaced with 0.318 cm (0.125 in.) panels from FS 600 to 740. Figure 2 depicts the strengthened skin and panel sections on the lower fuselage. Phase 2 testing then followed. Phase 2

The Phase 2 tests involved three flights: One with the fairing ram-air covers-on, one with the covers-off, and one baseline flight with the fairing and equipment removed from the aircraft. With the fairing removed, the only non-standard structures protruding from the aircraft were two aluminum mounting flanges 7.62 cm (3 in.) high, 40.64 to 55.88 cm (16 to 22 in.) long, and the support/beef-up doublers. The baseline testing duplicated the fairing installed covers-off profile. The data collected were then directly compared to determine the noise due to the fairing. Figure 4 shows the increase in overall sound pressure level due to the fairing versus the pressure microphone fuselage stations for the 300 KIAS, 4572 meters (15000 ft.) PA test condition. Also plotted is a linear least squares curve fit. The difference varied from 26 dB immediately behind the fairing to 11 dB 342.9 cm (135 in.) aft of the fairing. A comparison between the spectra obtained with and without

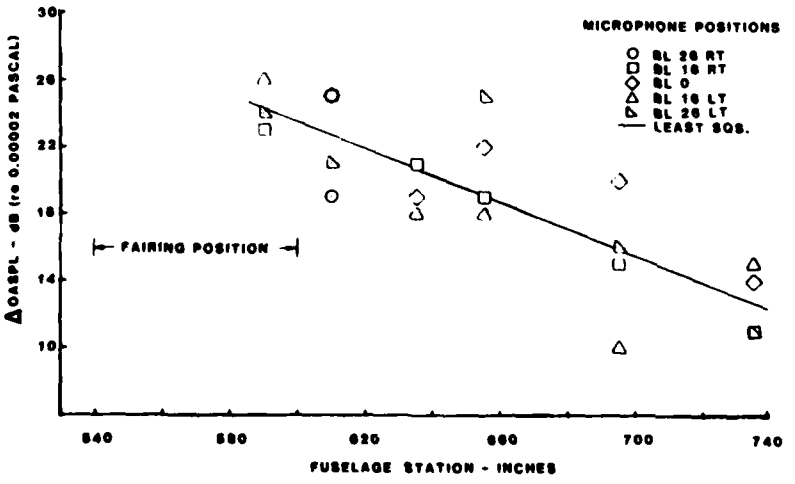

FIG. 4 OVERALL SOUND PRESSURE LEVEL DIFFERENTIALS AT 300 KIAS AND 15000 FEET PA

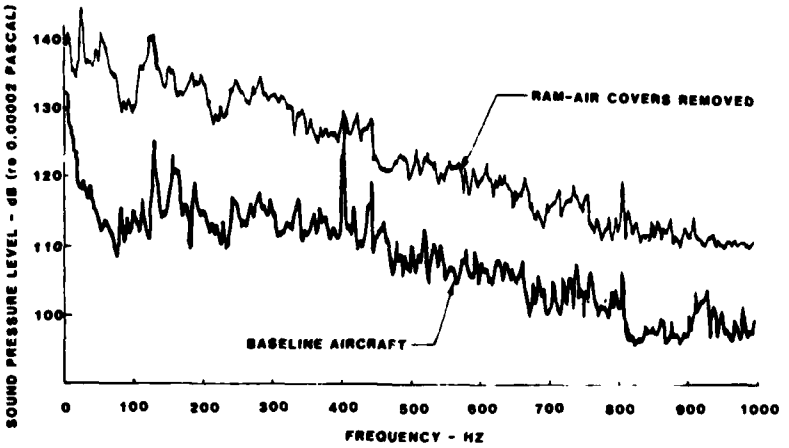

FIG. 5 COMPARISON OF NARROWBAND (2 HZ) SPECTRA FOR STRAIGHT AND LEVEL FLIGHT AT 225 KIAS AND 15000 FEET PA - *MICROPHONE 9*

the radome fairing is shown in Figure 5. Installation of the fairing resulted in a 10-20 dB increase in the spectra.

The noise data were also evaluated for the different configurations and airspeeds. Figure 6 presents profiles of airspeed versus overall sound pressure levels for the centerline mounted microphones. Data were from the three configurations at 4572 meters (15000 ft.) PA for both landing gear up and landing gear down, and for airspeeds between 200 KIAS and 325 KIAS. The sound pressure levels generally rose as airspeed increased and the highest levels were found at the locations immediately behind the fairing (see Figure 2). For the fairing-on configurations, the noise levels for the gear down conditions were noticeably lower than for gear up due to the nose gear wake effects. Also of note, the covers-off noise levels tended to be slightly lower than those with covers-on for the same speeds.

The additional instrumentation in Phase 2 allowed another sonic fatigue evaluation of areas which could still be fatigue sensitive. The same procedure for predicting fatigue life was followed as was described earlier. After review of these data, it was determined that the beefed-up structure could withstand the buffeting and sound pressure levels, but that the standard skin panels and substructure might still be subject to early fatigue and possible failure. Therefore, special inspection requirements were identified to detect any structural abnormalities. These consisted basically of preflight and postflight visual inspections for such things as radome delamination and fatigue cracks of aircraft frames and crossmembers. Airspeed limit restrictions were also placed on the testbed aircraft.

After conclusion of the airworthiness flight test program and subsequent system test missions, fatigue cracks were induced by the

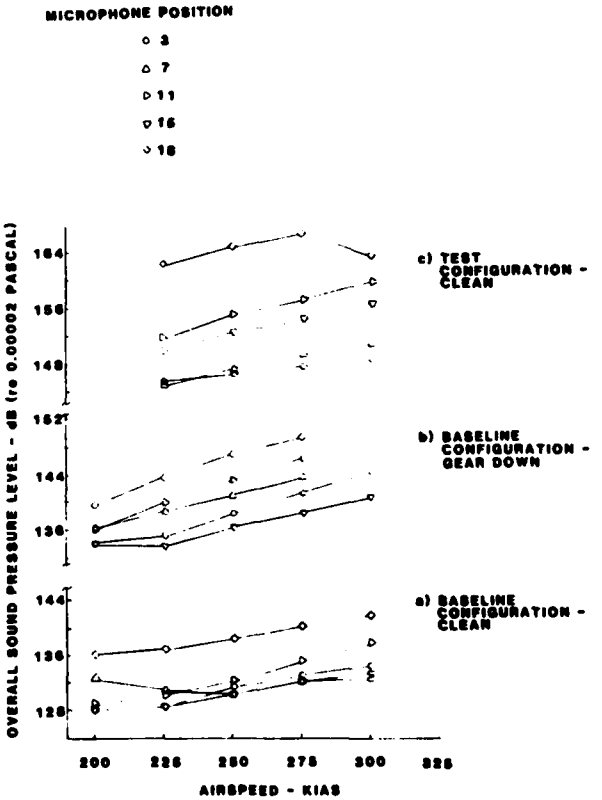

FIG. 6 OVERALL SOUND PRESSURE LEVEL AS A FUNCTION OF AIRSPEED FOR CENTERLINE MICROPHONES

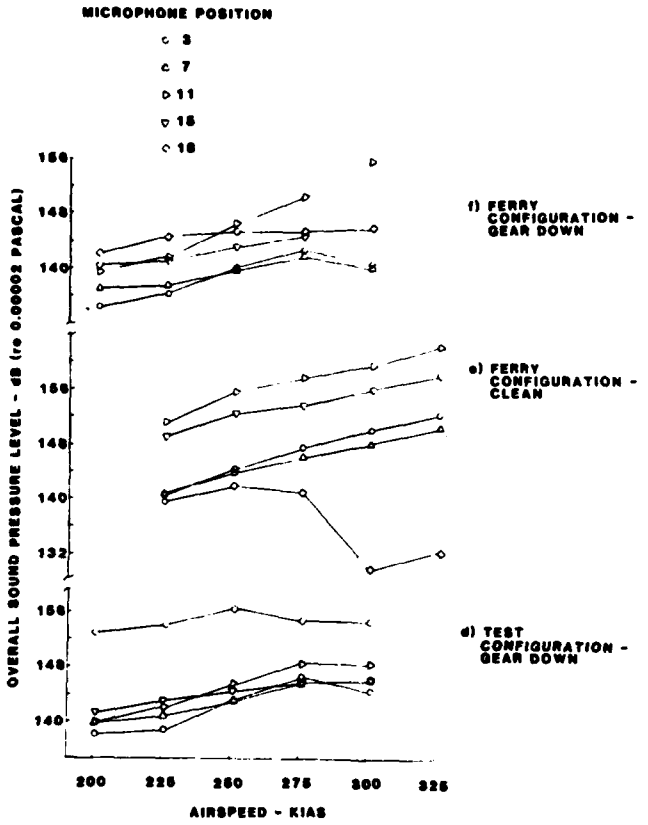

FIG. 6 (CONTINUED)

hostile flow environment behind the fairing resulting in the formation of a hole in an access door. Figure 7 shows the location of this hole relative to the fairing.

CONCLUSIONS

The objects of the aerodynamic evaluation were met. The modifications were certified as airworthy within certain operating limits. The structural integrity of the modification was demonstrated to 315 KEAS/0.88 Mach and 2.0g. Aerodynamic buffeting and noise levels encountered on the aircraft panels aft of the modifications were severe which prompted a sonic fatigue analysis. The results of the fatigue life analysis indicated that the probability of sonic fatigue failures were considered to be high with the structures analyzed. Based on the results of this analysis and knowledge of the damage to hinges, a strengthening program was undertaken to insure the integrity of the affected panels. Since this program involved only a temporary fairing installation (400 flight hours) on the aircraft, an aerodynamic fix was not adopted. Other aircraft panels behind the fairing that were not replaced were shown to be susceptible to early fatigue and should be inspected frequently. The operational envelope should be restricted to minimize the effects of the buffeting and noise on the aircraft fatigue life.

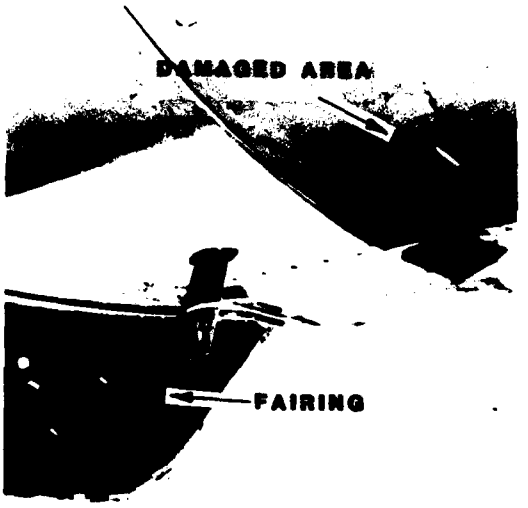

FIG. 7 FATIGUE DAMAGE CAUSED BY FLOW ENVIRONMENT

REFERENCES

1. Severyn, T.P. "PECM Aerodynamic Evaluation", 4950th-FTR-80-8, April 1980.

2. Miller, V.R. et al, "Flight Measurements of the Dynamic Environment for the PECM Radome Fairing", AFFDL-TM-79-31-FIBE, July 1979.

3. Miller, V.R. et al, "Flight Measurements of the Dynamic Environment for the PECM Radome Fairing Following Airframe Modifications", AFWAL-TM-80-50-FIBE, April 1980.

4. Rudder and Plumbee, "Sonic Fatigue Design Guide for Military Aircraft", AFFDL-TR-74-112, May 1975

AN UPDATE OF SPACECRAFT DYNAMIC ENVIRONMENTS INDUCED BY GROUND TRANSPORTATION

M. R. O'Connell

Jet Propulsion Laboratory
California Institute of Technology
Pasadena, California

An update to the JPL spacecraft transportation dynamic environments data base has been developed based on data from recent transportation of spacecrafts. Vibration levels are significantly lower than those measured in 1966, while the shock response spectra are nearly the same. JPL ground shipping criteria and shipping practices, which have been very successful in preventing damage, are also summarized herein.

Introduction

Recent spacecraft transportation vibration data is significantly lower than that in JPL's previous transportation data base. An updated transportation dynamic data base is presented in this paper along with JPL's transportation criteria and shipping methods. The older data in this paper was obtained by JPL during the Ranger and Surveyor programs, Reference 1. The new data is based on the transportation of two JPL space projects; IRAS (Infrared Astronomical Satellite) and WF/PC (Wide Field and Planetary Camera).

IRAS was an earth orbiting satellite which observed the infrared spectrum in space. WF/PC is a large camera which will be placed in earth orbit in the large NASA Space Telescope. The 3 spacecraft transportation configurations discussed in this paper are shown on Figures 1, 2, and 3. Air ride vans, similar in size and configuration to typical large moving vans, were supplied by contractors who specialize in moving electronics.

Damage experienced during the shipment of some early spacecrafts during the 1960's was traced to defective air ride van suspension systems. This led to a program of vibration measurements taken during spacecraft transportation which has continued on recent projects. In addition, a criteria was established at JPL for screening air ride vans to be used for shipping spacecrafts and large instruments. Some programs have also incurred increased cost due to hardware safety analyses based on unrealistically high transportation levels. In at least one case, an analysis indicated that a large instrument's flight mounts might not survive a cross country trip in an air ride van. However, a loads analysis based on later data indicated that it would be possible to ship the instrument on its flight mounts provided that they were properly qualified.

Transportation Criteria

The criteria requires that an empty air ride trailer floor have no instantaneous responses greater than 1 Grms (between 0-300 Hz) when driven on paved roads or freeways. A trailer is checked by this criteria just prior to its use in moving a spacecraft or large instrument. If it fails to meet the criteria, it is returned to the moving company for repair or replacement. Any replacement or repaired trailer is likewise tested. It has been found that both the trailer and truck tractor must have air suspension to meet this criteria.

Shipping Practices

Shipping practices were also developed at JPL that have produced a record of failure free shipments in recent years, Reference 2. Trucks that have both air ride tractors and trailers are used to transport spacecrafts. A spacecraft or large instrument is typically mounted in its own nitrogen purged transporter and sometimes is mounted on isolators within the transporter. The transporter is chained and blocked to the air ride van floor in a "hard mount" configuration, usually in the trailer center. Past experience has shown that the dynamic environments are generally more benign and more predictable at the center of the van floor than at either end, Reference 1. Chains, which secure the spacecraft transporter, are preloaded so as to preclude relative motion or "banging" between the trailer floor and the transporter. Transporters with wheels are shipped with blocks between its axles and the trailer floor to prevent bottoming of the transporter suspension. Ground support equipment was also loaded into the air ride van.

The air ride trailer floor and often the spacecraft itself (or space instrument) is

instrumented with accelerometers to monitor the transportation dynamic environments. Data is recorded on a portable 14 channel FM tape recorder. As a protective measure, an audible alarm is wired to a key accelerometer on the trailer floor or the spacecraft and is set to go off in the truck cab if instantaneous accelerations exceed 1 Grms. The truck driver will be immediately alerted in this manner if there are excessive inputs to the spacecraft. A filter is used in the alarm channel to eliminate accelerometer signals above 300 Hz. This eliminates extraneous alarms induced by high frequency signals which do not represent damaging accelerations for the spacecraft. If too many alarms are heard in the cab, the driver slows down to reduce the spacecraft inputs. Visible bumps in the roads are also avoided when possible. Some spacecrafts are moved only during daylight hours to minimize risk. Spacecraft movements are also supported by scout and support vehicles.

Isolators have also been used to protect some hardware and spacecrafts during transportation. The need for isolators during a move is determined by a conservative loads analysis. IRAS was supported in its transporter by 4 wire isolators and had a resonance on its isolator system of 15 Hz. This is illustrated in Figure 2. IRAS was installed in a mail box shaped "can" without any wheels. Both the trailer floor and the transporter were instrumented by triaxial accelerometer blocks. The transporter was chained to the trailer floor as previously described.

WF/PC was transported in a somewhat different configuration, Figure 3. WF/PC was mounted on three stiff mounts that were designed for vibration testing which did not simulate the dynamic properties of the flight mounts. WF/PC was mounted in a 4-wheeled transporter on its vibration test mounts. The transporter axles were blocked to raise the transporter wheels off the air ride trailer floor. Also, 1/4 inch hard rubber pads were placed between the blocks and the trailer floor. The transporter was then chained down to prevent banging of the transporter with the floor. The transporter, the WF/PC radiator, a WF/PC mount and the air ride van floor were instrumented with accelerometers, Figure 3. The spacecrafts of Reference 1 were shipped in the same transporter used for WF/PC but without the rubber pads beneath the transporter axial blocks, Figure 1.

Figure 1. Surveyor, 1966, Trailer Floor Vibration Summary

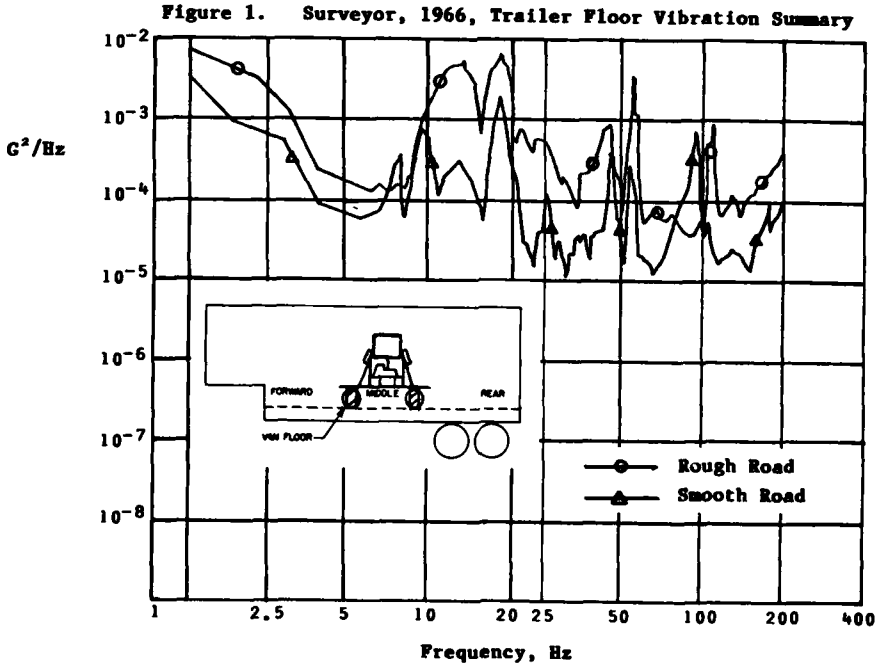

Figure 2. IRAS Van Floor Transportation Vibration Summary

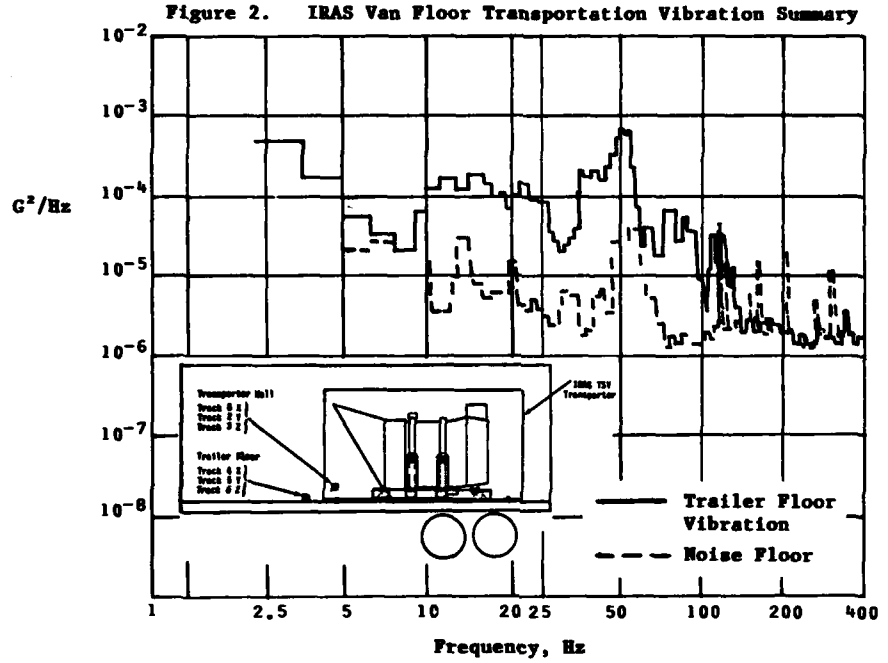

Figure 3. WF/PC Transportation Vibration Summary

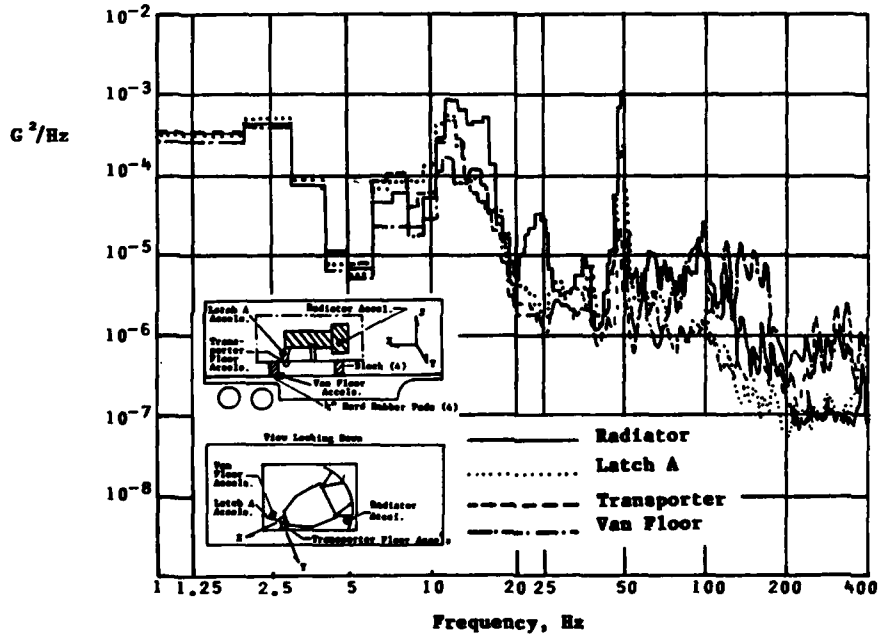

Data Acquisition/Reduction

The transportation data of Reference 1 was recorded during trips to Kennedy Space Center, Florida, from Pasadena, California. About 85% of the travel time involved smooth highways in good repair, Reference 1. The IRAS transportation data was recorded on smooth, interstate highways during travel to Denver, Colorado from Pasadena. WF/PC transportation data was recorded on interstate highways between Goddard Space Flight Center, Maryland, and Pasadena. During the recent trips, about 97% of the time involved smooth roads in good repair.

JPL transportation vibration data was reduced in the form of Acceleration Spectral Density (ASD) plots for steady state events and shock response spectra for transient events. ASD plots were generated with a bandwidth of ¼ Hz. Probability levels and maximum vibration levels were found in the old data base for smooth and rough roads, Reference 1. The data from Reference 1 presented herein are envelope summary plots. Vibration data from the more recent transits was enveloped. Owing to the low level of the data no differentiation between smooth and rough roads was made for the new data. Shock response data in the old data base assumes a dynamic amplification (Q) of 10. The recent shock response spectra were analyzed with Q = 15 or 20, as noted, and then enveloped. In all cases the vibration and shock response was highest in the axis normal to the truck bed.

Vibration Evaluation

IRAS transportation (trailer floor) vibration data measured in 1981 was significantly lower than the levels of Reference 1. Vibration data from Reference 1, circa 1966, is summarized on Figure 1. Rough and smooth road vibration levels are shown for the Surveyor spacecraft on the figure. The rough road levels are 5 - 10 dB higher than the smooth road data throughout the entire data spectrum. A summary envelope of the vibration data from IRAS is given on Figure 2. The peak at 50 Hz probably represents a localized vibration mode of the trailer or transporter structure. Above 100 Hz the vibration data is below the data system noise floor which was recorded with the truck parked. The envelope of the IRAS vibration data (.0002 G^2/Hz) was nearly 10 dB lower than the maximum rough road level of Reference 1, Figure 1. The smooth road data of Reference 1 is much the same as the IRAS data except for some peaks between 5 and 20 Hz. These comparisons are shown on the summary plot, Figure 4.

WF/PC transportation data measured in 1984 confirmed the IRAS data trend of lower vibration than Reference 1. Figure 3 summarizes the envelopes of the WF/PC transportation vibration data measured on the air ride van floor, the WF/PC radiator, a WF/PC mount and its transporter floor. It can be seen that except for the cantilevered radiator, there was very little vibration amplification in the WF/PC instrument.

Figure 4. WF/PC, IRAS and Surveyor Smooth Road, Transportation Trailer Floor Vibration

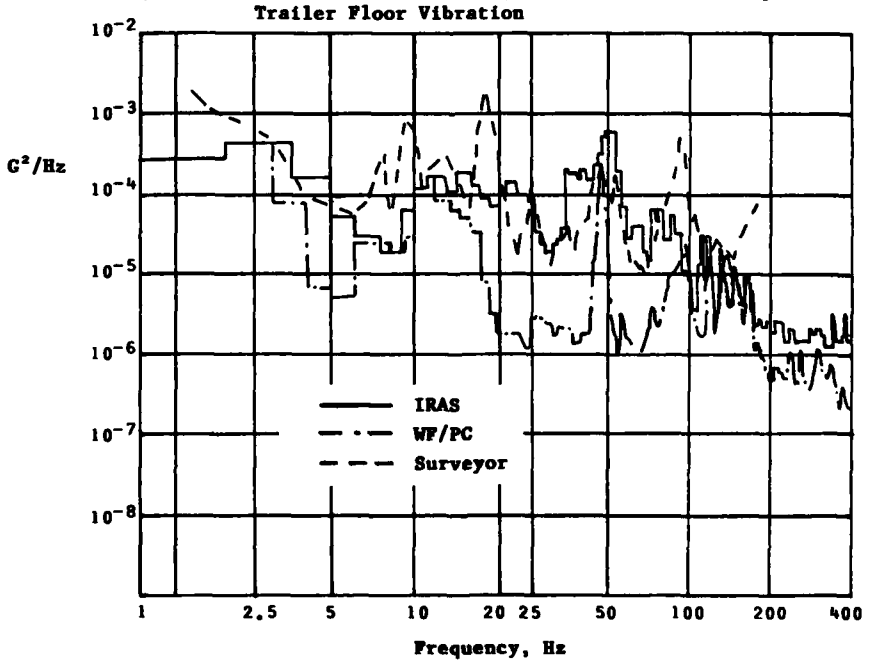

Between 10 and 50 Hz the van floor vibration was 10 dB lower than the IRAS transportation vibration data. This may be due to the 1/4 inch hard rubber pads under the WF/PC transporter blocks. The WF/PC vibration levels were at or below the transportation vibration of IRAS and Surveyor (smooth roads only), Figure 4.

Shock Evaluation

The maximum trailer floor shock response levels summarized in Reference 1 are given on Figure 5. The data was taken on 3 different spacecraft transits with the configuration shown on Figure 1. The 3 curves of Figure 5 shows the envelope of the shock response (Q = 10) at the forward, middle and aft portions of the trailer floor. The enveloped IRAS trailer floor shock response levels (Figure 6, Q =20) were 4 dB higher than the levels of Reference 1 between 40 - 60 Hz. The IRAS random vibration data also exhibited a peak centered at 47 Hz, Figure 2. This peak seems to be peculiar to the IRAS transportation configuration. Above 60 Hz the IRAS data was comparable to the shock response of Reference 1. These comparisons are shown on the shock response summary plot, Figure 8.

The WF/PC shock response data (Figure 7 and 8, Q = 15) was very similar to those of Reference 1 above 15 Hz. Below 15 Hz WF/PC levels were 3 - 4 dB higher than those in Reference 1.

The data on summary Figure 8 was analyzed with 3 different dynamic amplifications (Q); Reference 1 (Q = 10), IRAS (Q = 20) and WF/PC (Q = 15). WF/PC shock response data analyzed with a Q of 20 was about 1 dB higher than the same data with a Q = 15. A similar shock response level change could be expected for the other shipping configurations with minor changes in Q of analysis. These differences are not large but should be taken into account when this shock data is applied to other hardware.

WF/PC Transportation Predictions

Environments for the initial WF/PC transits were conservatively based on the Reference 1 vibration levels and the shock response levels from Reference 1 and IRAS (1966 and 1981). An analysis showed that the WF/PC flight mounts may not survive these environments. For this reason and because the mounts had not yet been qualified, WF/PC was transported on its stiff vibration test mounts. These mounts were designed to simulate the WF/PC center of gravity with respect to the mounts but had much greater stiffness than the flight mounts. After WF/PC transportation data was obtained, Figures 3 and 7, a revised analysis showed that adequately qualified flight mounts would survive transportation without damage or vibration induced fatigue.

Figure 5. Reference 1 Maximum Shock Response Summary

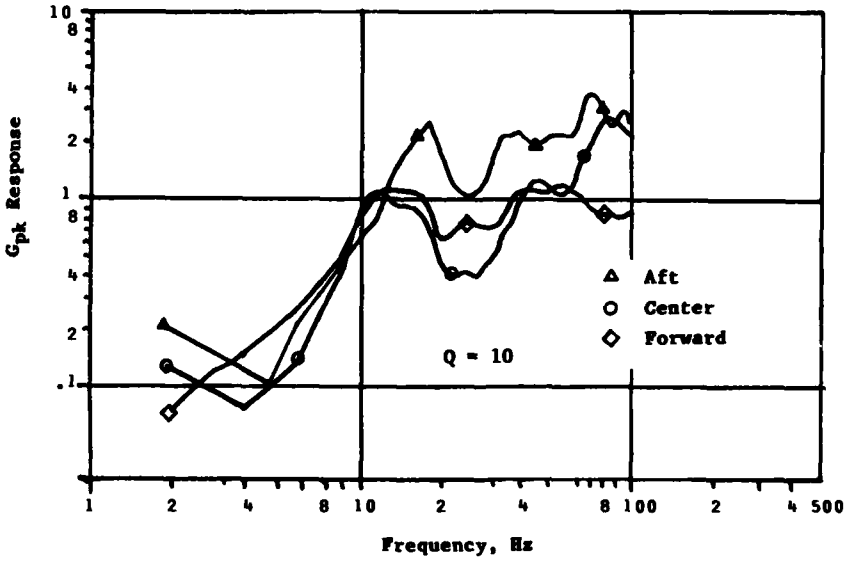

Figure 6. IRAS Trailer Floor Shock Response Summary Envelope

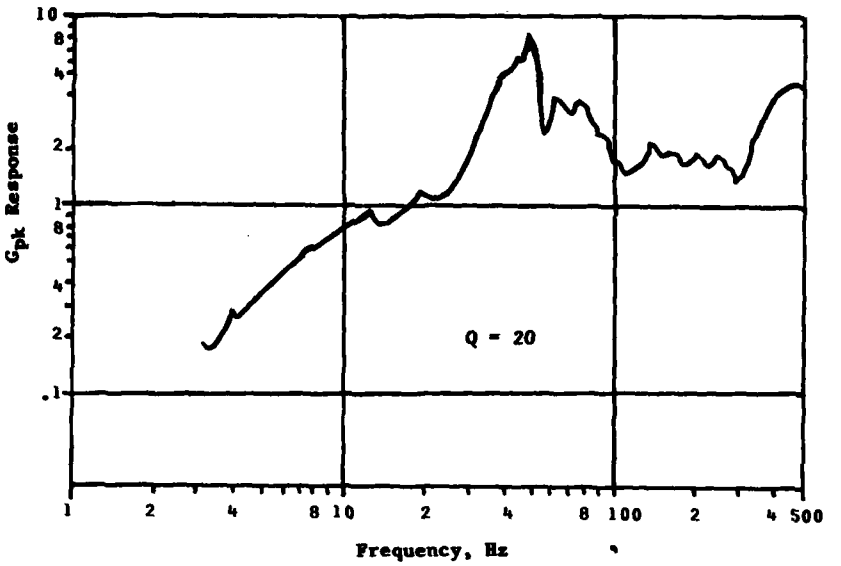

Figure 7. WF/PC Shock Response Summary Envelopes

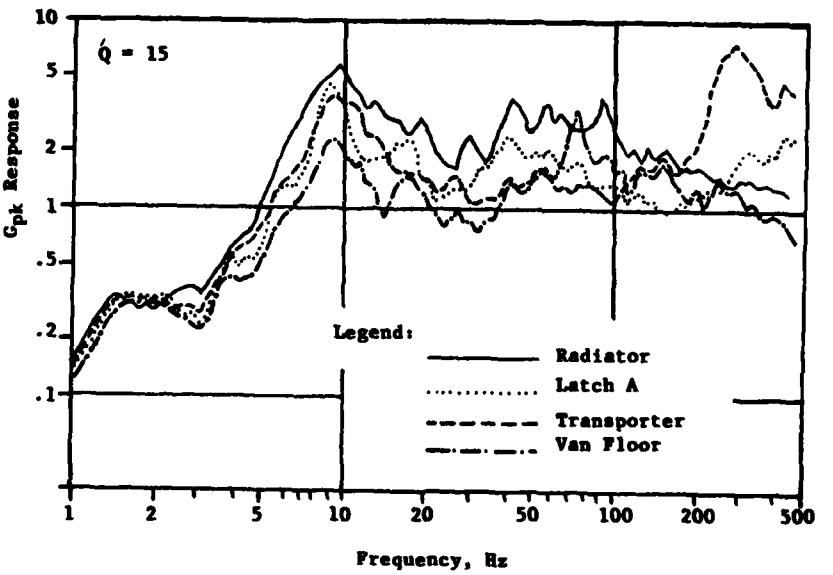

Figure 8. WF/PC, IRAS, Reference 1 Shock Response Summary

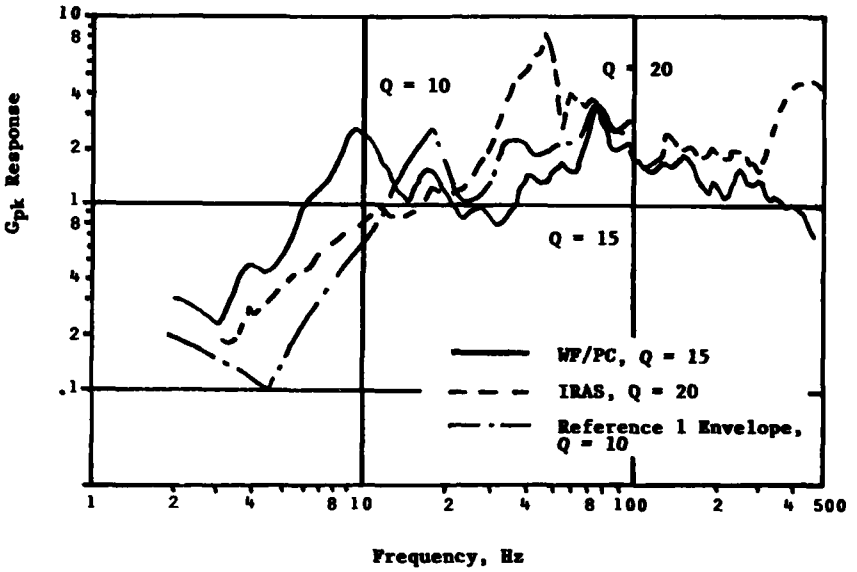

Conclusion

Recent vibration data is lower than that measured in 1966. Shock response levels were, however, much the same as before. This seems to indicate that road discontinuities and trailer responses to them are the same as in the 1960's. The envelope of the recent vibration data also matches the envelope of the Reference 1 smooth road data. Therefore, the differences in the vibration levels (Reference 1 rough road vs recent data) are probably due to improvements in the general condition of cross country roads.
The transportation data obtained during these JPL experiences may be applied in predicting transportation environments for other spacecrafts and space systems. The applicability of the revised data base depends on a number of factors. These include the payload and shipment configuration and the implementation of adequate truck screening and shipping practices as outlined in this paper. Attention should be given to road quality when planning transportation routes since poor roads can significantly increase vibration levels and the number of transient events. The higher rough road vibration levels from Reference 1 would still apply to less improved roads.

The study program described in this paper was carried out at the Jet Propulsion Laboratory, California Institute of Technology, under contract with the National Aeronautics and Space Administration.

References

1) "The Dynamic Environment of Spacecraft Surface Transportation", Technical Report No. 32-876, J. W. Schlue, Jet Propulsion Laboratory/NASA, March 15, 1966.

2) "JPL Design Requirement, Shipping and Handling Equipment for Electronic Assemblies, Subassemblies and Cables", DM 500448, Revision B, 1972.

DISCUSSION

Mr. Richards (Hunting Engineering, Ltd.): For the last two or three years they have been doing a probability density of truck vibration data. It includes the vibration and the shocks. Have you considered doing that, rather than assuming stationary data, taking the vibration from very select sections, and finding the peak responses to a probability density of the data?

Mr. O Connell: We really didn't have the time or the money from the projects to do much of an elaborate probability analysis of the data. They were in a hurry to get their answer; "What did our payload see when we moved it?"

Mr. Richards: How did you select the vibration data?

Mr. O'Connell: We ran a strip chart of the entire trip, and we looked for characteristically different steady state events. For instance, one was a very low event; we got a sample of that. One was the highest event we saw; we also got a sample of that. It was the same with the transient events; we just looked on the strip charts for the highest readings we could find.

Mr. Richards: So, the vibration was the highest case that you experienced, the 95% case?

Mr. O'Connell: Yes. The things we saw were the maximum envelope of the data throughout the trip.

Mr. Popolo (Grumman Aerospace Corporation): First of all, I was surprised you were going up so high in frequency. Most of your vibration data indicated the major disturbances were below 100 Hz; yet you had an RMS system that could give you a response between 0 and 300 Hz. If you do reject one of your trucks, are you able to tell that particular manufacturer where his difficulties might be, or why his trucks cannot meet your spec?

Mr. O'Connell: On the truck issue, no. If something is obviously wrong with the suspension, they will put the truck in their shop and look at it.

Mr. Popolo: Haven't you tried to identify a frequency with a problem of any sort?

Mr. O'Connell: No. We did no elaborate analysis like that. In response to your comment about the major disturbances being below 100 Hz, that is true. Most of our data above 100 Hz is the noise floor.

Mr. Popolo: Are you considering limiting the shock and vibration requirements to 100 Hz?

Mr. O'Connell: Yes, that is true for the vibration. But, for shock, just because the vibration data above 100 Hz are in the noise floor, doesn't mean all the shock data are. So, the shock data above 100 Hz could be real.

Mr. Silver (Westinghouse Electric Corporation): How did you measure the RMS value for the instantaneous sensor that the driver uses?

Mr. O'Connell: The signal from the accelerometer is run through a 0 to 300 Hz filter first. We did that because in one particular trip we found that rocks hitting the bottom of the trailer floor would set off the alarm. It was obviously just a very high frequency signal that set off the alarm, and it did not have anything to do with damage to the instrument. So, we put a filter in the system that would eliminate extraneous high frequency signals.

Mr. Silver: Your RMS value would be somewhat of a function of hitting a series of bumps. As your wheels go over the road, they get into many discontinuities. Even though they are rather minor, you will see almost a continuous function that will probably be the high level. So, if you get into that at a certain speed, there is very little you can do about it. It has already happened by the time you get a signal.

Mr. O'Connell: That is true. We go through an RMS meter-type instrument.

Mr. Silver: Did you find that the driver had to respond to the instantaneous sensor quite a bit?

Mr. O'Connell: If the driver goes by himself, he really doesn't have to. But on the large projects, like GALILEO or VOYAGER, he is accompanied by support vehicles and personnel. I think somebody even rides with him in the cab, and they know what he is doing. They can monitor him, and they can slow him down if they do get too many alarms. If it is still a problem when they slow down, then they will stop the truck and try to figure out what is wrong. For instance, in the case of the rocks hitting the bottom of the trailer, they figured out what was happening and decided it was no problem and kept on going.

Mr. Silver: Do you use a commercially available standard air ride van?

Mr. O'Connell: Yes, we do. There are contractors who specialize in shipping electronics equipment.

Mr. Baca (Sandia National Laboratories): I assume the data you showed were just from the vertical direction for the bed. Did you look at the other directions?

Mr. O'Connell: We did, and the levels were lower than those in the vertical direction. So, for safety purposes we usually assume the same levels in all three directions for the loads analysis.

Mr. Baca: Some of our data at Sandia show the order of magnitude is similar in the other two directions as well, although the vertical levels do tend to dominate. Do you actually qualify your payloads for transportation, or do you do a separate test so that this has some implications for the way you qualify your hardware?

Mr. O'Connell: No, we don't. We normally put specifications on the shipping equipment and on the shipping container itself. We do an analysis to see if our flight environments at the spacecraft level will envelope the transportation environments. That is partly why we are interested in this, and that is partly why the spacecraft projects are interested in this. But, we do not normally qualify for transportation because our flight environments are generally more severe.

SEISMIC LOADS

RELIABILITY OF STRUCTURES SUBJECTED TO MULTIPLE BLAST LOADS

A. Longinow and J. Mohammadi
Civil Engineering Department
Illinois Institute of Technology
Chicago, Illinois

and

H. S. Napadensky
Fire & Explosion Research
Illinois Institute of Technology Research Institute
Chicago, Illinois

In the design of hardened structures, both military and civilian, the design load environment is generally defined by means of a single weapon size, range and height of burst. However, in the course of its life span, a hardened structure may be subjected to a single weapon load environment that is more intense than the one it was designed to resist. It may also be subjected to multiple blast loadings. These are likely to have different peak load intensities, pulse shapes and durations, and may arrive at the structure from different directions. The time span between the various bursts is also expected to be different. A given structure will experience damage to the extent that the imposed blast load is more intense than the design blast load. Also, the extent of additional damage from subsequent loadings will be in direct proportion to the imposed load intensity, pulse shape and the "available" strength of the structure, i.e., the extent to which its strength has been degraded due to previous loadings. Currently, available manuals dealing with the design of structures to resist accidental explosions or blast loadings produced by nuclear or conventional weapons do not specifically consider the response of structures subjected to multiple blast loads. Specific design criteria relative to this effect do not appear to have been formulated. This paper examines the problems involved in predicting the response of structures when subjected to multiple blast loads. In this formulation the structure is modeled as a single degree of freedom system with a resistance function which provides for an approximate degradation in its strength. The method considers uncertainties in both structural and blast load parameters. The blast load and resistance are assumed to be lognormally distributed. A failure probability is computed after each blast. Individual failure probabilities are combined to yield the probability of collapse. The method of analysis is described. Its application is illustrated by means of an example problem. Its limits of applicability and needs for further research are described.

INTRODUCTION

In the design of blast resistant structures, the design load environment is generally specified in terms of a load-time history produced by a given weapon size detonated at a given range from the structure. Procedures (Ref. 1,

2, 3, 4) for the design of such structures are fairly well established, and when a structure is designed in accordance with these procedures, there is generally little doubt but that it will survive the design load environment to a satisfactory degree. What such design procedures fail to address is the reliability of the given structure when subjected to load environments other than the design environment.

In the course of its life span, a blast resistant structure may be subjected to a single blast load that is more intense than the design load. It may also be subjected to multiple loads. These may have different peak load intensities, pulse shapes, durations and may arrive at the structure from different directions. They may arrive at times such that no merging of the blast loads is produced (see Fig. 1), or they may arrive at such times that merging of the individual pulses takes place, (see Fig. 2).

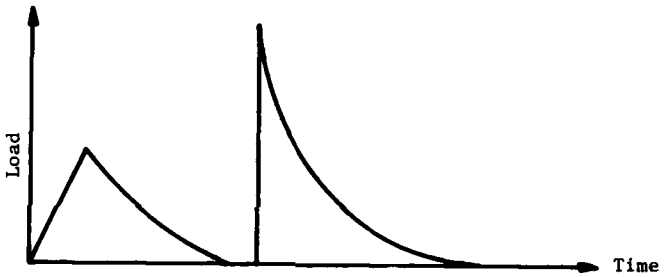

Fig. 1 Blast Loads Separated in Time

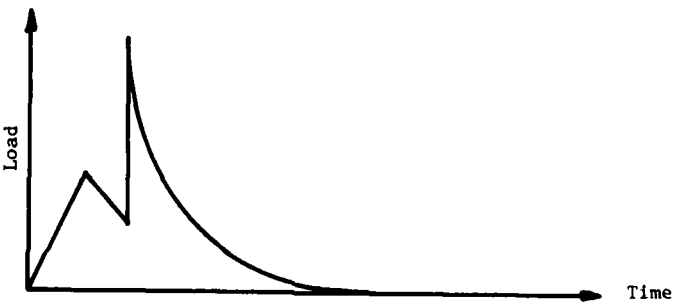

Fig. 2 Merged Blast Load

The structure in question will experience damage to the extent that the imposed blast load environment is more intense than the design environment. The extent of additional damage from subsequent loadings will depend on the "available" strength of the structure, i.e., on the extent to which its strength has been degraded due to previous loading(s).

Evaluation of the reliability of structures subjected to blast loads involves a definition of the load environment followed by a structural analysis, and all of it in a probabilistic format.

The load environment needs to be defined in terms of the number of blast loads, peak intensities and durations, time between blasts, sequence of loadings, direction from which the loads emanate, and probabilities and variabilities associated with each of these parameters.

Structural analysis procedures must be capable of considering the effects of multiple loadings both in the elastic and post-elastic ranges of response, probability of failure modes and variability of materials.

Currently available manuals dealing with design of structures to resist accidental explosions, Ref. 1 and 2, or blast loadings produced by nuclear weapons, Ref. 3 and 4, do not specifically consider the response of structures subjected to multiple blast loads.

Specific design criteria relative to this effect do not appear to have been formulated.

This paper examines the problem of structural response in a multiple load blast environment. The objective is to briefly review the state-of-the-art bearing on the problem, suggest an analysis procedure in general terms, and to point out research areas that need to be pursued to improve results.

The following sections of this narrative present a simple example problem which demonstrates that multiple blast loadings can significantly decrease the useful life of a structure if such are not considered in the design stage.

Due to the non-deterministic nature of the problem, the method described considers the failure probability of the structure after each blast. The structure is modeled as a single degree of freedom system with a resistance function which provides for an approximate degradation in strength. The method considers uncertainties in both structural and blast load parameters. Load and resistance are assumed to be lognormally distributed. A failure probability is computed after each blast.

The method of analysis is described. Assumptions and limits of applicability are noted. In the example problem the resistance of the structure is approximated by means of an effective linear resistance based on a bilinear resistance function. It is subjected to a series of identical blast loads. Failure probabilities are computed and combined. Results indicate that even as few as three repeated blast loads can significantly increase the probability of failure even for cases with a relatively high R/F ratio. The R/F (peak resistance to peak load intensity) ratio can be looked at as a measure of the relative strength of the structure or as an indication of its range from the point of detonation.

GENERAL ASSUMPTIONS

(i) The structure is modeled as a single-degree of freedom system.

(ii) The applied load is assumed to consist of a series of step loads (see Fig. 3) of different peak intensities, F_i.

(iii) The resistance capacity of the structure is represented by means of an elasto-plastic resistance shown in Fig. 4. The yield and maximum displacements are represented respectively, by X_y and X_m. The stiffness of the elastic part is $k = R(X_y)^{-1}$ in which R is the resistance capacity.

(iv) The applied blast load will leave the structure undamaged if the ratio of load to resistance is less than 1/2, i.e., $F/R \leq 1/2$.

Fig. 3 Load Function

BASIC FORMULATION

The resistance function shown in Fig. 4 is further idealized by means of an "effective" linear resistance function shown in Fig. 5. The effective displacement X_e is found by equating the energy corresponding to elasto-plastic case and that of the corresponding linear curve, Ref. 5. Such linearization yields

$$X_e^2 = X_y^2 \, (2X_m/X_y - 1) \qquad (1)$$

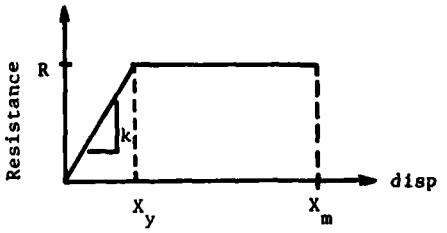

Fig. 4 Actual Resistance

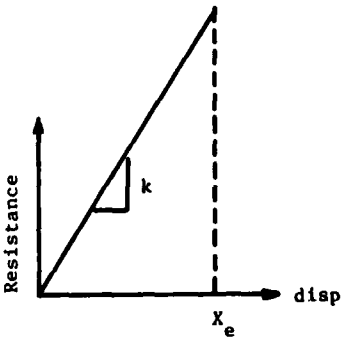

Fig. 5 Effective Resistance

Introducing the ductility ratio $Z_i = X_m/X_y$, Eq. (1) may be written as:

$$X_e^2 = X_y^2 \ (2Z_i - 1) \qquad (2)$$

or

$$Z_i = X_e^2/2X_y^2 + 1/2 \qquad (3)$$

Given the step load shown in Fig. 3, the maximum response of the linear system is, Ref. 5.

$$X_e = 2F_i/k = 2F_i \ X_y/R \qquad (4)$$

In the light of Eq. (4), Eq. (3) becomes

$$Z_i = (2F_iX_y/R^2)/2X_y^2 + 1/2$$

$$= 2/(R/F_i)^2 + 1/2$$

$$= 2/\theta_i^2 + 1/2 \qquad (5)$$

where $\theta_i = R/F_i$.

Damage is likely to occur if $F_i \geq R/2$. This corresponds to $Z_i \geq 1$. Thus the probability of damage P(D) is:

$$P(D) = P(Z_i \geq 1) \qquad (6)$$

Using arbitrarily a lognormal probability distribution for θ_i, Ref. 6, the probability of damage is:

$$P(D) = \phi\left(\frac{\ell n \ \bar{Z}_i}{\Omega_{Z_i}}\right) \qquad (7)$$

Where $\phi(.)$ = the standard normal probability function, $\bar{Z}_i$ = the mean of Z_i and Ω_{Z_i} = the coefficient of variation (C.O.V.) of Z_i representing the uncertainty in Z_i. If $\bar{\theta}_i$ and Ω_{θ_i} are respectively the mean and C.O.V. of θ_i, $\bar{Z}_i$ and Ω_{Z_i} are calculated as (Ref. 7)

$$\bar{Z}_i = 2/\bar{\theta}_i^2 + 1/2 \qquad (8)$$

$$\Omega_{Z_i} = 8\Omega_{\theta_i}/(4 + \bar{\theta}_i^2) \qquad (9)$$

in which (Ref. 6)

$$\bar{\theta}_i = \bar{R}/\bar{F}_i \qquad (10)$$

and

$$\Omega_{\theta_i} = (\Omega_R^2 + \Omega_{F_i}^2)^{1/2} \qquad (11)$$

where $\bar{R}$ and $\bar{F}_i$ are, respectively the means of R and F_i and Ω_R and Ω_{F_i} are the respective C.O.V.'s.

COLLAPSE OF THE SYSTEM

The collapse of the structure may be defined as a ductility level above which the system suffers extensive damage so that failure is certain. If M represents this ductility level, collapse is represented by $\mu_i > M$ where μ_i is the overall ductility of the system at the time of the ith blast load, whereas Z_i is the ductility due to the ith blast only. The value of μ_i depends on the previous ductilities μ_1, μ_2, ... μ_{i-1}. The probability of collapse, $P(C_i)$ at the ith blast load depends on whether or not $Z_i > 1$. From the total probability theorem (Ref. 6), the probability of collapse is:

$$P(C_i) = P(C_i|Z_i>1) \ P(Z_i>1)$$

$$+ P(C_i|Z_i\leq 1) \ P(Z_i\leq 1) \qquad (12)$$

where $P(C_i|Z_i>1) = P(\mu_i>M)$; whereas $P(C_i|Z_i<1)$ depends on the ductility at (i-1)th blast. This can be postulated as $P(C_i|Z_i\leq 1) = P(\mu_{i-1}>M)$. Eq. (12) therefore, becomes:

$$P(C_i) = P(\mu_i>M) \ P(Z_i>1)$$

$$+ P(\mu_{i-1}>M) \ P(Z_i\leq 1) \qquad (13)$$

The probability $P(\mu_i>M)$ may be calculated as follows.

After application of F_{i-1} as part of a series of loads $F_1, F_2, \ldots, F_n$ if $Z_{i-1}>1$, a permanent displacement $X_{p_{i-1}}$ will be produced. This displacement will be added to the displacement produced by load F_i (see Fig. 6). For the effective linear system, under the action of F_i the system starts from rest with a permanent displacement $X_{p_{i-1}}$, and the total displacement X_{e_i} (see Fig. 7) is

$$X_{e_i} = X_{p_{i-1}} + 2F_i/k \qquad (14)$$

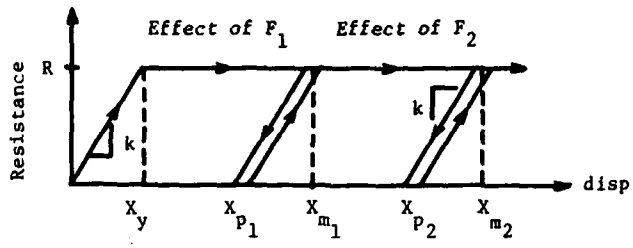

Fig. 6 Action of Repeated Loads

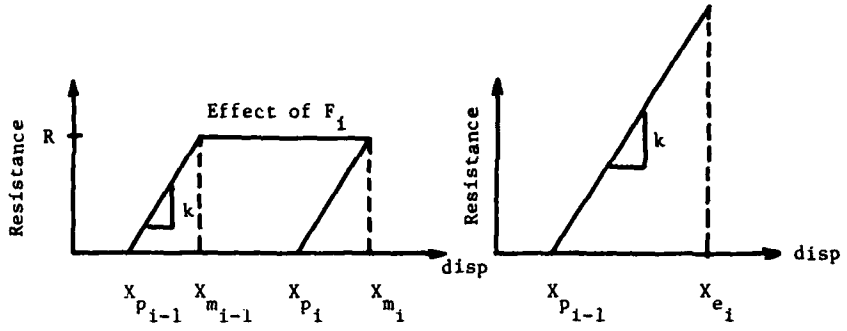

Fig. 7 Elasto-Plastic and Effective Linear Resistance

If $\mu_i = X_{m_i}/X_y$ a relationship between μ_i and μ_{i-1} may then be derived based on equating the energy of the elasto-plastic system and that of the linear one, (see Fig. 4 and Fig. 5), i.e.,

$$\mu_i = \mu_{i-1} + 2/\theta_i^2 - 1/2 \qquad (15)$$

For a special condition of i=1, there is no previous permanent displacement. This condition leads to $\bar{\mu}_o = 1$ so that Eq. (15) may still be used for i=1. Assuming lognormal distributions for μ_i and Z_i tne collapse probability at ith blast may then be calculated in terms of $\bar{\mu}_i$ and Ω_{μ_i} the C.O.V. of μ_i.

$$P(C_i) = \{1-\phi[(1/\Omega_{\mu_i}) \ln(M/\mu_i)]\} \cdot \phi[(1/\Omega_{Z_i}) \ln(Z_i)] + \{1-\phi[(1/\Omega_{\mu_{i-1}}) \ln(M/\bar{\mu}_{i-1})]\} \cdot \{[1-\phi(\ln Z_i)/\Omega_{Z_i}]\} \qquad (16)$$

SPECIAL CASES

For a large $\bar{\theta}_i$, μ_i may be smaller than $\bar{\mu}_{i-1}$. This, of course, is not possible. It is therefore, more appropriate to set $\bar{\mu}_i \geq \bar{\mu}_{i-1}$ as a necessary condition in this formulation.

If for every blast, $\bar{\theta}_i > 2$, $\bar{\mu}_i$ remains constant and equal to 1. Although Ref. 8 specifies this condition as a no failure case, the present formulation still yields a value for failure probability. This is because of the uncertainties associated with F_i and R.

NUMERICAL ILLUSTRATIONS

For a structure under repeated identical blast loads, the collapse probabilities for different $\bar{\theta}_i$ ranging from 1.0 to 2.0 were obtained using the above formulations. The uncertainties associated with F_i and R are taken as 20%. Furthermore a ductility level M=2 is assumed for defining the border-line between failure and no failure. The results (see Fig. 8) show that even for relatively large $\bar{\theta}_i$ (i.e., $\bar{\theta}_i$, = 2.0) the collapse probability may become significant after the 3rd or fourth blast load.

SUMMARY AND CONCLUSIONS

A method was formulated for studying the probability of failure of structures when subjected to repeated blast loads. It was applied to the analysis of a structure subjected to a series of identical blast loads. Results indicate that even as few as

three repeated blast loads can significantly increase the probability of failure even for cases with a relatively high R/F. The R/F ratio can be looked at as indicating the relative strength of the structure or as an indication of its range from the point of detonation.

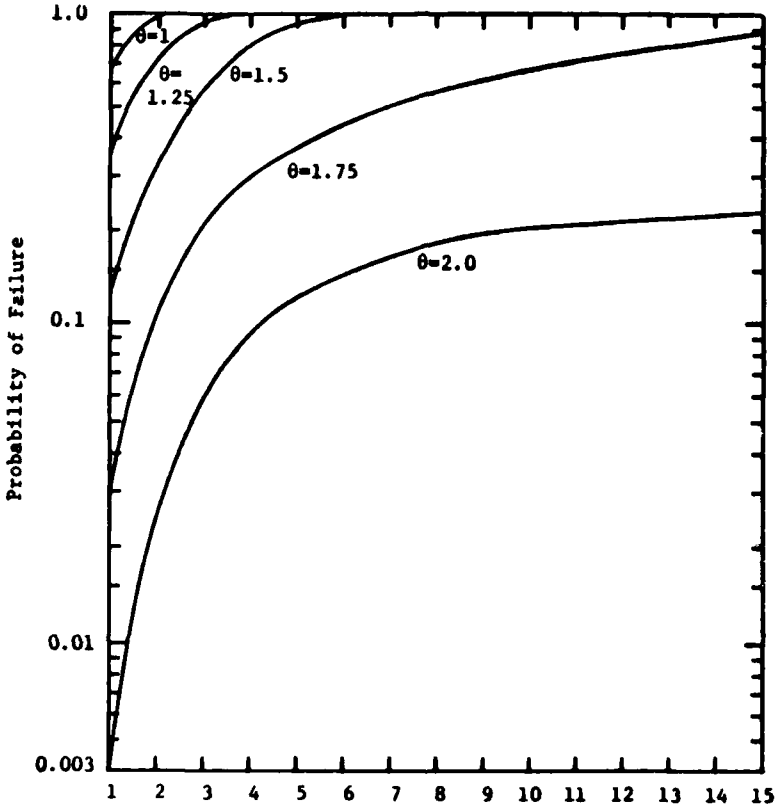

Fig. 8 Sample Illustration

The reason for using an "effective" resistance function (Fig. 5) instead of the actual bilinear resistance (Fig. 4) in performing the analysis, is that for an elasto-plastic resistance function and a step load (Fig. 3) the ductility Z_i is highly non-linear, i.e, (Ref. 9)

$$Z_i = \frac{1}{2(1-1/\theta_i)} \qquad (17)$$

This results in high uncertainties in Z_i when the ratio of $1/\theta_i$ approaches unity. The problem is only slightly improved when using decaying load functions. This subject area needs further analysis.

The method of analysis presented here can be extended to consider a variety of different loadings and resistance functions. For the designer of blast resistant structures, this method is a potentially useful tool for evaluating the reliability of candidate designs.

One major difficulty with the analysis of structures subjected to multiple loads beyond the elastic range is the fact that experimental data capable of reliably representing this behavior is very sparse. Construction of resistance functions for such structures involves additional uncertainties.

REFERENCES

1. "Structures to Resist the Effects of Accidental Explosions," TM 5-1300, Departments of the Army, Navy, Air Force, June 1969.

2. W. E. Baker, et al., "A Manual for the Prediction of Blast and Fragment Loadings on Structures," U.S.

Department of Energy, DOE-TIC-11268, November 1980.

3. R. E. Crawford, et al., "A Manual for Design and Analysis of Hardened Structures," AFWL-TR-74-102 Air Force Weapons Laboratory, Air Force Systems Command, Kirtland Air Force Base, NM 87117.

4. "Design and Analysis of Structures to Resist Nuclear Weapon Effects (With Emphasis on Blast Resistant Design)," ASCE - Manuals of Engineering Practice - No. 42, 1983 Edition.

5. N. M. Newmark, and E. Rosenblueth, Fundamentals of Earthquake Engineering, Prentice-Hall, Inc. Englewood Cliffs, N.J. 1971.

6. A. H-S. Ang., "Structural Risk Analysis and Reliability-Based Design," Journal of Structural Division, ASCE, Vol. 99. ST9, pp. 1981-1910, Sept., 1973.

7. A. H-S. Ang., and W. H. Tang, Probability Concepts in Engineering Planning and Design, Vol. I - Basic Principles, John Wiley and Sons, N.Y. 1975.

8. P. Weidlinger, "Structures Under Repeated Blast Loads," Rand Corporation, March 1961.

9. J. M. Biggs, Introduction to Structural Dynamics, McGraw-Hill Book Company, 1964.

SHOCK ENVIRONMENT IN A CIVIL DEFENSE BLAST SHELTER

T. R. Slawson, S. C. Woodson, and S. A. Kiger
US Army Engineer Waterways Experiment Station
Vicksburg, Mississippi

A series of 12 dynamic tests were conducted on 1/4-scale structural models of a civil defense blast shelter. The dynamic loading was generated using a High Explosive Simulation Technique (HEST) and simulated the overpressure from a large-yield nuclear detonation at peak overpressures ranging from approximately 0.23 MPa (34 psi) to 1.09 MPa (158 psi).

Two types of structural models were tested. One was a simple reinforced concrete box-type model with a one-way roof representing a segment of one bay of the shelter. The other model consisted of multiple bays with interior beam-column supports. The tests were conducted with the structures buried in sand, clayey sand, and clayey sand with gravel backfill materials. In-structure acceleration data recorded during the tests were used to generate shock spectra at damping equal to 0, 5, and 10 percent of critical. These shock spectra can be used to evaluate equipment and occupant survivability and, if necessary, design shock isolation for equipment and/or occupants. Results indicate that at a frequency of 10 Hz, the peak accelerations vary from about 5 g's at 0.23 MPa (34 psi) to about 20 g's at 1.09 MPa (158 psi).

INTRODUCTION

In support of the Federal Emergency Management Agency (FEMA) Key Worker Blast Shelter Program, the Waterways Experiment Station (WES) was tasked to verify the proposed design of a 100-man civil defense shelter. The shelter was designed to resist the effects of a 4,184-TJ (1-Mt) nuclear weapon detonation at 0.34 MPa (50 psi) peak overpressure. The structural design criteria and levels of initial and residual radiation associated with the threat weapon dictated an earth-covered or buried structure. The shelter design is a simple box-type, shallow-buried structure constructed of poured-in-place reinforced concrete. The walls, roof slab, and floor slab are one integral structure with structural steel frames providing interior supports for the one-way reinforced concrete roof slab. The roof clear span-to-thickness ratio is 13.2 and the depth of burial (DOB)-to-clear span ratio is 0.36.

WES performed 6 static and 12 dynamic tests (approximately 1/4-scale) to verify the structural design of the shelter and to investigate the effects of backfill type, DOB, concrete strength, and repeated hits on structural response. Two types of structural models were tested. One model (Type 1) was a multiple bay, reinforced concrete, box-type element with a structural steel frame providing an interior support for the roof slab. The Type 1 box was used to investigate the complete structural design of the prototype shelter. The Type 2 element was a single span, open end, reinforced concrete box-type element used to investigate the effects of backfill type, concrete strength, DOB, and repeated hits on structural response. Table 1 indicates the type element used in each test, backfill types, nuclear weapon simulations, and maximum roof response. The backfill types used in the tests were flume sand, clayey sand, and clayey sand with gravel. Dynamic testing was accomplished using the HEST as described in Reference 1. Dynamic tests were performed at overpressures ranging from 0.23 MPa (34 psi) to 1.09 MPa (158 psi). Results of the dynamic tests showed that the safety factor on overpressure was greater than three, which provided adequate reserve capacity to resist repeated hits.

These dynamic tests were performed primarily to investigate structural response and capacity. However, the capacity of the blast shelter may be limited by survivability of its inhabitants and equipment rather than structural survivability.

This paper describes the dynamic tests

(approximately 1/4-scale) and analyzes the shock environment within the shelter as scaled from these test data.

TEST DESCRIPTION AND RESULTS

The test configuration and accelerometer location are shown in Figure 1. The test bed was constructed in a 6.1-m by 6.1-m by 2.1-m

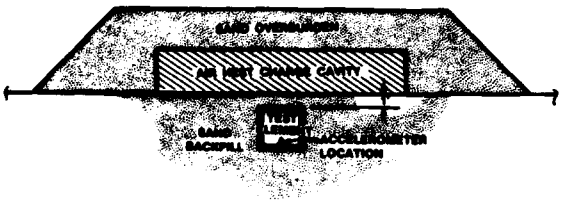

Fig. 1 - Test configuration and accelerometer location

(20-ft by 20-ft by 7-ft) excavated pit. Backfill was placed and compacted in 6-in. lifts from the floor of the excavation to a DOB of 0.3 m (1 ft) over the instrumented structure for each test. After backfilling, the HEST charge cavity was constructed on the ground surface above the model structure. The charge cavity consisted of a wooden framing system covered with plywood. The 5.49-m by 4.57-m by 0.91-m (18-ft by 15-ft by 3-ft) charge cavity contained the high-explosive detonating cord which was located in a plane 0.3 m (1 ft) below the top of the cavity. The charge cavity was covered by 0.91 m (3 ft) of uncompacted sand overburden confining the blast pressure to simulate the peak overpressure and overpressure decay of a nuclear weapon detonation. The number of strands of detonating cord in the charge cavity was varied to increase or decrease the peak simulated overpressure.

Table 1 is a test matrix showing nuclear weapon simulation data, backfill type, and structure response for the tests pertinent to this paper. A typical airblast pressure record is shown in Figure 2. The weapon simulations, listed in Table 1, were determined by

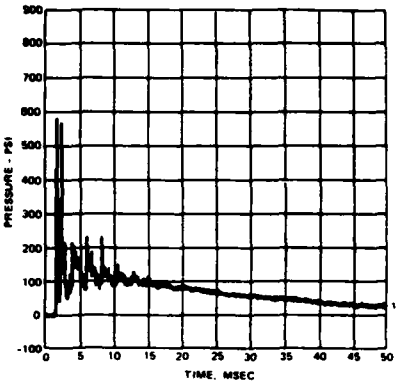

Fig. 2 - Typical airblast pressure record

a least squares fit of nuclear overpressure time histories, as defined by Speicher and Brode in Reference 2, to airblast pressure data recovered in each test. The duration of the fit was 20 msec. A typical accelerometer record is shown in Figure 3. The accelerometer location is shown in Figure 1.

IN-STRUCTURE SHOCK

In-structure shock is typically represented in terms of shock spectra. Shock spectra are plots of the maximum responses (in terms of displacement, velocity, acceleration, etc.) of all possible linear oscillators with a specified amount of damping to a given input base acceleration-time history. Predictions of shock spectra for the prototype shelter were made by Applied Research Associates, Inc. (Reference 3). Figure 4 is the predicted vertical shock spectra for the prototype shelter

Table 1. Test Matrix and Results

Test	Element Type	Backfill	Simulated Weapon Yield TJ	(kt)	Simulated Peak Overpressure MPa	(psi)	Maximum Roof Response cm	(in.)
D1	1	Sand	60	(12)	0.88	(127)	1.42	(0.56)
D3	2	Sand	1,251	(299)	0.23	(34)	0.15	(0.06)
D3A	2	Sand	1,435	(343)	0.43	(62)	0.48	(0.19)
D3B	2	Sand	41,506	(9,920)	0.41	(60)	0.79	(0.31)
D3C	2	Sand	75	(18)	0.89	(129)	1.65	(0.65)
D5	2	Clayey Sand	322	(77)	1.09	(158)	3.10	(1.22)
D7	2	Clayey Sand with Gravel	243	(58)	0.92	(134)	2.64	(1.04)
D8	2	Sand	25	(6)	0.92	(134)	1.27*	(0.50)*

* Permanent deflection only for test D8, maximum response was not measured.

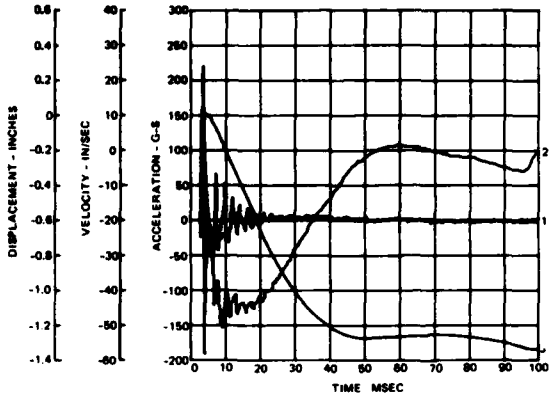

Fig. 3 - Typical floor acceleration record

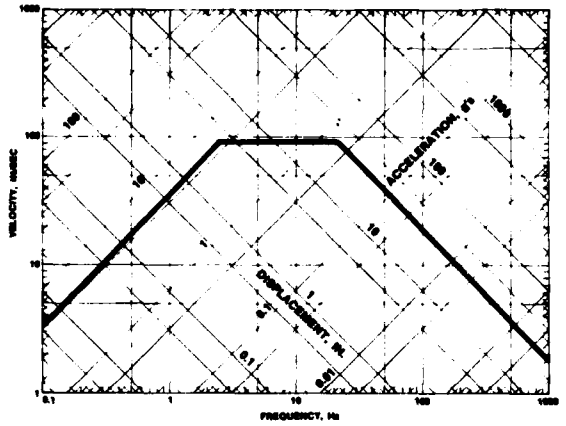

Fig. 4 - Predicted shock spectra

due to a 4,184-TJ (1-Mt) surface burst at 0.34 MPa (50 psi) peak overpressure.

Vertical shock spectra were generated from acceleration data recovered in the dynamic tests (approximately 1/4-scale) listed in Table 1 using a computer code developed at WES. These spectra were scaled up to the prototype shelter and were calculated using damping of 0, 5, and 10 percent of critical. The experimentally determined shock spectra are shown in Figures 5 through 12. A comparison of the experimentally determined shock spectra with the predicted shock spectra shows that maximum values of displacement, velocity, and acceleration are less than predicted. Note that the experimentally determined shock spectra may not be representative of shock spectra due to a nuclear detonation at frequencies higher than approximately 15 to 20 Hz due to the low-frequency oscillations in the ground surface airblast loading that is characteristic of the HEST charge cavity.

A comparison of the scaled vertical shock spectra for tests D3, D3A, D3B, and D3C shows increased velocities, displacements, and accelerations with increased overpressure. A comparison of shock spectra for tests D1 and D8

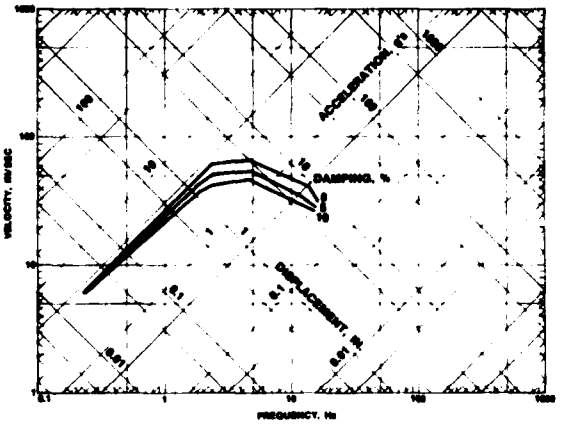

Fig. 5 - Scaled vertical shock spectra from Test D1

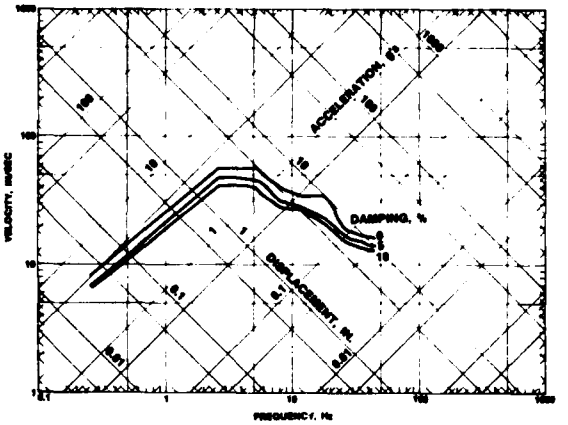

Fig. 6 - Scaled vertical shock spectra from Test D3

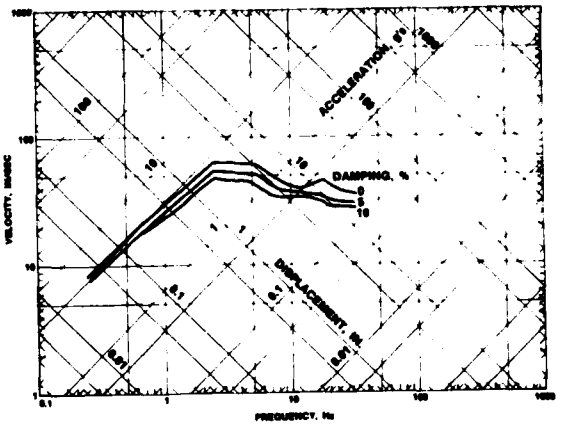

Fig. 7 - Scaled vertical shock spectra from Test D3A

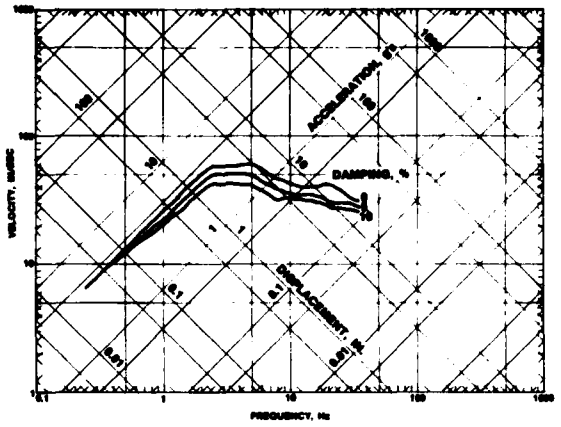

Fig. 8 - Scaled vertical shock spectra from Test D3B

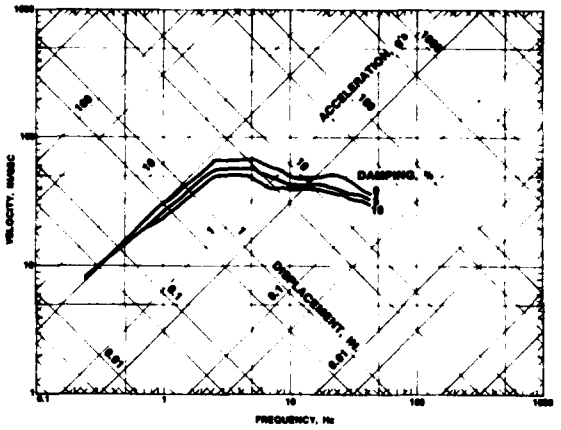

Fig. 9 - Scaled vertical shock spectra from Test D3C

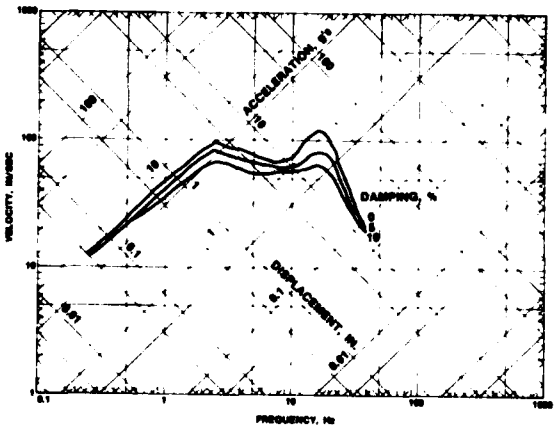

Fig. 10 - Scaled vertical shock spectra from Test D5

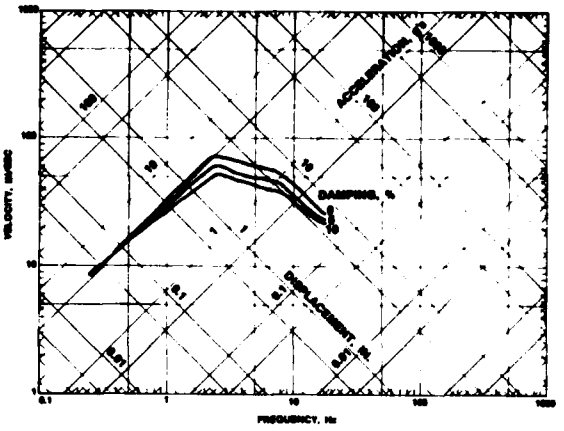

Fig. 11 - Scaled vertical shock spectra from Test D7

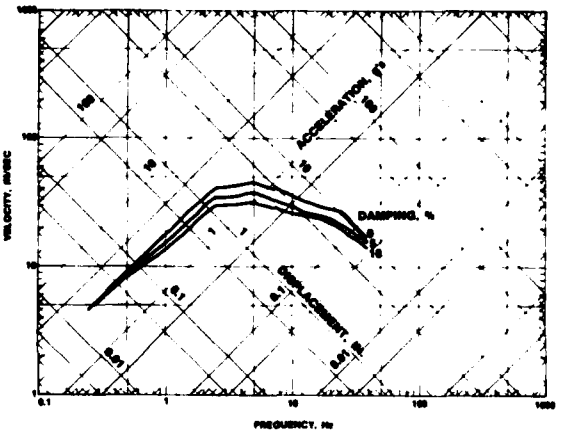

Fig. 12 - Scaled vertical shock spectra from Test D8

with shock spectra for tests D5 and D7 shows increased shock levels for the tests in lower shear strength backfills.

SURVIVABILITY

Figures 5 through 12 represent vertical shock spectra for the prototype Key Worker Blast Shelter at peak overpressures ranging from 0.23 MPa (34 psi) to 1.09 MPa (158 psi). These shock spectra can be used to determine if shock isolation is needed for a given piece of equipment, provided fragility curves or shock resistances for the equipment are known. Alternatively, these shock spectra can be used to write shock resistance specifications that equipment must be able to withstand. Figure 13 compares experimentally determined shock spectra for tests D1 and D3 with safe response spectra for typical floor-mounted equipment from Reference 4. Reference 4 also contains safe response spectra for other equipment that may be of interest. Figure 13 shows that communication equipment may need to be shock isolated to survive.

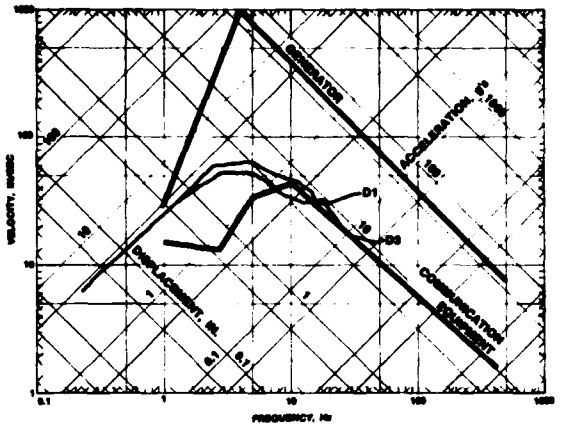

Fig. 13 - Comparison of shock spectra from Tests D1 and D3 with response spectra for typical floor mounted equipment

References 5 and 6 discuss human shock tolerance. The effects of shock on personnel inside the structure depend on the magnitude, duration, frequency, and direction of the motion. Also the position of the man at the time of shock influences its effect. References 5 and 6 conclude that a standing man will receive compressive injuries in the body-supporting bones if the upward floor acceleration exceeds 20 g's during a long-duration loading. The injury threshold increases as the duration of the load decreases. Reference 6 recommends using a maximum design acceleration of 10 g's at frequencies at or below man's resonant frequency in the standing position (10 Hz). Experimentally determined shock spectra show that, at the shelter design overpressure, no injury would occur. Tests at higher overpressures slightly exceed the safe design limit of 10 g's; however, injury may not occur unless all the man's weight is supported by one leg for accelerations less than 20 g's. Since human shock tolerance is higher in the seated and prone positions than in the standing position, the probability of injury decreases.

Impact injuries occur at much lower accelerations than compressive bone fractures. Generally, impact injuries may occur at accelerations of 0.5 to 1 g for an unrestrained man in the standing or seated positions. These injuries are the result of falling and hitting the floor or other objects. Impact injuries may be reduced by padding or restraining to prevent movement.

CONCLUSIONS AND RECOMMENDATIONS

Based on the results of 1/4-scale dynamic testing, in-structure shock in the Key Worker Blast Shelter are within acceptable limits for occupants and equipment, other than communication devices. Impact injuries might be a problem but can be eliminated by padding impact surfaces or restraining personnel to prevent falls. Survivability of shock-sensitive equipment, such as communications equipment, can be achieved by shock isolation.

REFERENCES

1. Wampler, H. W., Leigh, G. G., and Furbee, M. E., "A Status and Capability Report on Nuclear Airblast Simulation Using HEST," Proceedings of the Nuclear Blast and Shock Simulation Symposium, November 28-30, 1978, Volume 1, General Electric - TEMPCO, Santa Barbara, California.

2. Speicher, S. J., and Brode, H. L., "Airblast Overpressure Analytic Expression for Burst Height, Range, and Time Over an Ideal Surface," PSR Note 385, November 1981 (with updates through November 1982), Pacific-Sierra Research Corporation, Santa Monica, California.

3. "Multiple Burst Damage Patterns and Ground Shock Analysis of Effects on Buried Structures," Progress Report No. 2 (Draft April 1982), Applied Research Associates, Incorporated, Alexandria, Virginia.

4. US Army Technical Manual TM 5-855-1, "Fundamentals of Protective Design for Conventional Weapons," 1984, US Army, Washington, D. C.

5. "Personnel and C-E Equipment Shock Tolerance," Summary Report, 1977, Boeing Aerospace Company, Seattle, Washington.

6. Crawford, R. E., et al., "The Air Force Design Manual for Design and Analysis of Hardened Structures," 1974, Air Force Weapons Laboratory, Kirtland Air Force Base, New Mexico.

DISCUSSION

Mr. Helfrich (Pacific Missile Test Center): Why was there such a large difference between the experimental results and the predicted results?

Mr. Slawson: When you predict shock spectra, you make the most conservative assumptions. You don't want to say anything you are not sure of, so you go the conservative route, and you will always tend to have higher amplitudes in spectra.

Mr. Helfrich: Do you have any plans to go back and look at your analytical models for predicting?

Mr. Slawson: We didn't actually predict the shock spectra, so I am not exactly sure how it was done. We will probably predict our own shock spectra. We have plans for a large scale test so that we won't have any problem with scaling effects of any uncertainties like that. So, that might be a better verification of the predicted shock spectra.

Mr. Peterson (Babcock & Wilcox): You briefly alluded to some of the scaling problems. Could you give us an idea how the reference you mentioned may have suggested how you would scale the overpressure?

Mr. Slawson: The overpressure does not scale. If you have a full scale 50 psi overpressure on the prototype, and if you do a quarter scale test, the overpressure is also 50 psi. You will use cube root scaling on the weapon, however. I didn't mention that the design was for megaton size weapons. So, if you use cube root scaling on quarter scale, we would test it with a 16-kiloton size weapon.

EARTHQUAKE INDUCED MOTION ENVIRONMENTS IN FRAMED BUILDINGS

A. Longinow
Illinois Institute of Technology
Chicago, Illinois

R.R. Robinson
IIT Research Institute
Chicago, Illinois

J. Mohammadi
Illinois Institute of Technology
Chicago, Illinois

Motions induced at various floor levels of high- and low-rise steel-framed buildings when subjected to an earthquake are examined. Three unbraced steel-framed buildings with heights of 24- 12- and 4-stories are modeled and analyzed when subjected to horizontal and vertical ground motions. The induced ground motions were modeled after the El Centro (1941) earthquake. Results include absolute horizontal and vertical displacement-time histories and response spectra curves for selected floor levels for each of the three buildings. Also included are seismic forces, i.e., moments, shears and axial forces induced in the columns of the three buildings during the dynamic response. Combined stresses based on dynamic response are compared with design stresses. Possible damage to nonstructural items and components such as elevators, motor generators, piping and lighting fixtures is examined qualitatively with regard to the seismic motion environments generated at the various floor levels.

INTRODUCTION

Three steel-framed buildings with heights of 24-, 12- and 4-stories were modeled and analyzed when subjected to horizontal and vertical ground motions produced by an earthquake. Elastic, dynamic analyses were performed. The objective was to study the motions that would be induced at the various floor levels of such buildings. The magnitude, duration and frequency content of such motions is of interest when placing nonstructural items (i.e., air conditioning equipment or storage racks) at various floor levels or when designing attachments for them.

The following paragraphs describe the seismic disturbance chosen for the study, the manner in which the three buildings were modeled and the type of analysis performed.

Results include (a) absolute horizontal and vertical displacement-time histories and corresponding response spectra curves at selected floor levels for each of the three buildings, and (b) moments, shears and axial forces that occurred in the columns of each of the buildings during the dynamic response.

Finally, possible damage to nonstructural components is examined qualitatively with regard to the seismic load environment generated at the various floor levels.

Results of this study should be of interest to individuals concerned with the safety of equipment in buildings when subjected to earthquake motions.

EARTHQUAKE GROUND MOTION

The seismic load environment for a building structure is most realistically represented by horizontal and vertical transient motions at the ground support of the structure. This technique was used in this paper to determine the response of several buildings to a representatively severe earthquake. An artificially generated waveform technique [1] was employed to define the motion history. The hypothetical horizontal and vertical seismic disturbances were generated using the parameters listed in Table 1. Corresponding acceleration waveforms produced are shown in Fig. 1 and 2. It is noted that the maximum magnitude of the generated waveforms are not all the same as the desired maximum values listed in Table 1. For example, the desired maximum horizontal acceleration was 0.32 g and the maximum obtained was 0.201 g. These differences occur because the SIMEAR computer code scales the waveform amplitudes such that the maximum values do not exceed the desired magnitudes. Several trials, with different sets of parameters, were required to obtain the relatively close correlation between the desired maximum amplitudes and those that were finally obtained.

The Housner response-spectrum intensity* evaluated for a damping factor of 0.2 is 40.5 inches and 19.5 inches for the horizontal and vertical seismic motions, respectively. The root mean square (RMS) of the horizontal and vertical acceleration and velocity waveforms are

	Horizontal	Vertical
Acceleration (g)	0.0731	0.0667
Velocity (inch/sec)	4.8600	2.6400

TABLE 1

SIMEAR COMPUTER CODE PARAMETERS
FOR GENERATION OF HORIZONTAL AND VERTICAL MOTION WAVEFORMS

Parameter	Horizontal	Vertical
1. Duration of Record (sec)	15.000	10.000
2. Time Increment of Generated Waveform (sec)	0.050	0.050
3. Intensity Function Parameters		
a. Exponential Decay Constant, α	0.185	0.278
b. Parabolic Buildup Duration, t_1	0.500	0.300
c. Time at Start of Exponential Decay, t_2	7.500	5.000
4. Desired Maximum Acceleration (g)	0.320	0.201
5. Desired Maximum Velocity (inch/sec)	15.500	7.000
6. Desired Maximum Displacement (inch)	5.250	1.250
7. Filter Spectrum Parameters[a]		
a. Shape Option	Acceleration	Velocity
b. Lowest Input Spectrum Frequency (cps)	0.1	0.1
c. Highest Input Spectrum Frequency (cps)	10.0	10.0
d. Fraction of Critical Damping	0.6	0.6
e. Undamped Natural Frequency (cps)	2.5	1.4
f. Decay Ratio/Octave for Lowest Frequency	6.0	6.0
g. Frequency at Start of Low Frequency Decay	0.5	0.5

[a]The built-in or prescribed spectrum of the filter option was used for these computer runs.

*Integral of the pseudovelocity response spectrum over the period of vibration range of 0.1 to 2.5 sec.

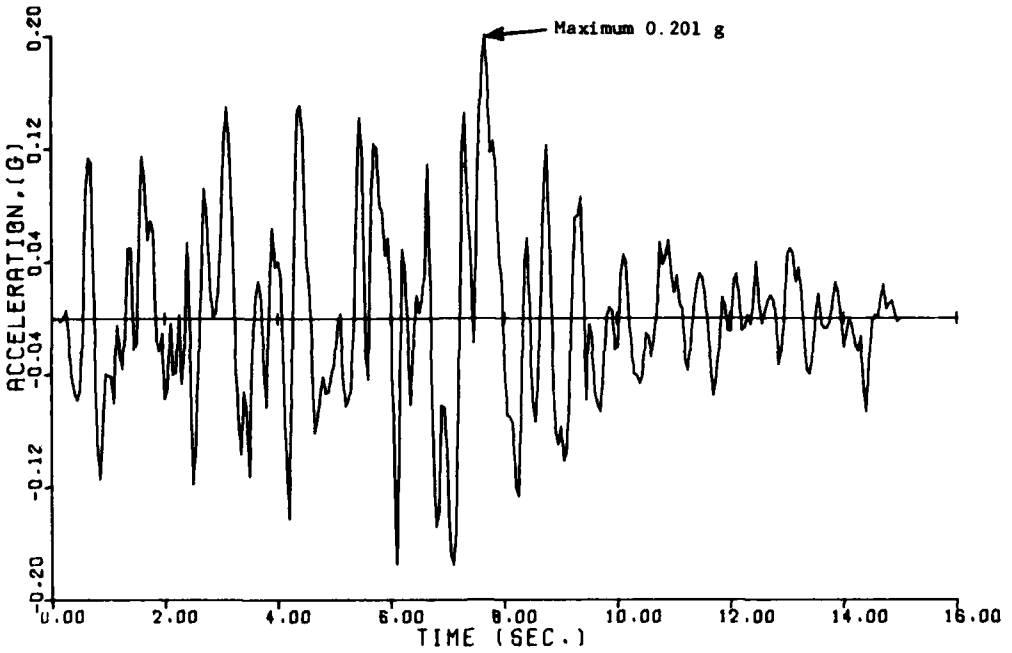

FIG. 1 HORIZONTAL GROUND ACCELERATION - TIME VARIATION

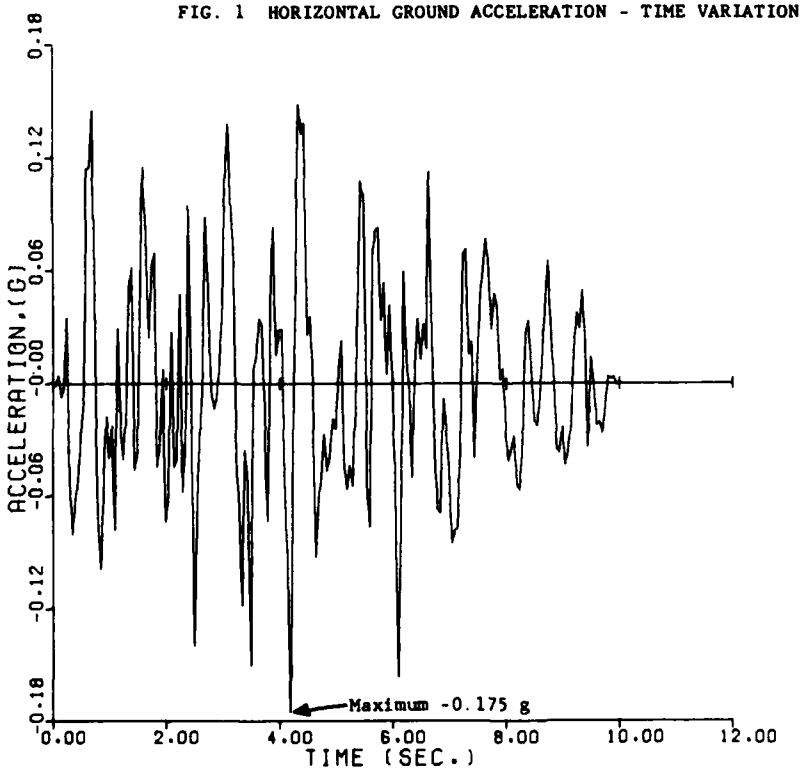

FIG. 2 VERTICAL GROUND ACCELERATION - TIME VARIATION

The response spectra for both the horizontal and vertical motions have been computed for damping factors of 0.01, 0.02 and 0.10. The results are presented in Fig. 3 and 4. Also shown on these figures are the maximum values of the displacement, velocity and acceleration from the time variation of the motions.

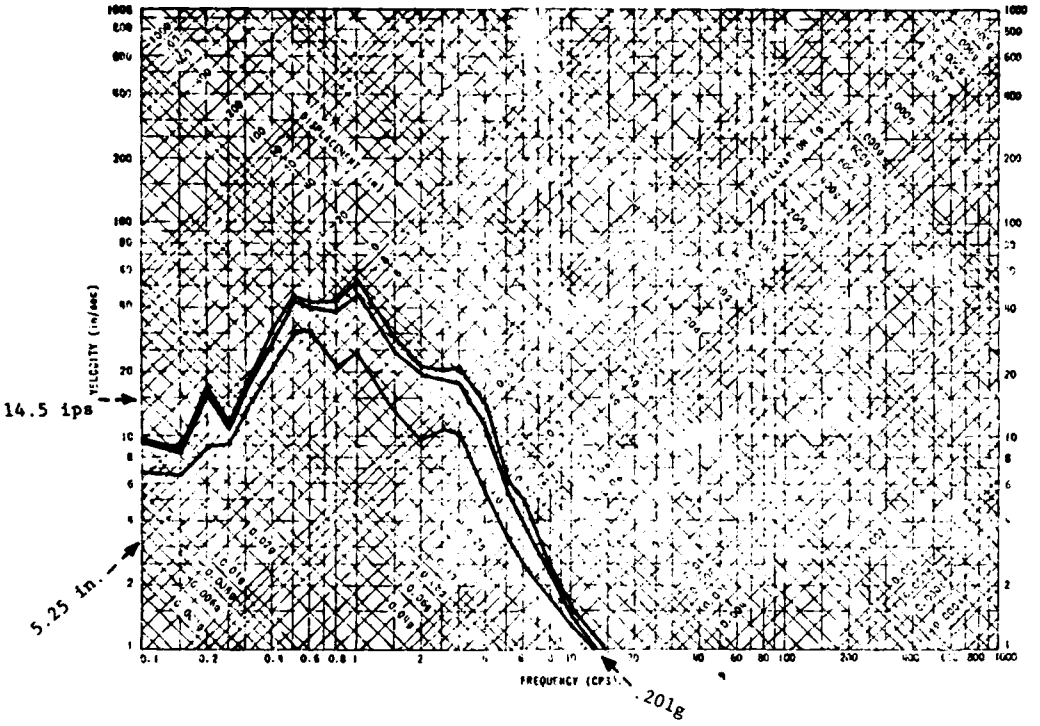

FIG. 3 RESPONSE SPECTRA FOR HORIZONTAL GROUND MOTION
(1, 2, and 10 percent damping)

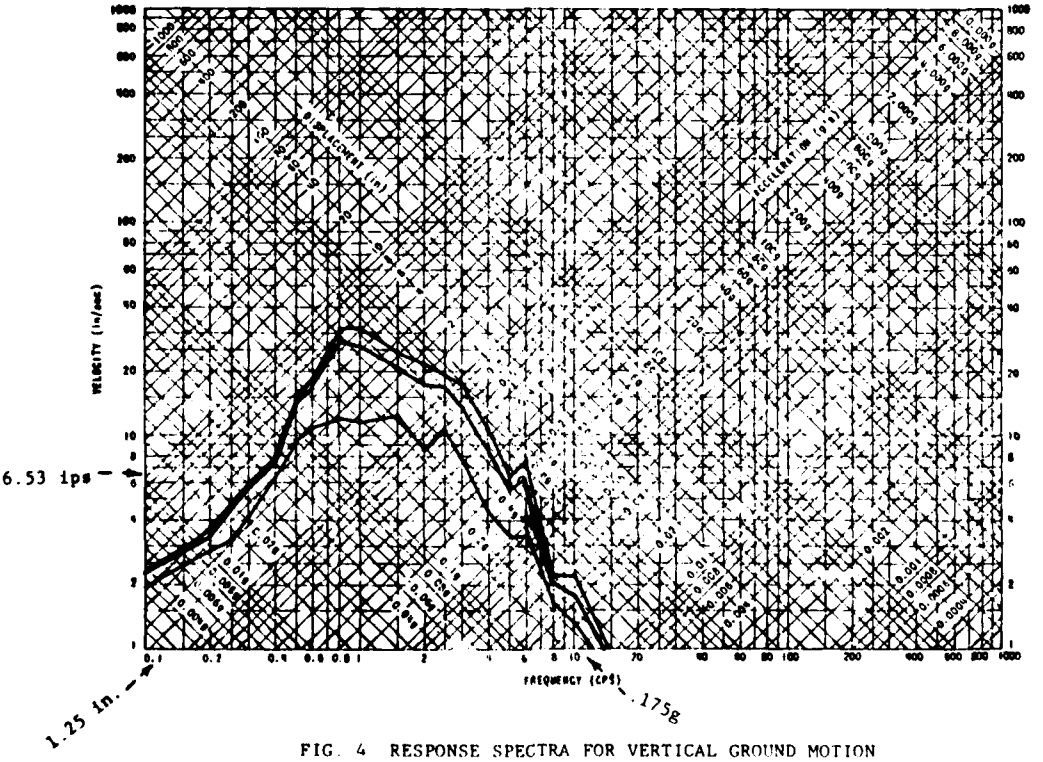

FIG. 4 RESPONSE SPECTRA FOR VERTICAL GROUND MOTION
(1, 2, and 10 percent damping)

STRUCTURAL IDEALIZATION

Structural characteristics for the buildings selected for this study were obtained from Ref. [2]. In this publication a 24-story, unbraced, steel frame building (see Fig. 5) was designed by two methods: (a) plastic analysis method, (b) allowable stress method. Two smaller buildings were obtained by eliminating lower floor levels from the 24-story design. By this method three buildings having identical geometries were selected for analysis, i.e., a 24-story building, a 12-story building and a 4-story building.

In the analyses performed, each structure was analyzed as though the floors are rigid and incapable of any extensional or flexural deformations. As such, the horizontal and vertical motions are uncoupled. Each building was further idealized as a cantilever with no rotation at the floor levels for the horizontal response analysis.

For the vertical response analysis, each structure was analyzed as a one-dimensional bar. A finite element model was defined for each of the three building structures by establishing a node point at each floor level.

An appropriate lumped mass was included at each node point and a beam finite element, which incorporated the lateral and vertical characteristics of the structure, was used between each pair of adjacent nodes. The finite element model for the 24-story building (Fig. 6) consisted of 25 node points, with the ground level node fixed, and 24 beam elements. The nodes above the ground level were constrained so that only translation motions could occur, i.e., the rotational degrees of freedom were eliminated at each node point. The lumped mass at each node was based on the dead load and one-half the live

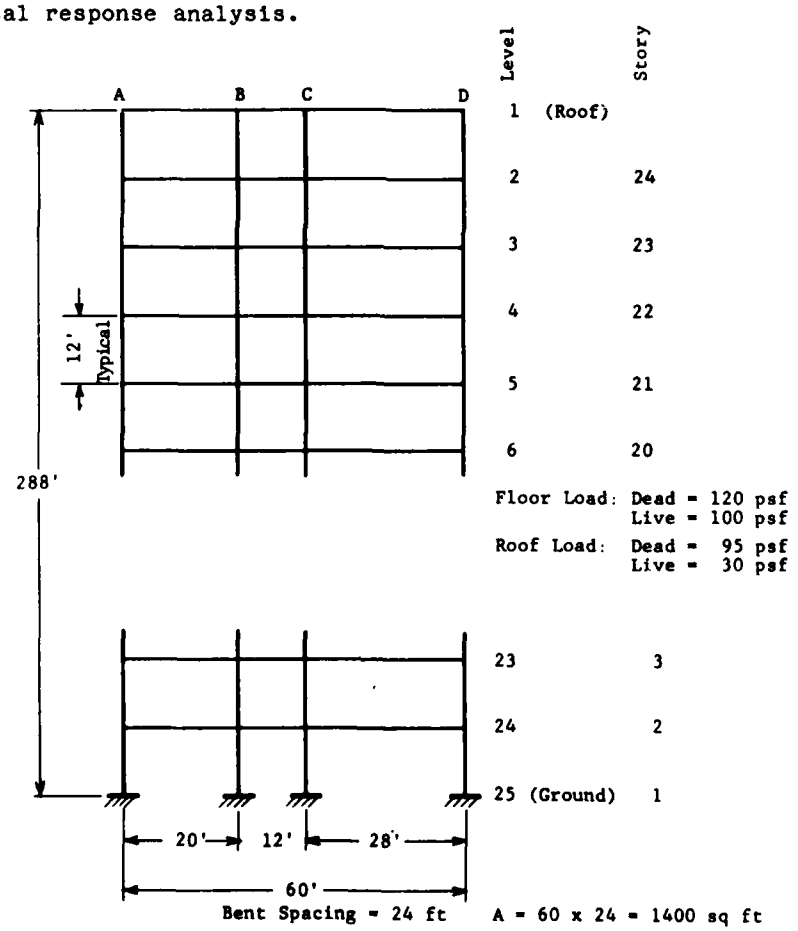

FIG. 5 24-STORY BUILDING - FRAME C (unbraced) Ref.[2]

load for each level associated with the building plan area (A=60x24=1440 sq ft) corresponding to one bent, there results

Roof Mass = (95 + 0.5 x 30) 1440/g
= 158,400/g
= 410 lb-sec^2/inch

Floor Mass = (120 + 0.5 x 100) 1440/g
= 244,800/g
= 634 lb-sec^2/inch

The important structural stiffness parameters for the analysis described are the moment of inertia of the columns (for horizontal stiffness calculations) and the cross-sectional area of the columns (for vertical stiffness calculations). Table 2 gives the sum of the principal moments of inertia for the four columns (for one bent) as a function of the building height. This moment of inertia is used to compute the lateral stiffness associated with the building plan area corresponding to one bent.

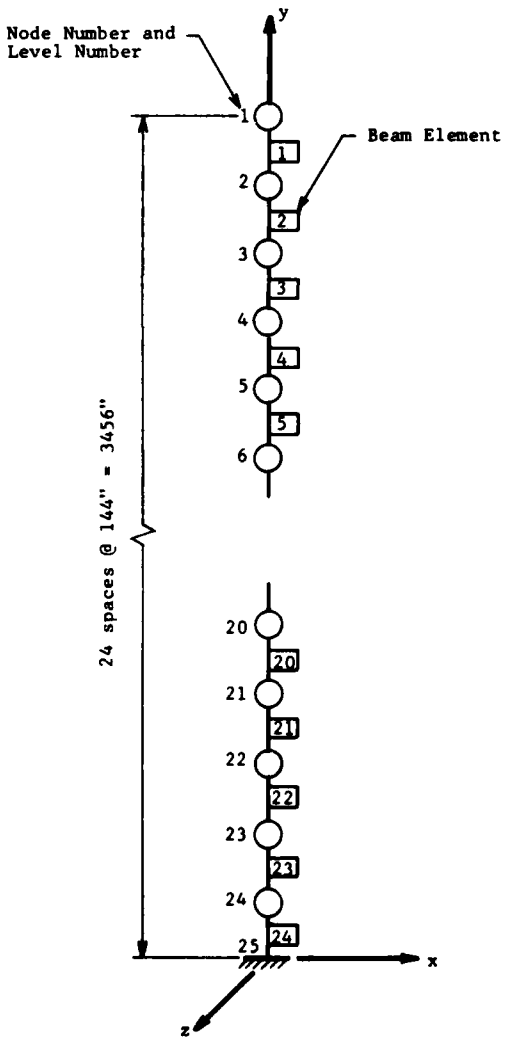

FIG. 6 FINITE ELEMENT MODEL OF 24-STORY BUILDING

The variation of the moment of inertia with height is illustrated in Fig. 7 for both design methods. A least squares procedure was used to obtain quadratic curves that best fit the data (see Table 2). Since the resulting moment of inertia curves for the allowable stress and plastic designs are quite close, an average curve was used to determine the variation of this parameter with height. This average curve is shown in Fig. 7 and defined as

$$I = a + bx + cx^2 \qquad (1)$$

Coefficients a, b, and c are given in Fig. 7. The moment of inertia for the finite element model for any beam element between any two node points or levels, i and i + 1, is obtained by evaluating Eq. (1) for x = i + 0.5.

The height variation of the cross-sectional area of the bent's four columns is shown in Fig. 8 for the two design cases considered in Ref. [2]. The weight per foot of height of the columns is also given on this figure and in Table 3.

Results shown in Fig. 8 were generated in a manner similar to that described in connection with the moment of inertia. As previously, the average cross-sectional area curve was used in the analysis. The cross-sectional area of the beam elements for the finite element model was obtained in a similar manner as was done for computing the amount of inertia.

As mentioned previously, the finite element models for the 12-story and 4-story buildings were each obtained by using the appropriate data from the upper story levels of the 24-story model. That is, the 12-story model was obtained by using the node and element data for nodes 1 through 13 and elements 1 through 12. All of the finite element and mass data described above was normalized by dividing the mass, moment of inertia and cross-sectional area parameters by the building plan area of A = 1440 sq ft. Thus, the parameters used in the computer analysis of each structure are those associated with a square foot of the building planform.

TABLE 2
MOMENT OF INERTIA ($INCH^4$) OF BENT COLUMNS
(ONE BENT) FRAME C - UNBRACED Ref. [2]

Level	Plastic Design	Allowable Stress Design
1-3	1572	2086
3-5	2278	3415
5-7	4236	4641
7-9	5720	6338
9-11	6756	7884
11-13	7568	8011
13-15	8639	9807
15-17	10191	11404
17-19	13380	13853
19-21	15578	16359
21-23	18164	18041
23-25	19467	21498

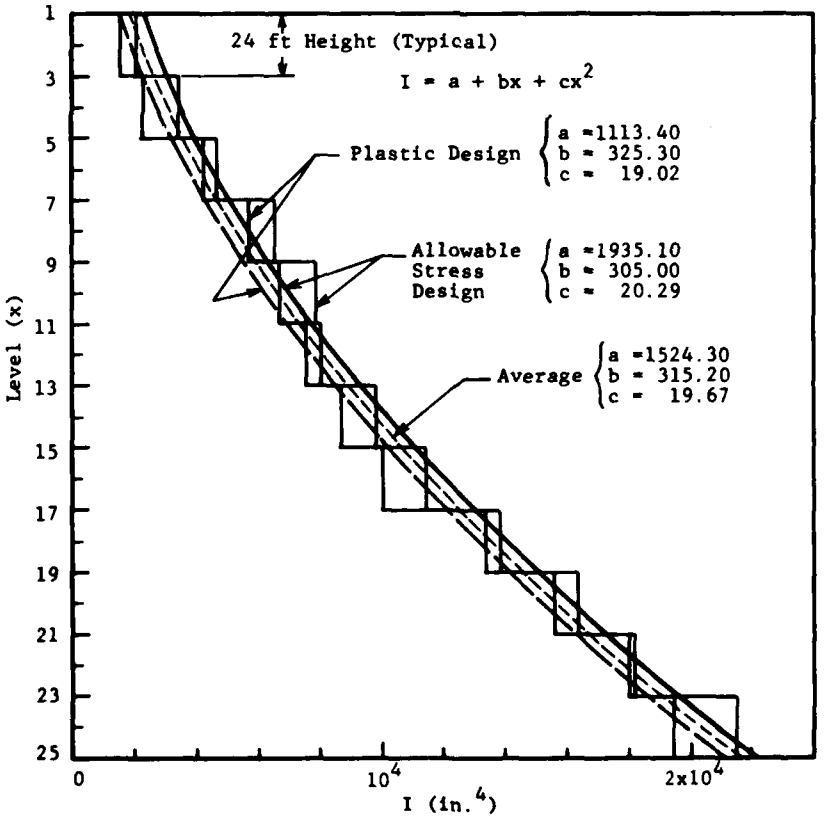

FIG. 7 MOMENT OF INERTIA (I) VARIATION OF BENT COLUMN

TABLE 3
WEIGHT/FEET OF HEIGHT (LB/FT) OF BENT COLUMNS
(ONE BENT) FRAME C - UNBRACED Ref. [2]

Level	Plastic Design	Allowable Stress Design
1-3	196	215
3-5	274	311
5-7	378	409
7-9	494	554
9-11	570	652
11-13	629	661
13-15	704	781
15-17	808	885
17-19	1008	1035
19-21	1139	1181
21-23	1285	1272
23-25	1374	1457

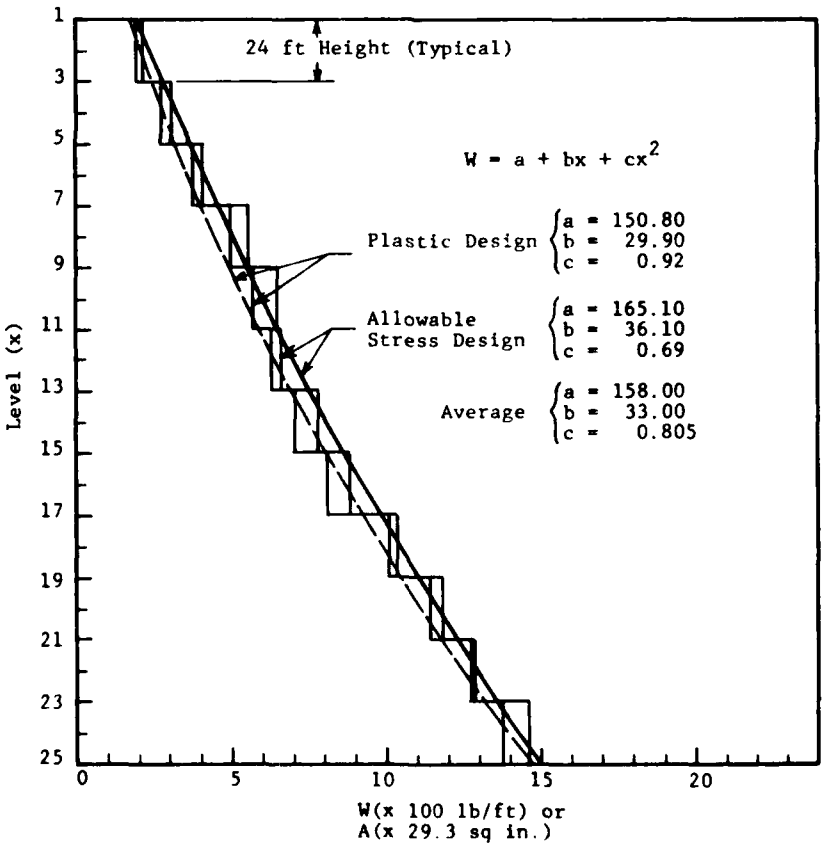

FIG. 8 COLUMN WEIGHT (W) AND CROSS-SECTIONAL AREA (A) VARIATION OF BENT COLUMNS

FREE VIBRATION ANALYSIS

Each of the finite element models for the three buildings was used to extract the modes and frequencies of vibration for several horizontal and vertical modes. The SAP IV computer code, Ref. [3], was used to perform the mode extraction operations. Table 4 gives the frequency of vibration for the first lateral mode and the first vertical mode for each of the three structures. For each of the structures, the first four modes of vibration are lateral modes and the fifth mode is the first vertical mode of vibration.

TABLE 4
FUNDAMENTAL LATERAL AND VERTICAL MODES
OF VIBRATION FOR THE 4-, 12-, and 24-STORY BUILDINGS

Building Model	Fundamental Frequency (cps)	
	Lateral Model	Vertical Mode
24 Story	0.484	3.06
12 Story	0.690	4.62
4 Story	1.473	10.39

DYNAMIC RESPONSE ANALYSIS

The step-by-step numerical integration procedure available in SAP IV was used to obtain the dynamic response of each of the three structures to the horizontal and vertical seismic acceleration waveform shown in Fig. 1 and 2.

The equations of motion, in matrix form, solved by the program are

$$M \ddot{u}_r + C \dot{u}_r + K u_r = - M \ddot{u}_g \qquad (2)$$

where

M = mass matrix

C = damping matrix

K = stiffness matrix

$u_r = u - u_g$ = relative displacement of the structure with respect to the ground

u = absolute displacement of structure

u_g = displacement of ground

and time derivatives are denoted by the dot notation. The damping matrix is determined by applying scalar factors (α, β) to the mass and stiffness matrices, i.e.,

$$C = \alpha M + \beta K \qquad (3)$$

It has been shown, (Ref. [4], that welded steel frame buildings (similar to those considered in this section), which are subjected to stresses less than one-half yield stress, are lightly damped and that 2 percent damping is a reasonable magnitude for this effect. The parameters, α and β, have thus been chosen so that 2 percent damping is provided for the lowest frequency horizontal and vertical modes. If ω_1 and ω_2 are the circular frequencies of the two modes and $\xi = 0.02$ is the damping factor, these parameters can be computed from

$$\beta = 2\xi/(\omega_1 + \omega_2) \qquad (4)$$

$$\alpha = \omega_1 \omega_2 \beta$$

The values used for each building are listed in Table 5.

TABLE 5
SAP IV DAMPING PARAMETERS
FOR 2 PERCENT DAMPING
($C = \alpha M + \beta K$)

Building Model	α	β
24 Story	0.105	0.00180
12 Story	0.151	0.00120
4 Story	0.324	0.00054

As indicated by Eq. (2) the SAP IV computer program computes building motions relative to the seismic

displacements. Since the absolute displacements of the building were sought, it was necessary to write a post-processor code which merged the ground displacements with the relative displacements.

Response spectra curves were also generated for the same points on each structure for which the motion history plots were generated. All response spectra curves were obtained for the single degree of freedom oscillators with 2 percent of critical damping. The following technique was used to obtain the absolute acceleration data for each point of interest on the structure. First, the relative displacements obtained from the solution of Eq. (2) were used to obtain relative accelerations. Newton's forward (I) and backward (II) interpolation formulas were used to compute the accelerations at the beginning and end of the time data. Sterling's formula (III) for central interpolation was used for the remainder of the data. The appropriate equations, using five data points for each interpolation scheme, Ref. [5], are

- Newton's formula (I) for forward interpolation

$$\ddot{y}_o = [11 (y_o + y_4) - 32 (y_1 + y_3) 42 y_2]/12h^2 \quad (5a)$$

- Newton's formula (II) for backward interpolation

$$\ddot{y}_o = (11y_{-4} - 56y_{-3} + 114y_{-2} - 104y_{-1} + 35y_o)/12h^2 \quad (5b)$$

- Sterling's formula (III) for central interpolation

$$\ddot{y}_o = (-y_2 + 16y_{-1} - 30y_o + 16y_1 - y_2)/12h^2 \quad (5c)$$

In these formulas, y_i denotes the data point (relative displacement) at the ith solution step relative to the point at which the acceleration is to be computed. These formulas are also based on equally spaced data at time intervals of h. The relative accelerations computed with these formulas were then added to the ground acceleration data to produce the desired absolute accelerations of the structure. These data are the basic input for the calculation of the response spectra curves included in the summary of results.

SUMMARY OF RESULTS

Absolute displacements for selected floor levels of each of the three buildings are shown in Fig. 9 through 18. In each of these figures, the ground motion is also shown for comparison with the building motion. The horizontal displacements are shown in Fig. 9 through 15 and the vertical displacements in Fig. 16 through 18. It is noted that the vertical structural displacements are not much larger than those of the ground motion for any of the buildings. However, the horizontal structural motions are significantly amplified with regard to the horizontal ground displacements.

Response spectra curves for selected stories of the three buildings are given in Fig. 19, 20, and 21. In these figures, the 2 percent damped ground spectrum curve is shown for comparison. Also shown along the edges of the response spectra graphs are the maximum displacement and acceleration from the time variation of the motions. In addition, the maximum ground velocity is also shown. Finally, the first two fundamental frequencies of vibration of the structure for horizontal response are indicated to show the correlation between this parameter and the amplification of the structure spectra for oscillator frequencies close to the natural frequencies of vibration of the structure.

Table 6 is included to show the comparison between the maximum horizontal response spectra magnitudes and corresponding maxima from the time history motions for the various stories of each building.

It is also of interest to examine the seismic forces in the building frame. The maximum axial force (P), shear force (V) and bending moment (M) that occurred during the dynamic response analysis are listed in Table 7 for several of the finite elements of each structure. These forces are for 1 sq ft of the building planform since the finite element properties were normalized by the building area associated with one bent, i.e., A = 1440 sq ft. The force resultants listed in the table are the internal forces at the lower end of each element. The finite elements were numbered sequentially from the top of the structure to the bottom; thus, element 1 corresponds to the roof level columns. Using the results from the 24-story building, the force

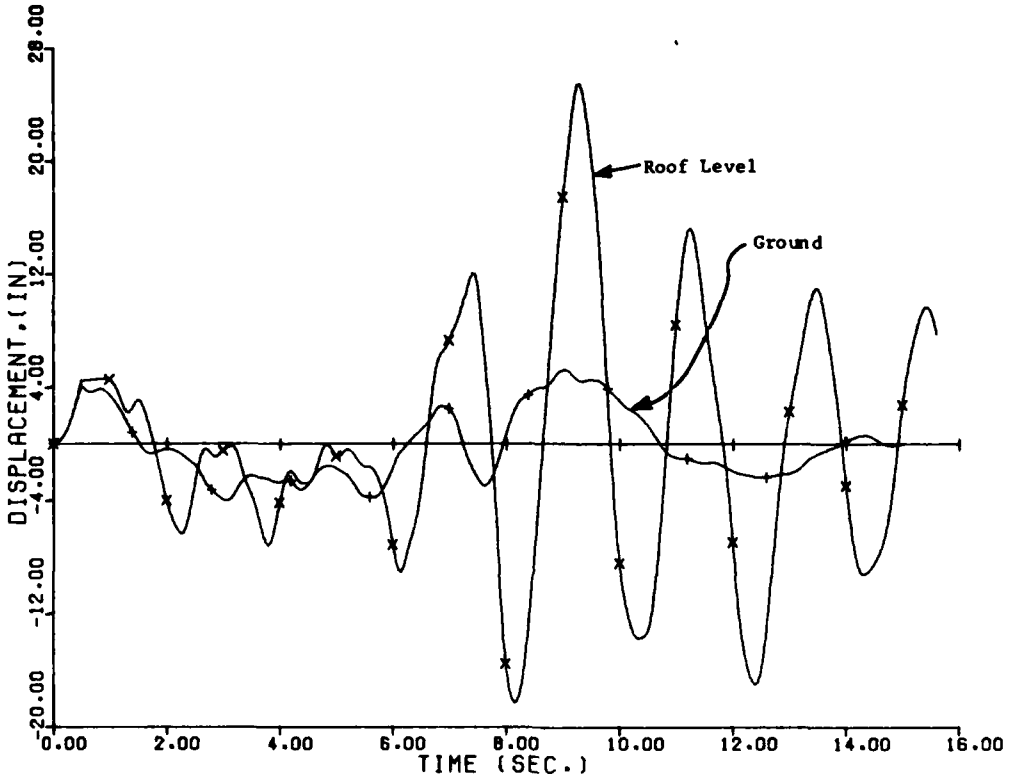

FIG. 9 HORIZONTAL DISPLACEMENT VARIATION - ROOF LEVEL OF 24-STORY BUILDING

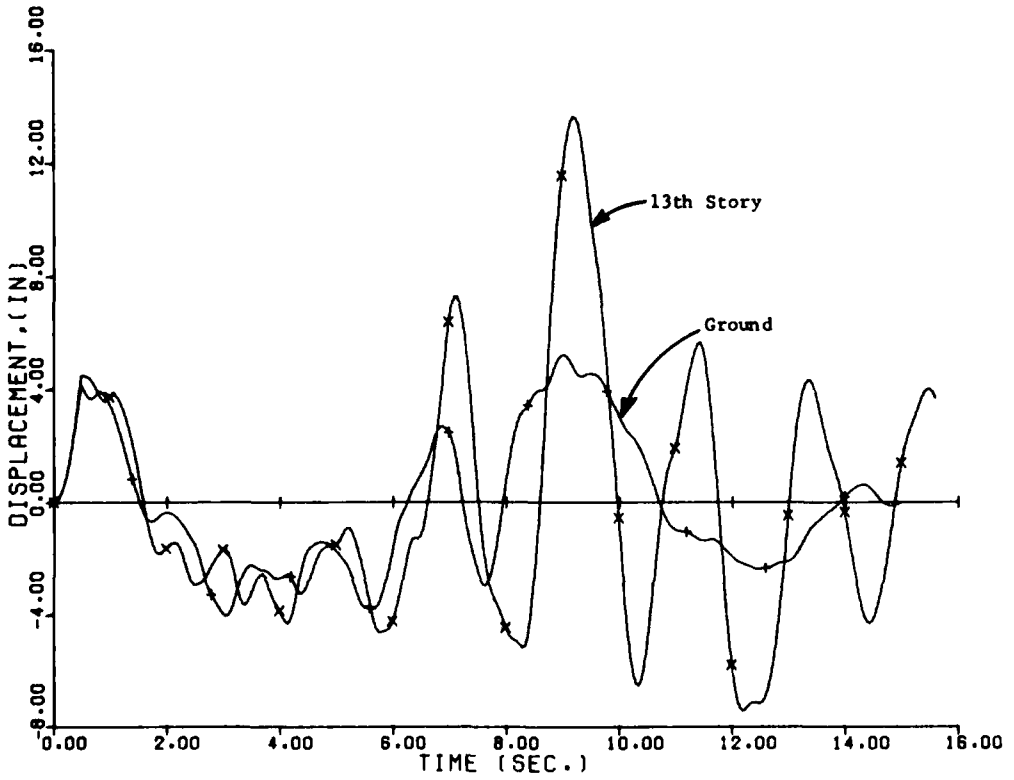

FIG. 10 HORIZONTAL DISPLACEMENT VARIATION - 13TH STORY OF 24-STORY BUILDING

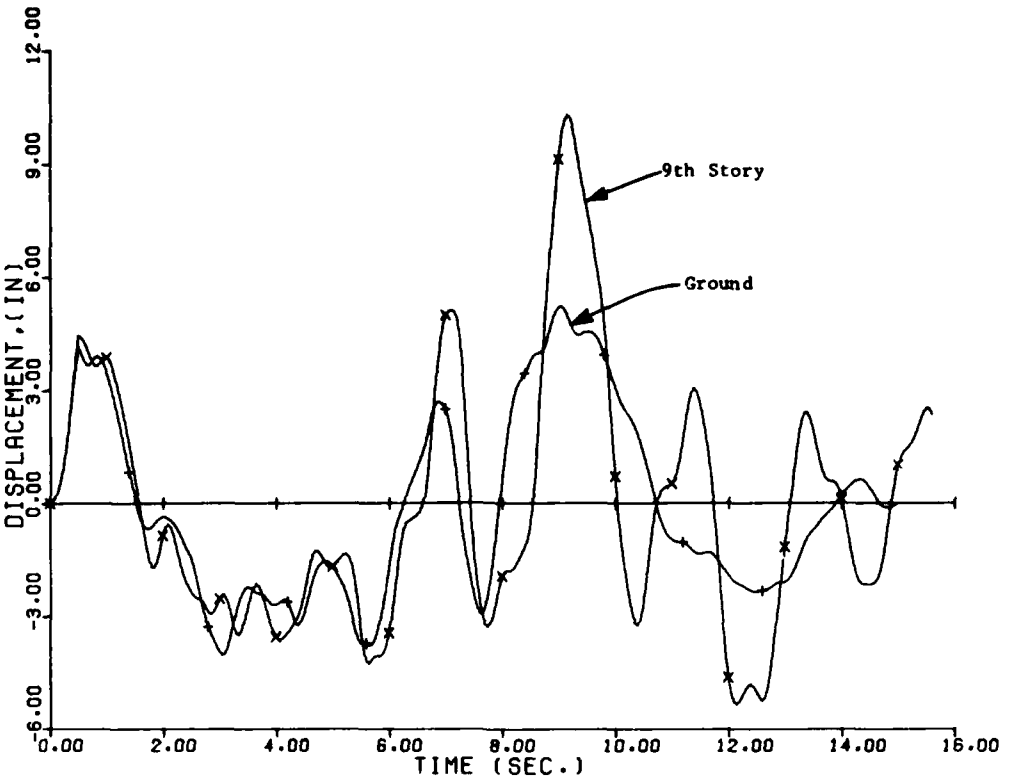

FIG. 11 HORIZONTAL DISPLACEMENT VARIATION - 9TH STORY OF 24-STORY BUILDING

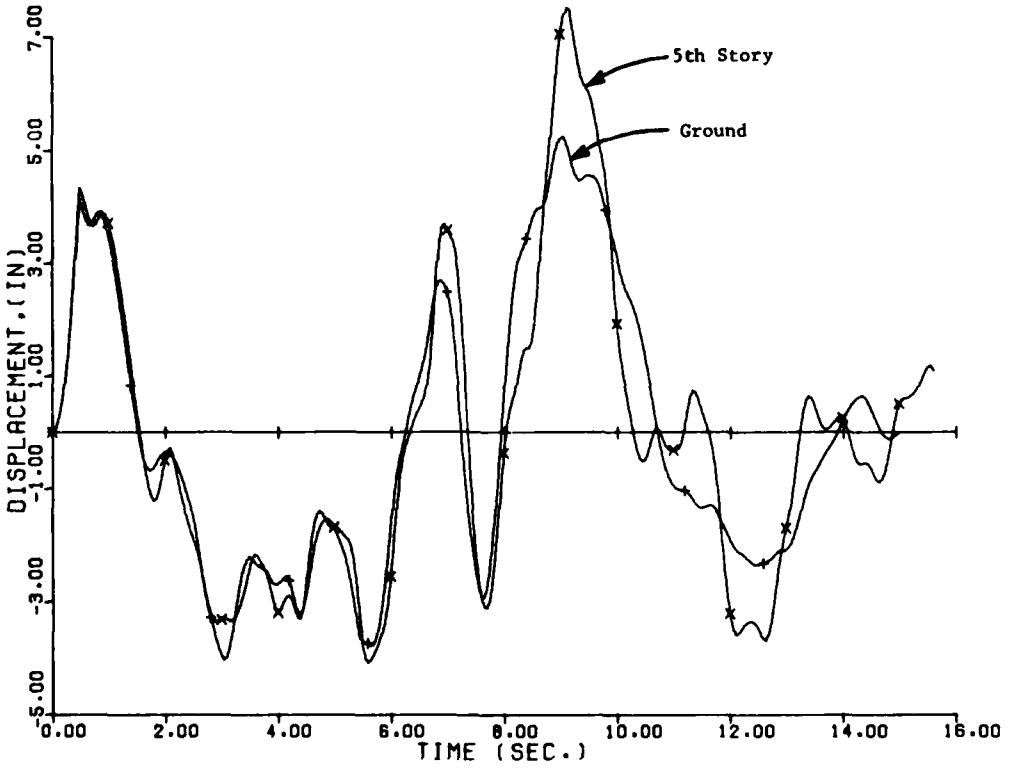

FIG. 12 HORIZONTAL DISPLACEMENT VARIATION - 5TH STORY OF 24-STORY BUILDING

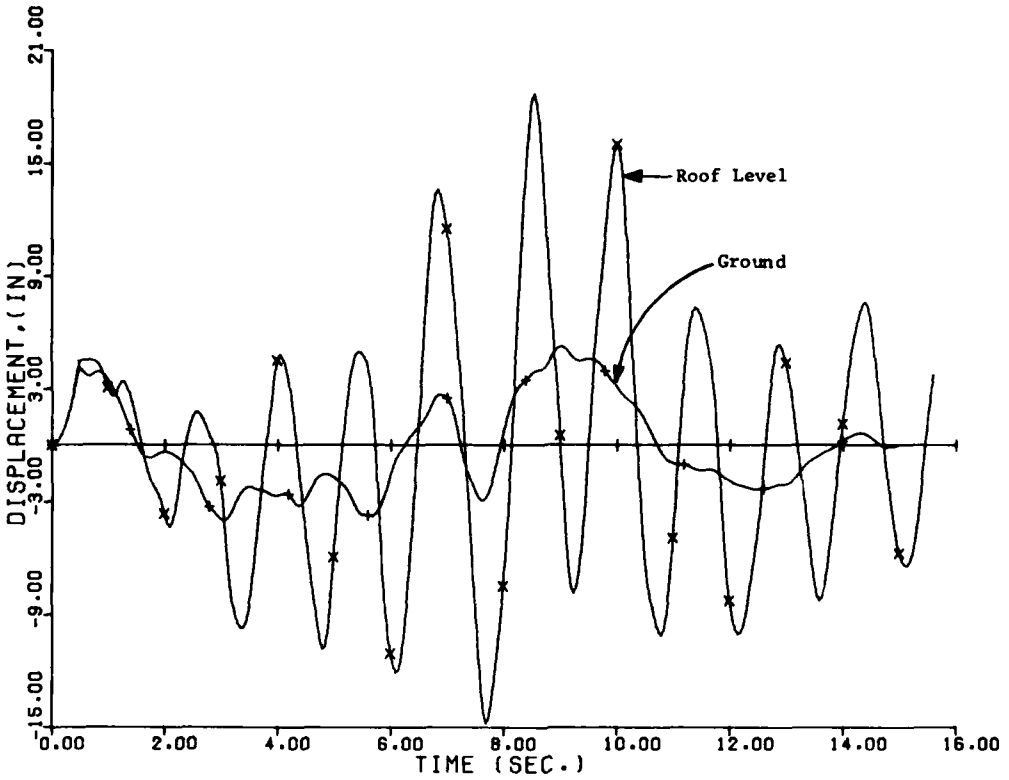

FIG. 13 HORIZONTAL DISPLACEMENT VARIATION - ROOF LEVEL OF 12-STORY BUILDING

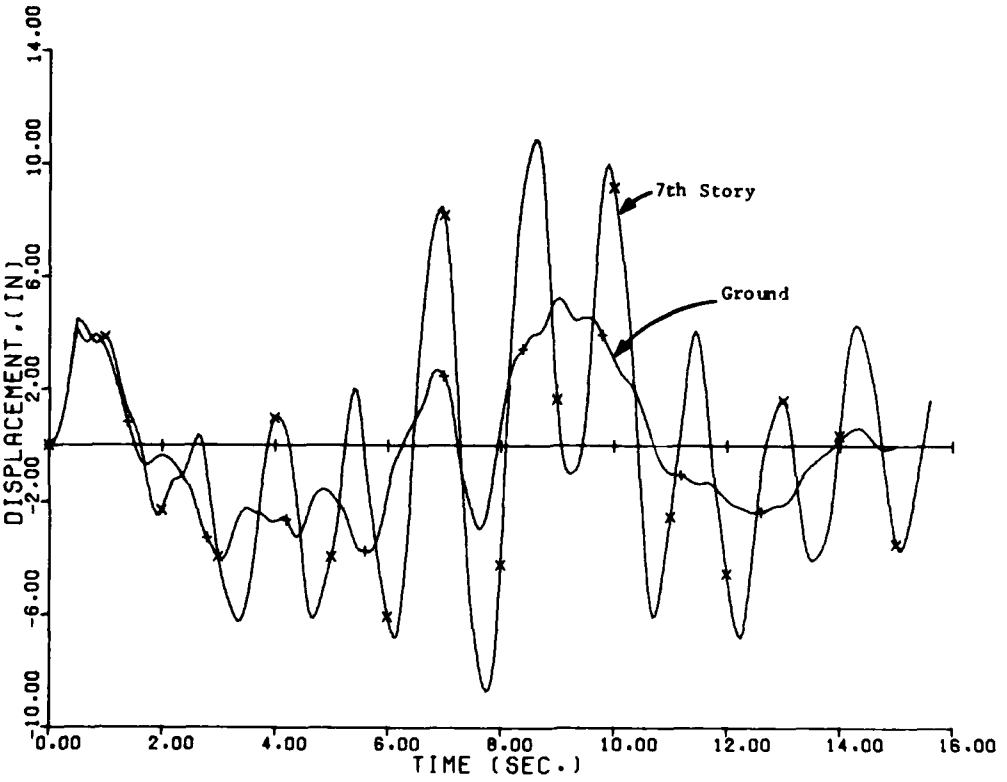

FIG. 14 HORIZONTAL DISPLACEMENT VARIATION - 7TH STORY OF 12-STORY BUILDING

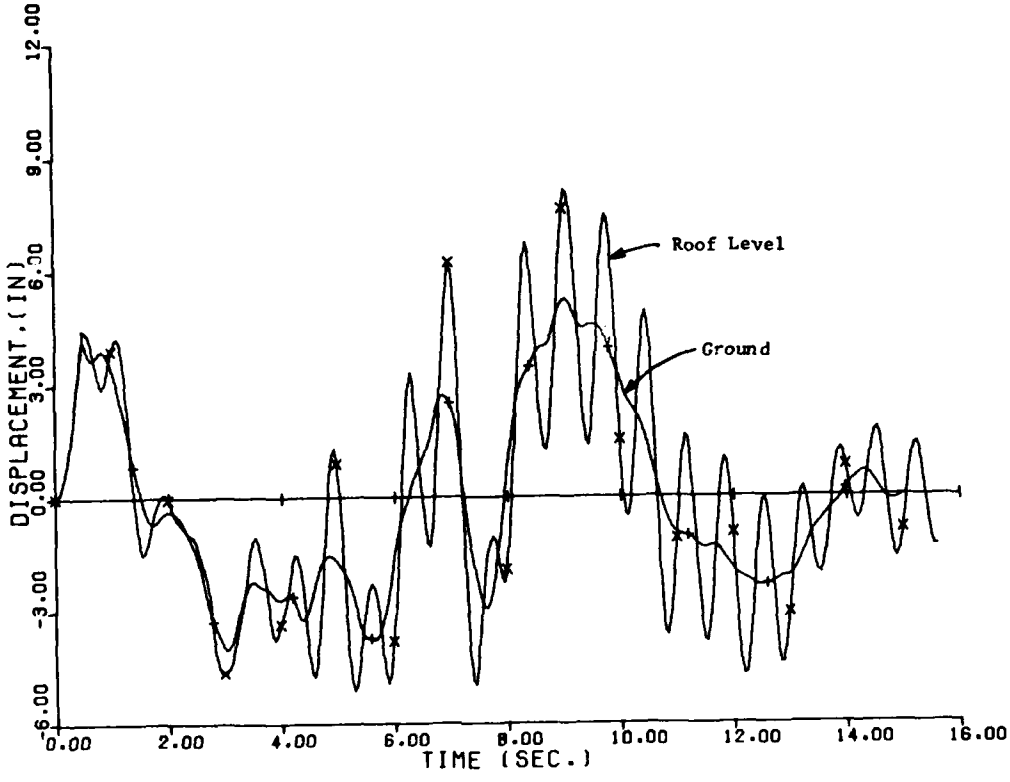

FIG. 15 HORIZONTAL DISPLACEMENT VARIATION - ROOF LEVEL OF 4-STORY BUILDING

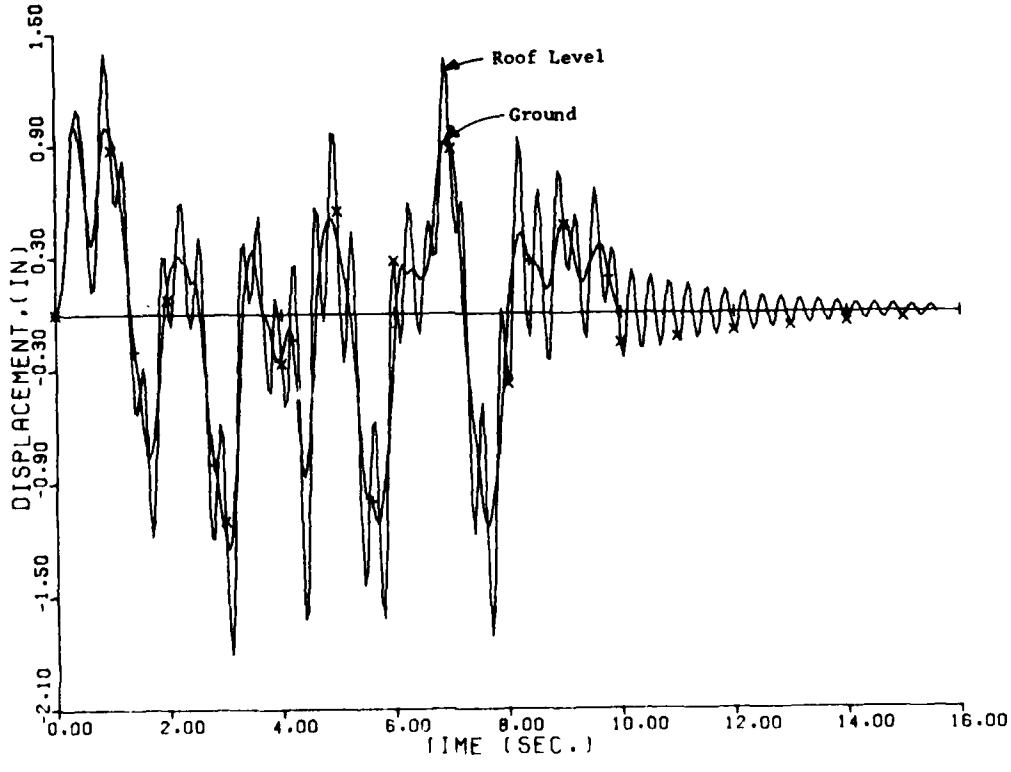

FIG. 16 VERTICAL DISPLACEMENT VARIATION - ROOF LEVEL OF 24-STORY BUILDING

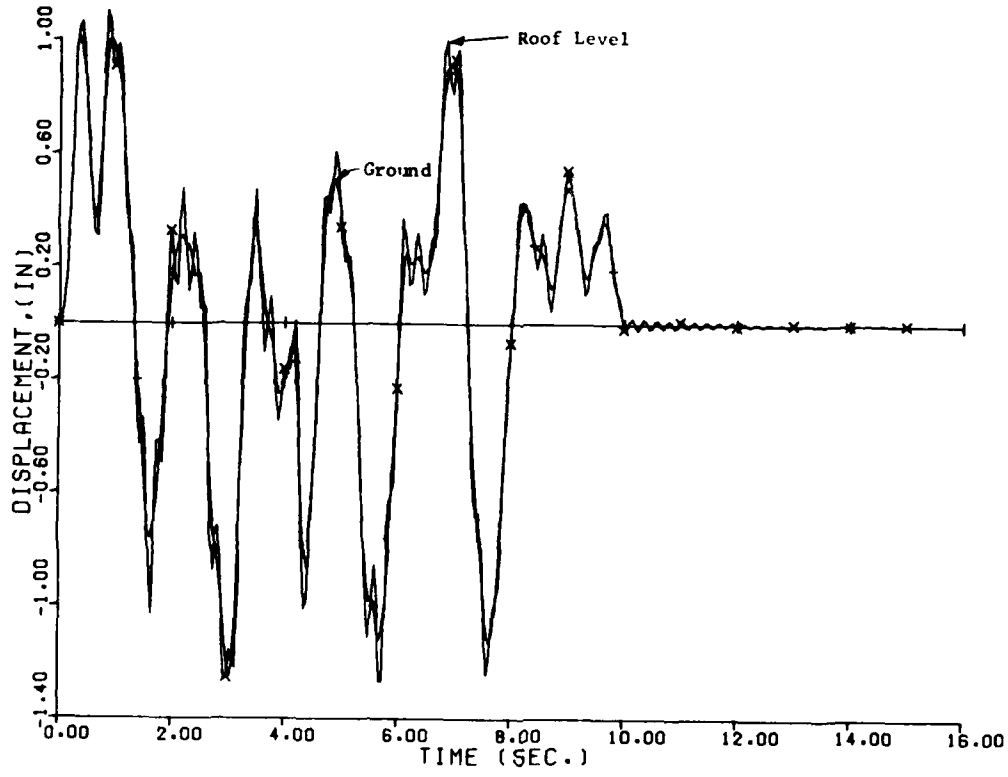

FIG. 17 VERTICAL DISPLACEMENT VARIATION - ROOF LEVEL OF 12-STORY BUILDING

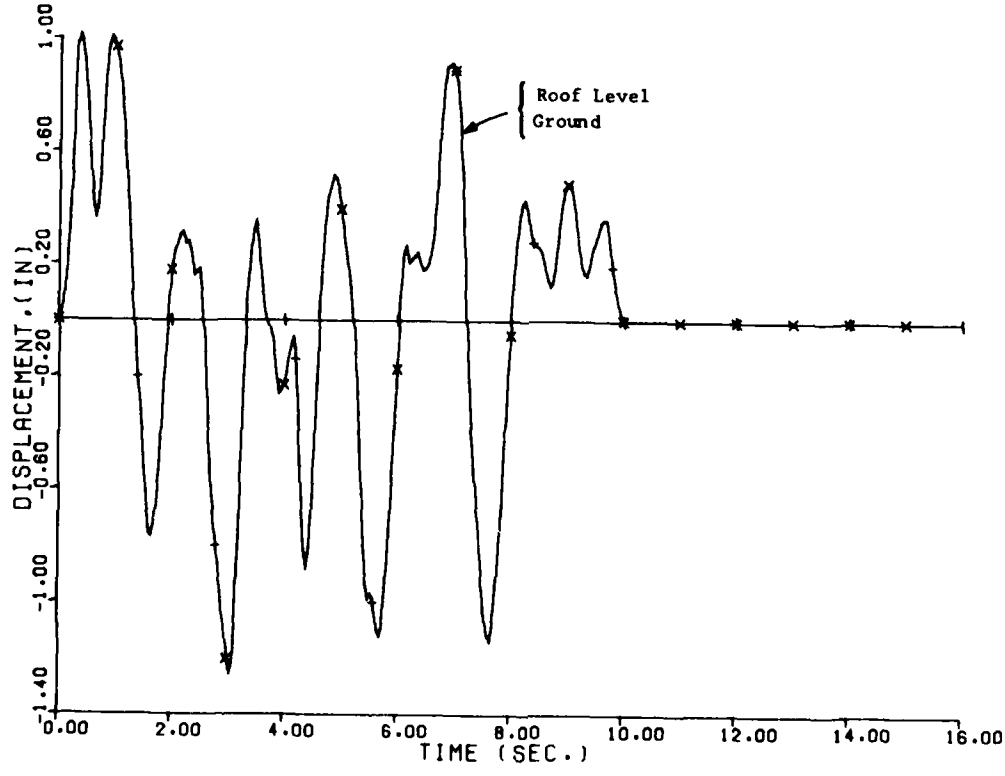

FIG. 18 VERTICAL DISPLACEMENT VARIATION - ROOF LEVEL OF 4-STORY BUILDING

resultants in the column at the ground level are obtained from element 24. For the members of the plastic design frame, the following structural properties are given for the bent columns at the ground level.

The maximum seismic unit stresses can be estimated by using average structural properties and assuming that one-fourth of the Table 7 forces are applied to the average section.

Section	A_{web} (inch^2)	S (inch^3)	A(inch^2)
W14 x 314	1.415 x 17.19	512	92.3
W14 x 342	1.545 x 17.56	559	100.6
W14 x 398	1.770 x 18.31	657	117.0
W14 x 320	1.890 x 16.81	493	94.1
TOTAL	115.63	2221	404.0

There results

$$\text{Seismic Shear Stress} = \frac{3}{2}\left(\frac{V}{A_{web}}\right)_{ave}$$

$$= \frac{3}{2}\ (1021 \times 1440/4)/(115.63/4)$$

$$= 19{,}100 \text{ psi}$$

$$\text{Seismic Combined Stress} = \left(\frac{P}{A}\right)_{ave} \pm \left(\frac{M}{S}\right)_{ave}$$

$$= \left[\frac{1691/4}{404/4} \pm \frac{73.5 \times 10^3/4)}{2221/4}\right] (1440)$$

$$= (53{,}680),\ (-41{,}630) \text{ psi}$$

Using a roof and floor live load of half the design values shown in Fig. 5 the axial load in the columns at the ground level for the dead and live loads is

$$P = 1440\ [(95+15) + 23(120+50)]$$

$$= 1440\ (4020) \text{ lb}$$

This axial load causes an average direct stress in the column of 1440(4020)/404 = 14,300 psi.

RESPONSE OF NONSTRUCTURAL BUILDING EQUIPMENT TO SEISMIC ENVIRONMENT

In this section, possible damage to such building components as elevators, motor generators, piping, and lighting fixtures is discussed with regard to the seismic load environment presented in the previous section. For the analysis of these nonstructural items, the appropriate loading is derived from the response spectra curves of the building.

The technique generally employed for this type of analysis involves first, an estimation of the nonstructural item's natural frequency of vibration, and then determining the seismic "g" loading (horizontal and vertical) and/or the relative displacement of the item from the appropriate response spectrum curves.

For example, if the item is relatively flexible, with a frequency less than approximately 0.2 cps, such as a suspended lighting fixture, for horizontal loading the relative displacement is the important response parameter since the g loading magnitudes are small for flexible items. A large relative displacement of an item can create a hazard since the item can be destroyed due to impacting an adjacent item or structural components such as building walls or columns. Collapse of the item can also be caused by the large relative displacements since these deformations may produce rupture strain magnitudes in critical support components.

If an item is very stiff, with a frequency greater than approximately 5 cps, such as a hard-mounted motor generator, the critical loading becomes the g loading since the relative displacement is small. Large g loadings can cause overstressing of the item's support components such as bolts or brackets and failure or yielding of these parts often creates electrical or mechanical malfunctions.

If a nonstructural item has a fundamental frequency of vibration between 0.2 and 5 cps, then failure may occur from either of the above mentioned effects. This observation is based on the horizontal seismic loading and building structures considered herein since the horizontal

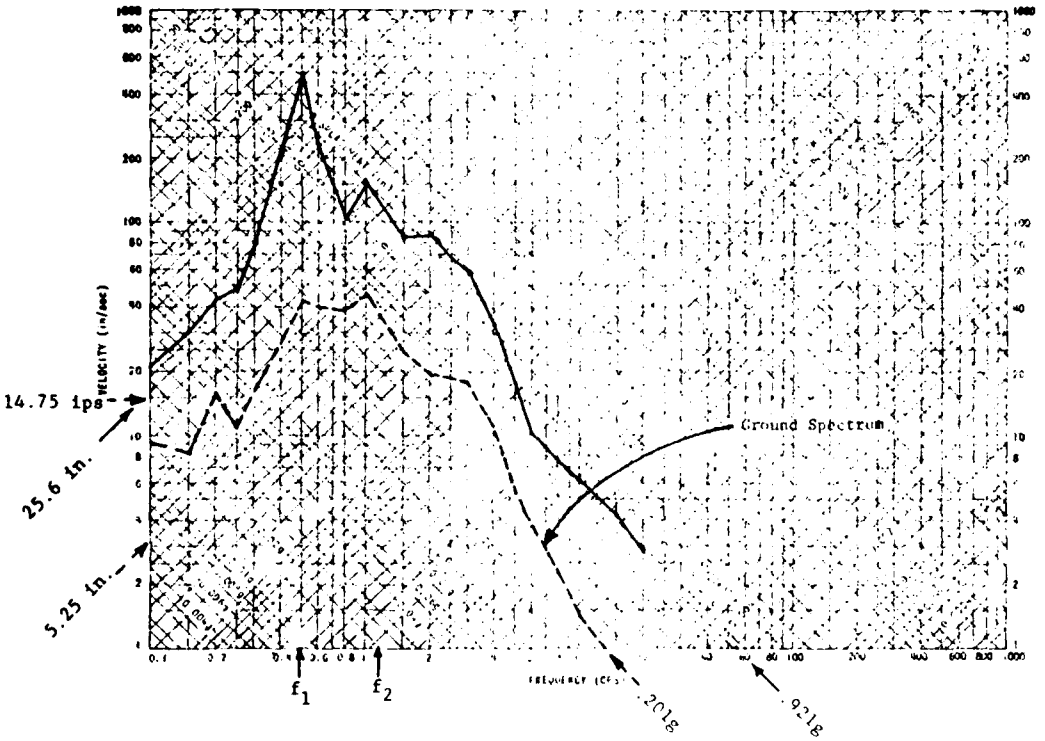

FIG. 19 HORIZONTAL RESPONSE SPECTRA - ROOF LEVEL OF 24-STORY BUILDING (2 percent damping)

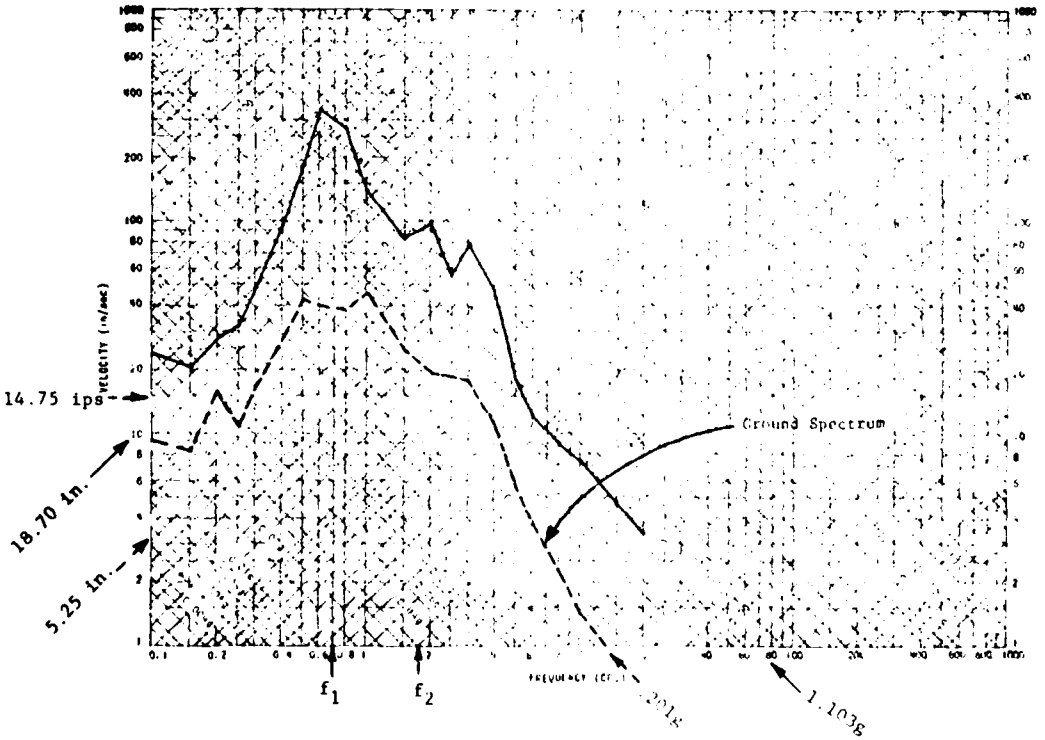

FIG. 20 HORIZONTAL RESPONSE SPECTRA - ROOF LEVEL OF 12-STORY BUILDING (2 percent damping)

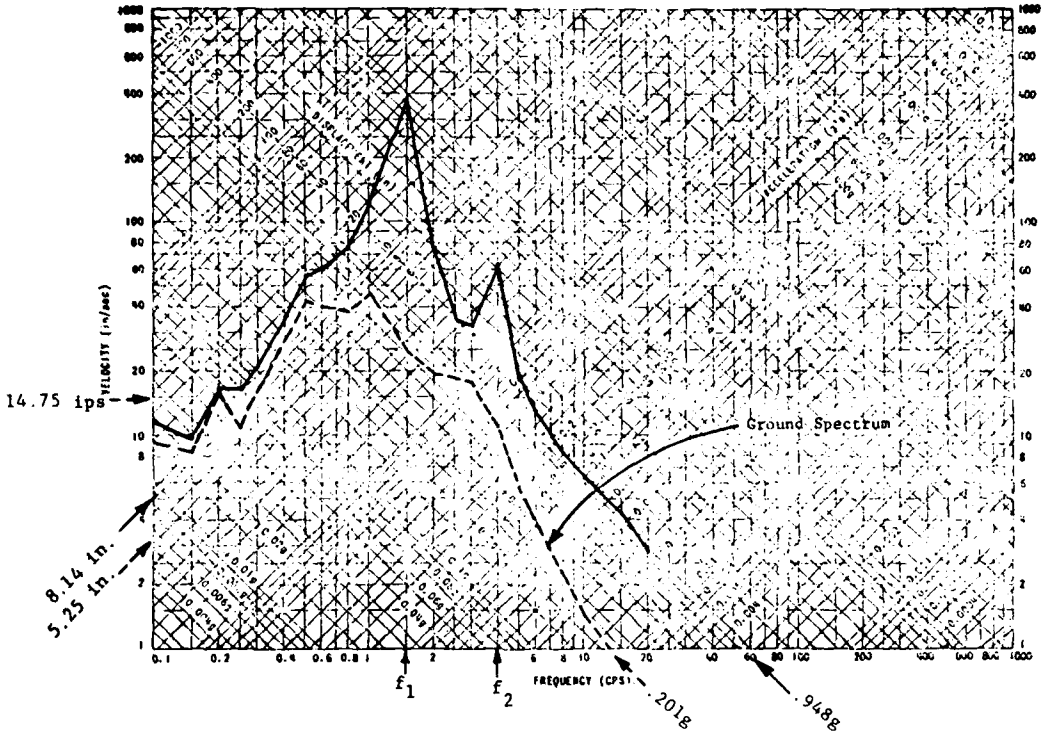

FIG. 21 HORIZONTAL RESPONSE SPECTRA - ROOF LEVEL OF 4-STORY BUILDING
(2 percent damping)

TABLE 6

MAXIMUM HORIZONTAL RESPONSE AT SELECTED FLOOR LEVELS

Floor \ Building		24	12	4	24	12	4
		Maximum Absolute Horizontal Displacement (inch)			Maximum Response Spectra Relative Displacement (inch)		
(Ground)	1	5.25	5.25	5.25	14.6	14.6	14.6
	5	7.50	8.40	8.10	18.1	37.1	39.9
	7	--	10.90	--	--	53.0	--
	9	10.30	13.70	--	35.6	68.9	--
	13	13.70	18.70	--	62.7	87.8	--
	17	17.70	--	--	95.5	--	--
	21	21.80	--	--	131.0	--	--
(Roof)	24	25.60	--	--	154.0	--	--
		Maximum Absolute Horizontal Acceleration (g)			Maximum Response Spectra Acceleration (g)		
(Ground)	1	0.201	0.201	0.201	0.857	0.857	0.857
	5	0.316	0.437	0.948	1.230	2.500	9.190
	7	--	0.540	--	--	2.230	--
	9	0.396	0.637	--	1.680	3.170	--
	13	0.402	1.103	--	1.600	3.860	--
	17	0.575	--	--	2.440	--	--
	21	0.679	--	--	3.360	--	--
(Roof)	24	0.921	--	--	3.940	--	--

TABLE 7

MAXIMUM SEISMIC INTERNAL FORCE RESULTANTS PER SQUARE FOOT OF BUILDING

Element	P (lb/sq ft)	V (lb/sq ft)	M (kip-inch/sq ft)
	24-Story Building		
1	60.4	78.6	5.7
4	403	380	27.4
8	797	671	48.3
12	1123	759	54.6
16	1383	879	63.3
20	1572	951	68.4
24	1691	1021	73.5
	12-Story Building		
1	47.7	95.8	6.9
4	315	462	33.3
6	459	565	40.7
8	568	583	41.9
12	685	715	51.5
	4-Story Building		
1	16.5	82.9	6.0
2	47.7	205	14.7
4	98.8	--	23.1

response spectra are considerably amplified with respect to the ground spectrum in this frequency range. Since a large number of nonstructural items have a natural frequency of vibration in this range (0.2 to 5 cps) it can be concluded that many failures will occur for these items located in the upper stories of buildings higher than five stories.

Such failures will be caused by the large relative horizontal displacements that occur during earthquakes of the magnitude considered in this study. Failures may also be caused from the high vertical g loadings that result in the upper stories of high-rise buildings. These loads can create uplift forces in excess of the tensile strength provided by the connection of the item to the building. It is also observed that very large horizontal g loads can occur in the upper stories of low-rise buildings and thus the connection strength of nonstructural items may be critical.

SUMMARY, DISCUSSION AND CONCLUSIONS

The objective of the effort described here was to study the motions that would be produced in high- and medium-rise steel buildings when subjected to motions produced by an earthquake. The magnitude, duration and frequency content of such motions is of interest when locating attached or unattached nonstructural items (secondary systems) on the various stories of such buildings.

Results of the three buildings analyzed in this study clearly indicate that horizontal motions induced at the base can be considerably magnified when transmitted to the upper stories. Vertical motions are substantially less magnified. Nonstructural items*

*The response of unattached items in the upper stories of buildings subjected to earthquakes is considered in Ref. [6].

may therefore need to be attached, isolated or judiciously placed such that damage to the building or to the item is minimized, as is the hazard to personnel.

The determination of the motion environment that a given item would experience in an earthquake environment is obviously the central issue. It is usually impractical to include such items in the analysis model representing the building. When such items are included then this may lead to an excessive number of degrees of freedom. There may also be a loss in calculational accuracy when the differences between the masses and stiffnesses of primary and secondary systems are significant. Therefore the equipment and the building are generally treated separately and the building response is used as input for equipment response analysis.

There are two ways in which the building response may be determined; (a) the response spectrum approach, and (b) the time history approach. The response spectrum approach, which makes use of the ground (base) spectrum at the site, is simple to apply. However it has the deficiency in that it provides, for a particular point in the building, only the maximum acceleration associated with each building mode. This information alone is insufficient for the dynamic analysis of an item of equipment supported at that point.

The time history approach (considered here) involves the input of an actual (or simulated) earthquake ground motion at the base of the building and determination of the time history of structural response. This method is theoretically the more rigorous but has the disadvantage that earthquake motion histories cannot be predicted. Also, there is the matter of significant computational efforts for large structures. Accuracy is lost when the decoupled, nonstructural system is "massive" in comparison with the primary system.

Over the past decade interest in this area has been increasing. When it concerns the input motions, both deterministic and nondeterministic random vibration analysis has been considered, Ref. [7], [8], [9]. Studies have also been performed, Ref. [10] to [14], which considered both coupled and decoupled systems. The random vibration analysis along with decoupling of primary and secondary systems seems to be the correct treatment for most structures in this area at this point in time. More studies along this line however are presently in progress.

REFERENCES

[1] M. Watabe, "SIMEAR Computer Program Simulates Earthquake", University of California, Berkeley, December 1972.

[2] G. C. Driscoll, Jr., and L. S. Beedle, et al., "Plastic Design of Multistory Frames", Lehigh University, Fritz Engineering Laboratory Report 273.20.

[3] K.-J. Bathe, E. L. Wilson, and F. E. Peterson, "SAP IV, A Structural Analysis Program for Static and Dynamic Response of Linear Systems", Report EERC 73-11, University of California (Berkeley).

[4] G. C. Hart, "Estimation of Damping for Building Design", Proceedings, Symposium on Tall Buildings, Planning Design and Construction, Nashville, TN, November 14-19, 1974.

[5] J. B. Scarborough, Numerical Mathematical Analysis, Johns Hopkins Press, 4th Edition, 1958.

[6] A. Longinow, E. E. Hahn, K-H. Chu, "Response of Unattached Objects to Earthquake Motions", Conference on Earthquakes and Earthquake Engineering, The Eastern U.S., Knoxville, TN, September 14-17, 1981.

[7] A. K. Singh, and A. H-S. Ang, "A Stochastic Model for Predicting Seismic Response of Light Secondary Systems", Proceedings of the 5th World Conference on Earthquake Engineering, Vol. 2, pp 2550-2553, 1974.

[8] M. P. Singh, and Y. K. Wen, "Nonstationary Seismic Response of Light Equipment", ASCE-EMD First Specialty Conference, Waterloo, Canada, May 1976.

[9] M. K. Chakrovorty, and E. H. Vanmarcke, "Probabilistic Seismic Analysis of Light Equipment Within Buildings", Proceedings of the 5th World Conference on Earthquake Engineering, Vol. 2, pp 2822-2828, 1974.

[10] P. K. Kassawara, Earthquake Response of Light Multiple Degrees of Freedom Secondary Systems by Spectrum Techniques, Ph.D. Thesis, University of Illinois at Urbana-Champaign, Urbana, IL, 1970.

[11] R. Villaverde, "Response Spectrum Method for Nonstructural Systems", ASCE-EMD 5th Specialty Conference, Laramie, WY, August 1984.

[12] A. K. Gupta, and J. M. Tembulkar, "Dynamic Decoupling of MDOF Secondary Systems", ASCE-EMD 5th Specialty Conference, Laramie, WY, August 1984.

[13] D. A. Gasparini, and C.-H. Ke, "Random Vibration of Cascaded Secondary Systems with Multiple Supports", ASCE-EMD 5th Specialty Conference, Laramie, WY, August 1984.

[14] T. Igusa, and A. Der-Kiureghian, "Non-stationary Response of Secondary Systems", ASCE-EMD 5th Speciality Conference, Laramie, WY, August 1984.

DISCUSSION

Mr. Mlakar (JAYCOR): Of the various simplifying assumptions you made, which one do you feel is the most important one to relax and treat more realistically?

Mr. Longinow: From the standpoint of a structural engineer alone, I think the structural response parameters are very important because you can be very off depending on how well you define your structure. I had conventional buildings in mind when I did this analysis, and there, the variability in parameters is very great. I assume you can design a hardened facility where you have control of your materials properties and of your geometry; maybe there, it is not as important. But, in conventional buildings these would be the most important parameters to me, and they are the ones we know the least.

DEVELOPMENT OF A 3KBAR STATIC CALIBRATION DEVICE

Charles D. Little, Jr.
U. S. Army Engineer Waterways Experiment Station
Vicksburg, Mississippi

The definition of increasingly severe dynamic test environments from explosive loadings for defense and military structures has required pressure and stress measurements on the order of several kilobars. To facilitate these measurements a static fluid calibration device was developed which enables transducer calibration to the 3 kbar pressure level. The device is constructed of high-strength steels and is a totally self-contained unit, needing no further means of confinement. The strength and stiffness of the device is sufficient for safe and routine loading of areas up to 64.5 cm^2 (10 in.) for the rated working pressure. The hydraulic system is composed of a hand operated, low volume pump, stainless steel tubing, check valves, fittings, and an input pressure gage, all of which are nominally rated at 7 kbar. Transducers with body thicknesses ranging from 2.54 to 8.89 cm (1 to 3.5 in.) and diameters from 8.89 to 12.7 cm (3.5 to 5 in.) are accommodated by the present design. In addition to transducer calibration, the device provides a useful vehicle for experimental transducer verification through determination of non-linear and hysteretic effects.

INTRODUCTION

Dynamic pressure levels for defense and military structural explosive tests have increased in severity dramatically in recent years. An extensive effort to develop instrumentation capable of successfully deferring the environment has been initiated as a result. As part of this effort, the U.S. Army Engineer Waterways Experiment Station (WES) has developed and produced a series of rugged experimental transducers made of high-strength, heat treated steel (Figures 1 and 2). It was desired to be able to calibrate the gages to very high pressures and establish gage response for a significant portion of the range of test levels. Dynamic pressure calibration capabilities to the desired levels were not fully developed or available, therefore a high pressure static calibration device was pursued.

Initial requirements of the static calibration device were established, with the foremost being the device's ability to adequately and safely contain the large forces generated by the calibration pressures. With areas up to 64.5 cm^2 (10 in.) subjected to initially desired pressures of 5 to 7 kbar, forces on the order of 3560 kN (800 kips) would be produced. In addition to containing these loads, the device was required to be small enough to be housed in existing calibration facilities and operated routinely in a reasonable amount of time per gage calibrated.

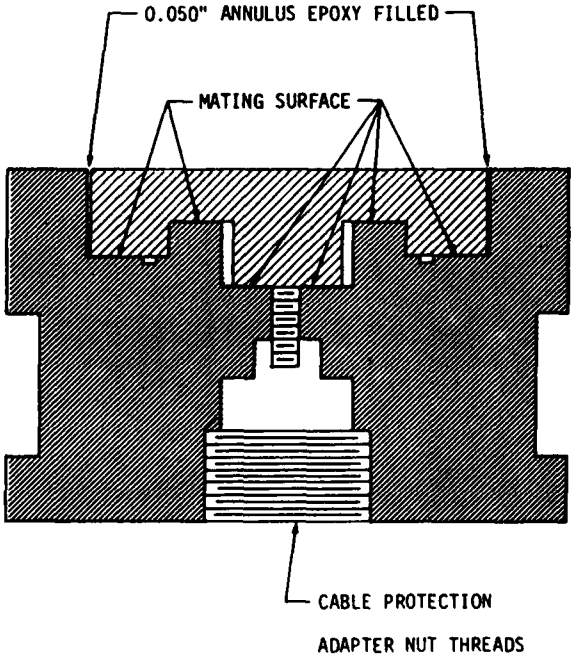

Fig. 1 - Schematic cross-section of WES Column Based Airblast (CBA) Gage

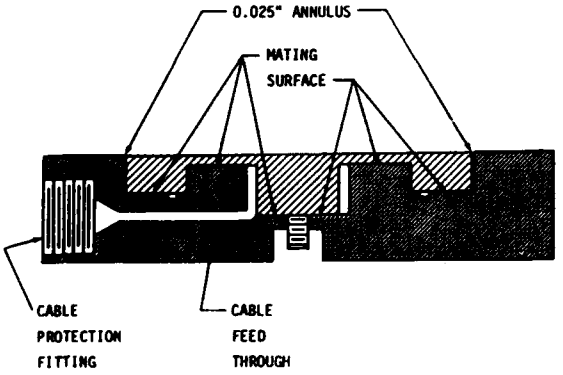

Fig. 2 - Schematic cross-section of WES Column Based Stress (CBS) Gage

DESIGN APPROACH

The initial concept of the device was one where a containment ring or frame would house a cylindrical pressure vessel which would load the gage face with pressurized hydraulic fluid. The gage would be secured to the vessel by a system of sliding, locking wedges, and sealed with metal seals or conventional o-rings. High-strength steel, similar to that used in the gages, would be required for all components.

Elastic theory formulae were used to design all members. Stress equations for pressurized thick-walled cylinders from Roark and Young[1] were used to size the pressure vessel. The method of moment distribution for a rigid frame was used to size the members of the containment frame. The locking wedges and shims were sized to adequately carry the bearing stress transmitted by the gage. All sliding components were heat treated to 50 Rockwell C hardness to prevent scouring of surfaces. The containment frame was not heat treated in order to retain a large range between yield and ultimate strengths. This would limit brittle-type failures should yield be exceeded. All components of the device were machined to very close tolerances.

The design pressure for the device was 5 kbar and the design load for the maximum loaded area was 3340 kN (750 kips). A detailed account of the design calculations is not attempted in this paper. Rather, a detailed description of the final product and its application to instrumentation calibration is presented.

DEVICE DESCRIPTION

The final design of the static calibration device is shown in Figure 3. The device

[1] Roark, Raymond J., and Warren C. Young, "Formulas For Stress And Strain," 5th Edition, McGraw-Hill, Inc., New York, 1975, pp. 504-505.

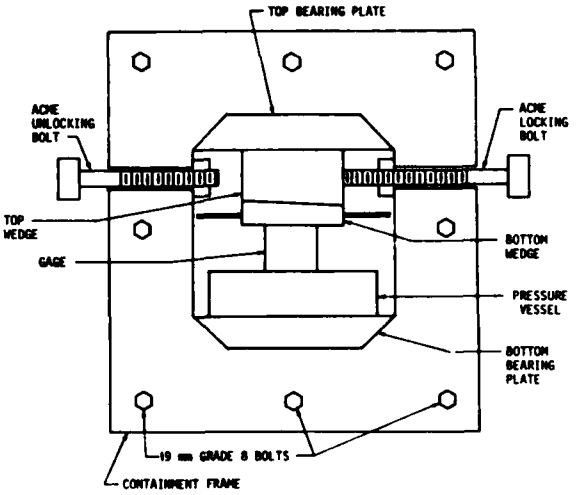

OVERALL DIMENSIONS

HEIGHT	61cm (24 in.)
WIDTH	56cm (22 in.)
DEPTH	30cm (12 in.)

Fig. 3 - 100 ksi calibration chamber, shematic

is constructed entirely of high-strength steel, and is completely self-contained. The weight of the device is approximately 545 kg (1200 lbs). To better describe the device, each component is examined in detail.

The containment frame makes up the bulk of the device and carries the loads generated by the calibration pressures. Two 15.24 cm (6 in.) thick plates of 4140 steel were used to construct the frame. The plates were machined to the overall dimensions shown in Figure 3, then bolted together securely in a laminated fashion with 19 mm (0.75 in.) Grade 8 bolts in the pattern shown. A tunnel-like chamber was then machined through the entire thickness of the bolted plates. The dimensions of the chamber are 35.56 cm (14 in.) in height, and 30.48 cm (12 in.) in width, with 5.08 cm (2 in.) fillets in each corner to minimize stress concentrations.

Two 5.08 cm (2 in.) thick trapezoidal shaped bearing plates fit in the top and bottom of the chamber. The plates are each bolted to the containment frame with eight 9.5 mm (3/8 in.) Grade 8 countersunk cap screws. The purpose of the bearing plates is to distribute the generated loads as evenly as possible to the containment frame. An even load distribution reduces the end and center moments of each member of the frame.

Hydraulic pressure is applied to the gage through the pressure vessel that rests on the bottom bearing plate (Figure 4). The pressure vessel is constructed from 25.4 cm (10 in.) diameter 4340 high-strength steel. The height

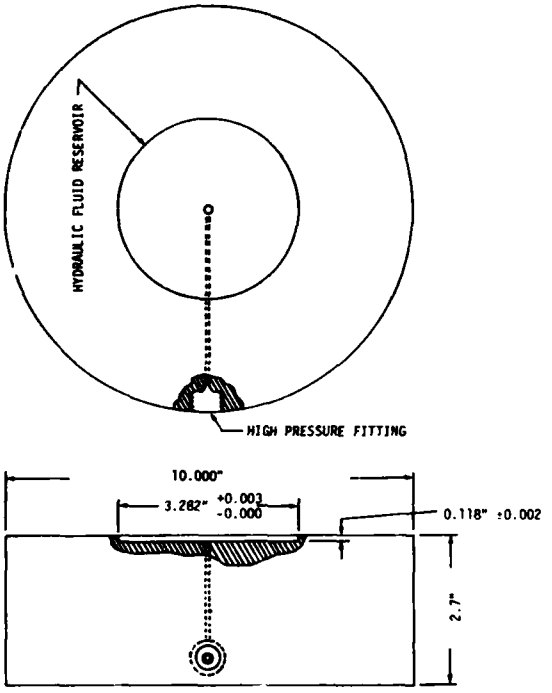

Fig. 4 - Pressure vessel, 100 ksi calibration chamber

of the vessel is 6.86 cm (2.7 in.). A 1.6 mm (1/16 in.) deep recess is machined in the bottom bearing plate to properly center the pressure vessel in the calibration device. A shallow fluid reservoir approximately 3 mm (0.118 in.) deep and 8.9 cm (3.5 in.) in diameter is machined in the top center of the vessel. This reservoir serves both as the hydraulic fluid chamber and the o-ring or metal seal groove. The pressure vessel is heat treated to approximately 50 Rockwell C.

Gages are centered, sensing face down, on the pressure vessel by aluminum gage alignment rings. The rings are thin, doughnut-shaped discs with a small lip on the outer edge that fits over the pressure vessel. The outer edge lip and the inside diameter are sized to fit snuggly, but not bindingly, around the pressure vessel and gage body, respectively. The rings have no structural significance, and serve only to center the transducer over the fluid reservoir.

The gages are held down securely on the pressure vessel by a series of locking wedges (Figure 5). The bottom wedge fits directly on top of the gage body, and is kept stationary by steel dowels. The dowels limit wedge movement to 1 cm by bearing against the inside walls of the containment frame. The sliding, interlocking top wedge is thicker than the bottom wedge, and travels on (and is supported by) guide rails bolted to the top bearing plate. A 3.18 cm (1-1/4 in.) Grade 8 acme bolt supplies the force required to interlock the wedges and

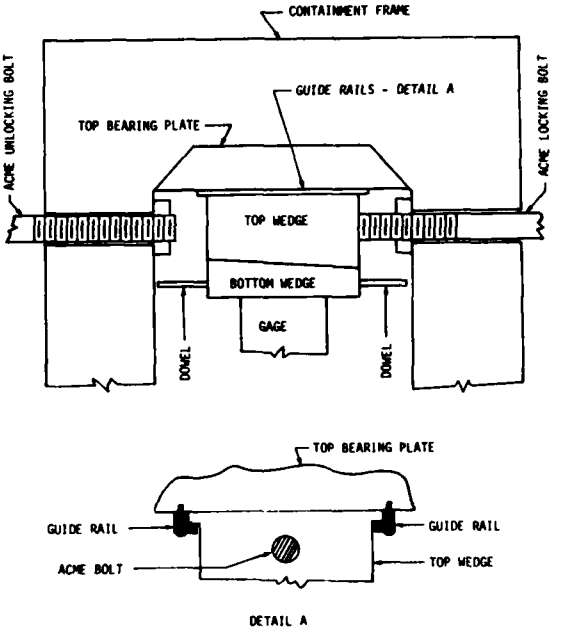

Fig. 5 - Wedge assembly, 100 ksi calibration chamber

secure the gage. The bolt enters the chamber area through a clearance hole bored in the side of the containment frame. The bolt threads through a captive nut bolted to the inside wall of the containment frame, and pushes directly on the top wedge. The bolt slides the top wedge along the guide rails until the top wedge engages firmly with the bottom wedge. Another acme bolt on the opposite side of the device disengages the top wedge after calibration in a similar manner. An assortment of shims are used to take up initial excess slack in the system and protect cable leads exiting from the gage body (Figure 6). The bottom wedge is approximately 2.54 cm (1 in.) thick and the top wedge is approximately 7.6 cm (3 in.) thick. The interlocking faces of the wedges are 15.2 cm × 15.2 cm (6 in. × 6 in.) in dimension and are sloped at an angle of 2.86°. Both wedges and all shims are heat treated to 50 Rockwell C.

A low volume hand pump, 6.35 mm (1/4 in.) stainless steel tubing, stainless steel valves and fittings, and an input reference pressure gage, all rated at 7 kbar, compose the hydraulic system of the calibration device. The hand pump (Pressure Products Industries) has a very low volume discharge of 0.5 cm^3 per stroke, and is easily operated at high pressures. All valves, fittings, and tubing (Superpressure, Inc.) are made of quality materials and are installed according to specifications. The input reference pressure gage (Heise) is a Bourdon tube gage and allows for pressure reading resolution to 7 bar.

Pressure seals between the gage face and

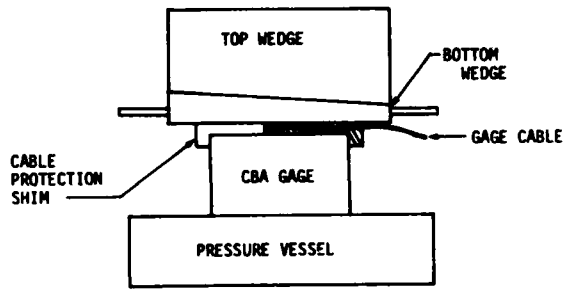

SHIM CONFIGURATION
WES CBA TRANSDUCER

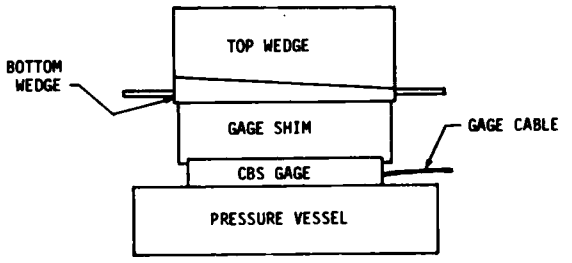

SHIM CONFIGURATION
WES CBS TRANSDUCER

Fig. 6 - Shim configuration, 100 ksi calibration chamber

the pressure vessel are made with standard 90 durometer o-rings (Parker) and flexible metal seals (Pressure Science Inc.). The metal seals are more durable but require a high machine finish on sealing surfaces, which is not always present on the gage face. Standard o-rings have proven effective in routinely sealing pressures to 3 kbar.

Additional features of the calibration device include a hinged door in front of the chamber opening to enclose the high pressure operation area, and a thin steel plate cabinet to shield all tubing and fittings. The present unit has the pump/input gage configuration mounted to the top of the device, although they could easily be housed in a separate console if so desired.

DEVICE PERFORMANCE

The first proof-test of the calibration device was to check the hydraulic system for leaks at high pressures. An extremely tight system was essential because of the small pumping volume and the need to stop and take transducer output readings frequently. The pressure vessel was shut off from the hydraulic system with a valve, and the system pressurized to approximately 5 kbar. When allowed to remain at 5 kbar for several minutes, the system relieved pressure at a very slow rate, which was deemed permissible. The test was repeated several times in order to properly exercise the system and seat all fittings.

The next proof-test was a check of structural strains. Strain gages were placed on the containment frame as shown in Figure 7. A gage was placed in the device and secured, with strain measurements recorded before and after the locking wedge was engaged. Pressure was increased in 1/3 kbar steps to 4 kbar, with strain readings taken at each step (Table 1). A strain distribution for the

TABLE 1. STRUCTURAL STRAIN PROOF--TEST, 100 KSI CALIBRATION CHAMBER

Working Pressures	Strain Gage 1 (uin./in.)	2 (uin./in.)	3 (uin./in.)	4 (uin./in.)	5 (uin./in.)	6 (uin./in.)
Before Locking Wedge	0	0	0	0	0	0
After Locking Wedge	+74	-16	+87	+10	+85	+62
5 ksi	+76	-18	+94	+11	+95	+67
10 ksi	+38	-27	+137	+12	+139	+96
15 ksi	+60	-44	+198	+17	+203	*
20 ksi	+82	-62	+263	+23	+269	+204
25 ksi	+108	-84	+338	+28	+345	+261
30 ksi	+125	-103	+399	+29	+408	+320
35 ksi	+143	-119	+460	+31	+469	+374
40 ksi	+157	-136	+516	+33	+528	+424
45 ksi	+179	-157	+578	+35	+590	+476
50 ksi	+199	-177	+641	+38	+655	+537
55 ksi	+215	-198	+707	+38	+719	+584
60 ksi	+237	-218	+777	+41	+795	+649

Note: (+) Indicates tension.

outer fibers of the side member section shown in Figure 7 was developed by linearly extrapolating between points of measured strain for the 2 and 4 kbar levels (Figures 8 and 9). Stress distributions were calculated from strains using the modulus of steel (Figures 10 and 11). The stress patterns indicate biaxial bending in the member, as well as tension. The amount of bending at the 4 kbar level produces deflections which severely hamper the operation of the seals. Although strains were within a safety factor of 2 at the 4 kbar

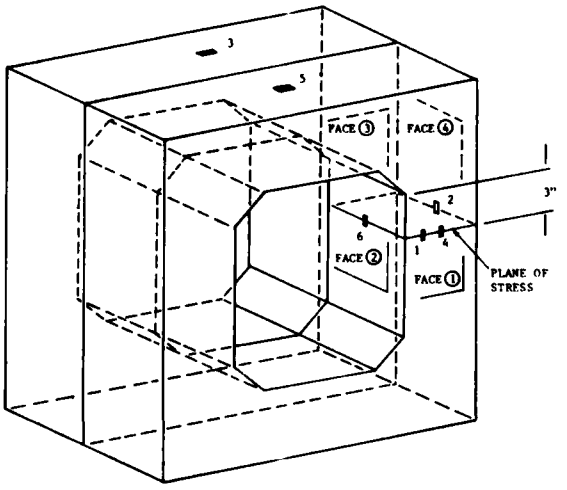

Fig. 7 - Strain gage locations for structure proof test, 100 ksi calibration chamber

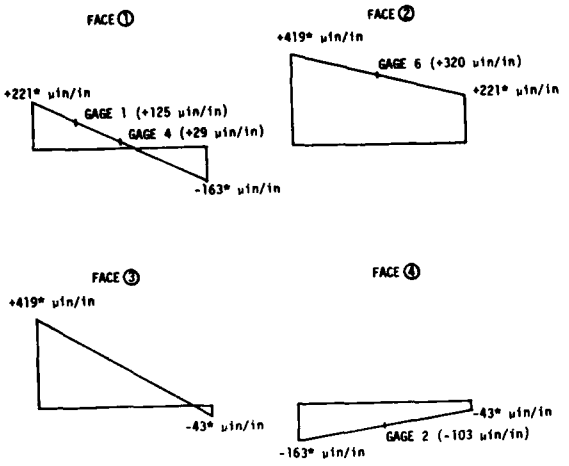

* Denotes extrapolated value

Fig. 8 - Strain distribution in containment structure side member section, 2 kbar pressure loading

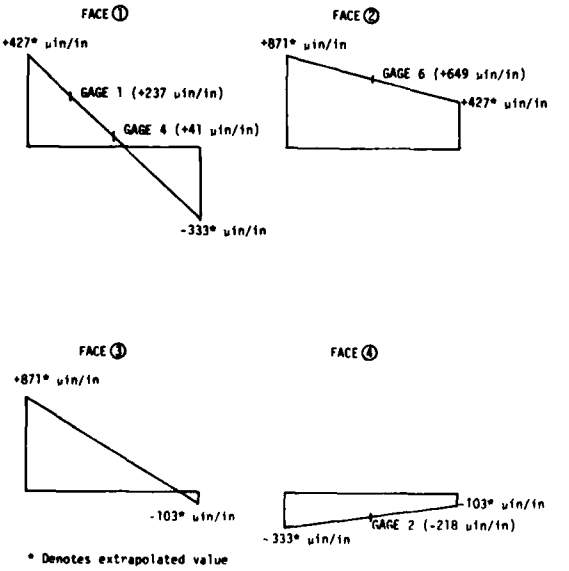

* Denotes extrapolated value

Fig. 9 - Strain distribution in constrainment structure side member section, 2 kbar pressure loading

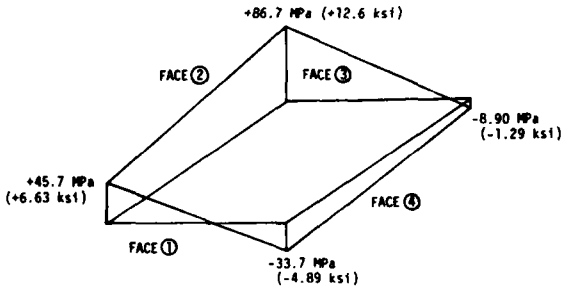

(-) Denotes compressive stress

Fig. 10 - Stress distribution in containment structure side member section, 2 kbar pressure loading

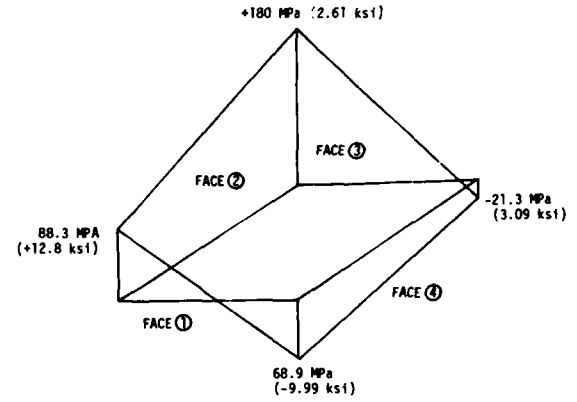

(-) Denotes compressive stress

Fig. 11 - Stress distribution in containment structure side member section, 2 kbar pressure loading

level, a rated working pressure of 3 kbar was established to reduce bending and improve seal performance. The close correlation of strains from Gages 3 and 5 indicates the plates composing the containment frame are bending similarly, and the bearing plates are distributing the forces somewhat evenly.

Calibration of the WES experimental gages is performed very satisfactorily. The turn around time per gage calibrated is approximately 15 minutes once the required calibration instrumentation is set up. A hindrance encountered in the calibration process is the slowness of the initial purging of the system due to the small volume of the pump. Several strokes of the pump are often required to remove entrapped air and fill all voids with hydraulic fluid.

Calibration of the experimental airblast gage has proven to be the most difficult, although not to a prohibitive extent by any

means. Tight pressure seals between the gage face and the pressure vessel are often difficult to maintain at pressures in the upper quarter of the device's working pressure. The problem stems from the gage itself, where the modulus and large thickness of the gage produce deflections that further hamper the o-ring's performance. Calibrations to the range of 2-2.5 kbar are nevertheless routine, and a reasonable range of static calibration can be obtained.

Calibration of the experimental soil stress gage is readily achieved to the full working pressure (3 kbar) of the device. Since the thickness of the soil stress body is considerably less than the airblast gage body, deflections are not as great, and pressure seals are more easily maintained. Calibrations to 3 kbar are routinely made using standard 90 durometer o-rings.

Use of the calibration device in test instrumentation development programs is very beneficial. Good resolution of calibration points for both the pressure build-up leg and the pressure release leg are easily achieved. Transducer characteristics such as nonlinearity and hysteresis are determined from this operation.

CONCLUSIONS

Difficulties experienced during the design, fabrication and operation of the calibration device have led to a list of draw-backs and their possible corrections. Probably the most restrictive problem of the device is the bending of the containment frame. Although bending related stresses are not severe, the resulting deflections produce a difficult situation in which to maintain tight seals at high pressures. An increase in thickness of the top and bottom frame members would increase their stiffness, allowing them to carry more moment and reduce the moment and bending in the side members. A one piece containment frame, rather than a two piece laminated frame, would also stiffen the device.

The small slope on the locking wedges provides only 0.5 mm of displacement for 1 cm of wedge travel, therefore a fairly tight assembly is required initially. This requirement is somewhat restrictive, and calls for a unique set of shims for each size transducer. An increase in wedge slope would increase displacements, although the increase in load transfered to the acme bolt, hence the containment frame, might be prohibitive.

The adaptability of the device to a wide range of transducer sizes is somewhat limited by the present design. The device was designed primarily for the WES experimental gages, and the pressure vessel fluid chamber is too large for small diameter gages. Pressure vessels specifically machined for a particular range of transducer diameters could easily be incorporated in the device since the pressure vessel is easily accessed and interchanged.

In summary, the final end product of the design effort was a calibration device capable of routine static calibrations of the WES experimental gages to the 3 kbar pressure level. The structural strains, within a safety factor of 2, and the low volume pump, 0.5 cm^3 per stroke, ensure a very safe operational unit. Despite the devices' somewhat crude locking mechanism, turn around time per gage calibrated is approximately 15 minutes. The calibration data obtained with the device decreases the uncertainties of transducer response at high pressures and, in turn, improves the quality of data acquired in high pressure explosive tests vital to military and defense structure test programs.

ACKNOWLEDGEMENTS

The author acknowledges with appreciation the assistance of Bob Welch and Brenda Young (Explosion Effects Division) in the planning of the calibration device and the preparation of this paper, respectively. Appreciation extends also to Lamar Sadler (Instrumentation Services Division), Dan Harmon and Jesse Ragan (Construction Services Division) for their labor and helpful suggestions in the construction, assembly, and start-up of the device.

D'ALEMBERT UNFOLDING OF HOPKINSON BAR AIRBLAST DATA

Howard G. White and Charles R. Welch
U. S. Army Engineer Waterways Experiment Station
Vicksburg, Mississippi

Strain gaged Hopkinson Bars are being used to make airblast impulse measurements in high pressure (172 MPa (25 ksi) to 621 MPa (90 ksi)) explosive environments. The data obtained are typically limited in time by the arrival of the reflected tensile wave from the dump end of the bar. For a bar 5.8 m (19 ft) long with a dump section of 4.0 m (13 ft), the record is approximately 1.6 msec long before the reflected wave is seen in the data. By manipulating that portion of the data that is effected by reflections we can increase the useful data time length by a factor of two to four. A simple data unfolding procedure based on an elastic D'Alembert solution for stress waves in a bar is presented in this paper. Bar gage airblast data unfolded using this procedure and the impulse data from these records are presented also.

INTRODUCTION

The levels at which military structures are dynamically tested has increased by a factor of ten over the past several years. As a result, the difficulty in defining the environment has risen by the same factor. The U.S. Army Engineer Waterways Experiment Station (WES) is producing several types of gages that can survive and accurately measure the severe airblast shock wave present in these tests. One gage is the Strain-Gaged Hopkinson Bar. The bar gage development was begun in order to confirm the early time (1-5 msec) pressure impulse from explosive sources. The airblast record from a bar gage should be as pure a measurement as can be made, and one should have confidence in the impulse generated from that record. A problem with the bar gage is that the record is only 1.5 to 2 msec in duration before the tensile reflection reaches the measuring point. There are two ways to increase the duration of the record. One is to increase the length of the bar and the other is to manipulate the data containing the reflected waves. The most cost effective solution was to develop a simple computer program to manipulate the data. Using an elastic D'Alembert solution for stress waves in a bar, an airblast record can be reconstructed from a bar gage containing several reflections.

THEORY

Recall that from a free surface, a compressive wave reflects as a tensile wave and a tensile wave reflects as a compressive wave. The WES bar gage is constructed in such a way that the dump end is not a totally free surface. As a result some of the input stress is transmitted to the material at the end of the bar. Therefore a reflection coefficient must be calculated. The coefficient for the dump end of the bar is the percentage of the input wave that is reflected as a tensile wave. This percentage may be determined empirically from the data record. It is the ratio of the peak of the reflected tensile stress to the peak input stress. Refer to Figure 1. The value of

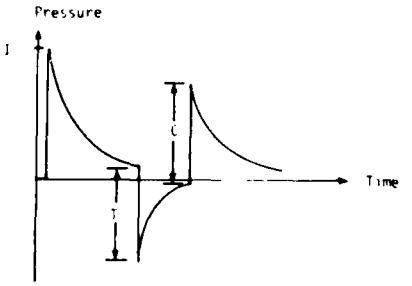

I = peak input stress
T = peak stress of tensile reflection
C = peak stress of compressive reflection
a = reflection coefficient for dump end of bar
b = reflection coefficient for input end of bar

Fig. 1 - Determination of reflection coefficients

the coefficient will always be less than one since stress is transmitted into the supporting material at the end of the bar. Likewise a reflection coefficient must be determined for the input end of the bar. This coefficient is the percentage of the tensile wave that is reflected as a compressive wave. This ratio may be determined empirically from the data record also. It is the ratio of the peak of the reflected compressive stress to the peak of the reflected tensile stress (Figure 1). For free end conditions this value will equal one since all of the tensile wave is reflected as a compressive wave.

For the case of one tensile reflection and one compressive reflection, the actual stress at any time, $0 < t < (4L - 2x)/c$, may be written as:

$$F(t) = f(t) + a*F[t-2*\{(L-x)/c\}] - a*b*F[t-2*\{(L-x)/c\}-2*x/c] \quad (1)$$

where:

F(t) = actual stress in bar
f(t) = measured stress in bar (output of gage)
L = length of bar
x = distance from input end of measuring point
c = wave speed in bar
a = reflection coefficient for dump end of bar
b = reflection coefficient for input end of bar

For any time t,

$$F(t) = f(t) + \sum_{n=1}^{\infty} a^n * b^{n-1} * F(t-n*2*L/c + 2*x/c) - \sum_{n=1}^{\infty} a^n * b^n * F(t-n*2*L/c) \quad (2)$$

This equation is an elastic D'Alembert solution for stress waves in a bar [1]. It also is the crux of the unfolding program. Equation (2) states that the actual stress in a Strain-Gaged Hopkinson Bar can be expressed as the sum of the measured stress in the bar, the tensile reflections and the compressive reflections. This is shown graphically in Figure 2. The unfolding program reconstructs the actual stress wave in the bar in this manner through the use of Equation (2).

PRESENTATION OF DATA

The WES Strain-Gaged Hopkinson Bar (Figure 3) is an adaptation from a design by Neil Baum of the Air Force Weapons Lab and the University of New Mexico [2]. The bar is a 5.8 m (19 ft) long piece of 2.54 cm (1 in.) diameter 1018 steel. Four foil strain gages

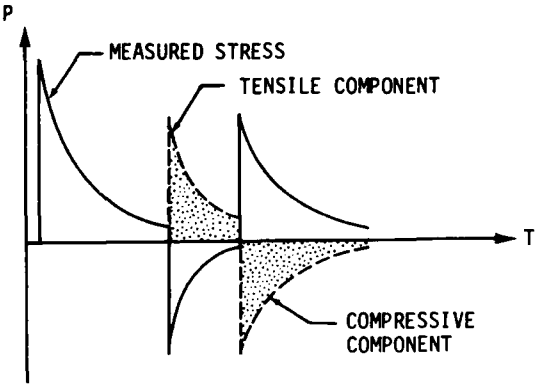

a. Components summed to obtain unfolded wave form

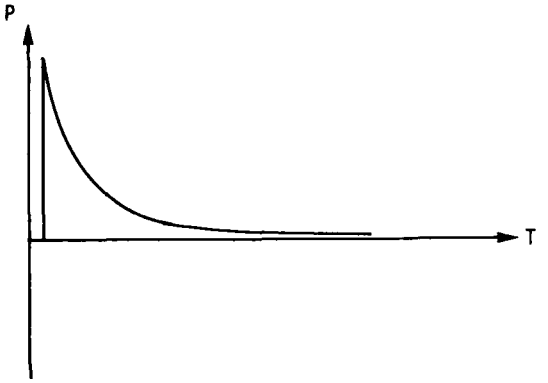

b. Unfolded wave form, as determined by equation (2)

Fig. 2 - Graphical presentation of method to unfold bar gage data

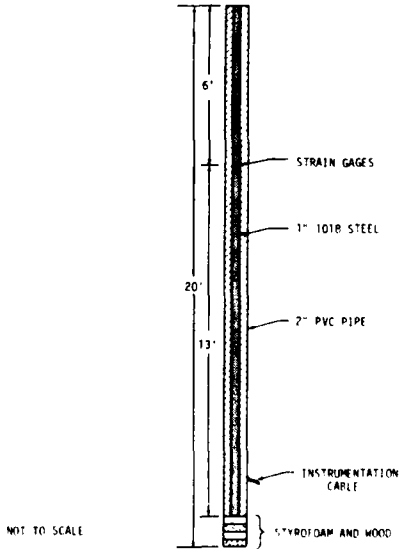

Fig. 3 - Schematic of WES Strain gage Hopkinson Bar

are connected in a full bridge configuration at a point 1.83 m (6 ft) from the input end of the bar, thus giving a dump end of 4.0 m (13 ft). The entire bar is encased in a 6.1 m (20 ft) long piece of 5.1 cm (2 in.) schedule 40 PVC pipe. The bar is supported by alternating layers of styrofoam and wood at the base. The instrumentation cable exits the PVC at a depth of 5.5 m (18 ft).

A record from a WES bar gage is shown in Figure 4a. This record contains one tensile reflection and a portion of a compressive reflection before cable failure occured. The unfolded wave form is shown in Figure 4b. The first and most obvious point to be addressed are the spikes present where each reflection begins. This can be attributed to a difference in the calculated round trip time of the input wave through the dump section and the actual round trip time. Figure 5a shows a theoretical bar gage record containing one tensile reflection. Recall that in order to unfold the data, the dashed curve in Figure 5b must be added to the original curve. The dashed curve represents the input wave multiplied times a reflection coefficient. Figure 5c shows the dashed curve shifted to the right. This represents a case where the calculated round trip time is greater than the actual round trip time. When the two are summed together a curve with spikes present is produced, such as the one shown in Figure 5d. The next point to be considered is whether or not the spikes present in the unfolded wave form are detrimental. One

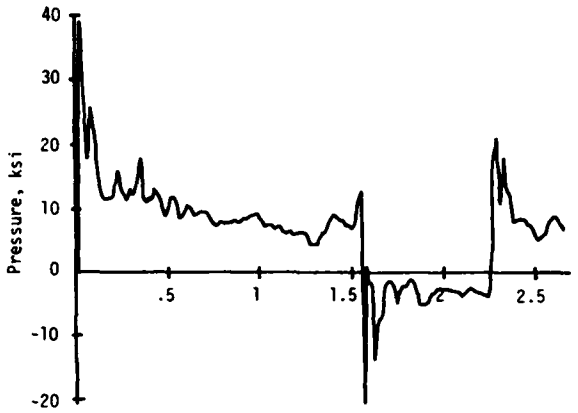

a. Airblast record from a WES bar gage

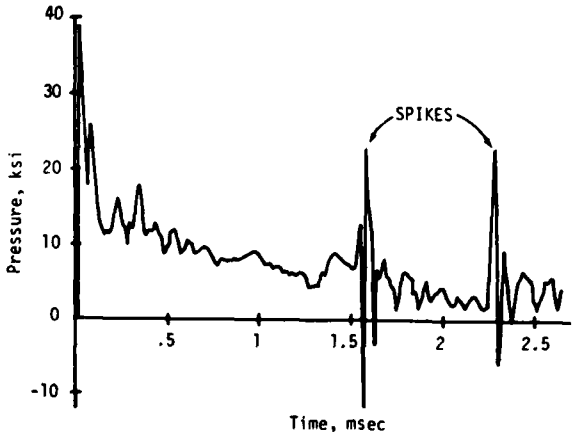

b. Unfolded airblast record

Fig. 4 - Bar gage data before and after the unfolding procedure

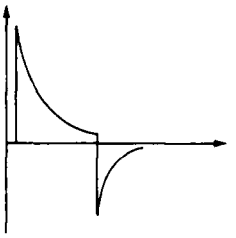

a. Measured stress

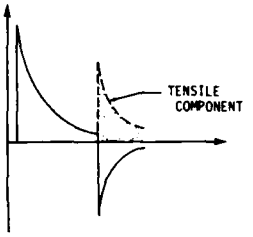

b. Curves summed to obtain unfolded wave form

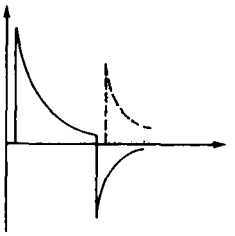

c. Tensile component is shifted

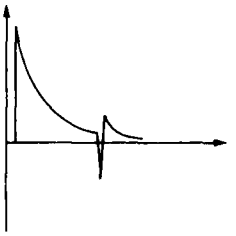

d. Spikes present in unfolded wave form

Fig. 5 - Graphical presentation of spikes produced during unfolding procedure

method of determining this is by looking at the integral of the wave form, that is, the impulse. Figure 6a shows the impulse of the original wave form. The sharp decrease in the impulse is due to the tensile reflection. The impulse of the unfolded wave form is shown in Figure 6b. The unfolded portion of the airblast record now produces an increase in impulse when the tensile reflection begins. Notice the general trend of the impulse curve is not severely effected by the presence of the spikes in the airblast record.

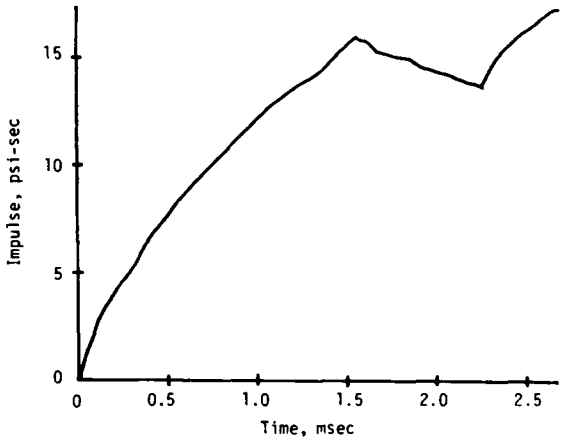

a. Impulse from bar gage record before unfolding

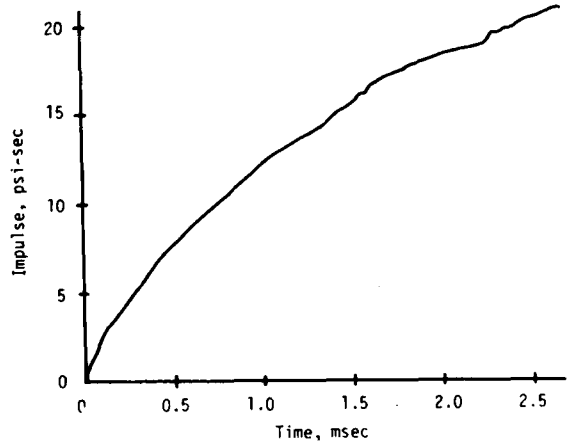

b. Impulse from bar gage record after unfolding

Fig. 6 - Airblast impulse data before and after the unfolding procedure

Another bar gage record is shown in Figure 7a. This record contains several tensile and compressive reflections. Notice in Figure 7b that the unfolded wave form has spikes present. The impulse of the original wave

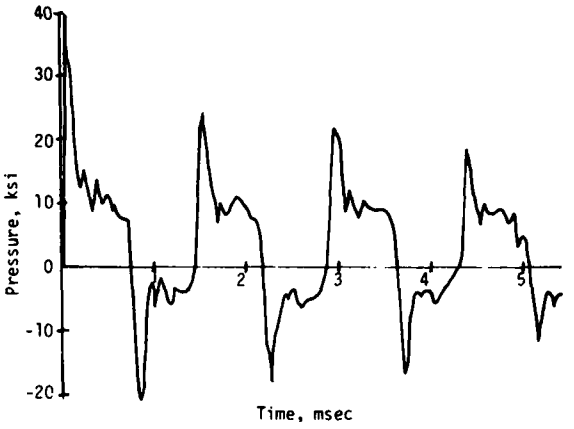

a. Airblast record from a WES bar gage

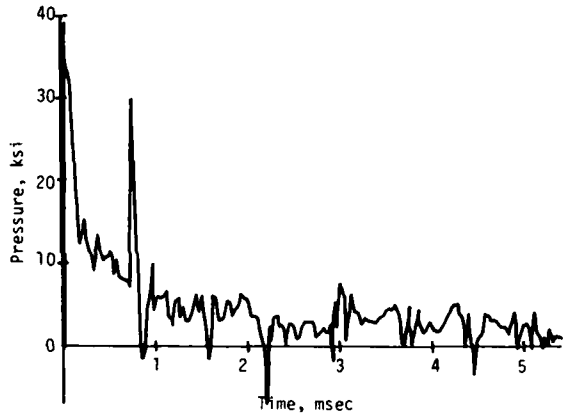

b. Unfolded airblast record

Fig. 7 - Bar gage data before and after unfolding procedure

form is shown in Figure 8a. The impulse generated from the unfolded wave form, shown in Figure 8b, indicates once again the general trend of the data is not effected by the presence of spikes. Hence the spikes are acceptable, although undesirable.

CONCLUSIONS

As was stated in the introduction, the purpose of this program was to extend the usable duration of the airblast record produced by the bar gage so early time impulse could be determined. Although more data is needed, the bar gage technique appears promising. It has been shown that the unfolding procedure presented here is a valid means of lengthening pressure impulse data obtained from Strain-gaged Hopkinson Bars.

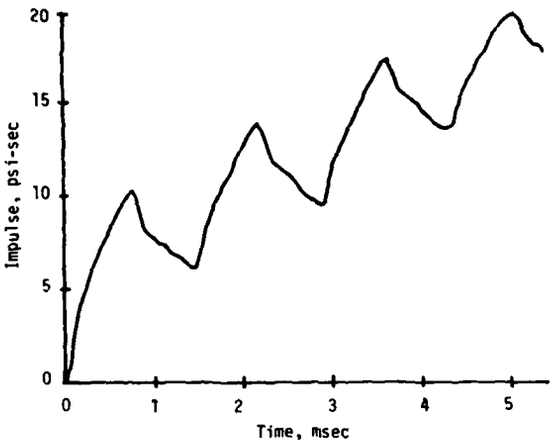

a. Impulse from bar gage record before unfolding

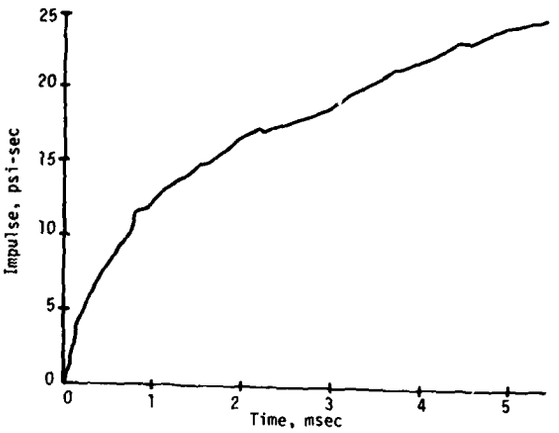

b. Impulse from bar gage record after unfolding

Fig. 8 - Airblast impulse data before and after the unfolded procedure

REFERENCES

1. Graff, Carl F., Wave Motion in Elastic Solids. Ohio State University: Ohio State University Press, 1975.

2. Private communication; Neil Baum, NMERI.

DISCUSSION

Mr. Chu (Endevco): What is the impact acceleration input to the bar?

Mr. White: 50,000 to 100,000 g.

Mr. Chu: Did you take the yielding of the bar into account? It was just a 1018 steel bar.

Mr. White: No. There is nothing significant about the 1018 steel except it was cheap, quick and easy.

Mr. Chu: We have a Hopkinson bar. At first we used a steel bar, but it yields at about 40,000 to 60,000 g . The yielding shows on the recordings.

Mr. Joachim: That doesn't significantly affect the results.

Mr. Chu: Is the bar reusable after that?

Mr. White: No. This is a one-time shot.

Mr. Serbyn (National Bureau of Standards): Did you use correlation analysis on these time histories?

Mr. White: In the abstract it said, "We will compare this to other impulse data from the same test." That is something that has not been done extensively. We are presently having trouble getting enough data quickly. We are also having some problem at higher testing levels with the column-base air blast gages, which Mr. Joachim and Mr. Ingram described, surviving these higher pressures, and we have a problem comparing that impulse with the impulse from the bar gage record. We haven't done an extensive comparison of impulse data at this time. But, that is something that this is developed for, and that is something that will be done.

DESIGN AND FIELD EXPERIENCE WITH THE WES 10KBAR AIRBLAST AND SOIL STRESS GAGE

Charles E. Joachim and Charles R. Welch
Research Civil Engineer and Research Physicist, Respectively
U. S. Army Engineer Waterways Experiment Station
Vicksburg, Mississippi

A family of shock transducers based on the classical load-cell geometry, i.e., the elastic compression of a column, is currently under development at the Waterways Experiment Station The transducers include an airblast gage, a soil stress gage, and a soil-structure interface stress gage These gages operate at considerably higher pressure ranges than previous elastic shock transducers. The airblast gage has provided long term (over 10 msec) measurements in blast environments of over 600 MPa (6 kbar). The soil stress transducer has made long term measurements of 400 MPa (4 kbar). The theoretical operating pressure range of the gages is approximately 1000 MPa (10 kbar) limited by the elastic limit of the gage body steel. The actual pressure range to date has been limited by acceleration induced failures of the strain gages and internal wiring. This paper describes the transducer development and presents some dynamic measurements produced from these gages.

BACKGROUND

A silo component test program was initiated at the Waterways Experiment Station (WES) in early 1983. The program has as its objectives proof test and development of silo components to survive in the close-in regions generated by a nuclear burst as simulated the High Explosive Simulation Techniques (HEST) tests. The lack of instrumentation to make measurements in the proscribed test environments for the silo components was recognized early as being a major technical problem for the program. Pressure transducers for monitoring long duration (over 10 msec) airblast in the HEST environment were of particular interest.

The highest pressure range HEST test where successful long duration airblast measurements have been made was a 103 MPa (15 ksi) HEST at about 50 KT yield simulation. These measurements were made with a Kulite 207 MPa (30 ksi) airblast gage using an 8-hole debris shield. Attempts to repeat these measurements at higher test levels or on subsequent HEST tests at the same pressure level were mostly unsuccessful. Short duration (<1.5 msec) HEST test airblast pressures up to 20 kbar have been measured with the S-Cubed bar gage. Thus, existing gages were not capable of making the high pressure long duration measurements required to define the HEST environment. This paper discusses the WES research effort to develop a long duration transducer capable of measuring airblast pressure and stress levels up to 10 kbar.

GAGES

The WES column based airblast (CBA) and column based stress gages were designed to respond in a linear elastic manner to loads in excess of 10 kbar This was accomplished by making the gages very stiff, removing as little as possible of the interior to accommodate the sensing elements and wiring. The CBA gage shown in Figure 1 is nominally 108 mm

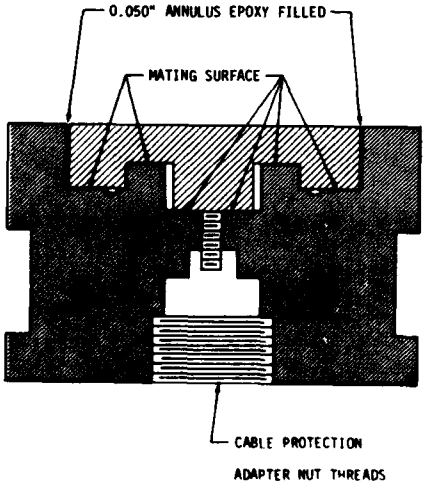

Fig. 1 - Schematic cross-section of WES Column Based Airblast (CBA) Gage

(4.25 in.) diameter and 68.6 mm (2.70 in.) high. The transducer consists of two pieces, a massive body and the smaller cap section which includes the strain gaged column sensing element. As shown in Figure 1 the two pieces are in intimate contact with a small annular void around the column. Mating surfaces are lapped to ensure uniform contact between the two pieces.

Foil strain (micro measurements Type CEA-06-062UW-350) gages are mounted on four flats milled into the column at 90° angles. A full bridge circuit is installed using two axial and two Poisson foil strain gages. Gage hook-up wires (36 gage teflon coated wire) are bonded to the column surface in the 2.54 mm (0.100 in.) annulus. Miniature solder techniques have been used to minimize the mass at connections to reduce acceleration effects. Cable connections are made in the base of the gage. Cables exit the gage inside 9.5 mm (3/8 in.) stainless steel tubing for cable protection.

The same design principles were applied to the CBS gage shown in Figure 2. This transducer has a nominal diameter of 127 mm (5.000 in.) and a thickness of 26.67 mm (1.050 in.) giving an aspect ratio of 4.76. The column diameter, 10.16 mm (0.400 in.), and the annulus around the column, 2.54 mm (0.100 in.), are identical in both the CBA and CBS designs. The cap thickness above the annular space is 2.54 mm (0.100 in.) in the CBS gage and the first CBA design. This dimension was later increased to the present 10.16 mm (0.400 in.) thickness for the CBA transducers. Semiconductor strain gages (Kulite S/UDP-350-160) were used for the CBS transducers.

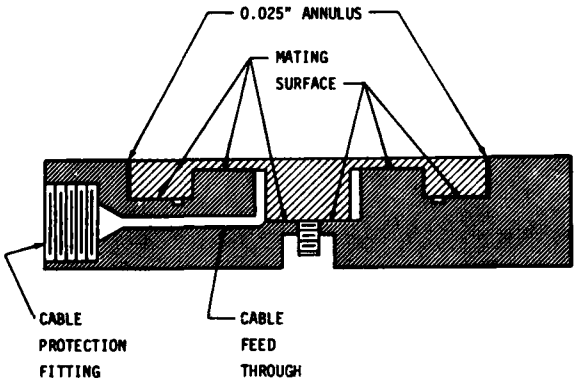

Fig. 2 - Schematic cross-section of WES Column Based Stress (CBS) Gage

DESIGN CALCULATIONS

Assuming the active area of the gage face to have a radius of (Figure 3)

$$R = (R_1 + R_2)12,$$

where:

R_1 = the radius of the outer wall of the annular space around the column, and
R_2 = column radius.

$$R = 11.43 \text{ mm } (0.450 \text{ in.})$$

The total load on the column for the maximum design pressure, P (10 kbar), will be;

$$F = P(\pi R^2)$$

$$= 41{,}879 \text{ kg } (92{,}245 \text{ lb})$$

Since there is a stud projecting from beneath the column the total load is carried by an area;

$$A = A_1 - A_2$$

where:

A_2 = area of the column, and
A_2 = area of the stud clearance hole.

Thus, A = 306 sq mm (0.4743 sq in.). Using these values the stress in the CBA and/or CBS gage column is computed to be;

$$\sigma = F/A = 136.9 \text{ kg/sq mm } (194.5 \text{ ksi})$$

Another failure mode in these gages is shear in the cap section around the column or in the material beneath the column. Let us first consider shear failure in the cap section. The CBA gage has a cap thickness T, (Figure 3) of 10.16 mm (0.400 in.). The shearing force is applied to the area of a ring with inside radius R, of 10.16 mm (0.400 in.) and outside radius R_2 of 12.7 mm (0.500 in.). This force is the applied pressure P (10 kbar), times the area of the ring;

$$F = P(2\pi(R_1 - R_2))$$

$$= 37{,}200 \text{ kg } (82{,}000 \text{ lb})$$

The area resisting this shearing force is;

$$A_s = 2\pi T_1(R_1 + R_2)$$

$$= 1{,}459 \text{ sq mm } (2.262 \text{ sq in.})$$

The calculated cap section shearing stress is;

$$\sigma_s = F/A_s = 25.51 \text{ kg/sq mm } (36.25 \text{ ksi})$$

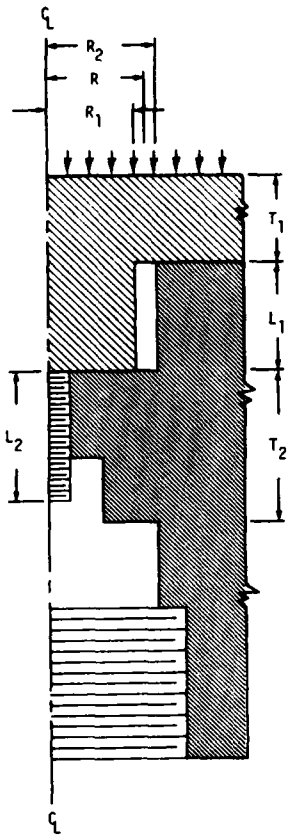

PARAMETERS

CBA

R_1 = 10.16 mm (0.400 in.)
R_2 = 12.70 mm (0.500 in.)
R = 11.43 mm (0.450 in.)
T_1 = 10.16 mm (0.400 in.)
T_2 = 17.78 mm (0.700 in.)
L_1 = 12.70 mm (0.500 in.)
L_2 = 15.24 mm (0.600 in.)

CBS

R_1 = 10.16 mm (0.400 in.)
R_2 = 12.70 mm (0.500 in.)
R = 11.43 mm (0.450 in.)
T_1 = 2.54 mm (0.100 in.)
T_2 = 11.43 mm (0.450 in.)
L_1 = 12.70 mm (0.500 in.)
L_2 = 8.26 mm (0.325 in.)

Fig. 3 - Design calculation parameters, WES column based airblast (CBA) and column based stress (CBS) gages

for the CBA gage. Since the cap radial dimensions are the same for both the CBA and CBS gages the shearing force is also the equal. The area resisting shearing of the cap is;

$$A_s = 2\pi T_1(R_1 + R_2)$$

where: T_1 is 2.54 mm (0.100 in.) for the CBS gage. The sheared area is calculated to be;

$$A_s = 364.8 \text{ sq mm } (0.5655 \text{ sq in.})$$

Using these values the calculated CBS gage cap shearing stress is;

$$\sigma_s = F/A_s = 102.0 \text{ kg/sq mm } (145.0 \text{ ksi}).$$

Now let us consider shear beneath the column. The force in the column (either CBA or CBS gage) is the total force on the column computer earlier;

$$F = 41{,}879 \text{ kg } (92{,}245 \text{ lb})$$

The area resisting this shearing force is;

$$A_s = 2\pi T_2 R_2$$

where T_2 is 17.78 mm (0.700 in.) in the CBA gage and 11.43 mm (0 450 in.) in the CBS gage. Therefore, the area resisting the shearing force in the CBA gage is;

$$A_s = 1{,}135 \text{ sq mm } (1.759 \text{ sq in.})$$

and the maximum shearing stress is;

$$\sigma_s = 36.90 \text{ kg/sq mm } (52.43 \text{ ksi})$$

beneath the column of the CBA gage. Similarly, the area resisting shearing forces beneath the column of the CBS gage is;

$$A_s = 729.7 \text{ sq mm } (1.131 \text{ sq in.})$$

and the maximum shearing stress is

$$\sigma_s = 57.40 \text{ kg/sq mm } (81.56 \text{ ksi})$$

Maximum design stress values are summarized in Table 1.

TABLE 1. MAXIMUM GAGE BODY STRESSES

	WES Gage Type	
	CBA	CBS
Axial Column Stress, kg/sq mm (ksi)	136.9 (194.5)	136.9 (194.5)
Cap Shearing Stress kg/sq mm (ksi)	25.51 (36.25)	102.0 (145.0)
Shearing Stress Beneath Column kg/sq mm (ksi)	36.90 (52.44)	57.40 (81.56)

MATERIAL

Initially gage bodies were machined from 1141 steel. This material was heat treated following machining. The gage bodies were normalized at 1575°F, reheated to 1500°F, oil quenched and tempered at 700°F. The treated steel had a Rockwell C hardness of approximately 42 and an approximate yield strength of 170 ksi. As HEST loadings were increased shear failures were experienced in the cap section around the column of the CBA gage. Cap thickness on these gages was 2.54 mm (0.100 in.). Two changes were made to overcome the problem:

(1) the cap thickness was increased by 7.62 mm (0.300 in.) to the present 10.16 mm (0 400 in.) as shown in Figure 1, and (2) 4340 steel was used in the manufacture of subsequent gages.

Loading properties of heat treated 4340 steel are shown in Figure 4.[1] Heat treatment for this material is normalized at 1600°F, oil quench and temper at 750°F. This procedure gives an approximate Rockwell C hardness of 42. As shown in Figure 4, the 750°F temper intersects the yield point curve at a yield stress of 200 ksi. Examination of maximum stress values in Table 1 shows stresses induced by the design load will not exceed the yield point of heat treated 4340 steel.

NATURAL FREQUENCY

An equation for the natural frequency of a column given by Graff[2] is:

$$f_n = (K^2/2\pi L^2)(EI/\rho A)^{1/2}$$

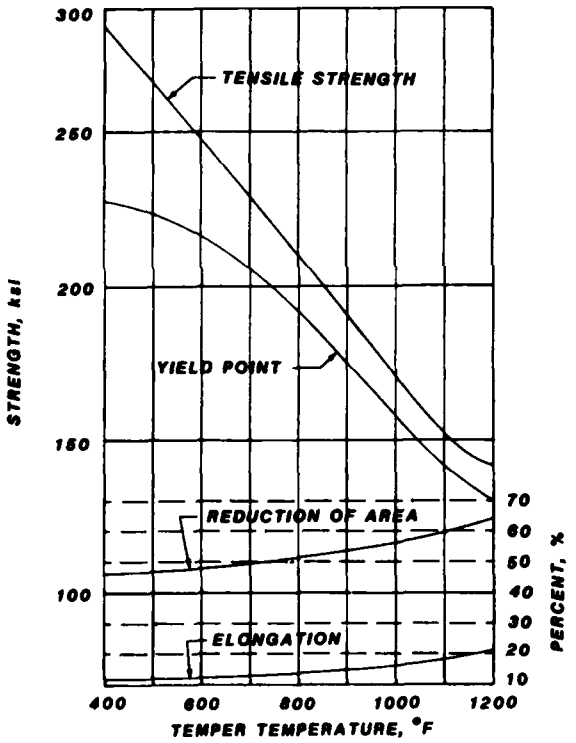

Fig. 4 - Properties of oil quenched 4340 steel. Treatment: normalize at 1600°F, reheat to 1475°F, and oil quench. Reference: "Modern Steels and Their Properties, Carbon and Alloy Steel Bars and Rods", Handbook 3310, Bethlehem Steel Corporation.

1 "Modern Steels and Their Properties, Carbon and Alloy Steel Bars and Rods," Handbook 3310, Bethlehem Steel Corporation.

2 "Wave Motion In Elastic Solids," Karl F. Graff, Ohio State University Press, 1975.

where K is a constant for a specified column end condition. Substituting:

$K = 4.73$ for fixed-fixed ends

$I = \pi R^4/4$

$A = \pi R^2$

$E = 2.04 \times 10^{10}$ kg/m^2 (29×10^6 psi)

$\rho = 800$ kg-sec^2/m^4 (15.22 lb-sec^2/ft^4)

Then $\delta_n(L^2R) = 8.99 \times 10^3$ m/sec (29.5×10^3 ft/sec). The other mode of vibration with waves bounding back and forth inside the column[2] is given by:

$$f_{nb} = C/2L$$

where $C = (E/\rho)^{1/2} = 5050$ m/sec (16,600 ft/sec). Then $f_{nb} = 2525/L$ (8282/L) For $f_{nb} < f_n$

$2525/L < 8990\ R/L^2$, L and R in meters, or

$8282/L < 29{,}500\ r/L^2$, L and R in feet.

$\therefore\ L < 3.56\ R.$

The column in the CBA and CBS gages has a length

$$L = 0.0127 \text{ m } (0.0417 \text{ ft})$$

and a radius, R = 0.0102 m (0.0333 ft).
Substituting in the above inequality:

$$L = 0.0127 < 0.119$$

$$f_{nb} < f_n \text{ and}$$

$$f_{nb} = 2525/0.0127 = 199 \text{ kHz.}$$

This is the lowest natural frequency of the column.

FIELD USE

All column based transducers are subjected to a fluid pressure calibration to check gage linearity and performance. Gages are routinely calibrated to 0.69 kbar with selected CBA gages loaded to 2.5 kbar. Selected CBS transducers are subjected to 3 kbar full face fluid pressure. Linearity is determined from a first degree least square goodness of fit calculation. Gages are rejected when the goodness of fit coefficient is less than 0.99.

Free-field HEST test placement of the CBA transducer is depicted in Figures 5 and 6.

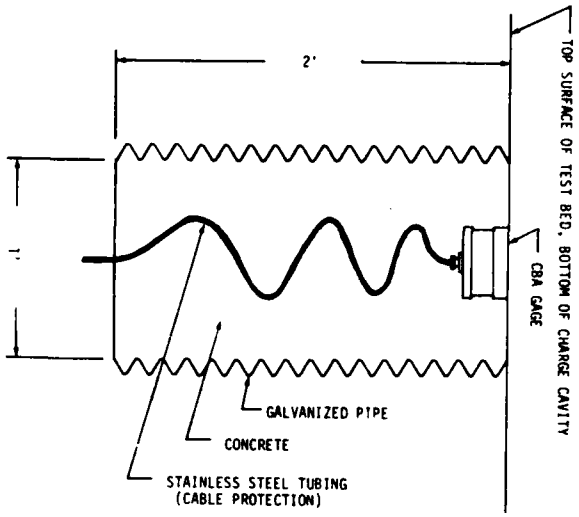

Fig. 5 - Typical CBA free-field surface flush installation

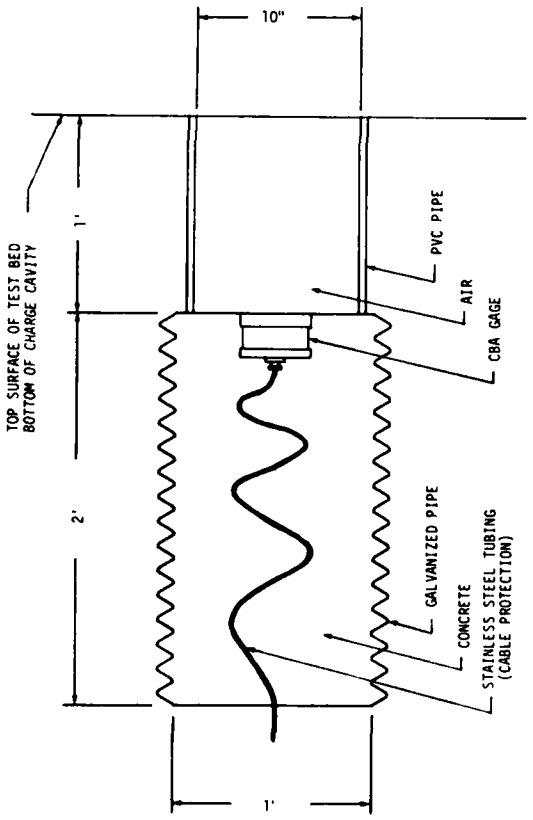

Fig. 6 - Typical CBA free-field recessed installation

Mounting in a concrete plug provides increased mass and inertia. Thus, the assembly resists early time movement by the very high pressure forces acting on the upper surface of the HEST test bed. Final gage mount displacements on the order of 2 m (6.6 ft) or greater occur at late time after the HEST charge cavity has begun venting.

Free-field CBA transducers were placed as shown in Figure 5 at the beginning of the test program. As charge yields and pressure levels were increased gage survivability decreased. After changing to 4340 steel, failures were primarily due to acceleration loadings on the internal strain measuring circuit. During this period some measurements were made by burying the gage-concrete assembly 0.3 m (1 ft) below the surface of the test bed. A recent improvement on this technique is shown in Figure 6. Here the sand backfill between the gage and the charge cavity has been replaced by a 0.25 m (10 in.) diameter air column. There are no data which indicate the effect on the magnitude of the peak pressure measurement. There is no doubt that high frequency pressure spikes are reduced or eliminated. Results to date indicate this technique has not significantly influenced total impulse at the surface of the test bed.

Typical HEST test beds are constructed by excavating a pit, then refilling the cavity with a controlled density backfill. Most of the testing to date with column based gages has been in sand backfilled test beds. The CBS gage is placed in the free-field as the backfill reaches the desired gage elevation. Care is taken to maintain the required backfill density around the gage. Stainless steel tubing is used to protect cables throughout the backfill.

SIGNAL CONDITIONING

The CBA and CBS gages were operated with constant current (10 ma) sources. The amplified signals were recorded on magnetic tape recorders operated in the FM mode. Overall frequency response of this system was 10 Khg.

MINI HEST RESULTS

A series of Mini-HEST tests were conducted to evaluate changes in CBA gage construction methods which might increase the survivability. The Mini-HEST test consists of a 0.915 m × 0.915 m × 0.152 m (3 ft × 3 ft by 6 in.) charge cavity with 1.22 m (4 ft) of masonry sand overburden. Four candidate CBA gages were tested at a time. All tests were designed to produce 379 MPa (55 ksi) overpressure or higher, with individual HE test charge densities ranging from 131 to 236 kg/m^3 (8.2 to 14.7 lb/ft^3). Four gages were grouted in a block of quick set grout as shown in Figure 7. The grout block was 45.7 cm (18 in.) deep.

A Mini-HEST test was conducted 9 August

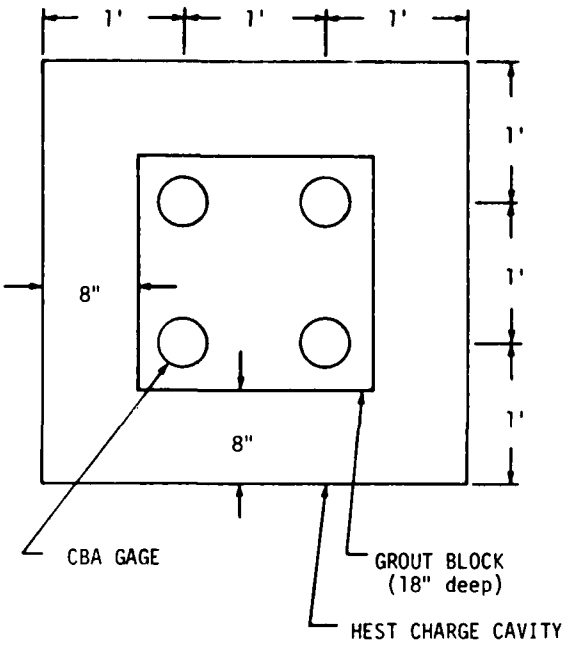

Fig. 7 - Mini-HEST CBA gage layout

1983 and used a charge density of 131 kg/m^3 (8.2 lb/ft^3) of Iremite 80. The Iremite 80 has about 12 percent more energy release (according to the manufacturer) than the Iremite 60 used in full scale HEST tests. The purpose of the first test was to insure that we could simulate the early time (0 to 2 msec) airblast loading generated in full scale tests and to test two types of lead wire tie down fabrication methods.

The gages were driven downward 2.1 m (6.9 ft) with two gages surviving post-shot. One CBA gage suffered internal wiring failure. The second gage failed as a result of a seating problem between the gage body and sensing element which allowed the hot explosive products inside the gage. All gage bodies behaved elastically throughout the test (i.e., no indication of plastic deformation of the gage). Successful airblast records produced by the test are shown in Figures 8 and 9. High noise levels were produced by gain settings on the tape recorder, required because foil strain gages were used to construct these gages. Peak airblast pressures of 177 MPa (25.6 ksi) and 207 MPa (30 ksi) were recorded from these gages.

The second Mini-HEST test subjected the CBA gages to a higher early time loading to determine if potting the annulus around the column would increase survival without degrading the recorded waveforms. The same charge density was used but the Iremite 80 was redistributed in the cavity so that the top layer was a solid layer of explosive. The gages were driven down 1.1 m (3.7 ft). Two gages produced reasonable pressure waveforms as shown in Figures 10 and 11.

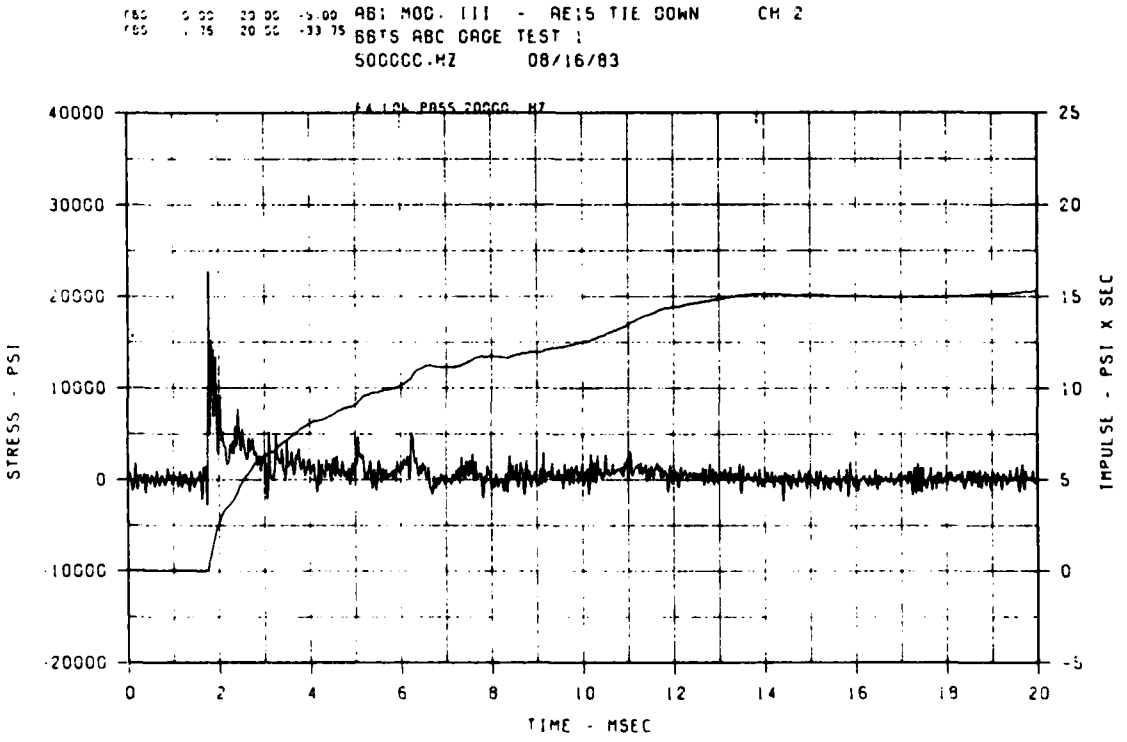

Fig. 8 - Mini-HEST CBA overpressure measurment, Test 1

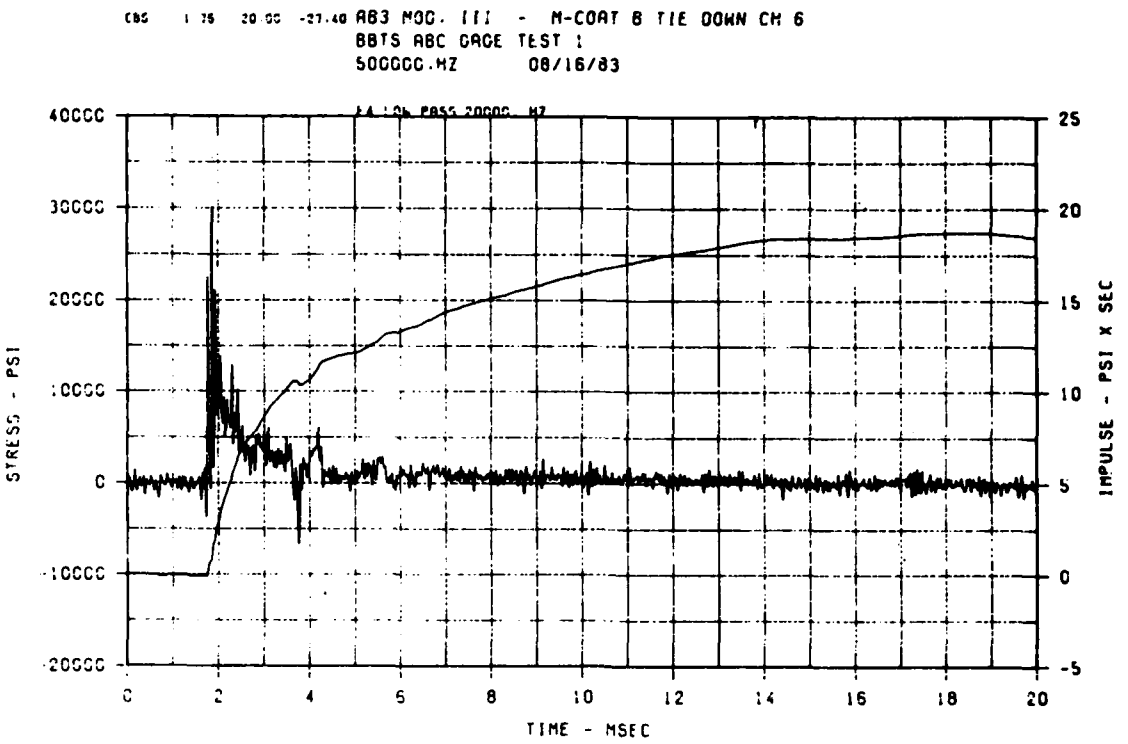

Fig.9 - Mini-HEST CBA overpressure measurement, Test 1

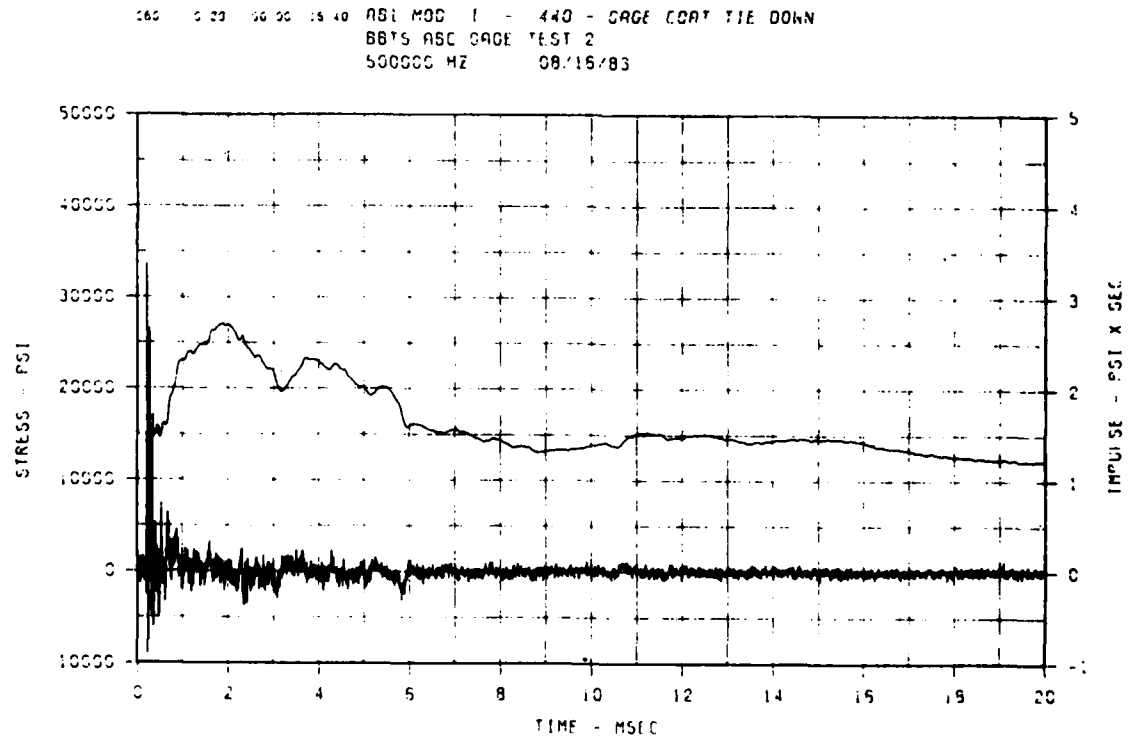

Fig. 10 - Mini-HEST CBA overpressure measurement, Test 2

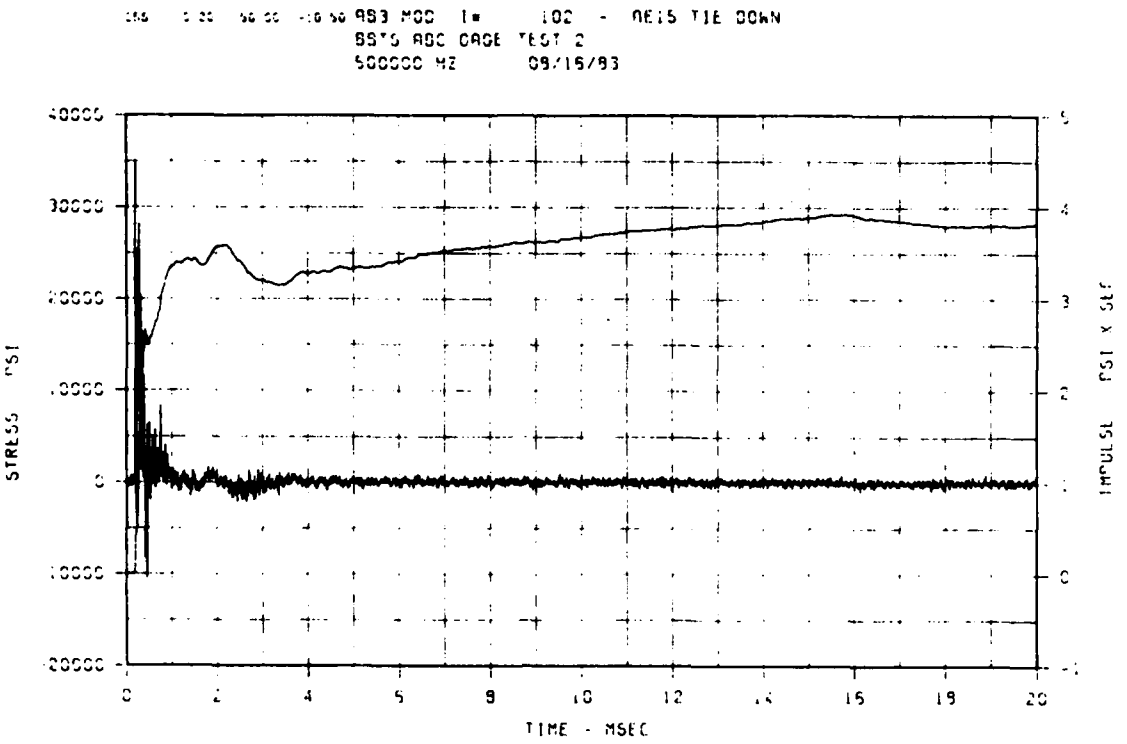

Fig. 11 - Mini-HEST CBA overpressure measurement, Test 2

These gages indicate slightly higher peak pressures (233 and 241 MPa (33.8 and 35 ksi)) than the first test but lower impulse values. One of the surviving gages was an earlier design with a T_1 value (Figure 3) of 2.54 mm (0.100 in.) and was machined from 440C stainless steel. An arc section broke off the outer edge of this gage body but the broken area did not pierce the gage cavity or damage the sensing element. The two gages which were potted (one with BI-WAX, the other with AE-15 epoxy) both failed electrically with one strain gage showing an open circuit in each gage. The three 4340 steel gage bodies show no indication of plastic deformation.

Mini-HEST Test 3 provided the most severe environment to date. The test configuration was similar to the first two except the charge cavity depth was increased to 20 cm (8 in.) (15 cm (6 in.) in earlier tests). The explosive (Iremite 60) was configured to yield a charge density of 236 kg/m^3 (14.7 lb/ft^3) and the overburden was increased by 2 ft laterally to prevent early time venting. All CBA gages were identical with 4340 steel and a soft adhesive (M Coat B) used to tie down internal circuit wiring. All four gages were overturned and driven downward 2.1, 2.1, 2.3, and 2.5 m (6.8, 6.8, 7.7, and 8.2 ft), respectively. Explosive gasses invaded the strain gage cavity destroying strain gages and/or connecting circuits of all four gages. Although these gages failed electrically the 4340 steel bodies survived with no indication of material failure. CBA fabrication procedures now include filling the annular space (as shown in Figure 1) with quick setting (5 minute) epoxy to prevent explosive gasses and/or calibration fluids from invading the sensor cavity.

Several CBA gages were sent to three commercial gage manufacturers for strain gaging and circuit shock hardening. The firms were Kaman Sciences (KSC), Kulite Semiconductor (KUL), and Micro Gage (MG). One CBA gage assembly by KUL, two by KSC and one by WES were included in Mini-HEST Test 11. An Iremite 60 charge design with a density of 184 kg/m^3 (11.5 lb/ft^3) was used. One CBA (KSC) gave a reasonable overpressure time history (Figure 12) indicating 294 MPa (42.6 ksi) peak pressure. The second KSC gage measured a peak value of 305 MPa (44.2 ksi) but failed at approximately 150 μsec after shock arrival. Post mortem indicates an internal circuit connection open and one strain gage tab failed at the glue line. The KUL assembled gage measured 632 MPa (91.7 ksi) (Figure 13) approximately twice the other peak values and is therefore questionable. Gage autopsy indicates failure at the cable connection in the base of the gage. The WES assembled CBA failed within microseconds of shock arrival and produced no useful data.

ADVANCED SILO HARDNESS RESULTS

The advanced Silo Hardness (ASH) Test Program is being conducted by the WES for the

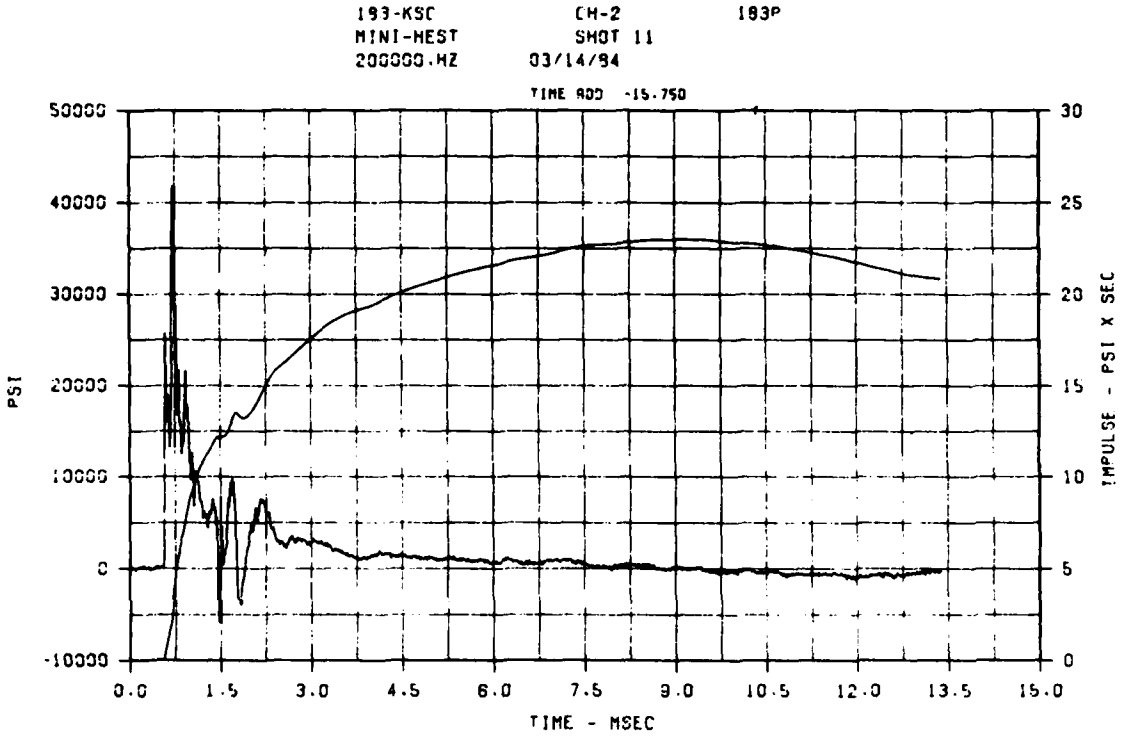

Fig. 12 - Mini-HEST CBA overpressure measurement, Test 11. Gage assembled by Kaman Sciences

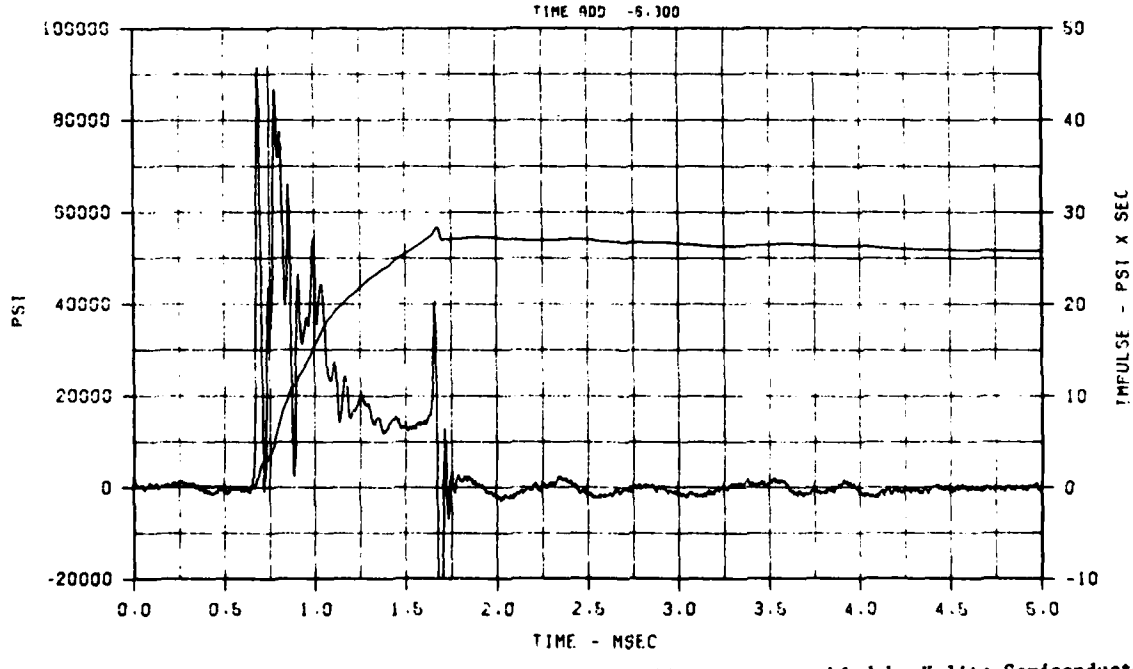

Fig. 13 - Mini-HEST CBA overpressure measurement, Test 11. Gage assembled by Kulite Semiconductor

Defense Nuclear Agency (DNA), Department of Defense (DOD) with testing at Ft. Polk, LA. Results from the ASH Reflection Cube Test (RCT-1) will be discussed herein. The RCT-1 Iremite 60 HEST charge is designed to provide a 244 MPa (50 ksi) peak overpressure above the 11 m by 11 m (36 ft by 36 ft) test bed. Airblast pressure measurements were unsuccessful. However, 25 successfull soil stress time history measurements were made at depths ranging from 0.3 to 1.8 m (1 to 6 ft) below the surface of the test bed.

A comparison of three CBS soil stress measurements at 0.3 m (1 ft) depth and at three different horizontal distances from the test bed centerline (0, 1.8 m (6.0 ft) and 3.7 m (12 ft)) is given in Figure 14. Although the peak data range from 121 MPa (17.6 ksi) to 184 MPa (26.7 ksi) the waveforms are reasonably consistent. The peak data scatter can be the result of variations in gage performance, soil density or HEST charge generated pressures. A similar plot for CBS gages at 0.6 m (2 ft) depth (Figure 15) shows good agreement of both peak data and waveforms.

Soil stress waveform variation with depth is shown in Figure 16. These gages are located at a horizontal distance of 1.8 m (6 ft) from the centerline and at depths ranging from 0.3 m (1 ft) to 1.2 m (4 ft). Here we see a broadening of the initial peak until at 1.2 m (4 ft) a reflection clips the peak.

CONCLUSIONS

The capability for peak overpressure

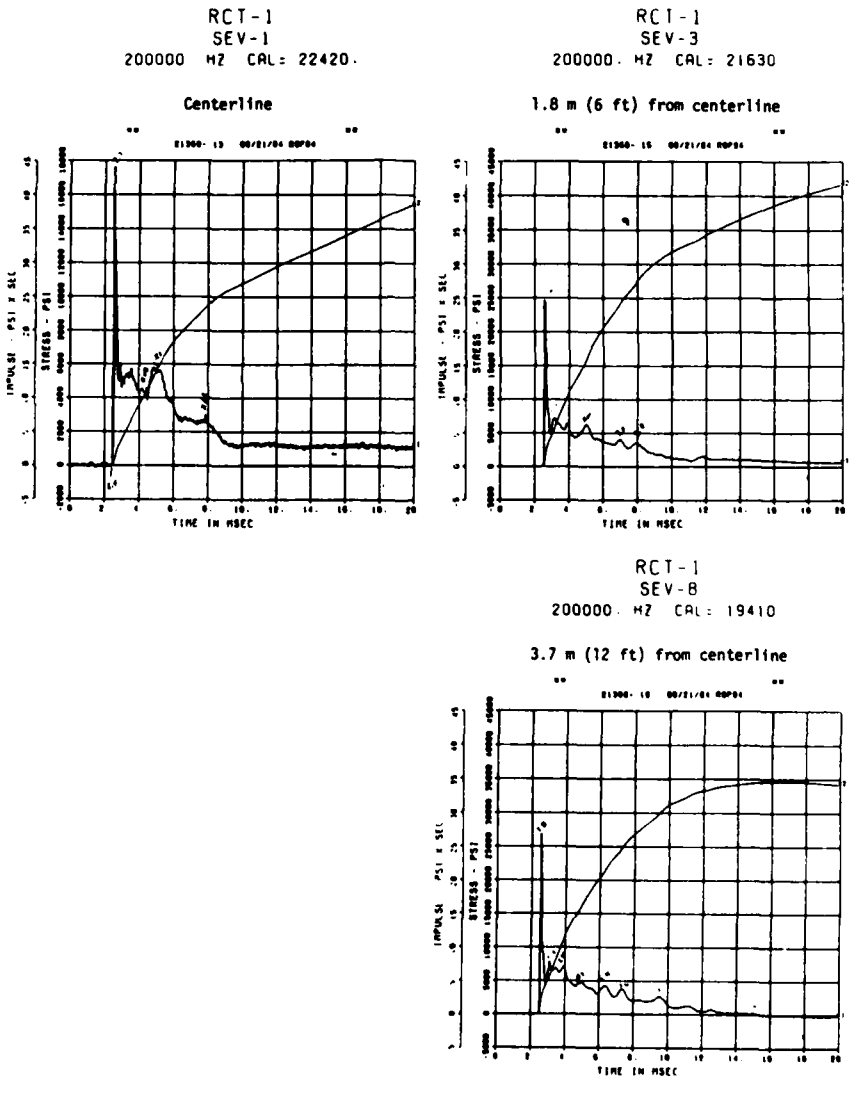

Fig. 14 - Comparison of CBS gage soil stress measurements at 0.3 m (1 ft) depth

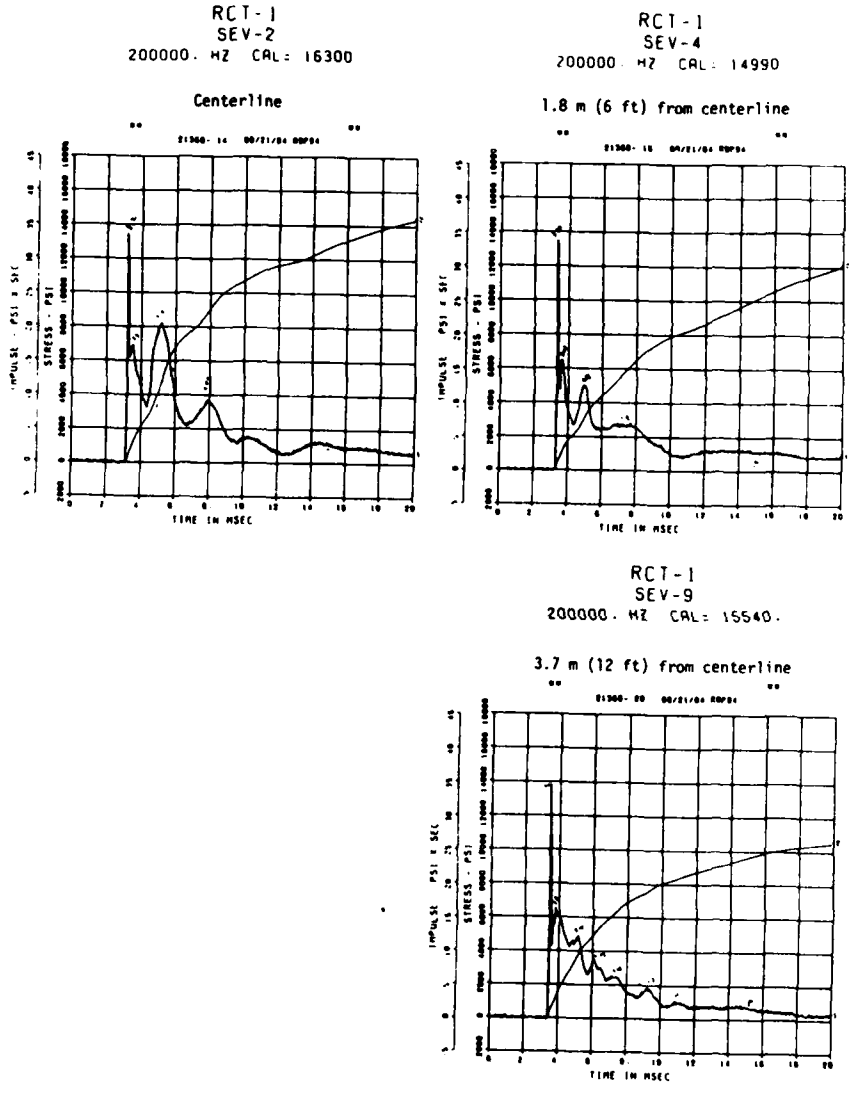

Fig. 15 - Comparison of CBS gage soil stress measurement at 0.6 m (2 ft) depth

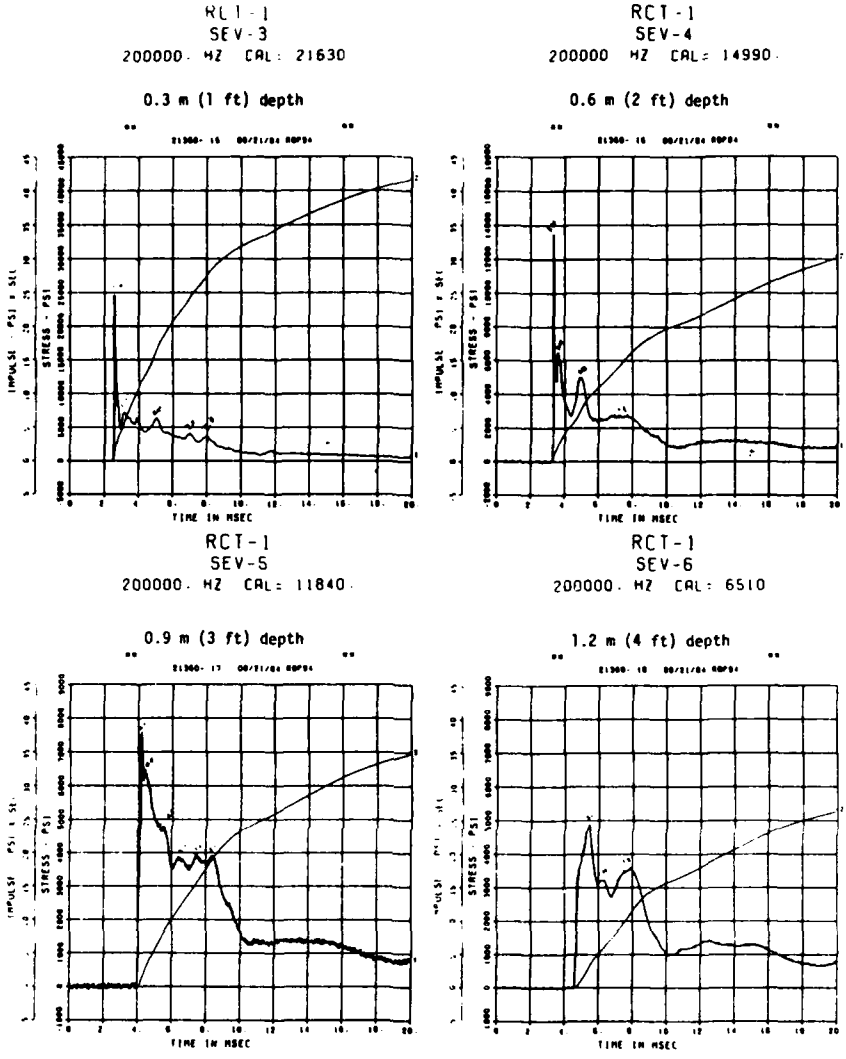

Fig. 16 - Comparison of CBS gage soil stress measurements at 1.8 m (6 ft) from centerline

measurements to at least 290 MPa (42 ksi) has been shown. These are high risk measurements. Losses of data are no longer attributable to failure of the gage body (steels). Rather, it is due to failures of strain gages and internal circuit components such as hook up wire, solder joints, etc. These items fail under the high accelerations associated with the high pressures close-in to the HEST detonation.

Peak soil stresses of at least 180 MPa (26 ksi) have been successfully measured with the WES CBS gage. These gages have been more successful mainly because the soil filters out the high frequency spikes associated with the surface airblast pressures close-in to the HEST charge. Therefore, the CBS gages do not experience the high g acceleration loadings which are causing failures of the CBA gage.

Work is continuing to harden failure sensitive components of both gage types. Ongoing static and dynamic testing of improved versions of these gage designs should result in acceptable gage performance levels that can then permit the designs to be commercialized within the near future.

DISCUSSION

Mr. Favour (Boeing Aerospace Company): What acceleration levels are you typically experiencing with those gages?

Mr. Joachim: We don't know for sure. We suspect something on the order of 100,000 g.

FLUID-STRUCTURE INTERACTION

STRUCTURAL RESPONSE OF PANELS SUBJECTED TO SHOCK LOADING

R. Houlston and J.E. Slater
Defence Research Establishment
Suffield, Ralston, Alberta, Canada

In combat operations, warships could be subjected to air blast and underwater shock loads capable of causing significant local damage. As part of a vulnerability and survivability study, this paper will concentrate on the prediction and measurement of the structural response of ship panels to free field air-blast explosions. Experiments with steel plates and a full scale stiffened panel are described in detail. Finite element modelling results are presented with a detailed correlation to experiment.

1. INTRODUCTION

Metal plates or panels are fundamental elements in many military structures. Ships, in particular, are composed primarily of stiffened metal panels that make up the hull, decks, bulkheads, and superstructure. In modern warfare, naval ships could be subjected to considerable air blast and underwater shock loads. Two distinctive types of response are induced by these loads. One is a local response of the ship panels and attached structure and equipment, while the other is a global response involving the whole ship in an overall flexural or whipping form of vibration. For effective warship design against air blast and underwater shock threats, a fundamental and detailed understanding of shock wave loading and the associated structural response is required. Knowledge in this area is also required for assessments of vulnerability and survivability of structures subjected to shock loading.

In recognition of these requirements, the Defence Research Establishment Suffield (DRES) has initiated a research program into shock wave-structure interaction to advance the state-of-art in structural response to air blast and underwater shock loading. Finite element codes are under development to predict the elastic and plastic structural response. Experimental tests have been carried out to measure the response and damage levels and to verify the computer code predictions.

This paper will present the prediction and measurement of the structural response of square plates and a Tee beam stiffened panel subjected to free field air-blast explosions. A ship is composed of a large number of such panels which may interact structurally with other components in a complicated way. To meaningfully isolate a particular ship's panel for analysis involves knowing reasonable boundary conditions to apply. These conditions could only be determined exactly by knowing how the rest of the ship structurally responds to a blast wave.

A typical ship's panel consists of a series of simple panels connected by beam stiffeners as shown in Fig. 1. As a preliminary step to the testing and analysis of the stiffened ship panel, a series of square plates were first tested. This testing sequence was then followed by the testing of a stiffened ship panel.

Figure 1. Photograph of Stiffened Panel

Both the stiffened panel and the square plates were mounted with the intention of approximating built-in boundary conditions. Built-in boundary conditions constitute a simplifying assumption in that: a) A panel with this type of boundary

condition can be mounted with relative ease for practical testing purposes; b) This case is readily defined in computer codes; c) Restricted variations from the idealized condition of a built-in boundary can be made both in practice and in computer codes for sensitivity studies with respect to the results from the idealized case.

In addition to the displacement and rotation boundary conditions on the panel edges, the blast pressure loading must be known. During the tests this was measured with pressure transducers just outside the boundary of the target panel.

In addition to boundary conditions, the panel response is also dependent upon the constitutive behaviour of the panel material. In the elastic range, Young's Modulus and Poisson's Ratio are sufficient provided the material response to stress is isotropic. In the plastic range of response, both the dynamic yield stress and strain hardening characteristics are required as additional information.

Since the amount of information that can be directly measured with transducers is limited, work is currently underway to correlate transducer outputs and plastically deformed profiles to computer code predictions. This procedure will enhance the interpretation of experimental results for the plates and stiffened panel. It will also provide valuable verification of the computer codes prior to the application of these codes to more complex problems that may involve an assemblage of panels.

This paper will present finite element and experimental results for both the square plates and stiffened panel subjected to air-blast loading. In Section 2, the experimental testing and finite element modelling of the square plates will be presented. Detailed correlations for the elastic response with finite element predictions will be made. Experimental and finite element results will also be presented for the case of severe plastic distortion. In Section 3, the results from experimental tests on the stiffened panel will be presented together with the results of finite element calculations for the elastic response.

2. SQUARE PLATES

2.1 Introduction

The main objective of the tests described in this section is to provide fundamental information on the structural response of a square plate with built-in boundary conditions to spatially uniform air-blast loadings with various magnitudes and durations. These tests provided an assessment of the performance of the pressure, acceleration, and strain transducers over a range of blast wave conditions. In addition, some preliminary checking of the computer code predictions with experimental results could be made.

2.2 Experimental Procedure

The trials were done in two series. The first series was done in the DRES Blast Chamber, which is essentially a room of dimensions 6.1 m × 6.1 m × 6.1 m with reinforced concrete walls, floor and ceiling (as shown in Fig. 2). The charges were suspended between 2 and 3 m above the target prior to detonation. The blast chamber facility had the advantage of providing a protected environment for assembly of the equipment and mounting and testing of transducers. However, charge size was limited to a maximum of 1 kg of high explosive. This size restriction limited the blast loading to about 700 kPa at 2 m standoff.

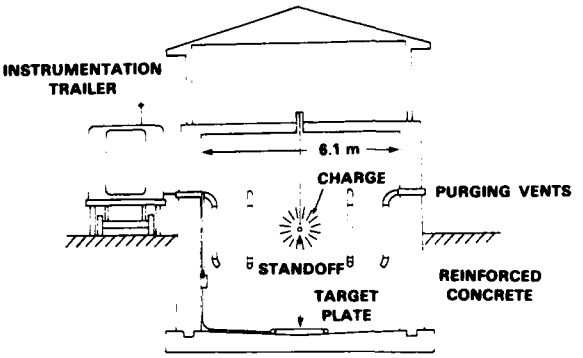

Figure 2. Blast Chamber Facility

The second series of trials was carried out at the Height-of-Burst (HOB) site on the DRES experimental range (Fig. 3). In this series, charges of 14.5 kg were suspended at standoff distances of 2.4 and 3.1 m.

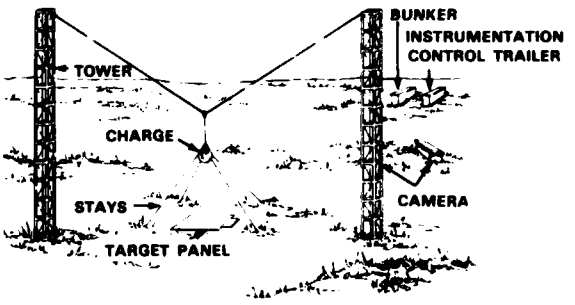

Figure 3. Height-of-Burst Site for Air-Blast Response Trials of Structures

2.3 Equipment and Instrumentation

Figure 4 shows the details of the plate mounting frame used in test series 1 and 2. The mounting frame consisted of four steel box beams which were

clamped to a base plate seated on the ground. The target plate was bolted to the box beams through the extension panels containing pressure transducers (PCB 113A24) mounted around the periphery. The arrangement was designed with the object of a) providing a rigid base for the plate, b) simulating as close as possible built-in boundary conditions for the plate, and c) providing an arrangement that would lead to a uniform pressure being applied to the plate during the time of significant structural response. The effective dimensions of all the plates were 508 mm × 508 mm (20″ × 20″). Plate thicknesses of 3.4 mm and 1.5 mm were used.

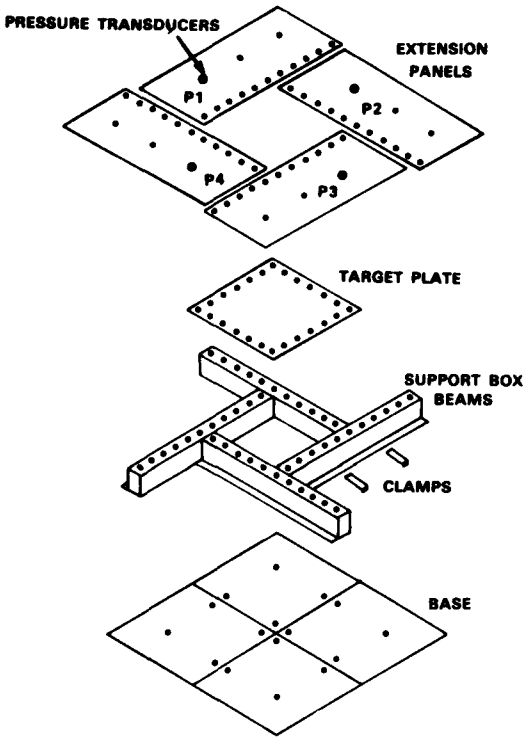

Figure 4. Exploded View of Plate Mounting System

Figure 5 shows a photograph of the target plate mounted in the Blast Chamber. The extension panels partly simulate an infinite boundary surface for the plate. They also increase the time lapse between the "free field" air-blast wave and the reflected air-blast waves from the walls of the chamber.

Figure 6 shows the transducer layout for the plate used in test series 1. Accelerometers (Endevco piezoresistive 2264) and strain gauges (CEA-06-W250A-120) were used. Transducer signals were recorded in analog form on magnetic tape in an instrumentation trailer (see Fig. 2 and Fig. 3). Prior to each test, a calibration voltage pulse was passed through each transducer for use in the signal processing of the results.

Figure 5. Photograph of Square Plate Mounted in Blast Chamber

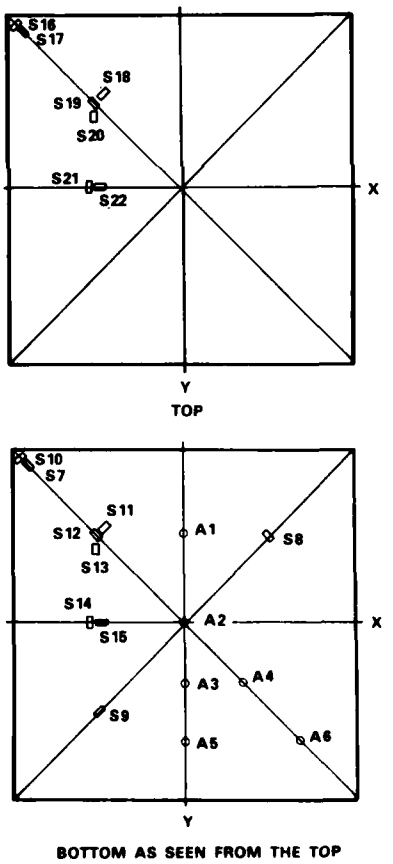

Figure 6. Strain Gauge (S) and Accelerometer (A) Positions for Test Series 1

2.4 Tests and Signal Processing

Table 1 outlines the significant parameters that were involved in the Blast Chamber tests all of which were done on the same plate. Test series 1 involved seven tests with instrumentation as outlined in Section 2.3. These tests were done with increasing charge mass to increase the pressure loading on the target surface. Pressure, acceleration, and strain were recorded in analog form and subsequently digitised at 50 kHz for pressure and acceleration, and 25 kHz for strain. A signal processing computer program was then written to enable the results to be studied. The signal processing program included the following capabilities:

1. Analysis of the pressure transducer waveforms to obtain the average pressure pulse arrival time, the positive phase duration, the peak overpressure, the rise time, the decay rate, and the maximum impulse.

2. Integration of the measured acceleration to obtain velocity and displacement with correction for baseline drift.

3. Fast Fourier transform analysis with optional filtering for any transducer output.

4. Automatic generation of a load file from the pressure transducer signals for a selection of finite element computer programs.

5. A general plotting capability for presentation of experimental results with the option of plotting finite element code predictions.

Table 1

SUMMARY OF THE BLAST CHAMBER TESTS WITH THE SQUARE PLATE

(Plate Thickness 3.4 mm)

TEST*	CHARGE MASS (g)	CHARGE STANDOFF (cm)	OVER PRESSURE (kPa)	PULSE DURATION (ms)
1	113	305	55.0	2.0
2	227	305	79.0	2.0
3	227	305	82.7	2.0
4	397	244	172	2.0
5	908	305	207	2.0
6	908	305	207	2.0
7	908	200	689	1.5

* All tests done on the same plate.

2.5 Discussion of Results

All tests for series 1 were done on a plate of thickness 3.4 mm and are summarized in Table 1. Tests 1 to 4 involved elastic response. The blast pressure loading had an approximately linear decay over typically 2 ms. Under these conditions essentially no permanent deformation on completion of the tests was found for peak pressures below 200 kPa. However, for pressure in excess of 200 kPa, very mild permanent central deflections of the plate were found (tests 5 to 7). Typically, about 0.3 mm permanent central deflection was found at 207 kPa peak pressure. At the maximum peak pressure loading of 689 kPa, about 1 mm permanent central deflection was found. In test series 2 (see Section 2.10), very large permanent deflections were observed.

The transducer time history signals were satisfactory. In the case of acceleration it was found that the high frequency response of the accelerometers necessitated filtering at 10 kHz.

Figure 7 shows a typical pressure transducer trace for test 1. The pulse profile from 1 to 7 ms shows a typical blast wave profile consisting of a positive phase of approximately 2 ms and a negative phase of about 5 ms. At approximately 7 ms a second shock was detected. This shock was identified as the reflection from the walls of the Blast Chamber. Many further reflected shocks were subsequently received.

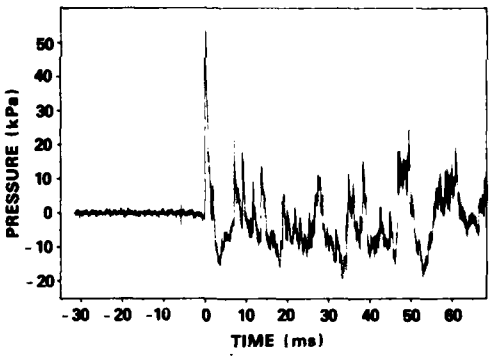

Figure 7. Plot of Pressure against Time for the Transducer P2

Figure 8 shows a typical acceleration trace from the acceleration transducer A2 at the centre of the plate. Double integration of the acceleration to obtain the displacement revealed a parabolic baseline drift of the displacement trace. This shape of drift would result from a constant offset of the acceleration trace. To determine an offset for correction of the acceleration baseline, thereby to remove the displacement drift, the following procedure was used: a) Fit a least-squares second degree polynomial (quadratic) to all the data points on the displacement trace; b) Differentiate the resulting polynomial twice to obtain the constant term (acceleration offset); c) Apply the offset to the acceleration data; and d) Re-integrate the modified

acceleration to obtain the corrected velocity and displacement. Over the range of 68 ms shown in Fig. 8, it was estimated by the technique outlined above that approximately a shift in the acceleration of 2G was necessary to correct for the displacement drift (approximately 50 mm at 68 ms). Application of the shift to the acceleration trace and a re-integration then gave the velocity and displacement traces shown in Figs. 9 and 10, respectively. These traces are a considerable improvement over the uncorrected ones. The fundamental frequency of vibration shown by the displacement curve is in reasonable agreement with the theoretical value of 118 Hz.

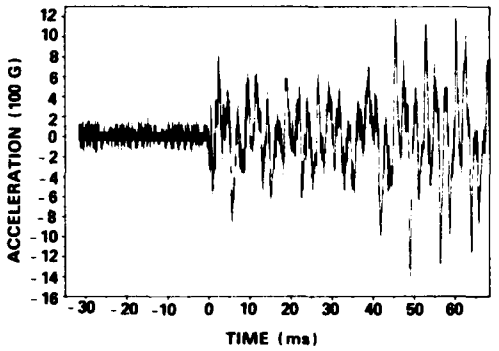

Figure 8. Plot of Acceleration against Time for the Transducer A2

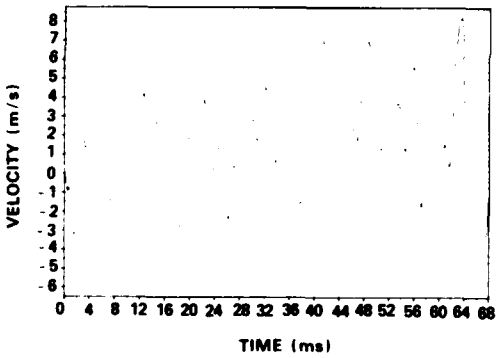

Figure 9. Velocity against Time from Integration of the Corrected A2 Signal

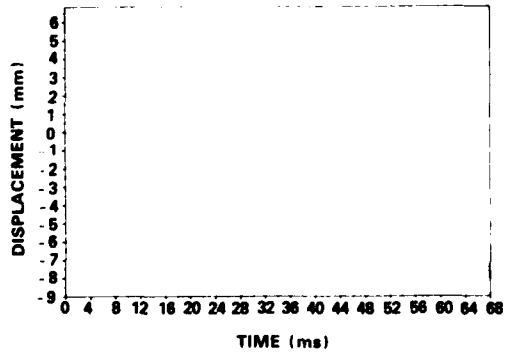

Figure 10. Displacement against Time from Double Integration of the Corrected A2 Signal

2.6 Construction of a Finite Element Model

In order to compare the elastic plate response from test series 1 with computer code predictions using the VAST computer code [1] for linear analysis, a finite element model of the plate was developed. Figure 11 summarizes the model. The model consists essentially of a square plate receiving a spatially uniform pressure wave. The boundary conditions are taken as fixed. The elements shown in Fig. 11 are parabolic shell elements. The number of elements and the distribution of element sizes were varied for optimization purposes in the numerical studies undertaken.

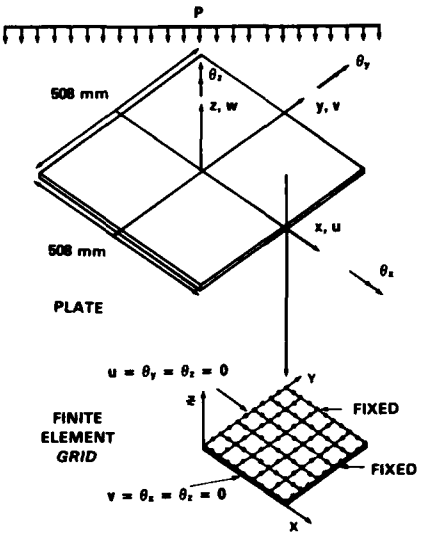

Figure 11. The Finite Element Model of the Plate

To provide some verification of the finite element model being considered, a series of mode shapes were computed with the VAST code using both the direct iteration and subspace iteration methods [2]. The mode shapes and frequencies were similar in both cases on noting that modes associated with multiple eigenvalues may not be unique. In addition, an HP 5432A Structural Dynamic Modal Analyzer was used to experimentally determine the mode shapes and frequencies [3]. For this purpose, a single accelerometer sensor was magnetically attached to the plate at a grid point 101.6 mm and 152.4 mm from adjacent sides. The plate was then struck with a hammer at a series of grid points. The Modal Analyzer was then able to resolve the vibration modes from the sequence of accelerometer signals received.

The results from the finite element calculations and the Modal Analyzer are presented in Fig. 12. The results indicate that the finite element model is able to approximate all the experimental mode shapes that were determined. There was also good agreement of the finite element and experimental frequencies.

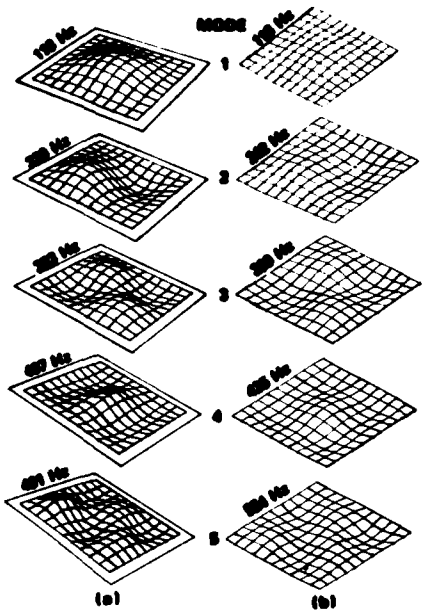

Figure 12. Mode Shape Patterns for Square Plate from (a) Modal Analyzer Tests and (b) VAST Program Predictions

Since the pressure loading function was considered to be spatially constant, only one quarter of the plate needed to be considered for the dynamic response calculation. Figure 13 shows the type of grid that was considered for a quarter plate. As indicated in the figure, a geometric series factor r was introduced to systematically adjust the element sizes to achieve the optimum accuracy. The basic purpose of this type of element size distribution was to allow the elements near the fixed boundaries and at the plate centerlines to approximate bending action more accurately.

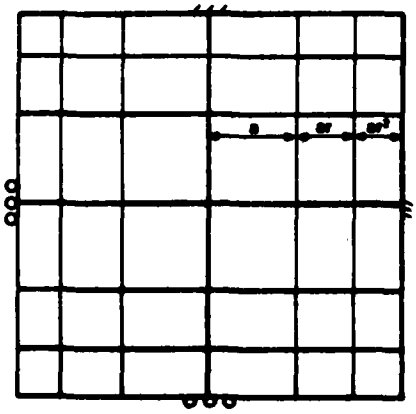

Figure 13. Illustration of the Geometric Variation of Element Size According to a Geometric Series Factor r = 0.7

To attempt to find a finite element mesh containing the minimum number of elements that would provide sufficient accuracy for the modelling of the plate response under a time dependent but spatially constant pressure loading, a series of analyses were undertaken [4]. In terms of the number of elements and factor r, different finite element meshes were constructed. For each mesh, a time independent spatially constant pressure loading of unity was applied and the static plate centre deflection compared with the analytical solution [5]. Figure 14 was constructed by plotting the percentage error in the finite element prediction with respect to the analytical solution against r for different numbers of elements. It was concluded that 25 elements with an r = 0.7 was a reasonable value to use for the prediction of static loading. There is little gain in accuracy between the cases of 25 elements and 36 elements. The 16 element case was rejected since it exhibits a greater sensitivity to a variation in r than does the 25 element case.

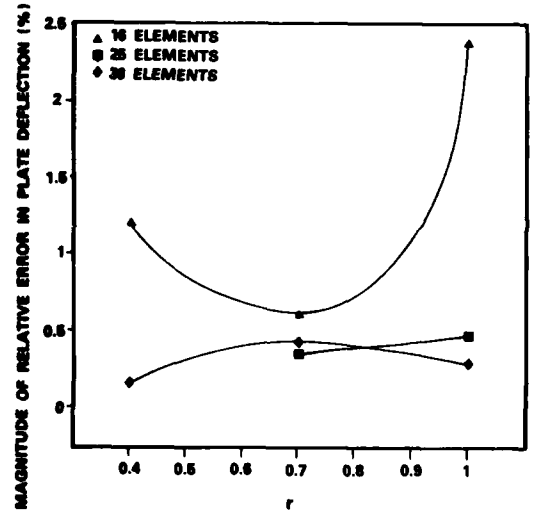

Figure 14. Plots of the Relative Error Magnitude (%) with Respect to the Exact Solution of the Finite Element Prediction of the Central Plate Deflection against the Geometric Series Factor r for the Element Size Distribution

The second series of tests on the finite element meshes was the evaluation of the fundamental frequency. Figure 15 shows the percentage error in the fundamental frequency with respect to the exact solution [5] against r for various numbers of elements. A value of r = 0.7 with 25 elements appears to be a good choice which was also the case for static loading.

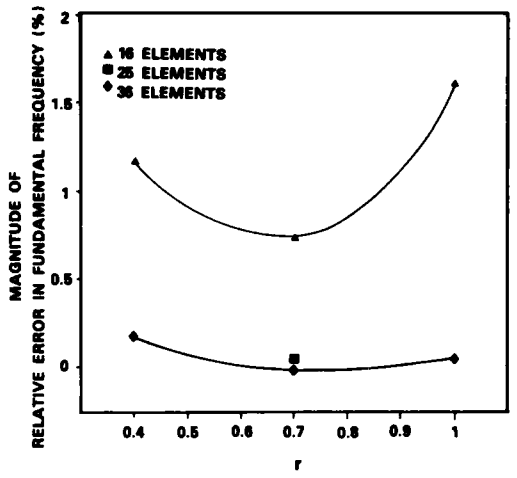

Figure 15. Plots of the Relative Error Magnitude (%) with Respect to the Exact Solution of the Finite Element Prediction of the Fundamental Frequency against the Geometric Series Factor r for the Element Size Distribution

On the basis of the results shown in Figs. 12, 14 and 15, the mesh shown in Fig. 16 was accepted as being adequate for a finite element study of the plate response to a blast wave.

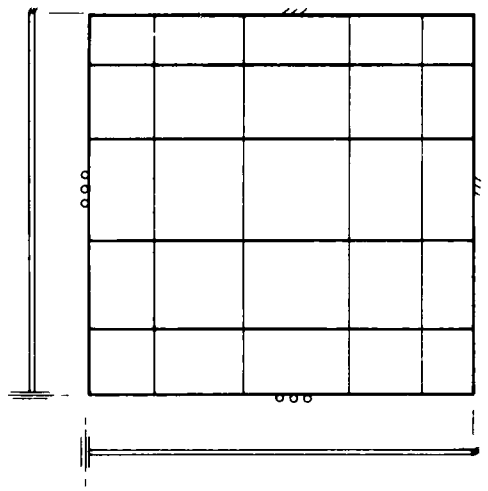

Figure 16. The Finite Element Model of the Square Plate

2.7 Construction of a Loading Function

Figure 7 showed a typical pressure time history trace from one of the pressure transducers. Approximately 7 ms after the primary shock was detected by the transducer, a second shock was received because of reflection from the walls of the Blast Chamber. Since the interest in this work is for free field blast waves the emphasis must be placed upon structural response prior to the detection of reflected shocks. Figure 17 shows comparative plots over the time range 0 to 7 ms for the pressure transducers P1, P2, and P3 shown in Fig. 4. The curves follow a similar trend which suggests that the assumption of a uniform pressure distribution over the plate is reasonable.

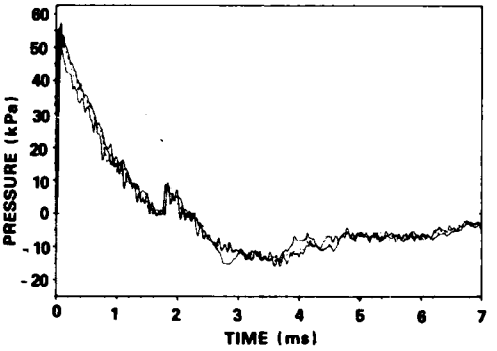

Figure 17. Plots of Pressure against Time for the Transducers P1, P2 and P3

To find an accurate spatially constant pressure loading function for the finite element calculations, the curves in Fig. 17 were averaged at each time point. Since the sampling rate from the analog signals was 50,000 samples per second, 350 time points were involved for each curve. The average load curve was next sampled at 0.1 ms, the time step to be used in the linear finite element calculation. Thus, averaged values of pressure at 70 time points were used to represent the loading function. The load was taken as zero for time greater than 7 ms.

2.8 Comparison of Predicted and Experimental Values of Acceleration, Velocity, and Displacement at the Plate Centre

With the finite element mesh shown in Fig. 16 and the pressure loading function found by averaging the curves in Fig. 17, a linear finite element analysis was performed to predict the plate elastic response. The plate material was assumed to be isotropic with Young's Modulus = 207 GPa, Poisson's Ratio = 0.3, and Mass Density = 7770 kg/m^3. The Newmark method [2] was used for the time

integration. Figures 18, 19, and 20 compare the finite element and experimental values of acceleration, velocity, and displacement, respectively, at the plate centre. The agreement between the experimental and finite element results is encouraging.

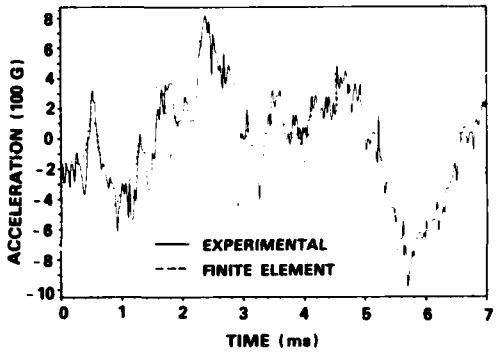

Figure 18. Plots of Experimental and Finite Element Acceleration against Time for the Plate Centre

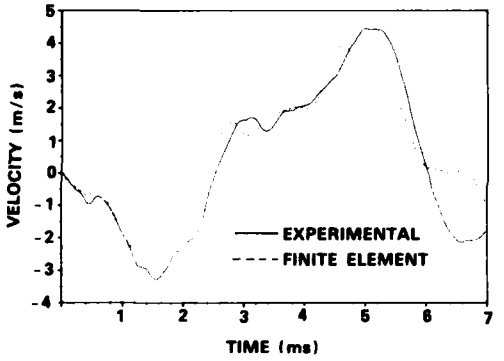

Figure 19. Plots of Experimental and Finite Element Velocity against Time for the Plate Centre

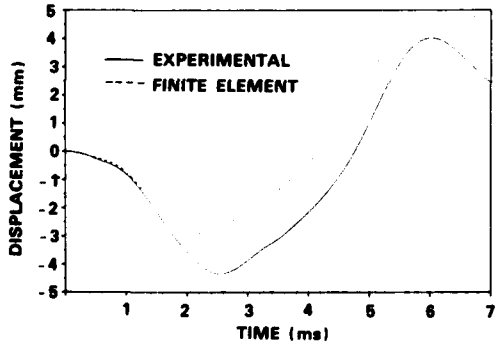

Figure 20. Plots of Experimental and Finite Element Displacement against Time for the Plate Centre

Figures 21 and 22 show the velocity and displacement plotted over a time range 0 to 18 ms. The comparison of the finite element and experimental results is still favourable even though the finite element results did not account for the reflected shocks that are seen after 7 ms in Fig. 7.

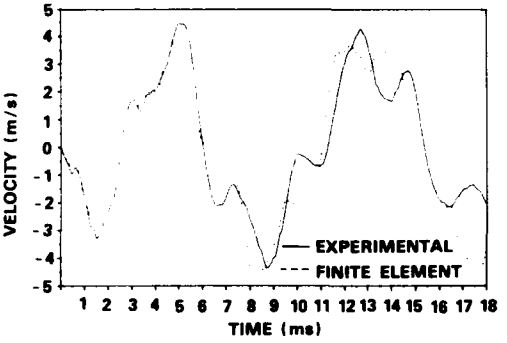

Figure 21. Plots of Experimental and Finite Element Velocity against Time for the Plate Centre

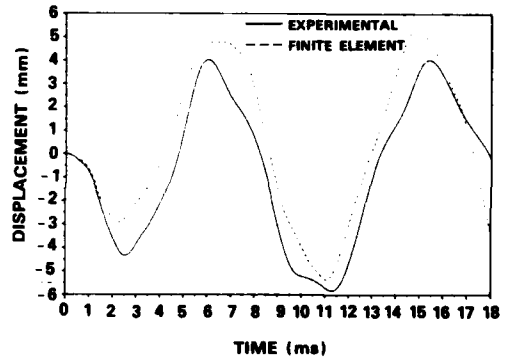

Figure 22. Plots of Experimental and Finite Element Displacement against Time for the Plate Centre

2.9 Detailed Description of the Displacement Response Predicted by the Finite Element Code

Figures 23(a) to 23(d) show the displacement contours for the plate at times of 0.4 ms, 0.8 ms, 2.2 ms (maximum downward deflection) and 6.0 ms (maximum upward deflection). At the start of the plate response, the centre of the plate stays flat and bending occurs near the fixed boundary edges. A bending wave then moves towards the centre from the edges. At $t = 0.8$ ms the maximum deflection occurs not at the plate centre but about one third of the distance along the diagonal line. At 2.2 ms the maximum downward deflection of the plate occurs and is at the plate centre. The plate then rebounds and at 6 ms the maximum upward deflection of the plate centre occurs.

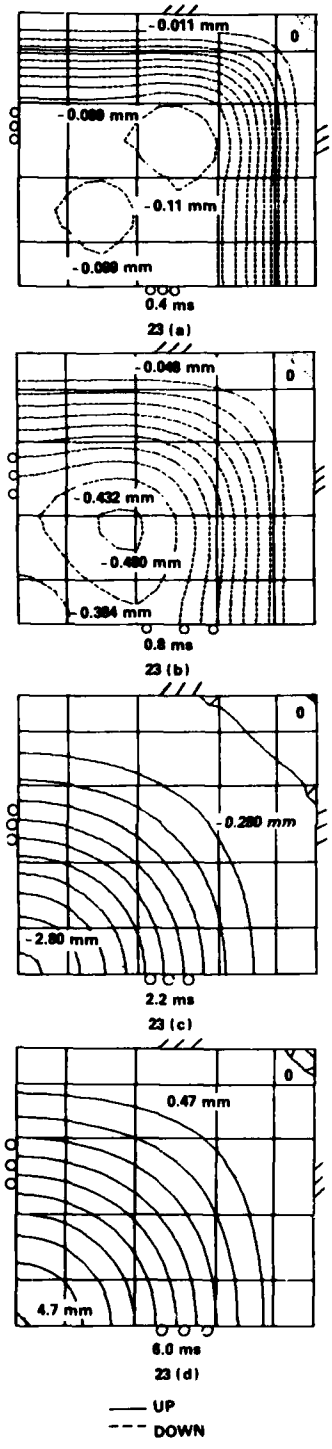

Figure 23. Displacement Contour Plots at Selected Times (Linear Analysis)

2.10 Behavior of the Square Plates Under Extreme Loading

The second series of tests on the plates was done at the DRES HOB site (Fig. 3) and is summarized in Table 2. All tests involved pressures in excess of 3400 kPa. Very large central deflections were observed in all cases. The critical areas of structural failure were the plate boundary edges and the geometrical centre of the plate. Tearing around the support bolts along the plate edges was apparent in all cases. In one case (test 5) actual perforation at the plate centre occurred. Figure 24 illustrates a typical result from these tests. A classical type of deformation pattern [6] is evident where plastic hinges emanate from the plate corners.

Table 2

SUMMARY OF THE HOB TESTS WITH THE SQUARE PLATES

TEST*	PLATE THICKNESS (mm)	STAND OFF (cm)	PEAK PRESSURE (kPa)	CENTRAL DEFLECTION (mm)
1	3.4	305	3720	38
2	1.5	305	3450	86
3	3.4	244	5520	52
4	3.4**	244	6890	47
5	1.5	244	6890	102

* All tests done with charge mass of 14.5 kg.

** Deformed plate from Blast Chamber tests.

The commercially available computer program ADINA [7] was run for one of the tests completed at the HOB site in order to compare the measured and predicted central permanent deflections and profile shapes. With the test 1 plate of thickness 3.4 mm, a permanent central deflection of 38 mm was found after the plate had been subjected to a blast wave with peak overpressure 3720 kPa and positive duration 1 ms. This case was typical of the results obtained and was thus selected for the analysis [8]. Two finite element models were considered. The first one consists of 72 triangular plate elements and is shown in Fig. 25(a). The second model consists of 200 plate elements and is shown in Fig. 25(b). In both cases, only one quarter of the panel was considered with symmetry boundary conditions along the centerlines and fully fixed boundary conditions along the edges.

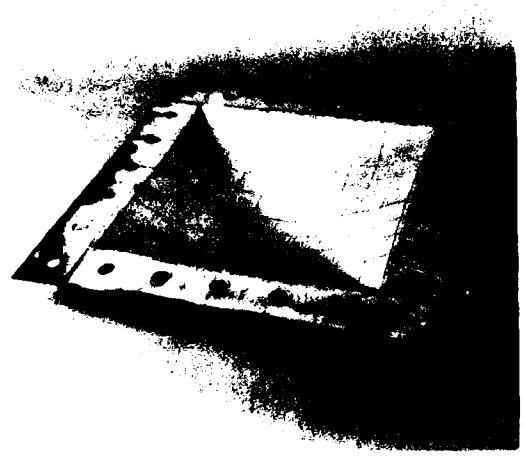

TOP

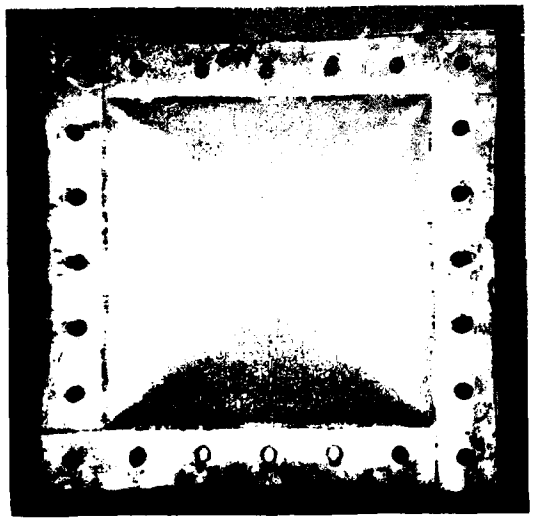

BOTTOM

Figure 24. The Final Deformed Shape after Test 2 at the HOB Site

As was done for the elastic calculations, the pressure loading function was assumed to be spatially constant and was constructed by sampling suitable points from the average pressure transducer curve.

A spatially isotropic material model described by a bilinear function was selected for the calculation. The following tabulated values of the material constants were used: Young's Modulus = 207 GPa, Poisson's Ratio = 0.3, Static Yield Stress = 345 MPa, and Tangent Modulus = 68.9 MPa.

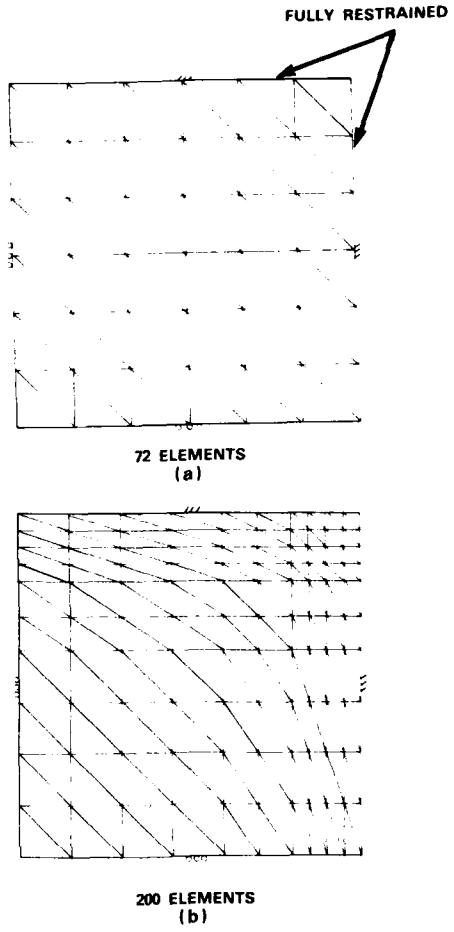

Figure 25. The Finite Element Meshes used for the ADINA Calculations on One Quarter of the Plate

For both meshes in Fig. 25, a full dynamic analysis was carried out. In each case convergence was attained with the stiffness matrix being reformed on alternate time steps and equilibrium iterations being performed on every time step. Newton iteration with Aitken acceleration was used. Three Gauss points were used for the element stiffness formation. Time integration was carried out with the Wilson-theta method. For the 72 element case convergence was attained over the range 0 to 10 ms with a time step of 50 μs. However, a time step of 5 μs was required for the 200 element case.

Figure 26 compares the final centerline deformed profile for the 200 element model with the experimental profile. Except for the fact that the experimental displacement profile is underestimated, the agreement is favourable.

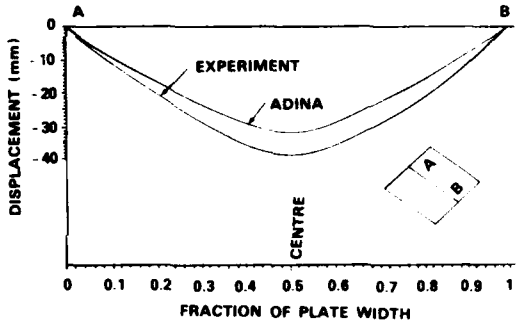

Figure 26. Comparison of the Final Deformed Shape of the Plate from HOB Test 1 and ADINA Program Predictions

3. THE STIFFENED SHIP PANEL

3.1 Introduction

The main objective of the tests to be described in this section is to provide some fundamental information on the structural response of a typical ship's stiffened panel. This structure is typical of that which makes up the hull and superstructure of a modern warship. It is intended that the results provide information on the characteristic behavior over a wide range of blast wave overpressures. As for the square plates, fixed boundary conditions are assumed. These conditions essentially assume that the rest of the ship is infinitely stiff and of infinite mass. The experimental panel should thus lead to overestimates of the deflections and stresses in relation to those encountered by a panel as part of a ship.

3.2 Experimental Results

At the time of writing, only one stiffened panel has been tested. The series involved 4 tests which were carried out at the HOB site. Table 3 summarizes the charge masses and standoff distances used. It is perhaps of interest to note that test 4 differed from the remaining tests in that the total charge detonated above the panel consisted of two identical charges that were detonated simultaneously.

3.3 Equipment and Instrumentation

Figures 27 and 28 show schematic drawings of the panel and mounting arrangement. The central area of the panel measuring 4.57 m × 2.44 m was supported over a hole 2.8 m deep as shown in cross section in Fig. 28. The sides of the panel were clamped with a series of box beam sections mounted at regular intervals. Auxiliary panels were used to cover the clamping arrangement to reduce unwanted reflections of the blast wave to a minimum. Figure 29 shows a photograph of the panel taken prior to the first test.

The panel was instrumented with pressure transducers, accelerometers, and strain gauges as shown in Fig. 30. Four pressure transducers were mounted around the periphery and two underneath the panel. Accelerometers were mounted at the centres of the panel segments, on the flange of one of the beams (A11), and on the panel boundary (A7). Strain gauges were also mounted in positions of estimated high strain both near the beams and at the panel boundaries. At each strain gauge position a gauge was usually mounted on each surface so that both membrane and bending action could be determined.

Table 3

SUMMARY OF THE HOB TESTS WITH THE STIFFENED PANEL

TEST	CHARGE MASS (kg)	STAND OFF (m)	PEAK PRESSURE (kPa)	DURATION (ms)	ACCELERATION* (g)	STRAIN** (με)	REMARKS
1	29.1	15.2	83	9.5	370	1300	Elastic
2	94.1	12.8	225	8.5	880	3000	Just Below Yield
3	94.1	10.1	476	8.0	1590	4000	Just Above Yield
4	188.1	7.3	6650	4.0	+	6400	Severe Plastic Deformation

* Average peak value for accelerometers located at panel centres.

** Average peak value for strain gauges located at panel edges.

\+ Accelerometers not mounted.

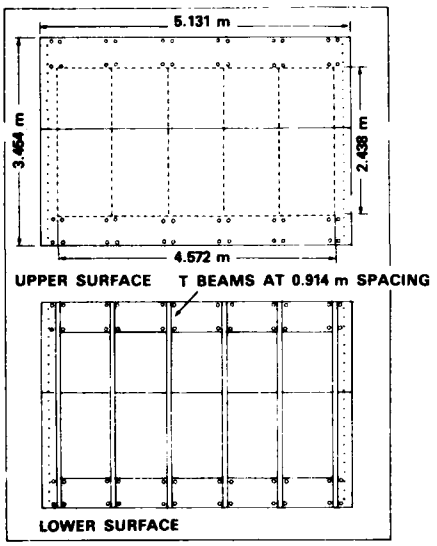

Figure 27. Stiffened Panel Geometry

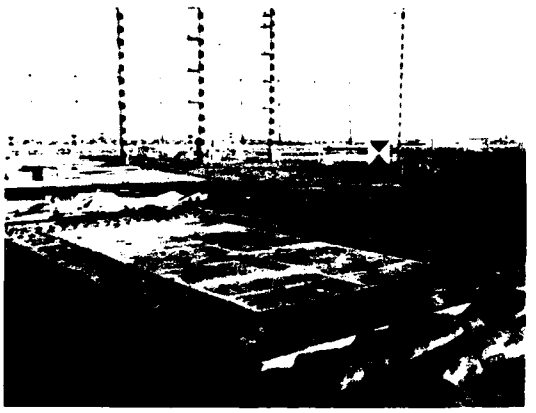

Figure 29. Photograph of Panel on Mounting Frame

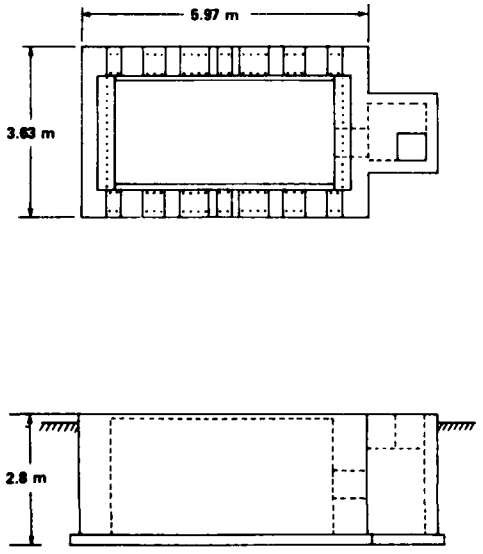

Figure 28. Mounting Frame to Support Panel for HOB Tests

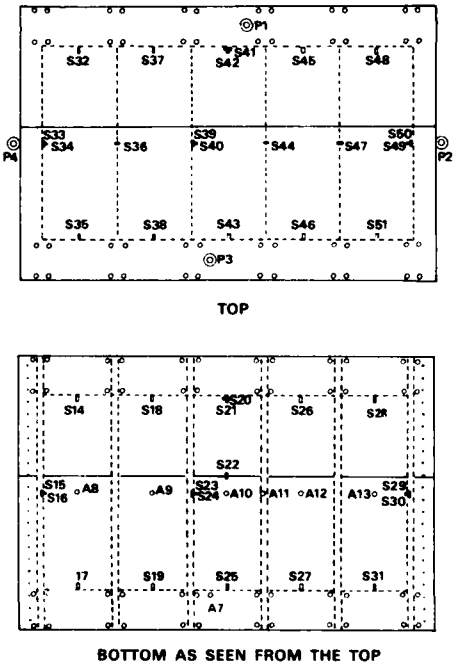

Figure 30. Sensor Locations on Panel
(P = Pressure, S = Strain, A = Acceleration)

3.4 Tests

Table 3 outlines the tests that were done on the stiffened panel. The pulse durations were typically between 8 and 9.5 ms except for test 4 where 4 ms was noted. From measurements of the permanent deflections in the panel after the tests it was concluded that test 1 involved purely elastic response. Test 2 and 3 were essentially just below and above significant yield of the panel, respectively. Test 4, which involved severe plastic deformation, was intended to reveal the mode of plastic collapse.

3.5 Discussion of Results

Figure 31 shows some sample transducer traces. The following observations can be made:

a) In comparison to the load curve in Fig. 17, Fig. 31 shows that the negative phase has been reduced appreciably in comparison to the positive phase. Also the positive phase duration has increased from approximately 2 ms to 7 ms.

b) The strain trace exhibits a fundamental period of approximately 25 ms. This is the fundamental period of just one of the rectangular panel segments between the beam stiffeners.

c) The acceleration trace shows the presence of several high frequency modes. However, the result is consistent with the strain trace.

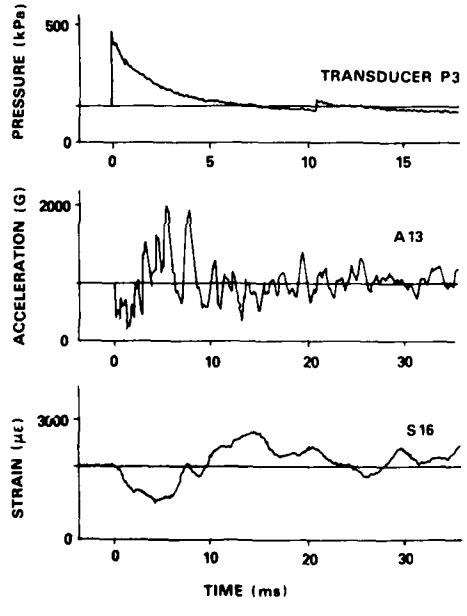

Figure 31. Pressure, Acceleration and Strain Records 94 kg Charge at 10.1 m Stand-off

Figure 32 shows the final deformed shape after test 4. The result indicates that each rectangular panel segment between the beam stiffeners has distorted to a similar shape and that significant distortion of the beam stiffeners themselves has occurred.

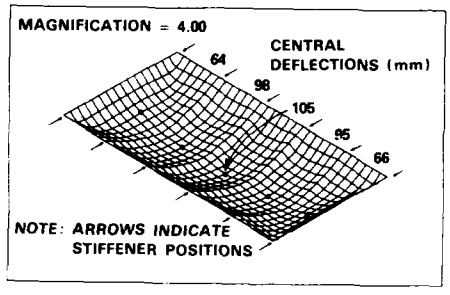

Figure 32. Experimental Panel Deformation after Final Shot

3.6 Construction of a Finite Element Model

Figure 33 illustrates one of the finite element models of the stiffened panel that has been considered. Fifty parabolic isoparametric shell elements are shown in this case. The beams were modelled using 3 node parabolic isoparametric beam elements. Other finite element models containing triangular plate elements with general beam elements have also been considered.

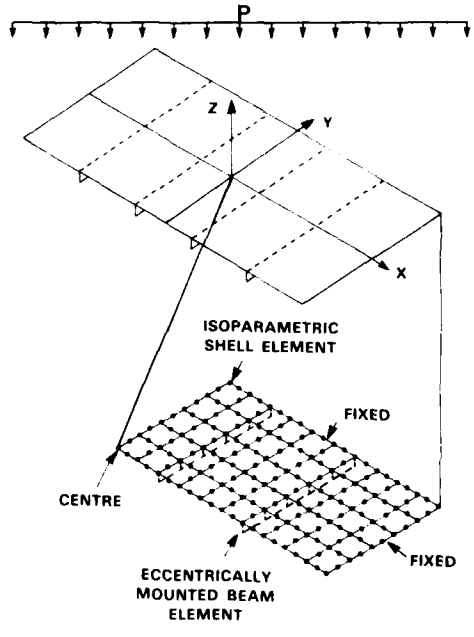

Figure 33. Finite Element Model of Stiffened Panel

3.7 Discussion of Finite Element Results

At the time of writing only a preliminary assessment of the stiffened panel with the finite element codes VAST and ADINA has been undertaken. The displacement contours of a dynamic elastic analysis with a triangular pressure loading function of duration 10 ms is shown in Fig. 34. The finite element result supports the experimental result in that the structural response of each rectangular panel segment is similar.

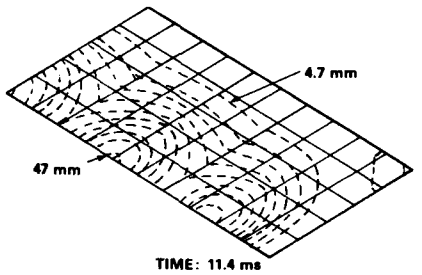

Figure 34. Contour Plot of Maximum Displacement of Panel (ΔP = 69 kPa)

4. CONCLUSIONS

A detailed finite element analysis of the square plates for the elastic response to blast waves resulted in very good correlation of the results to experiment. Only minor refinements in element size and time step are expected to be required to resolve some of the minor discrepancies noted. The finite element prediction of the final deformed shape after plastic deformation under extreme loading for a square plate also showed reasonable comparison to experiment.

Experiment has revealed the general nature of the stiffened panel response to a blast wave. The general features of the displacement patterns observed experimentally are supported by preliminary finite element code predictions.

5. ACKNOWLEDGMENT

The authors gratefully acknowledge the ADINA analysis [Ref. 8] discussed in Section 2.10 that was done by Mr. N. Pegg at the Defence Research Establishment Atlantic. We are also grateful to Mr. S. Marsden for conducting the finite element model parametric study [Ref. 4, used in Section 2.6] while working at DRES as a summer research assistant. We would also like to thank Mr. D. Ritzel and Mr. G. Rude of the Shock and Blast Group at DRES for their assistance with the experimental work. We also thank the personnel of the Computer Group, the Field Operations Section, the Electronic Design and Instrumentation Group, and the Photo Group at DRES for their assistance during the DRES field trials.

6. REFERENCES

1. "Vibration And STrength Analysis Program (VAST): User's Manual, Version #02", MARTEC LTD., November, 1982.

2. Bathe, K.J., **Finite Element Procedures in Engineering Analysis**, Prentice-Hall, Inc., 1982.

3. Slater, J.E. and Houlston, R., "Dynamic Analysis of Beams and Plates Subjected to Air-Blast Loading", The 3rd International Modal Analysis Conference, Orlando, Florida, January 28 - 31, 1985.

4. Marsden, S., "Private communication".

5. Roark, R.J. and Young, W.C., **Formulas for Stress and Strain**, 5th Edition, McGraw-Hill, 1975.

6. Johnson, W., **Impact Strength of Materials**, Edward Arnold (Publishers) Ltd., 1972.

7. "ADINA, A Finite Element Program for Automatic Dynamic Incremental Nonlinear Analysis", Report AE 81-1, ADINA Engineering, Inc., September, 1981.

8. Pegg, N., "The Use of VAST, ADINA, ADIDAT, and ADIPOS in Nonlinear Dynamic Blast Analysis", Defence Research Establishment *Atlantic, Internal Report DREA RN/H/84/7*, October, 1984.

DISCUSSION

Voice: What was the effective highest frequency in your linear analysis of the modes of the structure?

Mr. Houlston: We used direct integration and a time step of .1 millisecond. We didn't use modal synchronization.

Voice: Did you do a modal analysis of the structure?

Mr. Houlston: We did a frequency analysis, and I think we calculated the first ten modes of the structure.

Voice: What was the highest frequency?

Mr. Houlston: It was approximately 5,000 Hz.

Mr. Petes (Kaman Tempo): At the standoff ranges that you used, which were large charges at the HOB facility, what was the planarity of the shock wave hitting the plate?

Mr. Houlston: The only indication we had from this was to compare the pressure transducer outputs which appeared to be quite good. The correlation between them was quite reasonable. We did do one test where we actually had a series of nine pressure transducers over the panel. We got quite good correlation.

Mr. Rentz (Naval Postgraduate School): What accelerometers did you use? How did you get the strain gages to adhere during the impulsive loading? Did you have any problems with the strain gages being blown off?

Mr. Houlston: We used piezoelectric accelerometers, and I think they went up to 4,500 g. We had to filter out the high frequencies above 10,000 Hz. We had a lot of very high frequency content in the acceleration measurements because the accelerometers tended to vibrate as a structure, themselves. So, filtering out the analog signals is almost essential.

Mr. Rentz: Did you get any strain gage measurements or were the displacements integrated from your accelerations?

Mr. Houlston: The displacements were integrated from the accelerations.

Mr. Rentz: Did you measure strains?

Mr. Houlston: Yes. We did obtain a series of strain readings, and they were quite reasonable on both surfaces; we could see the bending action quite well.

GENERALIZED DYNAMIC ANALYSIS OF INTERACTIVE FLUID-STRUCTURE TRANSIENT RESPONSE

J. E. Boisvert and B. E. Sandman
Naval Underwater Systems Center
Newport, RI 02841

A generalized classical analytical method is formulated for the solution to the response of submerged structures excited by transient forces. The approach is directly applicable to numerous problems where transient structural response in the presence of a heavy fluid medium is of fundamental interest. The proposed methodology, which captures the complete spectral distribution of frequency and wavenumber, is capable of describing response to unlimited space-time waveforms of transient loading.

The methods employed in the development of a generalized analytical approach utilize a complete basis of functional influence coefficients in both the space and time domains. These influence functions are generated in terms of a series summation which represents the response under space-time impulses. Subsequently, a convolution integral of the actual space-time input distribution function with the influence functions provides the final solution to the in-fluid structural response under any chosen or described form of the input loading. The implementation of this analytical approach is achieved without employing asymptotic assumptions or approximations of the relative fluid loading. The form of the analytical approach is directly applicable to the solution of submerged, transient response of any structure which can be characterized in terms of generalized, in-fluid dynamic influence functions.

The titled problem is discussed in specific terms for a submerged finite flat plate carrying a concentrated mass. Numerical examples are presented which are unique and clearly demonstrate the power of the approach. Results are presented for pressure and force pulses, initialization loading, and simultaneously translating-oscillating loading. A comparison of in-water and in-vacuo response is given for each of the examples. In addition, the analysis considers the determination of the transient farfield radiated pressures which are generated in the acoustic fluid field due to the motion of the excited structure.

INTRODUCTION

In modern applications both marine and aerospace structures frequently encounter deterministic and/or random dynamic forces in their operating environment. These transient loadings manifest themselves as shock waves, concentrated forces, cavitation, flutter, turbulence excitation, as well as numerous others. The continued emphasis upon the control of noise and vibration necessitates a clear understanding of the characteristics governing the dynamic structural response. In addition, for structures vibrating in a dense fluid medium, a strong coupling is exhibited and the fluid-structure interaction *system* becomes of primary concern since the effect of heavy fluid loading significantly alters the apparent characteristics of the isolated structure. Therefore, an accurate mathematical description of the system must include the simultaneous solution of both sets of field equations with continuity of normal velocity enforced at the fluid-structure interface.

Previous analysis [1-3] centered on the prediction of the steady-state response of in-vacuo and in-fluid structures. There, it was shown that for a dense fluid medium, the velocity and pressure distributions for the fluid and structure can be represented on the surface by an infinite basis of orthogonal functions. Hence, the characteristics of the fluid and structure at the interface are decomposed into matrices that exhibit the self and mutual impedances or mobilities of the orthogonal set of functions. The present work adopts the same methodology and proposes a formulation which allows for the direct prediction of the transient response of fluid-

loaded structures excited by arbitrary forcing functions. In this investigation,the generalized method is illustrated as applied to the transient vibration of a finite rectangular plate and its accompanying acoustical radiation, for several representative classes of dynamic excitation.

I. *Exemplified Theory: Fluid-Plate Interaction*

Consider a simply-supported finite rectangular plate submerged in a fluid and excited by an arbitrary forcing function. The motion of the plate interacts with and induces acoustic radiation into a semi-infinite half-space of fluid. For the consideration of in-fluid transient response over a finite time interval T, the input loading can be represented by the general expression

$$q(x,y,\tau) = \frac{D}{L^3}\sum_{K=-\infty}^{\infty}\sum_{m=1}^{\infty}\sum_{n=1}^{\infty} a_{mn}(K)X_{mn}(x,y)e^{i\omega_K\tau} \tag{1}$$

where

$$\omega_K = \frac{\pi K}{T} \tag{2}$$

is the non-dimensional frequency and

$$\tau = c_p t/L \tag{3}$$

is the non-dimensional time with c_p the sound velocity of the plate material, and

$$X_{mn}(x,y) = \sin\frac{m\pi x}{L}\sin\frac{n\pi y}{b} \tag{4}$$

are the normal in-vacuo modes of the simply-supported plate of length L and width b.

The parameter D is the flexural rigidity of the plate given by

$$D = \frac{E\sigma^3}{12\,(1-\nu^2)} \tag{5}$$

where ν denotes Poisson's ratio, E the modulus of elasticity of the plate material, and σ is the thickness of the plate.

It is assumed that the time period of observation, T, is large and provides adequate representation of the time history for the radiation damped response due to the arbitrary dynamic forcing function. The impulsive dynamic loading is represented as a unit impulse applied at $\tau = 0$, and concentrated at the point (x_o, y_o) on the plate

$$q(x,y,\tau) = \delta(\tau)\delta(x-x_o)\delta(y-y_o) \tag{6}$$

Equating (1) and (6), and using the orthogonality of the normal function and the methods of inversion we obtain the impulsive dynamic loading coefficients

$$a_{rs}(x_o,y_o) = \frac{1}{2T}\frac{L^3}{D}\frac{X_{rs}(x_o,y_o)}{\iint_A X_{rs}^2(x,y)dA} \tag{7}$$

where $dA = dxdy$ is the element of surface area of the plate.

The general expression for the impulsive response of the plate due to the impulsive excitation of Eq. (6) is given by

$$h(x,y,x_o,y_o,\tau) = L\sum_{K=-\infty}^{\infty}\sum_{m=1}^{\infty}\sum_{n=1}^{\infty}\Delta_{mn}(K,x_o,y_o)X_{mn}(x,y)e^{i\omega_K\tau} \tag{8}$$

where the Δ_{mn} are the impulsive modal displacement coefficients [1]

$$\Delta_{mn}(K,x_o,y_o) = \sum_{r=1}^{\infty}\sum_{s=1}^{\infty} Y_{mnrs}(K)a_{rs}(x_o,y_o) \tag{9}$$

and Y_{mnrs} is the mobility of the fluid-plate system with a_{rs} given by Eq. (7). It is noted that the expression in Eq. (8) is symmetric with respect to the interchange of the observation and excitation points (x,y) and (x_o,y_o).

Hence, using the principle of reciprocity, the following equality holds

$$h(x,y,x_o,y_o,\tau) = h(x_o,y_o,x,y,\tau) \tag{10}$$

Equation (8) thus represents the response of the plate under a space-time impulse, with the initial conditions equal to zero. Since the system is linear, the transient response of the fluid-loaded plate is obtained by superposition which is expressible by a general convolution integral of the form

$$w(x,y,\tau) = \int_0^{\tau}\iint_{A_o} h(x,y,x_o,y_o,\tau-\beta)q(x_o,y_o,\beta)dA_o d\beta \tag{11}$$

where $q(x_o,y_o,\beta)$ is the arbitrary dynamic loading with $\beta \geq 0$, and $dA_o = dx_o dy_o$.

In consideration of the radiated pressures, which are generated in the acoustic field due to the motion of the plate, the development is analogous to the formulation of the plate response, i.e., an impulsive acoustic pressure is formulated and subsequently, a convolution integral

of the actual space-time excitation and impulsive acoustic pressure provides the solution for the transient acoustic radiation of the strongly coupled fluid-structure system.

The acoustic field with sound velocity c_f is governed by the three-dimensional wave equation

$$\nabla^2\Psi = \frac{1}{c_f^2}\frac{\partial^2\Psi}{\partial t^2} \quad ; z>0 \tag{12}$$

where ∇^2 is the Laplacian in Cartesian coordinates and $\Psi(x,y,z,t)$ is the velocity potential given by

$$\Psi(x,y,z,t) = Lc_p \sum_{K=-\infty}^{\infty} \bar{\Psi}_K(x,y,z) \exp(i\omega_K c_p t/L) \tag{13}$$

where $\bar{\Psi}_K$ is the function for spatial variation [1]. The accompanying acoustic pressure is determined by

$$P(x,y,z,t) = -\varrho_f \frac{\partial\Psi}{\partial t} \tag{14}$$

where ϱ_f is the mass density of the medium. At the fluid-structure interface ($z = 0$), the continuity of normal velocity requires

$$\left.\frac{\partial\psi}{\partial z}\right|_{z=0} = \frac{\partial h(x,y,x_o,y_o,t)}{\partial t} = \frac{c_p}{L}\frac{\partial h(x,y,x_o,y_o,\tau)}{\partial\tau} \tag{15}$$

where $\partial h/\partial\tau$ is the impulsive velocity of the plate excited by the impulse loading of Eq. (6).

It was shown in [1] that the general expression for the farfield acoustic pressure radiated from the plate is expressible as

$$P_K(R_f,\theta,\phi,x_o,y_o) = \frac{6}{\pi}\frac{\varrho_f}{\varrho_p}\left(\frac{L}{\sigma}\right)^3 i\omega_K \iint_{A_1} \left.\frac{\partial\bar{\Psi}_K}{\partial z}\right|_{z=0} \frac{e^{-i\Lambda_K R_f}}{R_f} \exp\left(i\Lambda_x\frac{x_1}{L} + i\Lambda_y\frac{y_1}{b}\right) dA_1 \tag{16}$$

where from Eqs. (13) and (15)

$$\left.\frac{\partial\bar{\Psi}_K}{\partial z}\right|_{z=0} = \frac{i\omega_K}{L}\sum_{m=1}^{\infty}\sum_{n=1}^{\infty}\Delta_{mn}(K,x_o,y_o)X_{mn}(x_1,y_1) \tag{17}$$

and Λ_K is the acoustic wavenumber,

$$\Lambda_K = \frac{\omega_K c_p}{Lc_f} \tag{18}$$

and

$$\Lambda_x = \Lambda_K L \sin\theta\cos\phi \qquad \Lambda_y = \Lambda_K b \sin\theta\sin\phi \tag{19}$$

which are defined in terms of the direction cosines of the farfield position and the length of the position vector R_f, as illustrated in figure 1.

The series expression for the transient impulsive farfield radiated acoustic pressure is obtained utilizing Eqs. (16 - 19)

$$P_I(R_f,\theta,\phi,x_o,y_o,\tau) = \frac{D}{L^3}\sum_{K=-\infty}^{\infty} P_K(R_f,\theta,\phi,x_o,y_o)e^{i\omega_K\tau} \tag{20}$$

Equation (20) therefore represents the farfield pressure radiated by the plate excited by the space-time impulse of Eq. (6).

In analogy with Eq. (11), the expression describing the transient farfield radiated pressure takes the form of a convolution integral

$$P(R_f,\theta,\phi,\tau) = \int_0^{\tau}\iint_{A_o} P_I(R_f,\theta,\phi,x_o,y_o,\tau-\beta)q(x_o,y_o,\beta)dA_o d\beta \tag{21}$$

where $q(x_o,y_o,\beta)$ is the same dynamic forcing function as found in Eq. (11). Hence, Eqs. (20-21) used in conjunction with Eqs. (7-11) currently provide the basis for the description of the time history of the fluid-loaded plate vibration and the associated farfield radiated pressure and represent the fundamental result of this work. It should be noted that although the above equations were derived for a plate, the method is applicable to obtain the transient response of any structure which can be characterized in terms of generalized, in-fluid dynamic influence functions.

II. *Numerical Investigation and Results*

For the purpose of illustrating the proposed methodology, three distinct cases of dynamic loading will be considered. The plate-fluid interaction problem chosen is described by the following geometric and material properties. The plate is considered to be a uniform homogeneous and isotropic material with an aspect ratio $b/L = 1.55$ and $\sigma/L = 8.52\times10^{-3}$. The damping factor was taken to be 0.1 for all cases. The response of the plate is computed by the solution of Eqs. (11) and (21) for both in-air ($\varrho_f/\varrho_p \cong 0$; $c_f/c_p = 0.066$) and in-water ($\varrho_f/\varrho_p = 0.37$; $c_f/c_p = 0.28$) vibration and radiation of an aluminum plate. A detailed discussion of the techniques employed to generate numerical values for the mobility matrix Y_{mnrs} (which contains the fluid-loading, plate-stiffness and concentrated mass terms) is given in Reference [1]. To avoid redundancy this discussion will not be presented in this study.

Basically, the relatively low frequency excitation and response of the fluid-structure system is of primary interest in these examples. In this regard, the solution is obtained by the numerical evaluation of the truncated series which ultimately appear in Eqs. (11) and (21). For the current study, a finite number of discrete frequencies (K = 300) were employed to capture the spectral characteristics of the response and associated radiation. Similarily, forty-nine degrees of freedom were ascertained to be sufficient to describe the low-frequency plate response and radiation by noting the negligible influence of expanding the truncated modal dimensionality. It is evident from the series formulation that high frequency response may be considered by increasing the number of discrete frequencies and modal dimensionality at the cost of a greater computational effort.

A. Spatially Uniform Pressure Pulse with Half-Sine Time Waveform

Consider a plane shock wave which impinges upon the plate at $\tau = 0$. The magnitude of the pulse is time dependent and is assumed to have a half-sine waveform of duration T^* and frequency $\omega^* = \pi/T^*$. The input dynamic loading is described by the equation

$$q(x,y,\tau) = Q_o \sin \omega^*\tau \quad ; 0 \le \tau \le T^* \qquad (22)$$

$$= 0 \quad ; \tau > T^* , \tau < 0$$

where Q_o is the magnitude of the applied pressure. Upon substitution of Eqs. (22) and (8) into (11) and performing the subsequent integrations, the time history was determined for the plate carrying a concentrated mass (equal to the mass of the plate) off-center at $x_m = 0.5L$, $y_m = 0.3b$. Figures 2 and 3 show the centerpoint dynamic response of the plate for the in-air and in-water cases respectively. The pulse duration was taken to be 4 ms and the magnitude of the applied pressure was 0.58 psi.

Figure 2 shows the initial response to be a superposition of the fundamental natural frequency of air-loaded plate ($\omega = 0.032$) and the pulse excitation frequency ($\omega = 0.083$). As time increases ($\tau > 1000$), the plate vibrates at the natural frequency, with the amplitude of displacement decaying towards zero. The in-water response is markedly different as shown in figure 3. Here, except for the first peak, the vibration occurs at the natural frequency of the water-loaded plate ($\omega = 0.017$). At the first peak, the plate is starting to respond at the pulse frequency, however, it is seen that the natural frequency is the dominant frequency of response, and essentially no superposition occurs. This result clearly shows the effect of the heavy fluid-loading on the plate response. It is noted that the late-time transient response of the plate is primarily due to the fundamental plate resonant frequency. The initial plate response is high frequency in nature and an accurate numerical calculation of Eq. (8) requires the use of eight resonant plate modes in the series summation.

The corresponding farfield radiated pressure histories are shown in figures 4 and 5. Again, as in the plate response, the in-air pressure history is characterized by a superposition of the pulse and natural frequencies. Also shown is the time delay, R_f/c_f, which represents the time for the sound to travel from the surface of the plate to the farfield position in the acoustic field. It is seen that the series representation exhibits strong cancellation in this region and it is remarkable that the series can represent this phenomena with a high degree of resolution.

Figure 5 shows the in-water pressure response. Unlike the plate response, the radiated pressure is characterized by a superposition of the pulse and natural frequencies, and the amplitudes are about one order of magnitude larger than the corresponding in-air case. This is expected since the sound-speed in water is over 4 times larger than in air. It is noted that the time-dependent pressure fluctuation around the static pressure (taken to be zero) is clearly visible in these (and the following) examples, and the farfield distance in-water is chosen such that the same time delay exists as in the in-air cases.

B. Initialization Loading - Concentrated Stationary Force

This example is described by a concentrated force of constant magnitude which comes on the plate at $\tau = 0$ and remains stationary throughout the observation period. The input loading for this case is

$$q(x,y,\tau) = Q_o \delta(x-x_o)\delta(y-y_o) \quad ; \tau \ge 0 \qquad (23)$$

$$= 0 \quad ; \tau < 0$$

where Q_o is the magnitude of the force concentrated at the point (x_o,y_o) on the plate. The magnitude of the force was taken to be 280 lb in this example. As before, the transient response is obtained by the substitution of Eqs. (23) and (8) into (11), and the farfield pressure is obtained by the substitution of Eqs. (23) and (20) into (21), followed by the evaluation of the integrals.

Figures 6 and 7 illustrate the predicted in-air and in-water centerpoint response of the plate subjected to the dynamic loading of Eq. (23). It is seen that in both cases, the plate responds at its fundamental natural frequency and eventually settles to a value which is the static deflection (Note: the static weight of water is neglected in figure 7). The farfield radiated pressures are shown in figures 8 and 9, where the farfield distances were chosen such that the same time delay exists for the in-air and in-water cases. It is noted that the additional oscillations for the in-water radiated pressure response are a result of the superposition of the plate fundamental and (3,3) mode resonances, where in terms of normalized amplitudes, the (3,3) mode displays the dominant radiation efficiency.

C. Translating-Oscillating Concentrated Force

Previous examples have described input loadings that were time dependent only. The following example extends the complexity to include spatial dependence. This spatial

dependence is limited to translation in one direction at a constant velocity. In addition, the point load has an oscillating component defined by an oscillation frequency. The dynamic loading is expressed as

$$q(x,y,\tau) = \quad (24)$$
$$Q_o \cos \omega_o \tau \delta(x - (x_e + v\tau))\delta(y - y_e) \; ; \; \tau \geq 0$$
$$= 0 \; ; \; \tau<0 \; ; \; \tau>1/v$$

where Q_o is the magnitude of the concentrated force which traverses the length of the plate in the x-direction, i.e., $x_e = 0$ and $y_e = 0.5$ b. The parameter ω_o is the non-dimensional circular frequency defined by $\omega_o = 2\pi fL/c_p$, where f is the frequency; and v is the non-dimensional velocity $v = V/c_p$, where V is the translational velocity.

Figures 10 and 11 illustrate the center point response due to the input loading of Eq. (24) with $Q_o = 280$ lb, $f = 994$ Hz, and $V = 596$ in/s. These figures clearly show a modulation effect in which the input loading produces flexural waves which propagate through the plate and are reflected from the boundaries and then interfere with the subsequent in-coming wave-fronts. The inference pattern is primarily produced by the first four resonant plate modes and the high frequency response which tracks the oscillation is essentially a result of non-resonant plate response. The maximum amplitudes occur when the incident and reflected waves are in phase at the observation point which in this case is the center-point. Wave trains are produced at a rate according to the oscillation frequency, and the interference of the wave trains is dependent upon the translational velocity. When $\tau = 1/v = 346$, the load moves off the plate and the plate oscillation decays rapidly and approaches zero.

The associated farfield radiated pressures are shown in figures 12 and 13. As in previous cases, the farfield distance was chosen such that the time delay is the same for both in-air and in-water cases. Again, the amplitudes for the in-water cases are much larger (peak values are over 2 orders of magnitude) than the corresponding in-air case, whereas the peak amplitudes of the plate response are roughly 5 times smaller for the in-water case due to the heavy fluid-loading.

III. *Conclusion and Summary*

The current study formulates and presents a generalized method for analyzing and solving a fluid-structure interaction system excited by arbitrary transient forcing functions. The method utilizes a complete basis of influence functions in both the spatial and temporal domains. It is shown that the in-fluid structural response is obtained from a general convolution integral, whose integrand consists of the product of the actual dynamic loading and the impulsive response expressed in series form. An analogous expression for the transient farfield radiated pressure is derived which follows from the direct coupling of the impulsive response of the plate and the acoustic fluid field.

The methodology is exemplified by application of the approach to the analysis of the vibration of a finite flat plate under several representative classes of dynamic excitation. In addition, the time history of the farfield radiated pressure is considered for each case. It is observed that the in-air and in-water results differ markedly for both the plate response and associated radiated pressure due to the strongly coupled nature of a structure vibrating and radiating in a heavy fluid. A distinct advantage of this approach is that the in-water mobility of the structure need only be generated once since all input waveforms can be considered in a convolution integral with the impulsive response. It is noted that since no asymptotic expressions for the fluid-loading are employed, the current approach has no limitation with regard to the frequency domain of transient inputs. In addition, by mere augmentation of the mobility matrix, the present approach is applicable to the consideration of multiple masses and the attachment of absorbers and other unique structural details. Although the examples were conducted for a plate, the form of the analytical approach is directly applicable to the solution of the transient response of any structure which can be characterized in terms of generalized in-fluid dynamic influence functions. Solution methods which solve for the frequency response in an efficient manner are necessary to utilize this method effectively.

REFERENCES

1. B. E. Sandman, "Fluid-Loaded Vibration of an Elastic Plate Carrying a Concentrated Mass", Journal of the Acoustic Society of America, vol.61, 1503-1510, 1977.

2. A. Harari and B. E. Sandman, "Vibratory Response of Laminated Cylindrical Shells Embedded in an Acoustic Fluid", Journal of the Acoustic Society of America, vol. 60, 117-128, 1976.

3. B. E. Sandman, "Spatial Fourier Decomposition: Analysis of Fluid-Loaded Structural Vibration", Proceedings of the 16th Midwestern Mechanics Conference, Dev. Mech. 10, 79-83,1979.

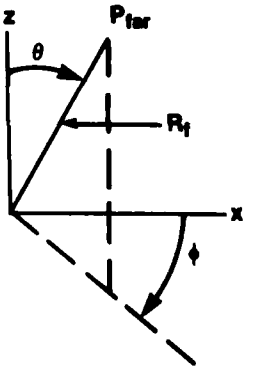

Fig. 1 - Construction of the Farfield of a Plane Radiator

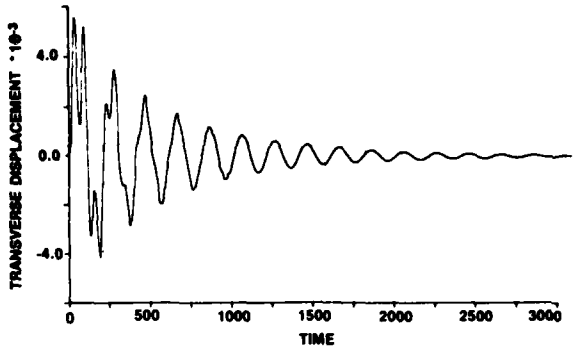

Fig. 2 - In-Air Centerpoint Dynamic Response of Aluminum Plate with an Aspect Ratio of 1.55 and Damping Factor of 0.1, Carrying a Concentrated Mass Off-Center at x_m = 0.5L, y_m = 0.3b, Excited by a 4ms Spatially Uniform Half-Sine Pressure Pulse

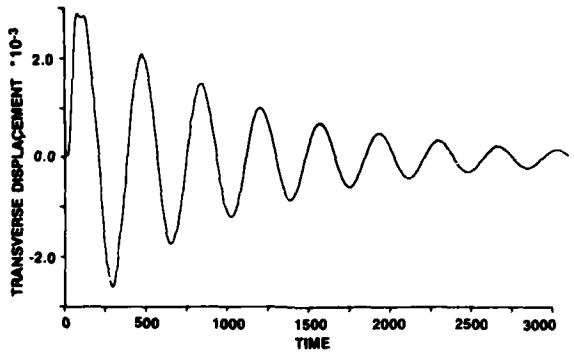

Fig. 3 - In-Water Centerpoint Dynamic Response of Aluminum Plate with an Aspect Ratio of 1.55 and Damping Factor of 0.1, Carrying a Concentrated Mass Off-Center at x_m = 0.5L, y_m = 0.3b, Excited by a 4ms Spatially Uniform Half-Sine Pressure Pulse

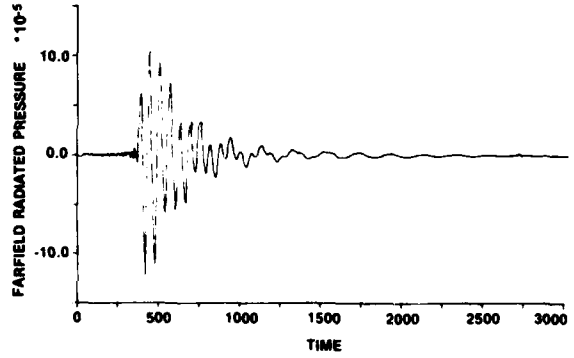

Fig. 4 - In-Air Transient Farfield Radiated Pressure of Aluminum Plate with an Aspect Ratio of 1.55 and Damping Factor of 0.1, Carrying a Concentrated Mass Off-Center at x_m = 0.5L, y_m = 0.3b, Excited by a 4ms Spatially Uniform Half-Sine Pressure Pulse. Farfield Observation Point is at a Distance of 25 x L Normal to the Plate

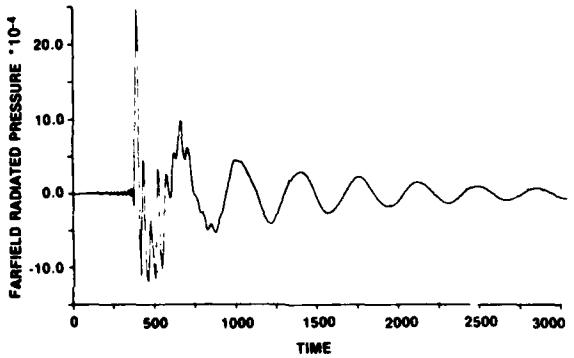

Fig. 5 - In-Water Transient Farfield Radiated Pressure of Aluminum Plate with an Aspect Ratio of 1.55 and Damping Factor of 0.1, Carrying a Concentrated Mass Off-Center at x_m = 0.5L, y_m = 0.3b, Excited by a 4ms Spatially Uniform Half-Sine Pressure Pulse. Farfield Observation Point, is at a Distance of 25 x L Normal to the Plate

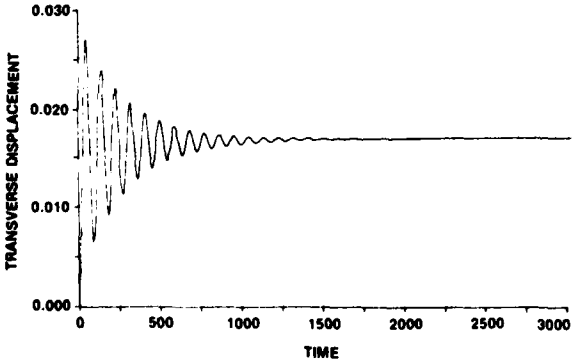

Fig. 6 - In-Air Centerpoint Dynamic Response of Aluminum Plate with an Aspect Ratio of 1.55 and Damping Factor of 0.1, Excited by a Stationary Concentrated Force Applied at the Centerpoint

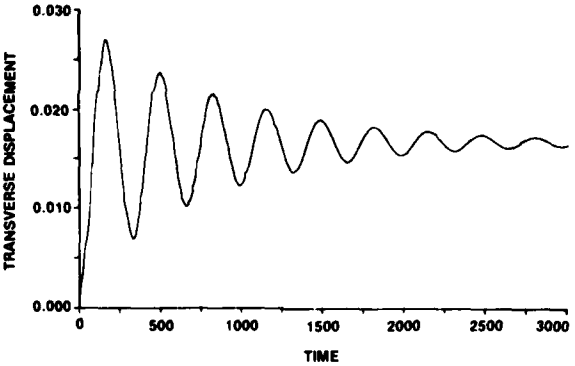

Fig. 7 - In-Water Centerpoint Dynamic Response of Aluminum Plate with an Aspect Ratio of 1.55 and Damping Factor of 0.1, Excited by a Stationary Concentrated Force Applied at the Centerpoint

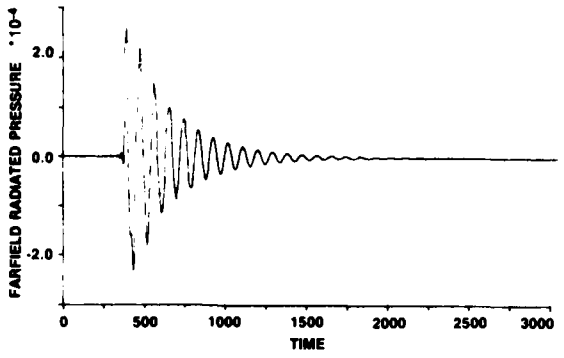

Fig. 8 - In-Air Transient Farfield Radiated Pressure of Aluminum Plate with an Aspect Ratio of 1.55 and Damping Factor of 0.1, Excited by a Stationary Concentrated Force Applied at the Centerpoint. Farfield Observation Point is at a Distance of 25 x L Normal to the Plate

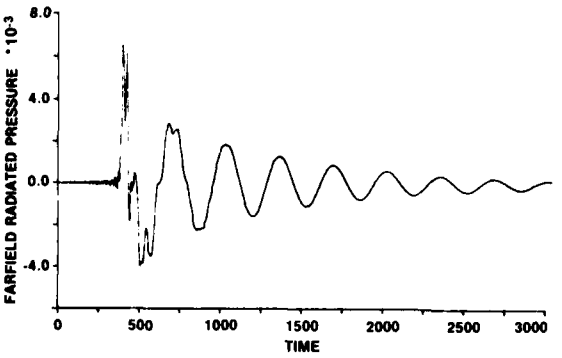

Fig. 9 - In-Water Transient Farfield Radiated Pressure of Aluminum Plate with an Aspect Ratio of 1.55 and Damping Factor of 0.1, Excited by a Stationary Concentrated Force Applied at the Centerpoint. Farfield Observation Point is at a Distance of 106 x L Normal to the Plate

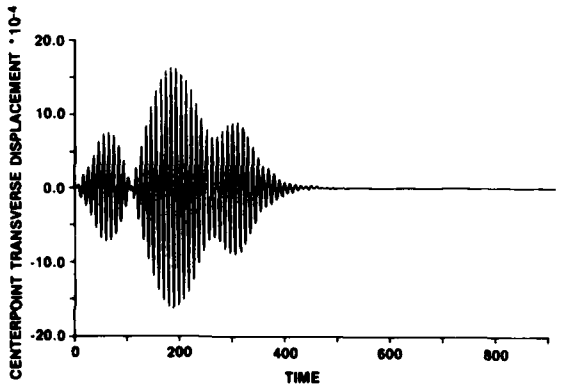

Fig. 10 - In-Air Centerpoint Dynamic Response of a Simply-Supported Aluminum Plate with an Aspect Ratio of 1.55 and Damping Factor of 0.1, Excited by a Translating/ Oscillating Concentrated Force with V = 596 in/s, f = 994 Hz

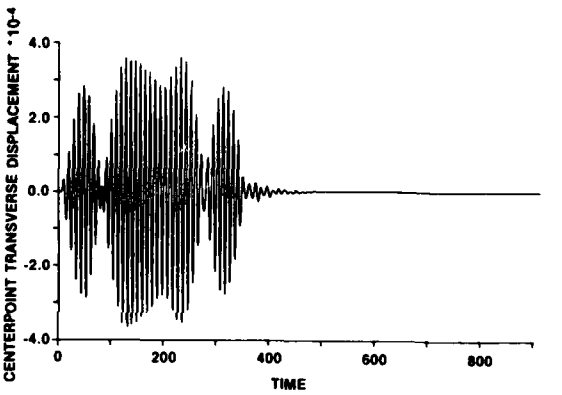

Fig. 11 - In-Water Centerpoint Dynamic Response of a Simply-Supported Aluminum Plate with an Aspect Ratio of 1.55 and Damping Factor of 0.1, Excited by a Translating/ Oscillating Concentrated Force with V = 596 in/s, f = 994 Hz

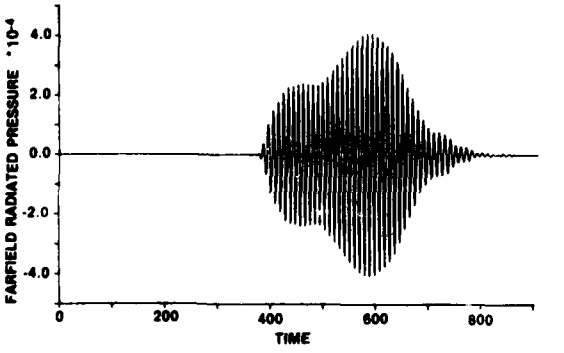

Fig. 12 - In-Air Transient Radiated Pressure of a Simply-Supported Aluminum Plate with an Aspect Ratio of 1.55 and Damping Factor of 0.1, Excited by a Translating/ Oscillating Concentrated Force with V = 596 in/s, f = 994 Hz Farfield Observation Point is at a Distance of 25 x L Normal to the Plate

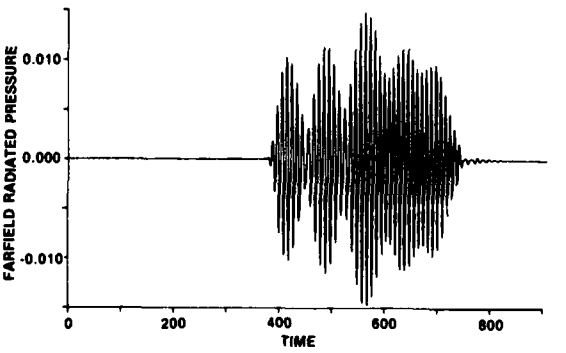

Fig. 13 - In-Water Transient Farfield Radiated Pressure of a Simply-Supported Aluminum Plate with an Aspect Ratio of 1.55 and Damping Factor of 0.1, Excited by a Translating/ Oscillating Concentrated Force with V = 596 in/s, f = 994 Hz Farfield Observation Point is at a Distance of 106 x L Normal to the Plate

ON THE FIELD EXPERIENCES OF UNDEX TESTING FOR A STIFFENED FLAT PLATE MODEL

T. R. Rentz* and Y. S. Shin**
Department of Mechanical Engineering
Naval Postgraduate School
Monterey, California 93943

ABSTRACT

An experimental investigation into the underwater shock-induced responses of a stiffened flat plate has been conducted. An air-backed flat plate with externally machined rectangular stiffeners and a clamped boundary condition was subjected to a shock wave loading by an eight pound TNT charge detonated underwater. The plate was instrumented to measure transient strains. The test structure acceleration and free field pressures were also measured. Pre-shot and post-shot calculations were performed using EPSA (Elasto-Plastic Shell Analysis) code. Many lessons were learned and important factors to be considered in the UNDEX testing are discussed.

INTRODUCTION

An experimental investigation into the underwater shock-induced responses of a stiffened flat plate has been conducted. The gross objective is three fold: (1) to investigate the tripping of stiffeners and its effect on gross shell responses using simple model, (2) to compare the experimental results with the predicted based on the existing computer code, and (3) to identify the problem areas and base technology needs in both experiment and prediction method.

The tripping effect is a lateral, torsional instability of the stiffener as it becomes suddenly unstable and fails under a load. Tripping is also viewed as a buckling and warping of the stiffener. In either case, the response of such structures as a stiffened flat plate or a cylinder with ring stiffeners will change dramatically when the functional character of the stiffeners is reduced after they have tripped. The need for this study and its applicability to Naval engineering is self-evident as stiffeners are incorporated in the structural design of all ships and submarines. The results of a previous series of tests on ship-type grillages have been described as "clearly demonstrating the significance of lateral-torsional instability (tripping) as a primary ductile failure mode for ship structure" [a].

DESIGN AND FABRICATION OF THE TEST STRUCTURE

The purpose of this research work is to conduct a series of experimental tests where plates of various stiffener types would be loaded by an underwater shock wave. The plate was geometrically similar to a ship's stiffened hull (or grillage) and air backed. This required a backing structure that was watertight and strong enough to be used throughout the test series. The plate was

* Lieutenant, United States Navy; formerly graduate student
** Associate Professor

subjected to large deformations, well into plastic regime, to ensure a good tripping effect in the stiffeners. As an aid in setting up and validating each test, it was necessary to model the test plate using a finite element computer code. Therefore, to ease the modeling requirements, the structure was kept simple throughout the design process. Well defined geometric and material properties and good boundary conditions were specified. As in any experimental test, the number of uncertainties were kept as few as possible.

Needed for the plate material was a common and easily machinable metal with the material properties of being initially isotropic and exhibiting very little strain hardening. 6061-T6 aluminum was selected because it has these properties and is readily available in the sizes required. It is easily machined and can be welded as well.

Upon receipt of the material, a section of the blank was removed and tension test specimens made from it. The uniaxial tension tests were conducted to characterize the 6061-T6 aluminum as having a yield stress (σ_y) of 43,200 psi and an ultimate stress (σ_u) of 44,900 psi. The recorded elongation is 11.5%.

As for the boundary conditions of the test panel, a clamped arrangement has proven in past shock tests to be most effective. The integral edge arrangement reported by Witmer and Wu [b] was adopted. This involved machining the test panel out of larger blank stock and leaving a massive edge on all four sides. Previous designs for a clamped boundary of a panel to be shock tested had employed such schemes as serrated clamps, massive bolts, or hardened faces, all of which had slipped to a degree. It was this final design of an integral edge which exhibits essentially no slip during loading [c].

The stiffeners were likewise integrally machined from the aluminum blank to eliminate any uncertainty that would arise from a welding procedure. All corners and intersections were rounded to remove any stress concentrators.

To model a typical ship's grillage requires the use of scaling laws. There are two important parameters, β and λ, for scaling of the grillage [d],

$$\beta = \frac{b}{t}\sqrt{\frac{\sigma_y}{E}} \qquad (1)$$

and

$$\lambda = \frac{a}{k\pi}\sqrt{\frac{\sigma_y}{E}} \qquad (2)$$

where

σ_y = material yield strength;

E = Young's modulus;

b = spacing of the longitudinal stiffeners;

t = plate thickness;

k = radius of gyration of longitudinal stiffener acting with an assumed effective width of plating denoted by b_e;

a = spacing of the transverse frames;

b_e = effective width of plating given by $b_e = b\,(\frac{2}{\beta} - \frac{1}{\beta^2})$.

The two parameters are defined such that β is a measure of the plate's slenderness ratio and λ is a measure of the slenderness of the longitudinal stiffeners [a].

A survey of typical ship's grillages yields [d]:

$$1 < \beta < 4.5 \text{ and } 0.15 < \lambda < 0.90.$$

The final dimensions of the test panel are shown in Figure 1. For the test panel, the calculated values of β and λ are 2.0 and 0.9 respectively. They fall within the range of a typical ship's grillage and the test panel is an acceptable model.

The final design is a panel 18 inches by 12 inches and 3/16 inch thick machined from a 2 inch thick aluminum blank measuring 33 inches by 27 inches. There are two stiffeners located symmetrically about the centerline. The stiffeners are on the exposed external surface so that the loading conditions at the center will be compressive in nature to make the stiffeners tripping.

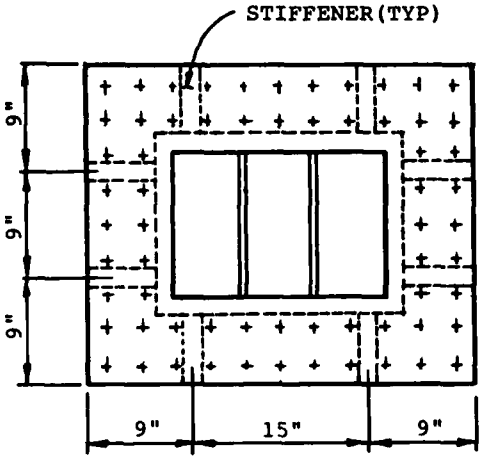

PLAN VIEW

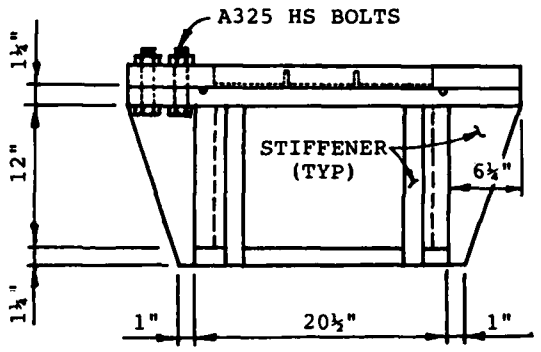

ELEVATION VIEW

NOTE: MATERIAL OF BACKING STRUCTURE IS A36 STEEL AND PLATE THICKNESS IS 1½".

Fig. 1 - Test Panel Configuration

A bolting arrangement between the test panel and the backing structure was designed to aid the clamped boundary conditions and to ensure a watertight seal throughout the loading. The final design is a double row of 64 bolts all around as shown in Figure 1. They are 1 inch in diameter, A325 high strength structural steel in a friction-type connection under single shear loading. An eyebolt is located at each corner for ease in handling and rigging.

The backing structure is entirely made of standard structural A36 steel, 1.25 inches thick. The details are shown in Figure 2. An O-ring gasket is fitted into the channel machined in the surface of the flange. A hull penetrator type connector is fixed to the bottom center to allow for internal instrumentation. A steel collar is welded around the exposed penetrator to prevent damage during handling and testing. The penetrator is a 24-pin model made by SEACON, part no. XSM-BCR. The mating connector used during the test is part no. XSM-CCP, with a 40 foot length of 16 gage cable attached. The backing structure weighs approximately 758 pounds. The test panel weighs 126 pounds, and the nuts and bolts weigh 111 pounds, for a total weight of the test structure of 1,000 pounds. This is massive and strong enough to withstand repeated shock tests. Figure 3 shows the backing structure during assembly and the assembled structure.

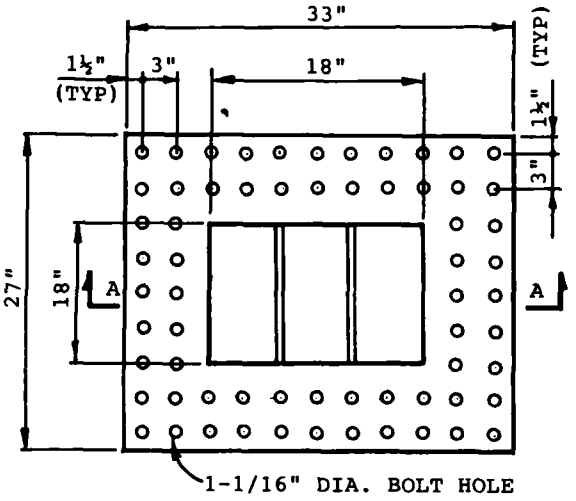

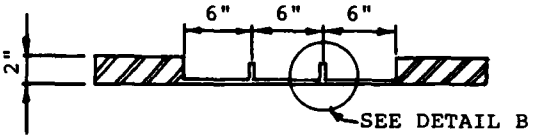

SECTION A-A

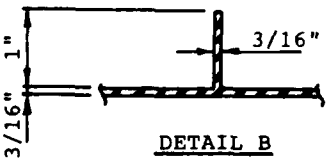

DETAIL B

Fig. 2 - Details of Backing Structure

TEST GEOMETRY

The inelastic response of the stiffened panel which this test is to examine requires that the plate undergo large deflections. The desired magnitude of these deformations is on the order of four plate thicknesses. To achieve this result, pre-shot computer calculations must be made which specify the appropriate charge weight and standoff distance.

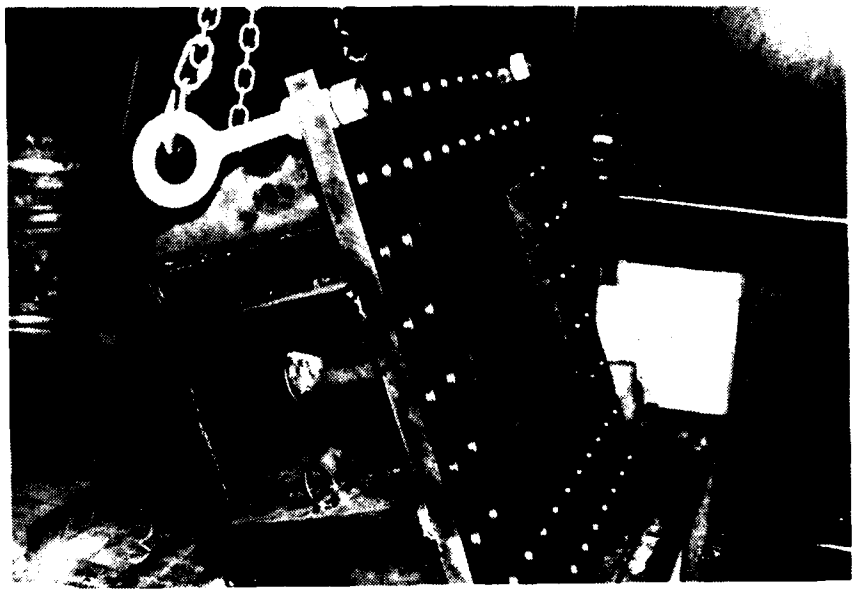

(a) Backing Structure During Assembly

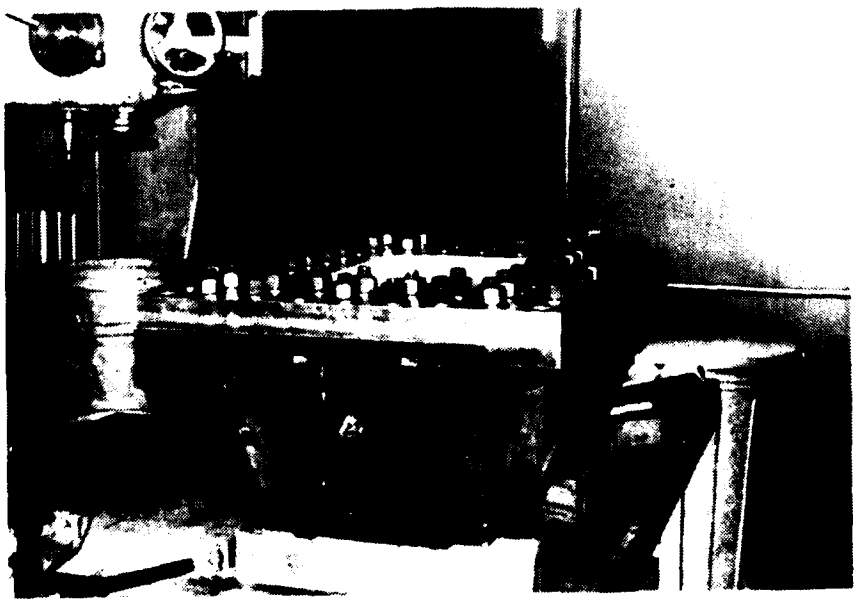

(b) Backing Structure with Test Panel

Fig. 3 - Backing Structure

To determine the pressure at a point as a function of time, an equation is written in a general form as [e]:

$$P(t) = P_{max}\, e^{-t/\theta} \qquad (3)$$

where the maximum pressure is

$$P_{max} = K_1 \left(\frac{W^{1/3}}{R}\right)^{A_1} \text{ psi} \qquad (4)$$

and the exponential decay constant is

$$\theta = K_2 (W^{\frac{1}{3}}) \left(\frac{W^{1/3}}{R}\right)^{A_2} \text{ msec} \qquad (5)$$

While the forms of these equations have been accepted as correct and invariant, the coefficients K_1, A_1, K_2, and A_2 are determined from data taken from numerous tests and are redefined as more accurate data is obtained. Due to the fact that the values will differ with different types of explosives, the first step in determining a test geometry would be to specify the explosive. An eight pound TNT charge was chosen due to its availability. The coefficients for TNT are:

$K_1 = 22{,}505$ $\qquad$ $K_2 = 0.058$

$A_1 = 1.18$ $\qquad$ $A_2 = -0.185$

The values of W and R are the charge weight in pounds and the standoff distance in feet, respectively.

The pre-shot calculations were performed using EPSA (Elasto-Plastic Shell Analysis) code to determine test model geometry, standoff distance in relation to eight pound TNT charge weight, selection of types of strain gages and accelerometers. The analysis indicated the best standoff distance between the eight pound charge and the test plate was nine feet.

As in any experimental investigation, the test environment must be as ideal as physically possible. The test conditions desired were that they be repeatable, that they concentrate on the effect of the shock wave loading, and that they remain clean and free from any of the secondary effects associated with underwater explosions. An attempt was made to eliminate or minimize such phenomena as bulk cavitation and cavitation closure, the reloadings from the explosive gas bubble pulse and bubble migration, and the surface cutoff and bottom reflection. The effects of cavitation closure and bubble migration have been mitigated by proper test geometry. Most of these phenomena are considered late time effects and are eliminated by only looking at the plate response during the first few milliseconds of pressure loading. Furthermore, this early time restriction allows for the modeling of the fluid/structure interaction in a most simple and convenient manner. The plate response may be determined by approximating the loading as the plane pressure wave. To consider the late time or even intermediate characteristics of the fluid/structure interaction would require entirely different approximations [f].

One of these late time effects which can be destructive in nature is the reloading generated by the explosive gas bubble. There are two distinct phenomena caused by the gas sphere: an expansion and contraction cycle which generates additional pressure pulses and thereby reloads the structure; and the tendency for the bubble to migrate towards a structure if it is close enough, and to then collapse upon it and do destructive work. Fortunately, empirical equations have been determined which permit the calculation of the bubble radius as a function of time and the time of the first closure pulse. These two equations are similar in form to the pressure equation. The coefficients are determined by the type of explosive and the variables are the charge weight and the charge depth. The general equation and its associated coefficients for TNT are as follows [e]:

Time of first closure pulse

$$T = K_5 \frac{W^{1/3}}{(D + 33)^{5/6}} \text{ sec} \qquad (6)$$

Maximum bubble radius

$$A_{max} = K_6 \frac{W^{1/3}}{(D + 33)^{1/3}} \text{ ft} \qquad (7)$$

$K_5 = 4.268$

$K_6 = 12.672$

An eight pound charge weight with a nine foot standoff distance has already been selected to produce the desired deformation. W = 8 pounds and charge depth in feet are run iteratively in these equations to satisfactorily meet two conditions. First, the time of the closure pulse is to be relatively late, well beyond the first few milliseconds.

Secondly, the charge depth needs to be such that, as the bubble expands to its maximum radius, it will break the surface of the water and vent to the atmosphere before it contacts the plate. This venting action is considered instantaneous and the bubble is prevented from expanding or contracting further if it breaks the surface when it is near its maximum radius. A ratio of charge depth to maximum radius in the neighborhood of .50 to .75 will ensure a good venting action. A charge depth of four feet was determined to produce the desired results. The calculations are shown below.

$$T = (4.268)\ \frac{8^{1/3}}{(4 + 33)^{5/6}} = 0.421 \text{ sec}$$

$$A_{max} = (12.67)\ \frac{8^{1/3}}{(4 + 33)^{1/3}} = 7.60 \text{ ft}$$

$$\frac{\text{Charge Depth}}{\text{Maximum Bubble Radius}} = \frac{4.0}{7.60} = 0.526$$

A charge depth of four feet is 53% of maximum bubble radius and it will therefore vent.

Another underwater explosion phenomenon which can be eliminated through the proper test geometry is the bulk cavitation effect. The region of water that will cavitate is a function of depth and range from the explosion source. The cavitation is created when the reflected wave from the surface passes through the water directly behind the primary wave front. Figure 4 depicts the generation of bulk cavitation (courtesy of Weidlinger Associates).

The effect this cavitated region has on the structure is that the plate will experience essentially no pressure loading while it is surrounded by cavitated water. However, when the combined forces of atmospheric pressure and the weight of the water above the region overcome the cavitating forces, the cavitation suddenly closes back up to generate a reloading on any structure within the region. Although the pressure associated with this cavitation closure can be calculated using available computer codes, these calculations are extremely involved. The best solution for the experimental test in question would be to remove the test structure from the cavitated region entirely. This necessitates the use of equations which define the extent to which cavitation will occur, based on charge size, type, and location. The

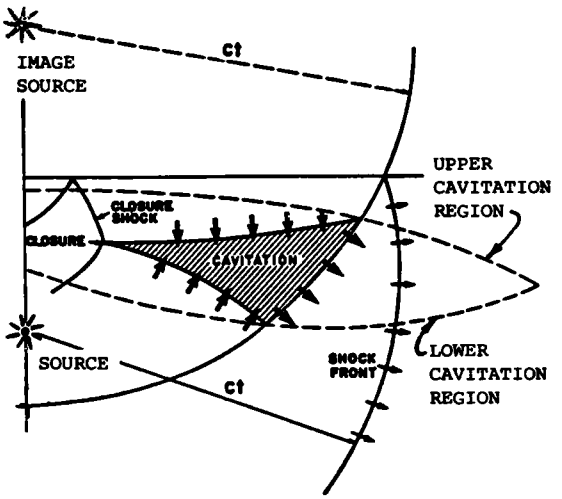

Fig. 4 - Development of Cavitation

region of bulk cavitation is calculated using Gordan-Costanzo Method and shown in Figure 5.

The result of all calculations is a vertical charge/plate orientation with the charge located directly over a flat, horizontal plate. The eight pound TNT charge would be suspended at a depth of four feet and the test structure nine feet beneath it at a depth of thirteen feet. Theoretically, this test geometry would create a test environment which is clean from those effects which are burdensome to calculate and reproduce while still producing the desired deformations in the plate.

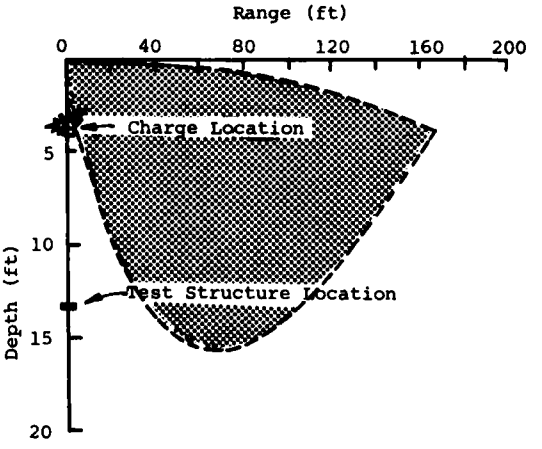

Fig. 5 - Region of Bulk Cavitation

The pressure gages used were one quarter inch tourmaline crystal gages, manufactured for the Navy at the Naval Surface Weapons Center. They are rated for a reliable sensing of pressures up to 10,000 psi, although greater pressures have been accurately measured with this type of gage. The Naval publication listing the specifications for the tourmaline gage [1] indicates that the quarter inch diameter gage is an adequate size gage for the test. As presented on page 16 of the report, the method of determination of proper gage diameter is:

θ, for explosive charge = .15 msec

t_D, transit time of shock wave across gage

$$t_D = \frac{0.25 \text{ inch}}{60{,}000 \text{ in/sec}} = 4.167 \times 10^{-6} \text{ sec}$$

$1.5t_D$, to account for oil filled boot

$$= 6.25 \times 10^{-6} \text{ sec}$$

$$\theta/1.5t_D = 24$$

and from the chart on page 17,

R_P = the pressure response ratio

(= the apparent pressure/actual peak pressure = .9793)

This is well within the acceptable correction limit of 15%. The pressure gage greatly affects the accuracy of the peak pressure measurement due to its finite size and, therefore, orientation of the gage is important. The publication indicates that all measurements and calibrations of the tourmaline gages are based on a sideways or horizontally positioned gage. It was not until after the test was it realized that the second gage, located on the side of the box in a vertical orientation, was not in the ideal position.

After the test structure was positioned in the water, the explosive charge was taken out to it and the detonators inserted. The charge was run down to depth and secured in position by a lanyard in the rigging. This ensured a center position over the plate. The eight pound TNT charge for which all pre-shot calculations were made was ordered by the WCSF. Although it is considered a standard stock item for the Navy, it proved difficult to obtain. A counter-proposal was made to use what was available: sixteen 1/2 pound TNT charges, which could be bundled together to form one charge. This configuration is shown in the lower right hand side of Figure 7. It was fixed with an exploding bridge wire (EBW) detonator inserted in each of the four center charges. The test was conducted on February 29th, 1984.

RESULTS AND INTERPRETATION OF DATA

This section will present the physical results of the test, then the data obtained, followed by a discussion on the limitations of the instrumentation, then the lessons learned from the test and methods of improving future tests of this nature.

Large deformations of the plate were achieved and the pattern, as seen in Figure 9 is as anticipated: symmetrical, with the greatest deformation in the center measuring 1.45 inches. EPSA predicted 1.24 inches as the maximum displacement at the center node at a very early time, 1.8 msec. A precise measurement of the final deformation was performed after the shot. A deformation measurement rig was designed which would support a dial indicator depth gage as it was traversed across the plate. The readings obtained are presented in Figure 10. These were taken before the plate was removed from the backing structure to preclude any relaxing that may occur when the plate is removed from its rigid support.

EPSA's results are considered very good. It must be understood that EPSA did not take into consideration any of the possible secondary effects which may have loaded the plate, most notably the afterflow loading generated by an accretion of water particles on the plate due to the downward and rigid body motion of the test structure. Moreover, some unpredicted plate responses also occurred which otherwise would have allowed the plate to deform to a greater extent. There was an unexpected shearing of the stiffeners from the edges at each end, as seen in Figure 9b. The other response that was not planned, but considered a likely occurrence should the loading be excessive, was a tearing of the plate at the center cavity. A close-up photo of the tear is shown in Figure 9b. The only other physical damage to the test structure was a parting of two shackles which attached wire ropes to one of the pneumatic fenders, a severe deformation of the brass terminal connection box on the side of the backing structure, and a shearing of the threads on the hardened plastic connector in the base.

PRE-SHOT ANALYSIS

A numerical analysis was performed using a finite element model of the test plate. The non-linear elasto-plastic plate responses (deformation, strain and stress) were predicted using EPSA (Elasto-Plastic Shell Analysis) code [g-k]. EPSA is a modified finite element computer code developed by Weidlinger Associates for the purpose of the analysis of submerged stiffened shells under shock loading. The theoretical basis of the code includes: (1) the nonlinear shell equations are of the Donnell-Vlasov type for the thin shells, (2) combined finite element/ finite difference technique for the shell element, (3) Doubly Asymptotic Approximation (DAA) for the fluid-structure interaction, and (4) the effects of local cavitation for the shock wave pressure variation.

The calculated displacements were used to check the test geometry to ensure the necessary deformation was occurring during the initial loading. Also, the calculated strains were used to select the type and locations of strain gages. The maximum value of strain was used to set the instrumentation levels prior to the testing.

Because this test assumes that theory can only accurately predict the plate response for the first few milliseconds of shock wave loading, EPSA was run for this limited time frame. The fluid-structure interaction used only a plane wave approximation which does not limit the analysis to early time. For an infinite flat plate, the structure radiates a plane wave. For a finite plate, there will be edge effects, but the plane wave approximation will suffice for many milliseconds. The later time effects within the code (the virtual mass approximation [VMA] in the doubly asymptotic approximation [DAA]) are turned off. The addition of VMA through the use of the DAA would not appreciably enhance the results in the case. Additionally, since EPSA was originally written to model cylindrical shells, either with or without internal stiffeners, modifications were made to permit the modeling of flat plates with external stiffeners. The details of modifications are described in Reference [k].

The discretization of the plate is shown in Figure 6. A quarter model of the plate was generated using the symmetry. The quarter plate is 16 elements by 10 elements with 187 nodes; each element would physically measure 0.52 inches by 0.60 inches. An application of the Courant stability criterion for finite element codes shows the timestep size to be sufficiently small to avoid numerical instability. This is also shown in Figure 6.

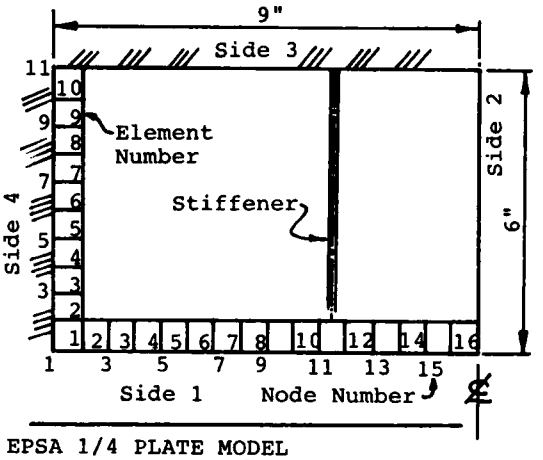

EPSA 1/4 PLATE MODEL
16 Elements by 10 Elements,
640 for Full Plate
Element Size: 0.6" x 0.5625"

FOR COURANT STABILITY CRITERION

Time Step Size, $\Delta t \leq (1/2)\delta_{min}(\frac{\rho}{E})^{\frac{1}{2}}$

$\delta_{min} = [(\frac{0.5625}{2})^2+(\frac{0.6}{2})^2]^{\frac{1}{2}}$

$= 0.4112"$

$\Delta t = (1/2)(0.4112)(\frac{0.000255}{10x10^6})^{\frac{1}{2}}$

$= 1.04\ \mu sec.$

Fig. 6 - Discretization Scheme for EPSA Model

The results show that the maximum displacement of 1.24 inches occurs at the center of the plate and at 1.8 msec after the arrival of the shock to the plate. The maximum strain of 0.063 occurs at the strain gage location #9 as shown in Figure 8. The maximum von-Mises stress of 55,305 psi is also calculated, which is well above the yield stress of 43,200 psi, which is located at the top of the center of the plate.

UNDERWATER SHOCK TESTING

With the design and manufacture of the test structure completed, a satisfactory test geometry determined, and a pre-shot analysis accomplished with a computer model, the next step in the experiment was to determine what instrumentation would be necessary, and where and how to attach it.

The usual suite of instrumentation for an underwater shock test consists of pressure gages in the free-field to sense the pressure loading generated by the charge, strain gages on the test surface to output strain and deformation, and velocimeters and accelerometers on the structure to measure the velocity and acceleration imparted by the impulsive load. The West Coast Shock Facility (WCSF) was selected as the site for the test due to several factors. The shock facility is located 120 miles north of Monterey in the South Bay of San Francisco.

Figure 7 shows the actual test geometry. Flotation for the test structure was provided by the two pneumatic fenders (cylindrical shaped). The strong back I-beam was removed prior to the shot, as it was used solely for positioning the rig into the water. A wire rope was run from the pier and shackled to the backing structure as a safety measure. This would be used to retrieve the structure from the bottom should the explosion part the supporting lines. Once the test rig was submerged and the strong back removed, the outhaul was taken across the water by boat to a parallel pier and drawn tight by a winch. The test was conducted between these two piers, approximately 100 feet from the nearest one, and in about 50 feet of water. The tide was high and little to no current was present.

The shock facility could support the test with 2 FM tape recorders which would allow for 24 tracks of data recording (14 tracks per recorder, 12 tracks for data, with one track for voice/countdown and one track for a one KHz time signal). It was decided that the 24 tracks be divided among two pressure gages, one accelerometer, and twenty one strain gages. No velocimeter was used during the test because there was not enough space inside the air-backing structure where it would be mounted.

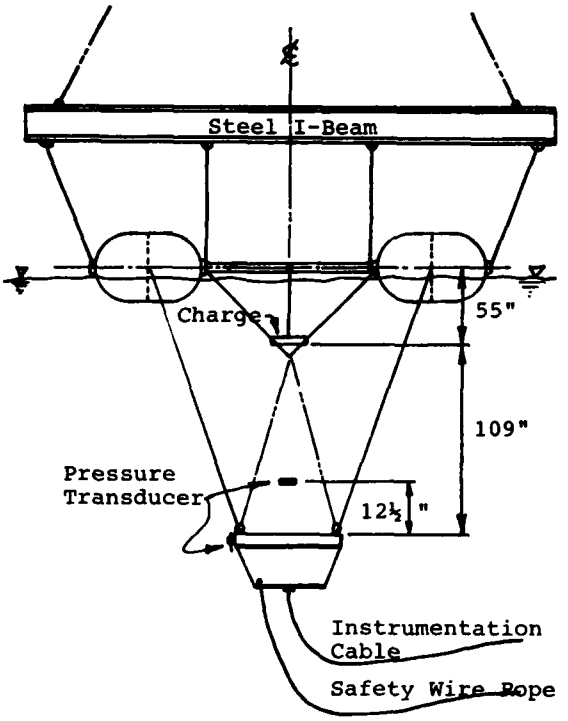

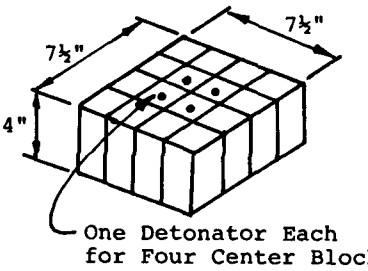

16 - 1/2 lb TNT Assembly

Fig. 7 - Test Rig at West Coast Shock Facility and Charge Assembly

The acclerometer used was an Endevco peizoresistive gage, model 2262-2000, with a range of ± 2,000 g. Ordinarily, an accelerometer would be mounted into the back of the plate so the acceleration imparted to it may be recorded. Additionally, this acceleration could be integrated to obtain a plate velocity, and integrated again for displacement. A calculation of the theoretical plate acceleration was made using the Taylor Flat Plate Theory to see if it was within the limit of the gage. The calculated acceleration amplitude was in the order of 69,000 g.

This is in excess of the Endevco accelerometer's rating or of any accelerometer. The plate is too thin and the impulse too severe to attach an accelerometer to it. The other alternative was chosen and the accelerometer was screw-mounted into the base of the backing structure. In this manner, responses of the entire test structure were monitored, and as discussed later, with good results.

Locations for the twenty-one strain gages were determined based on the following considerations: symmetry, maximum plate response, stiffener response, and finite element discretization. Gages were located in the X and Y directions so that the recorded output could be compared to the EPSA output. Pairs of gages were positioned in the center cavity of the panel to record maximum plate response and a pair was positioned on the underside of the plate, internal to the backing structure, to check out fiber strains against an exterior pair of gages. The balance of the strain gages were divided among the stiffeners and the plate. They were mounted on the top of the stiffeners and on the sides, both in the Y direction only.

Figure 8 shows the strain gages fixed to the exterior surface of the test panel. The strain gages used were Micro Measurements type EA-06-250BG-120, 120 ohm, rated at 3% to 5% strain limit in tension or compression. The cement used was Permabond 910. The details of bonding techniques can be found in Reference [k].

An adhesive sealant was required to secure the strain gage lead wires to the plate. On this aspect, the advice of the engineers at the Underwater Explosion Research Division of DTNSRDC, Norfolk, VA was followed. A saltwater resistant epoxy was applied directly on the gages and the wires. This smoothed out while setting to allow for good hydrodynamic flow. The material is a dichromate sealant manufactured by Products Research Corporation and labelled 1422A1, the last digit being a 1 hour work life.

The locations of the free field pressure gage are shown on the test geometry sketch, Figure 7. One is located a foot above the center of the plate and suspended by elastic shock cord and manila line. The location of this gage was selected so that it would sense the same pressure wave which

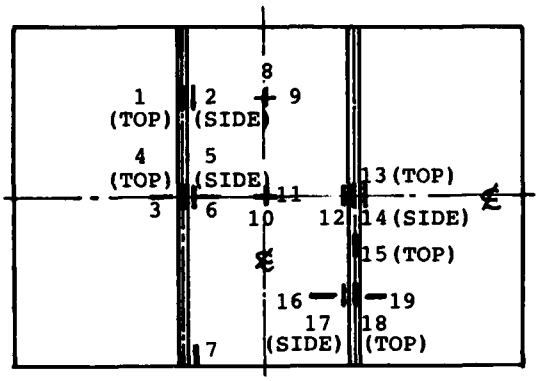

(a) External Face of Test Plate

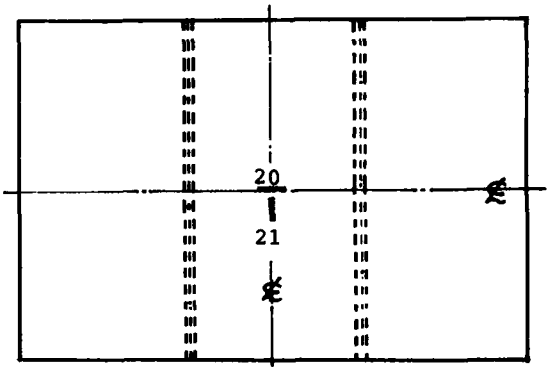

(b) Internal Face of Test Plate

Fig. 8 - Strain Gage Locations of Test Plate

loads the plate. This was considered an important enough criteria to locate the gage above the plate, even though the reflected positive wave from the plate surface would reload the gage at approximately 0.4 msec.

The second pressure gage should therefore be located away from the test structure, preferably out in the free field, on an arc of the same radius as the plate. Rigging limitations prevented this arrangement, so it was positioned at the same radius as the plate by clamping it to the side of the test panel. A mounting block, three inches thick was fixed to the panel so the gage would be somewhat removed from the boundary effects that the incident pressure wave would create at the fixed edges of the panel.

POST SHOT MEASUREMENT IDENTIFICATION NUMBERS

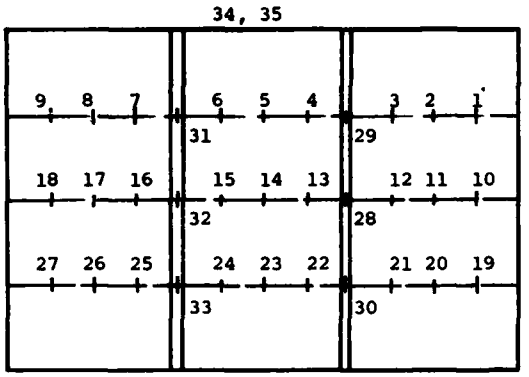

1)	0.226	2)	0.466	3)	0.689	4)	1.122
5)	1.186	6)	1.125	7)	0.687	8)	0.473
9)	0.234	10)	0.293	11)	0.599	12)	0.855
13)	1.376	14)	1.453	15)	1.384	16)	0.887
17)	0.609	18)	0.306	19)	0.221	20)	0.428
21)	0.591	22)	0.918	23)	0.978	24)	0.912
25)	0.587	26)	0.431	27)	0.221	28)	1.153
29)	0.909	30)	0.703	31)	0.909	32)	1.149
33)	0.739						

34) Length of tear 8.0

35) Maximum displacement difference along tear 0.478

All measurements in inches

Fig. 10 - Post Shot Deformation Measurements

After the shot, an accurate EPSA prediction of stresses in the plate was finally produced. Figure 11 shows the von Mises stress levels for the quarter plate model at time 1.2 msec after the shock wave loads the plate. The maximum stress is 55,305 psi, well above the yield stress of 43,200 psi. It is located at the top of the center cavity, suggesting that the plate should tear first at this point of maximum stress. The experimental results confirm this.

A shearing of the stiffener at the ends is not indicated by the stress plot. To understand this tearing phenomenon, it requires a description of the way EPSA treats stiffened elements. To model the stiffener running through a column of elements, EPSA determines the mass of the 1 inch by 3/16 inch stiffener and adds the corresponding amount to the shell elements in the column. The orthotropic nature of a stiffened element is

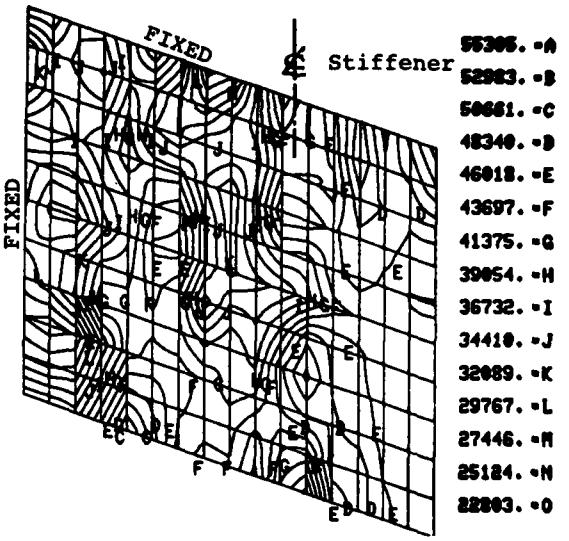

Fig. 11 - von Mises Stresses Predicted by EPSA

handled in the following manner. For each of these elements, strain increments are used to compute stress resultants in the shell. These same strain increments are transformed to the centroid of the stiffener. Using constitutive equations for a beam, these strains are converted to stresses in the stiffener. Finally, these stress resultants are used to modify the membrane forces and bending moment in the plate element in the direction which the stiffener runs. The final result is a single stress at the mid thickness of the plate. With the current method of EPSA output, stresses cannot be evaluated at the extreme fibers of a stiffener, nor at the fixed boundary where shearing occurred. EPSA, like all other finite element codes, outputs stresses at the centroid of the plate element. Hence, by making the element size smaller, stresses close to the boundary can be computed.

It was successful to record test data on all twenty-four channels. As to the quality and the worth of the data, that is still to be determined. A description of the appearance of some typical recordings are contained herein, along with reproductions of the traces, but there is insufficient room in this paper to include all data histories.

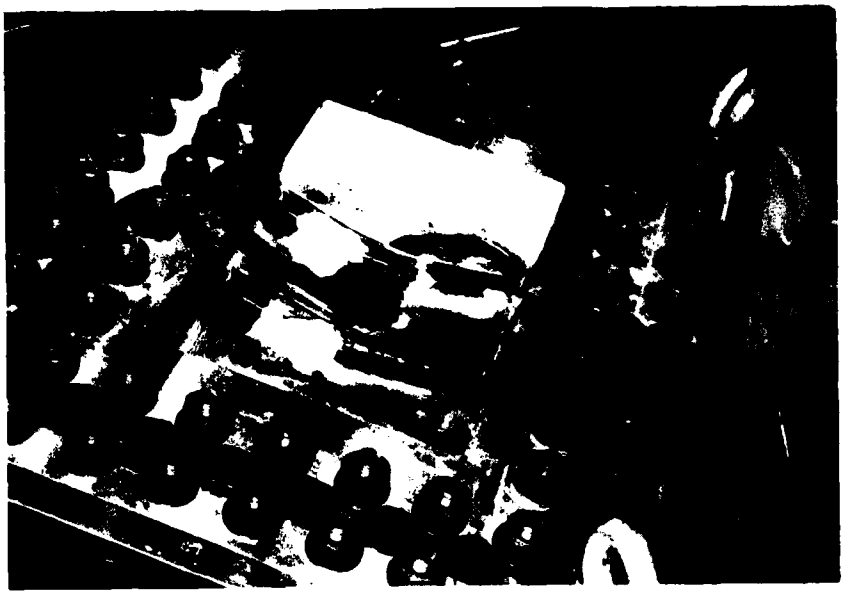

(a) Test Panel Deformation

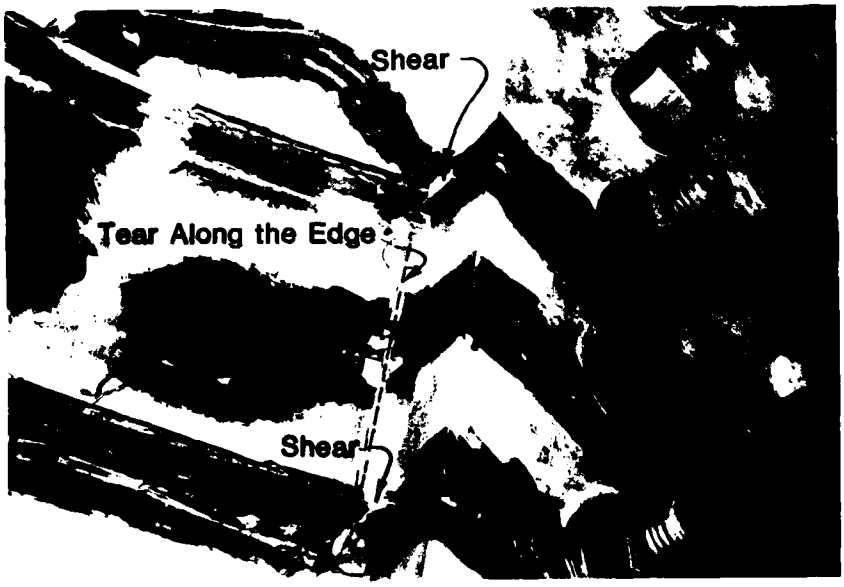

(b) Stiffener Sheared at End

Fig. 9 - Test Panel Damages

It shows the deformation pattern and the stiffeners with only a slight out-of-plane twist. It is evident that the tripping effect desired did not take place. Also to be noticed is that a few of the strain gages became detached from the stiffeners during the test. One of them is lifted above the stiffener surface. It is also observed that the shearing of the lead wires which were laid on top of the stiffeners parted at the same instant each of the stiffener ends sheared.

Data reduction at the test site consisted of a tape playback into a Visicorder unit. All of the strain gage histories, pressure and accelerometer histories were displayed on visicorder paper, along with the calibration signal for each of the above and a one kHz time signal. Reference [k] describes the instrumentation and recording procedure. Tape playback was at 7-1/2 ips and Visicorder speed was 80 ips. This was for an initial look at the data and for later reference.

The recorded histories from the two pressure gages appear as though the ratings of the instrumentation may have been exceeded. Also, it appears as if there is a signal driving the instrumentation beyond its maximum setting of 10,000 psi and causing its output to maintain this peak throughout the time of shock wave loading. Figure 12 is a reproduction of the Visicorder output.

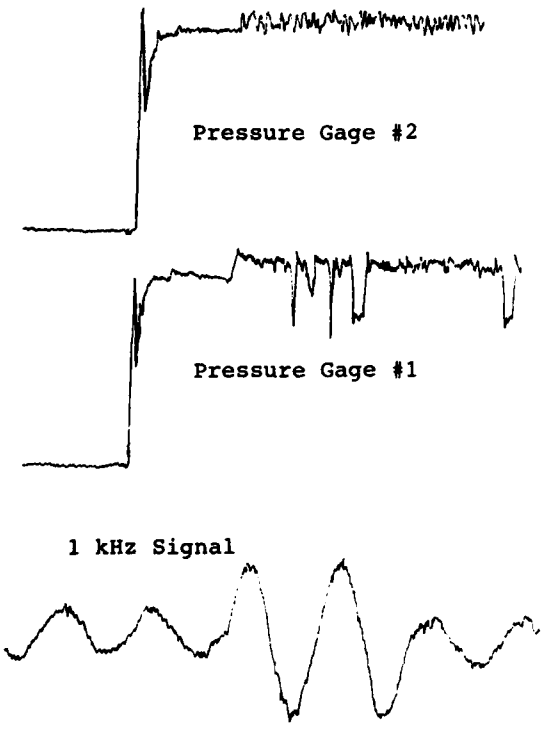

Fig. 12 - Visicorder Output for Pressure Gages

Shown are the traces for pressure gages one and two, located one foot above the panel and on the side of the panel respectively, and for the 1 kHz time signal. Calibration of the amplitude in the time domain was performed by a simple procedure of laying measurements on a 3 inch x 5 inch card from the calibration signals and the 1 kHz time signals, then transferring them to the pressure history.

At the test site, the recording charge amplifiers were set to a maximum of 10,000 psi (exactly what seems to be recorded on both gages). As shown earlier, theory predicted an incident pressure from an eight pound spherical TNT charge to be 3,950 psi. One would suspect that the actual pressure developed by the use of 16 one-half pound charges may have been somewhat greater. Post-shot inspection revealed physical damage to both pressure gages. The leads inside the oil-filled sensing boot had become detached on one gage and the four tourmaline crystals in the other gage were delaminated. The time at which this damage occurred is unknown and such damage would have caused erratic readings.

Other damages for the excessive amplitudes include the possibility of a calibration error in the instrumentation or, as reported in the Compendium of Underwater Explosions Research [m], the multiple charges have a much enhanced effect over a normal, homogenous charge of equal weight. The pressures from each of the charges may be additive when they are detonated sympathetically. There is much research left to be done in this area of what is called the multiple charge effect. For example, the pressure generated by a single one-half pound charge and sensed at eight feet away is:

$$P = 22505 \left(\frac{0.5^{1/3}}{8}\right)^{1.18} = 1473 \text{ psi}$$

When using sixteen of these charges and they are arranged in such a manner that sympathetic detonation is induced, 16 x 1,473 = 23,569 psi. This is enough pressure to saturate amplifiers and damage pressure gages. In view of this, some of the questions raised include whether or not some or all of the charges were detonated sympathetically, or if there could have been a delayed effect due to the geometry of the TNT block. The authors fully believe that the shape and height of the plume was very different from that of a standard spherical charge. There may have been a concentrating or jet effect of the pressure due to the stacking and the geometry of the

charges. To quote directly from Cole, page 229, "... it can be expected that charges that do not have spherical symmetry will give rise to a shock wave which is not symmetrical, and differences in form of the wave at different points around the charge are in fact observed."

This statement leads one to question what shape of pressure history curve would be generated from the rectangular block of TNT used during the test. Fluid nonlinearities also affect the propagation of a shock wave and are difficult to predict, model, or reproduce. As an added note, the equivalent weight of TNT required to produce 10,000 psi incident pressure at eight feet is 65 pounds. Questions such as those raised above can only be answered through further experimentation and proper pressure field measurements. Cole concludes his chapter on pressure waves by stating that "while an exponential curve is a simple and convenient approximation to the form of an underwater shock wave, it is by no means a perfect representation, and in some circumstances, is a rather poor one." The question of what was the true pressure loading experienced by the plate may never be known. The data records are presented in the report for possible future insight and understanding.

Without the knowledge of the loading history of the plate an accurate prediction/comparison of the strains induced in the plate is impossible. A best fit correlation was attempted between the recorded strains and those predicted by EPSA for the two possible loading extremes; the smallest being an eight pound charge and the greatest being a sixty-five pound charge.

As can be seen from the strain comparison (Figure 13), nothing generated by the computer seems to come close to agreeing with the recorded data. All twenty-one of the strain records are difficult to interpret. There is an excessive amount of high frequency noise imposed on what may be a valid strain signal within the first few milliseconds. However, this noise could not be filtered out electronically. Curve fitting could be attempted, but to even do this would lead to suspect results. Erroneous signals were surely generated as the lead wires to the gages were pulled and twisted. They were glued to the plate surface

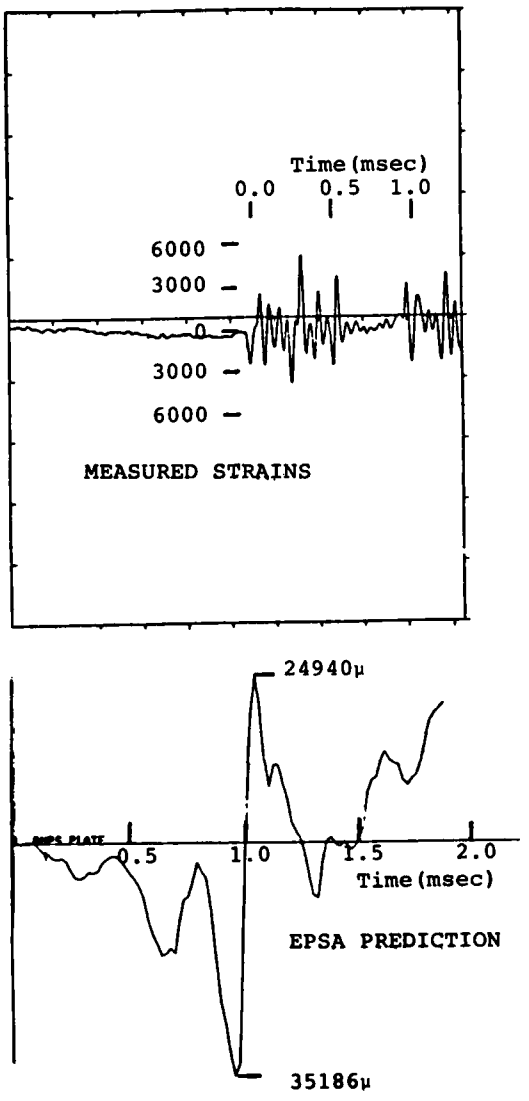

Fig. 13 - Measured Strains and EPSA Prediction

which was undergoing large deformations in very early times. Also, the lead wires which ran across the stiffeners were parted when the stiffeners sheared. Moreover, severe damage was done to the leadwire connection box on the side of the backing structure; wires were stripped and broken as the shock wave opened the box to the environment. Recommendations to avoid some of these problems in future tests are included later in this chapter.

Only the amplitudes of the first two peaks are tabulated; the validity of the subsequent recording is questionable. It is thought that the first sharp peak in the strain histories is the firing pulse signal.

The one instrument record which is readable and shows good results is the accelerometer history. This is shown in Figure 14 with the integrated velocity and displacement records. The three records appear as they should: the integration of an impulse is a step and the integral of a step is a ramp function.

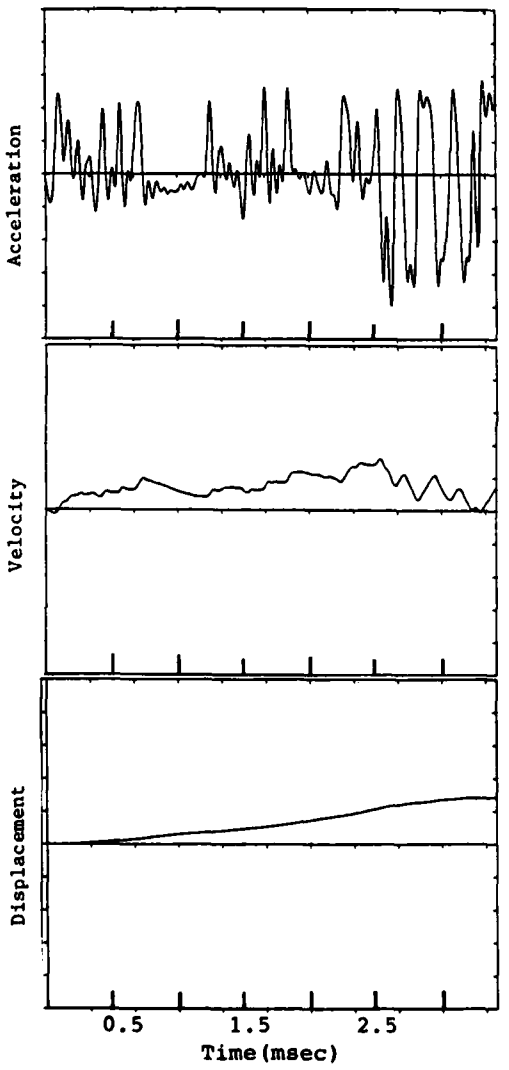

Fig. 14 - Measured Acceleration and Integrated Values for Velocity and Displacement: Backing Structure

Each of the instrument records clearly shows the firing pulse impressed on the electronic signal. This indicates that the wiring configuration was such that it was particularly susceptible to noise pickup and electrical interference. The first singular voltage spike is identified as the firing signal because it appears in each of the records in similar form. It is followed by a "dead-time" on each record where no other signals occur for at least 1.8 msec. This time corresponds to that necessary for the shock wave to travel nine feet from the charge to the plate. The shape of the firing pulses, and of many of the other sharp peaks on the records, are too similar and cause one to question why. An explanation is found in the Shock and Vibration Handbook by Harris and Crede [n]. It presents a thorough discussion on how improper or inadequate sensing, recording, and playback equipment will limit the frequency of signals which can be accurately measured. For example, listed on page 17-15 of the reference, the upper limit of FM magnetic tapes is 5,000 Hz, a light beam galvanometer is limited to 50,000 Hz, and AC carrier amp with demodulator is 5,000 Hz, and the same for an AC power supply. These numbers are representative only, and the equipments are not the same as those used during the test. However, the characteristic rise time for an impulse shock wave is five or six microseconds (as limited by the tourmaline 1/4 inch gage). This means that the electronic equipment must be sensitive to 200 kHz. The tape recorders used were Ampex 1300's which are rated at 20 kHz as a response time. This is precisely the recorded rise times for the firing pulses and peak signals on the data records. It is evident that the limitations of the equipment were exceeded during this shot. What should be used for tests of this nature are FM tape recorders with a much better response time, such as an Ampex 2200 or a Honeywell 101. A note of caution, however, is that the higher the frequency of the recording, the poorer the signal to noise ratio. Considerations must be given to a proper arrangement of filters and playback speeds to obtain the best records. Oscilloscope photography has provided good response histories in past experiments. This method should always be considered a possibility.

LESSONS LEARNED AND RECOMMENDATION

To properly set up the electronics for an underwater explosion test is an art in itself. Many lessons were learned and some of them will be briefly mentioned as items that should be considered in any future tests:

1. There must be a zero time signal on one of the data channels. This is necessary during the analysis phase so the time code, the gage histories, and the zero time can be lined up to measure small differences in arrival times.

2. If clipping of the signals is present, ensure that it is not caused by the playback electronics being oversensitive.

3. For the tourmaline pressure gage calibration, the Q-step method described by Cole (pages 182-3) is highly recommended.

4. There are corrective techniques to back out actual peaks in signal records should they be rounded due to equipment limitations. One of these methods is discussed by Ronald Tussing in his text on page 33 [1].

5. The firing circuit should be coupled to a transformer so as not to be grounded with the other gages. In this test, magnetic/inductive pick-up through the cables is thought to have caused the firing signal to be impressed on the other lines and perhaps creating a signal of such magnitude as to overdrive the amplifiers. In future tests it is essential that the cable used to transmit the firing voltage be positioned as far away from the recording lines as possible.

A chapter in Harris and Crede's text is titled "Interference and Noise in Transmission Cables." It brings out many important considerations and the means to correct them. For example, on page 12-21, it defines electrical interference or pickup as "Noise components superimposed on the desired signal due to the proximity of the connecting cable to the electromagnetic field of an electrical disturbance" ... "and 'static-type' disturbances from switching transients are the worst offenders." A solution offered is the use of properly shielded cables and the correct grounding of the circuit in relation to the electronic equipment.

Another source of signal interference mentioned by the text comes from the movement of the signal carrying-cables. On page 12-26 it cautions that "Noise is generated when the cable is suddenly squeezed, bent, struck, or mechanically distorted. Peak noise voltages from this source were frequently as large as the actual acceleration signals being recorded." A shock test is a dynamic phenomena and lead wires to instrumentation will be twisted and pulled as the shock wave impinges on them and as the plate deforms. There seems to be almost no way to eliminate this problem; however, there may be methods to reduce the effect this has on the signal. Rather than fixing the strain gage lead wires directly to the plate with the PRC adhesive/sealant, it is recommended that a sheath or tube arrangement be devised to permit the lead wires to move as the plate deforms. This should be done at least in the immediate area of the test panel where large displacements will occur.

Additional considerations must be given to the use of the correct type of strain gage. There are special high-elongation gages which can measure up to 10% strain with accuracy. Also pointed out in Reference [n] is that the dynamic type gage will have the greater gage factor and provide maximum possible electrical signal for a given strain. The use of an iso-elastic foil will have a greater gage factor than constantan and therefore a greater resistive charge for a given strain.

Another important aspect of the use of strain gages is that they are bonded properly to the test specimen. As pointed out by Harris and Crede on page 17-5, the proper functioning of a strain gage is completely dependent on the bond. One must use the manufacturer's recommended cement and follow the directions closely. Incorrect strains will result if the bond is not completely over the entire area of the gage, or if it becomes partly or fully detached during the test.

The recording of transient strains under dynamic loads is a mostly difficult task, as brought out by the work at M.I.T. by Dr. Witmer [o]. In a series of shock tests performed at the Aeroelastics and Structures Research Lab, only about 0.2 msec of data was the best that could be obtained.

Although the severity of the impulse for the experiments was much greater than that for the underwater shock test, the environment was much more controlled. The problems most often encountered were gage detachment and lead wire rupture. A very helpful procedure for the bonding of strain gages is presented by Dr. Witmer in his report, particularly with regard to the use of backing material to cover the gage.

As a final caution in this discussion on the instrumentation of a shock test, it would be wise to thoroughly check out the electronic recording set-up just prior to the test so that it is well known what will be the character of the signals, as distinct from interference noise. Suggested is a simple procedure of turning off all power supplies and striking the plate to see the strain gage response within the elastic regime. It is also most important for the individual conducting the test to have a complete understanding of both the nature of the test (including underwater shock phenomena, material response of the test structure, the desired results, etc.) and the electronic measuring and recording of the data. Both of these go hand-in-hand and must be tailored to provide meaningful data.

One final recommendation for future work in this area is a redesign of the test panel to allow for better tripping of the stiffeners. A single stiffener in the longer direction of the test section will provide a greater area for a stiffener to suffer compression. In any case, it is hoped that the work to date has paved the way for further research in this field of study.

REFERENCES

a. John C. Adamchak, David W. Taylor Naval Ship Research Center Report 79/064, "Design Equations for Tripping of Stiffeners Under Inplane and Lateral Loads," Oct. 1979.

b. R. Wu, and E. Witmer, "Analytical and Experimental Studies of Nonlinear Transient Responses of Stiffened Cylindrical Panels," AIAA J., Vol. 13, No. 9, pp. 1171-1178, Sep. 1975.

c. E.A. Witmer, R.W-H. Wu, and F. Merlis, Army Materials and Mechanics Research Report 74-29, "Experimental Transient and Permanent Deformation Studies of Impulsively-Loaded Rings and Cylindrical Panels, both Stiffened and Unstiffened," Apr. 1974.

d. C.S. Smith, "Compressive Strength of Welded Steel Ship Grillages," Journal of the Royal Institute of Naval Architects, No. 4, Oct. 1975.

e. R.H. Cole, "Underwater Explosions," Princeton University, Princeton, New Jersey, 1948.

f. T.L. Geers, "Residual Potential and Approximate Methods for Three-Dimensional Fluid Structure Interaction Problems," J. Acoustic Soc. Am., Vol. 49, No. 5, pp. 1505-1510, May 1971.

g. R. Atkatsh and R.P. Daddazio, "Dynamic Elasto-Plastic Response of Shells in an Acoustic Medium: User's Manual for the EPSA Code," Technical Report No. 27, Office of Naval Research, Mar. 1980.

h. "Elastic-Plastic Behavior of Plates and Shells," DNA 3954T, Weidlinger Associates, New York, New York, Mar. 1976.

i. M.P. Bieniek, J. Funaro and M.L. Baron, "Numerical Analysis of the Dynamic Response of Elasto-Plastic Shells," Tech. Report No. 20, Office of Naval Research, Nov. 1976.

j. R. Atkatsh, M.P. Bieniek and M.L. Baron, "Dynamic Elasto-Plastic Response of Shells in an Acoustic Medium: Theoretical Development for the EPSA Code," Technical Report No.24, Office of Naval Research, Jul. 1978.

k. T.R. Rentz, "An Experimental Investigation into the Dynamic Response of a Stiffened Flat Plate Loaded Impulsively by an Underwater Shockwave," Masters Thesis, Department of Engineering, Naval Postgraduate School, Monterey, California, Jun. 1984.

l. Ronald B. Tussing, Naval Surface Weapons Center Report 82-294, Accuracy and Response of Tourmaline Gages for Measurement of Underwater Explosion Phenomena," 1 Jul. 1982.

m. A. Booker and C. Harrington, "The Multiple Charge Effect," Underwater Explosion Research, A Compendium of British and American Reports, Office of Naval Research, Department of the Navy, Vol. 1, p. 1121, 1950.

n. C.E. Crede and C.M. Harris, "Shock and Vibration Handbook," 2nd ed., McGraw-Hill Book Company, 1976.

o. E.A. Witmer, et al., United States Army Ballistics Research Laboratories Report 134, "Experimental Studies of Explosively-Induced Large Deformations of Flat Circular 2024-0 Aluminum Plates with Clamped Edges and of Free Thin Cylindrical 6061-T6 Shells," Jan. 1974.

DISCUSSION

Mr. Schittke (IABG, West Germany): What was your test configuration? Did you have a central charge directly beneath the object, or was it semi-lateral?

Mr. Rentz: No. We used a single, eight-pound TNT charge in a vertical orientation above the plate underwater at a nine-foot standoff.

Mr. Schittke: Was the charge lying on the bottom, or was it suspended?

Mr. Rentz: The charge itself was four feet underwater. The plate was suspended 13 feet underwater, directly below the charge.

Mr. Schittke: If I remember correctly, you calculated a detonation pulse duration of about two milliseconds. Did you check to see if the original detonation pulse length was over at that time?

Mr. Rentz: Yes. It was over; two milliseconds was all we looked at using the EPSA code. It had decayed, and the pressure wave had passed by that time. I think the full decay was on the order of 1.4 to 1.5 milliseconds.

Mr. Allen (Honeywell, Inc.): When you use the EPSA code, you have two options on the stiffeners; they can either fail right away or they can be present. Which option did you use?

Mr. Rentz: We used a very basic version of EPSA; the option you mentioned was not available to me at the time.

Mr. Allen: When we used EPSA, we tried it both with and without the stiffeners failing right away. We got slightly different results when we used both options.

Mr. Rentz: No. We didn't use that, but I will look into that and see if it is available in our version.

Mr. Allen: Before you selected that code, did you verify it by looking at marine stiffened cylinders? Have you correlated your predictions with test data?

Mr. Rentz: No. That wasn't the intent of my thesis work. I wanted to get this program off the ground and to open the way for future thesis students who possibly may want to take this on for research. I didn't look at the explosive power meter. Were you referring to the EPM shots?

Mr. Allen: Yes.

Mr. Rentz: No. I didn't try to correlate with those.

ANALYSIS OF CAVITATION CAUSED BY SHOCK WAVE INTERACTION WITH A RESTRAINED MASS

Robert T. Handleton
David Taylor Naval Ship Research and Development Center
Underwater Explosions Research Division
Portsmouth, Virginia

A method for obtaining the motion of a restrained mass loaded by an underwater shock wave is developed through an analysis of the opening and closing of cavitation at the mass. Without making energy assumptions beforehand, the derived motion of the mass is used to calculate the fraction of the incident shock wave energy absorbed by the restraint over a range of parameters. The energy study provides a basis for judgments of the fraction of incident energy absorbed by a yielding surface.

INTRODUCTION

In the sense that all relevant physical processes are included, an exact solution for the cavitation caused by the relief of an underwater pressure wave is hard to obtain because questionable assumptions are made in modeling the phenomenon. A degree of error is introduced when the opening of cavitation is determined with the restraint inactive and the closure determined with the restraint active. Also, lumped parameter models include or omit initial water displacement at the time of cavitated particle kickoff and imply a questionable dissipation of energy as heat during cavitation closure. These considerations and others lead to some variation in the treatment of cavitation and the complexity of solutions. In this paper the restraint on a target mass is taken as constant and is active in the determination of both the opening and closing of cavitation, and cavitation is assumed initiated at absolute zero pressure. Under these conditions the cavitation process and the consequent displacement of the mass may be studied using equations integrable in closed form as was done in Ref. [1] for a free surface.

OBJECTIVE

The objective of this theoretical study is to provide the necessary cavitation parameters and predict the motion of a mass per unit area loaded by an underwater shock wave and restrained by a constant force per unit area. An additional objective is a study of the fraction of the incident shock wave energy per unit area absorbed by the restraint. The energy study will be undertaken after the solution for the motion of the mass has been obtained.

APPROACH

The analysis is one dimensional and an exponential shock wave is assumed. Hydrostatic and atmospheric pressures are present on the wet and dry sides of the mass, respectively. Also, a constant force resisting the mass when it is in motion is present. The situation may be modeled by an air backed piston sliding with a constant friction in a water filled cylinder. This simple model allows both the study of the cavitation produced by the relief of the shock wave through the restrained motion of the mass and the study of the total displacement of the mass, including the component produced by the closure of the cavitation (spray loading). Assumptions relating the energy absorbed by the restraint to the shock wave energy are not made. The energy relationship is derived from the total mass displacement.

MECHANICAL MODEL AND ANALYSIS

An exponential shock wave interacting with a mass is shown in Fig. 1. Individual water particles are

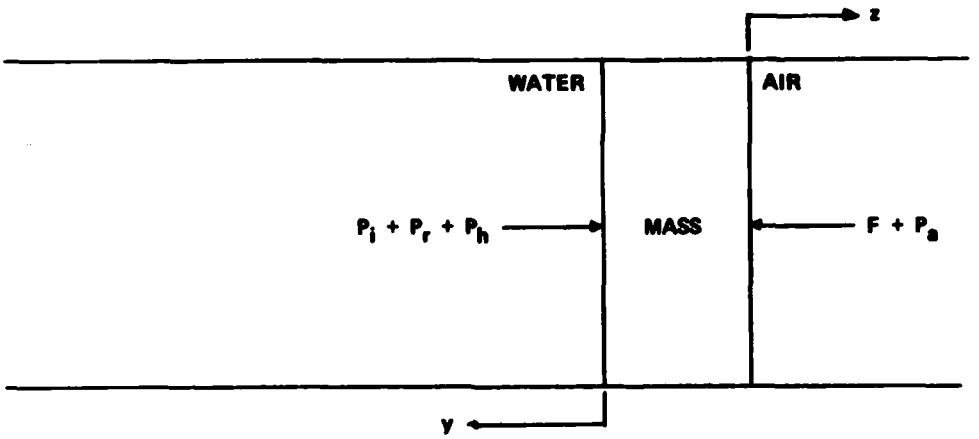

Fig. 1 - Shock Wave Interaction with Mass

identified by the undisturbed distance (y) from the mass to the water particle under consideration. The displacement of a particular water particle or the mass with respect to inertial coordinates is z. Time (t) is taken as zero at shock wave arrival at the mass which is located at y = 0. The mass is restrained by a force per unit area which is a constant (F) when the mass is in motion. When the mass is stationary the force is that between zero and F necessary to keep the mass in equilibrium with the hydrostatic pressure (P_h) and the atmospheric pressure (P_a). The shock wave parameters of peak pressure (P_o) and decay constant (θ) are assumed given along with the mass per unit area (m) of the mass. The density of water and the speed of sound in water are ρ and c respectively.

The incident pressure (P_i) as a function of t and y is given by the equation:

$$P_i(t,y) = P_o e^{-\frac{t+\frac{y}{c}}{\theta}} \qquad (1)$$

Under the pretense that water is a linear medium, the reflected pressure (P_r) as a function of t and y may be found by making use of the relationship:

$$P_i(t,0) - P_r(t,0) = \rho c \dot{z}(t,0) \qquad (1a)$$

The resulting solution for P_r is given by the equation:

$$P_r(t,y) = -P_o\left(\frac{1+\lambda}{1-\lambda}\right) e^{-\frac{t-\frac{y}{c}}{\theta}} + \left(\frac{2P_o}{1-\lambda} - N\right) e^{-\frac{t-\frac{y}{c}}{\lambda\theta}} + N \qquad (2)$$

where $\lambda = \frac{m}{\rho c \theta}$ and $N = F + P_a - P_h > 0$

The incident and reflected pressures given by Eqs. (1) and (2) are all that is necessary to calculate motion when the mass is moving forward and water is considered a linear medium. The velocity and displacement of the mass calculated from Eqs. (1) and (2) are given by Eqs. (3) and (4) respectively.

$$\dot{z}(t,0) = \frac{P_o}{\rho c}\left[\frac{2}{1-\lambda} e^{-\frac{t}{\theta}} - \left(\frac{2}{1-\lambda} - \frac{N}{P_o}\right) e^{-\frac{t}{\lambda\theta}} - \frac{N}{P_o}\right] \qquad (3)$$

$$z(t,0) = \frac{P_o\theta}{\rho c}\left[\frac{2}{1-\lambda}\left(1-e^{-\frac{t}{\theta}}\right) - \lambda\left(\frac{2}{1-\lambda} - \frac{N}{P_o}\right)\left(1-e^{-\frac{t}{\lambda\theta}}\right) - \frac{N}{P_o}\frac{t}{\theta}\right] \qquad (4)$$

For the purpose of this analysis, cavitation will be said to occur when the absolute pressure in the water drops to zero. No treatment for non-zero breaking pressures will be given. Under this condition, the equation determining the time of cavitation at a given location in the water is:

$$P_i + P_r + P_h = 0 \qquad (5)$$

providing the cavitated region is expanding supersonically at the location in question. The reason the supersonic expansion restriction must be put on Eq. (5) is that P_r was derived assuming a linear medium and cannot be used at locations in the water already reached by communication that cavitation has occurred elsewhere. In the most general situation cavitation starts at some distance from the mass and moves both toward and away from the mass. The limits of applicability of Eq. (5) may be determined by taking the total derivative of Eq. (5) with respect to time and substituting for dy/dt both minus and plus the speed of sound to determine the limits of applicability toward the mass and away from the mass respectively. A relationship between the time (t_o) and location (y_o) at which the expansion of the cavitated region toward the mass becomes subsonic is given by:

$$-c\,\frac{\partial\left(P_i+P_r+P_h\right)}{\partial y} + \frac{\partial\left(P_i+P_r+P_h\right)}{\partial t} = 0 \qquad (5a)$$

and results in:

$$\frac{t_o - \frac{y_o}{c}}{\theta} = \frac{\lambda}{1-\lambda}\ln\frac{\frac{2}{1-\lambda} - \frac{N}{P_o}}{\lambda\left(\frac{1+\lambda}{1-\lambda}\right)} = w_o \qquad (6)$$

Eq. (6) solved simultaneously with Eq. (5) for t_o and y_o gives the limits of applicability of Eq. (5) for determining the expansion toward the mass. Repeating the above procedure for expansion of the cavitated region away from the mass shows that the expansion is always supersonic approaching sonic velocity at $y = \infty$, $t = \infty$, and Eq. (5) applies without reservation. Eq. (6) suggests that the time of cavitation (t) and the location (y) at which it occurs be solved for in terms of the parameter w where $w = (t - y/c)/\theta$. Accordingly, from Eq. (5):

$$t = -\frac{\theta}{2}\left\{-w + \ln\left[\left(\frac{1+\lambda}{1-\lambda}\right)e^{-w} + \right.\right. \qquad (7)$$
$$\left.\left. - \left(\frac{2}{1-\lambda} - \frac{N}{P_o}\right)e^{-\frac{w}{\lambda}} - \left(\frac{F+P_a}{P_o}\right)\right]\right\}$$

and

$$y = -\frac{c\theta}{2}\left\{w + \ln\left[\left(\frac{1+\lambda}{1-\lambda}\right)e^{-w} + \right.\right. \qquad (8)$$
$$\left.\left. - \left(\frac{2}{1-\lambda} - \frac{N}{P_o}\right)e^{-\frac{w}{\lambda}} - \left(\frac{F+P_a}{P_o}\right)\right]\right\}$$

with w varying from w_o down to w_2. The lower limit of the w range, w_2, is the value of w which makes t and y in Eqs. (7) and (8) infinite. This is the value of w which makes the argument of the natural log term zero. The parameter (w_1) determining the time and location at which cavitation first occurs may be found by solving for the value of w which minimizes Eq. (7). This procedure results in the following equation which must be iterated to solution for w_1.

$$0 = -2\left(\frac{1+\lambda}{1-\lambda}\right)e^{-w_1} + \frac{F+P_a}{P_o} +$$
$$+ \left(\frac{2}{1-\lambda} - \frac{N}{P_o}\right)\left(\frac{1+\lambda}{\lambda}\right)e^{-\frac{w_1}{\lambda}} \qquad (9)$$

The water particle velocity (u) immediately after cavitation has occurred is found from Eq. (5) and the equation $u = (P_i - P_r)/\rho c$ and is:

$$u = \frac{2P_o}{\rho c}\left\{\left(\frac{1+\lambda}{1-\lambda}\right)e^{-w} - \left(\frac{2}{1-\lambda} - \frac{N}{P_o}\right)e^{-\frac{w}{\lambda}} + \right.$$
$$\left. - \frac{F+P_a - \frac{P_h}{2}}{P_o}\right\} \qquad (10)$$

EXPANSION OF THE CAVITATED REGION

A sketch of the cavitated region versus time may be made from the two points represented by w_o and w_1 and two sonic asymptotes. The parameters w_o and w_1 are found from Eqs. (6) and (9) respectively and their time and location coordinates are found from Eqs. (7) and (8). These points along with the sonic asymptotes of the curve are plotted as shown in Fig. 2 and the curve sketched in. The sketch in Fig. 2 shows that cavitation starts at some distance from the mass and rushes both toward and away from the mass. Depending on the numerical values in the problem, the point specified by w_o may have a negative y co-ordinate. In that case, cavitation stops when it reaches the mass (y = 0). In a previous discussion w_o was shown to be the point on the cavitation curve beyond which the equations used to determine cavitation do not apply. It will now be shown that if cavitation does not reach the mass, cavitation gets no closer to the mass than the location at which the expansion becomes subsonic [2] described by w_o. This follows from a study of the velocity of water particles in cavitation as w_o is approached. A plot of the water particle velocity from Eq. (10) versus w or y has a slope approaching zero as the point w_o is approached. This means that cavitation at w_o is instantly closed and the closure curve starts at w_o or at the mass, if cavitation reaches the mass. Care must be taken when calculating the expansion of the cavitated region to make certain that the mass is still moving forward when the expansion toward the mass becomes subsonic. The solution for the expansion of the cavitated region is

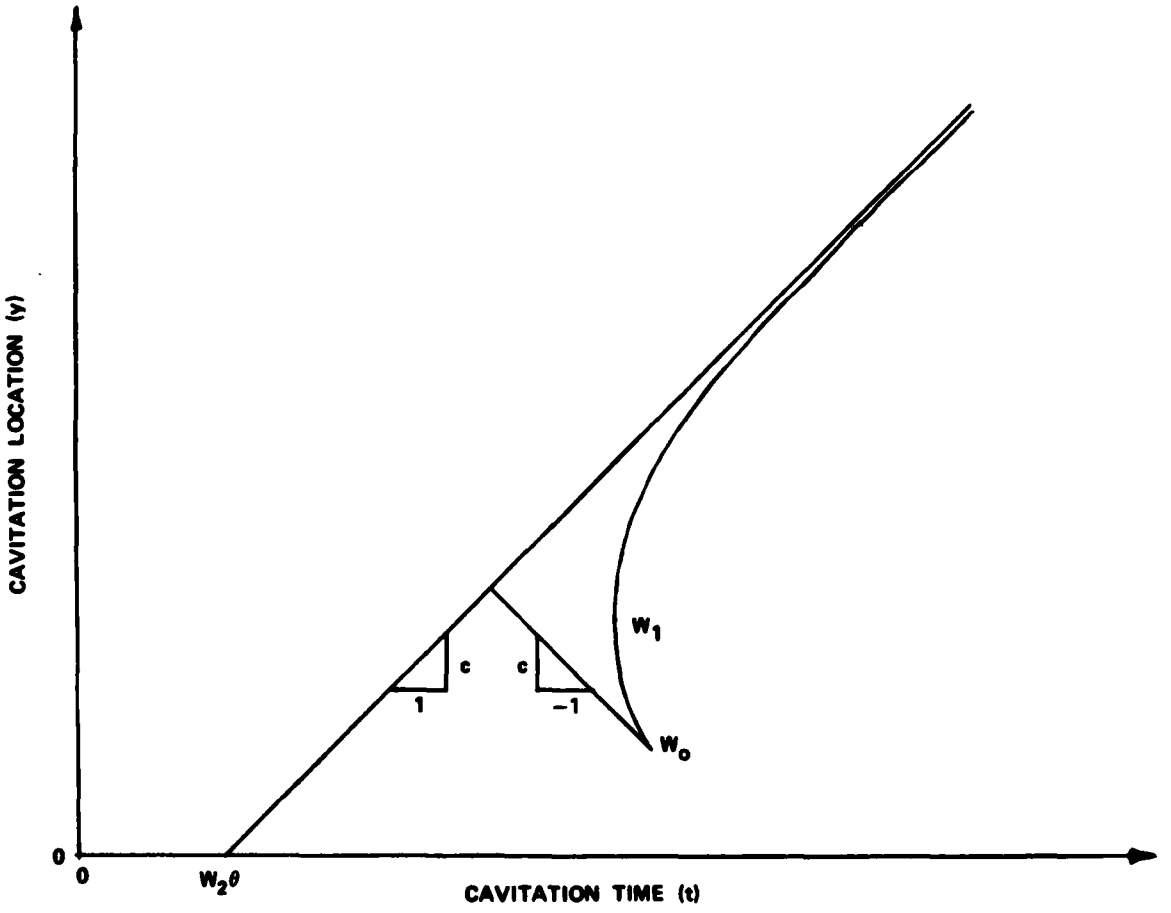

Fig. 2 - Expansion of the Cavitated Region

restricted to values of P_o, P_a, P_h, F, and λ for which the expansion becomes subsonic before the mass velocity goes to zero.

CAVITATION CLOSURE AND MASS DISPLACEMENT

Cavitation closure is of interest because it increases the loading and consequent motion of submerged structures. The preceding equations were developed to support the solution for the closure curve and the displacement of the mass. A closure model taking into account the successive kickoff of water particles and their initial displacement at cavitation can be formulated as in Ref. [3], but successive kickoff and initial displacement effects tend to cancel each other in the closure solution and, for simplicity's sake, will be ignored. The closure model is based on the following assumptions:

1. At all locations cavitated water particle kickoff is taken as being simultaneous with the kickoff occurring closest to the mass and is given by Eq. (10).

2. At all locations, the water particle displacement when kickoff occurs is taken as being equal to the displacement of the mass at the time cavitation occurs closest to the mass.

To specify the closure model using the stated assumptions and derive describing equations, it is necessary to regard the kickoff velocity given by Eq. (10) as a function of y rather than w. The closure model is shown in Fig. 3. In the most general situation closure begins at the point w_o at a time t_o and a distance y_o from the mass. The time between closure at any y and closure at y_o is τ, and the distance the mass moves after closure begins at w_o is x. Momentum and displacement equations determining closure and the motion of the mass are given by Eqs. (11) and (12) respectively as in Ref. [1].

$$(\rho c\theta\lambda + \rho y)\dot{x} = (\rho c\theta\lambda + \rho y_o)u_o + \rho\int_{y_o}^{y} u\,dy - (F + P_a)\tau \tag{11}$$

for

$$\dot{x} \geq 0$$

and

$$x = u\tau \tag{12}$$

When Eq. (11) is integrated with respect to time and substitution for x is made from Eq. (12), the following equation for τ results.

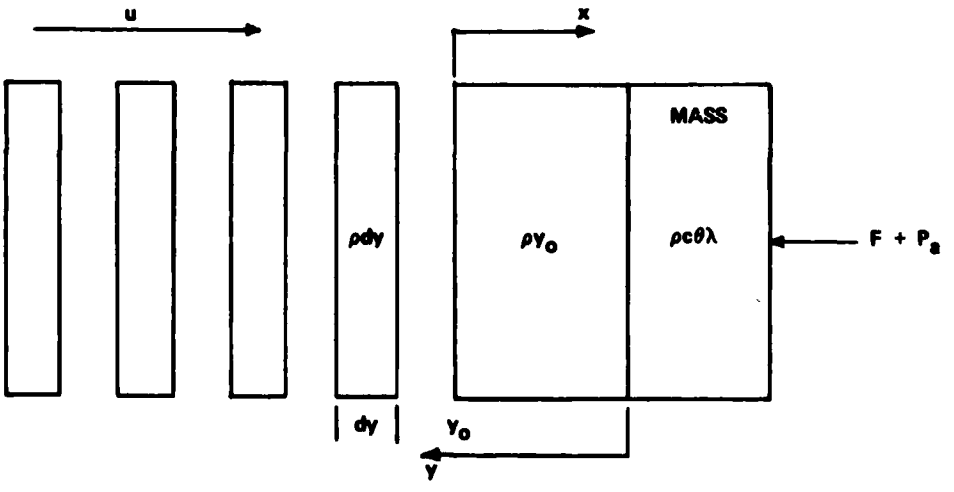

Fig. 3 - Closure Model

$$\tau = \frac{2\rho}{F+P_a}\left[(c\theta\lambda + y_o)u_o + \int_{y_o}^{y} udy + \right.$$
$$\left. - (c\theta\lambda + y)u\right] \qquad (13)$$

The peak displacement of the mass occurs when its velocity slows to zero. When x is obtained by differentiation of Eq. (12) and set equal to zero, the following equation is obtained:

$$0 = (c\theta\lambda + y_o)u_o + \int_{y_o}^{y} udy + \qquad (14)$$
$$-2(c\theta\lambda + y)u$$

Eq. (14) determines the value of w at which mass displacement is maximum. The integral in Eqs. (13) and (14) may be determined in closed form providing the term $P_h/2$ in Eq. (10) is ignored and the variable is changed to w. This results in

$$\int_{y_o}^{y} udy = \frac{P_o}{\rho c} c\theta\left[\left(1-\lambda\right)\left(\frac{2}{1-\lambda} - \frac{N}{P_o}\right)e^{-\frac{w}{\lambda}} + \right.$$
$$\left. + \frac{F+P_a}{P_o} w\right]\Bigg|_{w_o}^{w} \qquad (14a)$$

For cases where cavitation reaches the mass (y = 0), the value for w at the mass is substituted for w_o in the closure equations. The complete solution for the displacement-time history of the mass consists of two piecewise connected parts. These are the linear solution given by Eq. (4) from shock wave arrival at the mass to the time cavitation occurs closest to the mass and the solution for the increase in displacement provided by the closure model. An example of the use of Eqs. (7) and (8) to determine the expansion of the cavitated region and of Eqs. (12) and (13) to determine the closure curve and the displacement-time plot for the mass will be given for the cases where:

$P_a = 0$

$P_h = 0$

$g = 32.2$ ft/sec^2

$\rho = 1.9876$ slugs/ft^3

$c = 5000$ ft/sec

$P_o = 700 \times 144$ psf

$\theta = .004$ sec

$F = 70 \times 144$ psf

and $\lambda = .005, .05,$ and $.5$

The requirement that the mass be moving forward when the expansion of the cavitated region toward the mass becomes subsonic restricts the range of parameters over which a solution can be obtained using the equations in this paper. A relationship between borderline parameters for the case where $P_a = 0$ and $P_h = 0$ is plotted in Fig. 4. Fig. 4 is obtained by solving Eg. (3) for the time at which the mass velocity is zero and equating that time to the time the cavitation expansion becomes subsonic at w_o, given by Eq. 7. The expansion and closure of the cavitated region for the above three cases are given in Fig. 5 and the displacement time histories of the mass are shown in Fig. 6. Fig. 6 shows the motion of the mass beginning at the onset of closure and ending at peak mass displacement.

ABSORBED SHOCK WAVE ENERGY

A calculation of the absorbed shock wave energy will be made for the case where hydrostatic and atmospheric pressures are taken as zero. The energy per unit area absorbed by the restraint is then Fz_{max} where F is the restraining force per unit area and z_{max} is the maximum displacement of the mass. The total incident shock wave energy per unit area is $1/2\ P_o\ (P_o\theta/\rho c)$. The fraction (k) of the incident energy absorbed by the restraint is:

$$k = \frac{Fz_{max}}{\frac{1}{2} P_o \frac{P_o\theta}{\rho c}} \qquad (15)$$

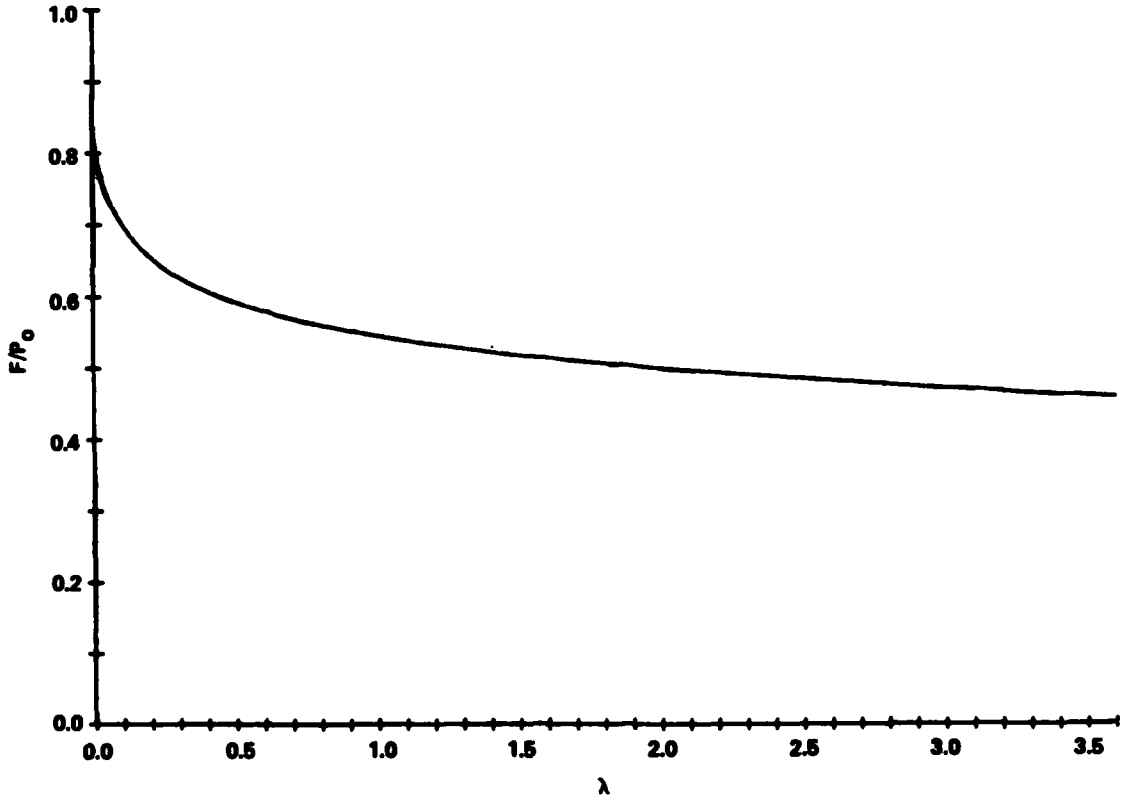

Fig. 4 - Borderline Parameters Restricting the Solution

The energy ratio is plotted in Fig. 7 versus the ratio of the restraint to the peak shock wave pressure for various values of λ. The energy ratio must be zero at $F/P_o = 2$ because the shock wave sees the mass as a rigid boundary. The solution for k given here cannot go all the way to $F/P_o = 2$ because it is restricted to parameters beneath the curve given in Fig. 4. The discontinuities in the slopes of the curves are at the values of F/P_o for which the expanding cavitation just reaches the mass. Cases with abscissa values less than those of the discontinuities represent situations where the cavitation rushes toward and reaches the mass. At greater abscissa values the cavitation does not reach the mass. An interesting observation from Fig. 7 is that the incident shock wave energy absorbed by the restraint increases with the restraint before decreasing toward zero.

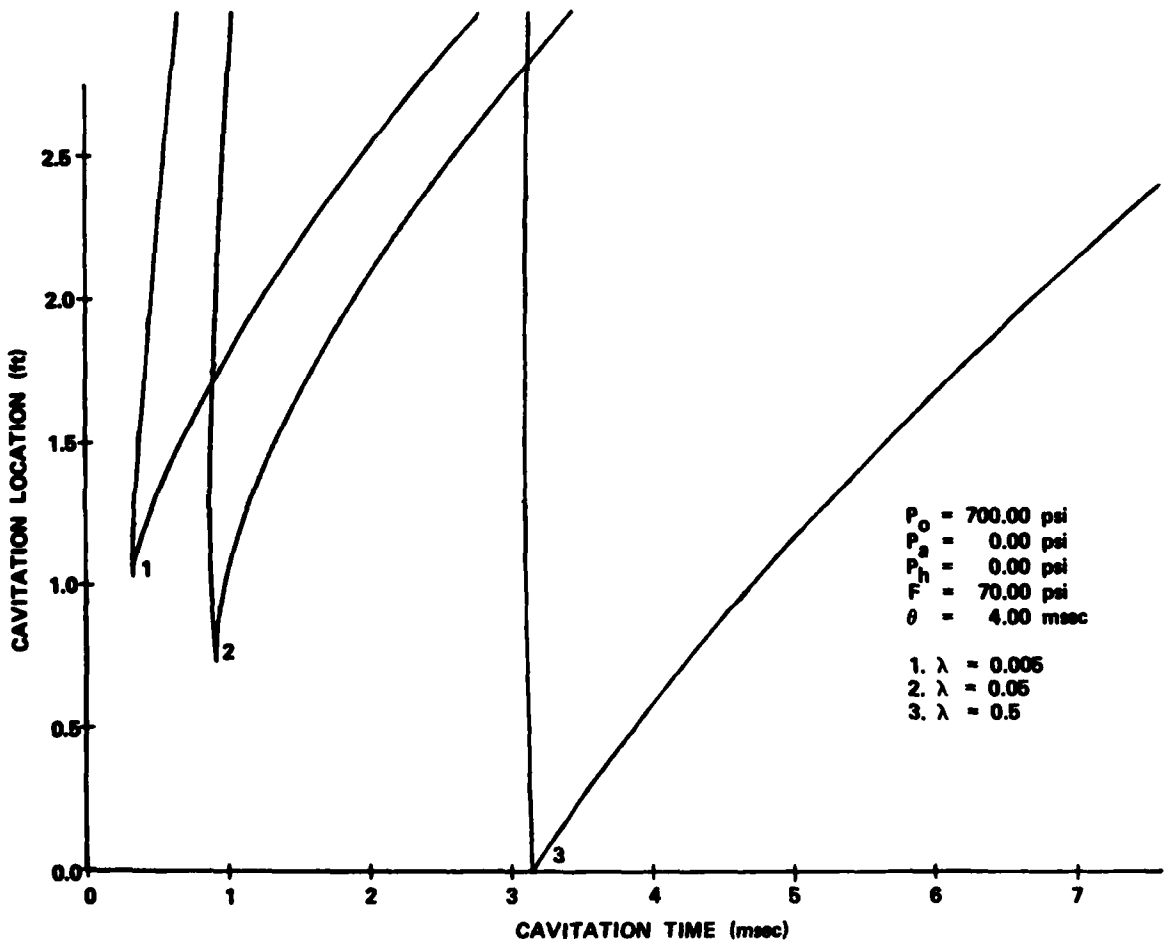

Fig. 5 - Expansion and Closure of the Cavitated Region for Selected Parameters

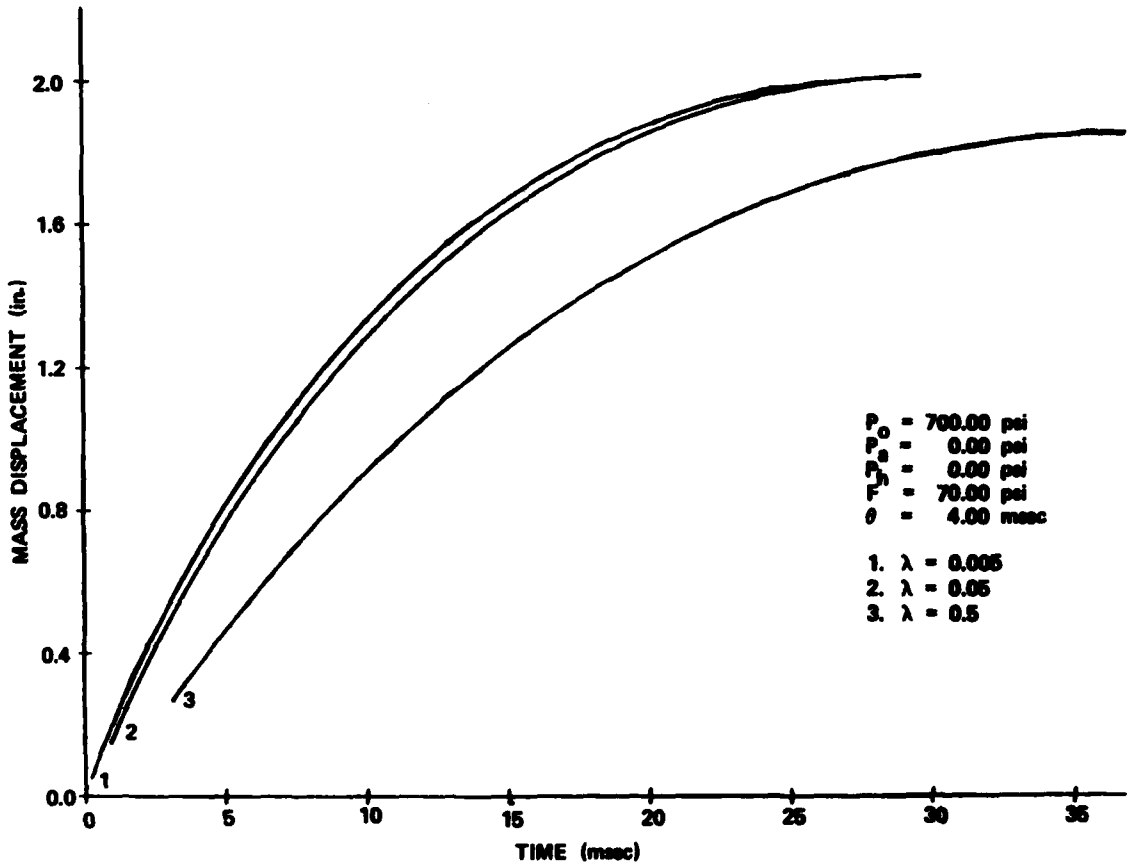

Fig. 6 - Displacement Time Histories of the Mass for Selected Parameters

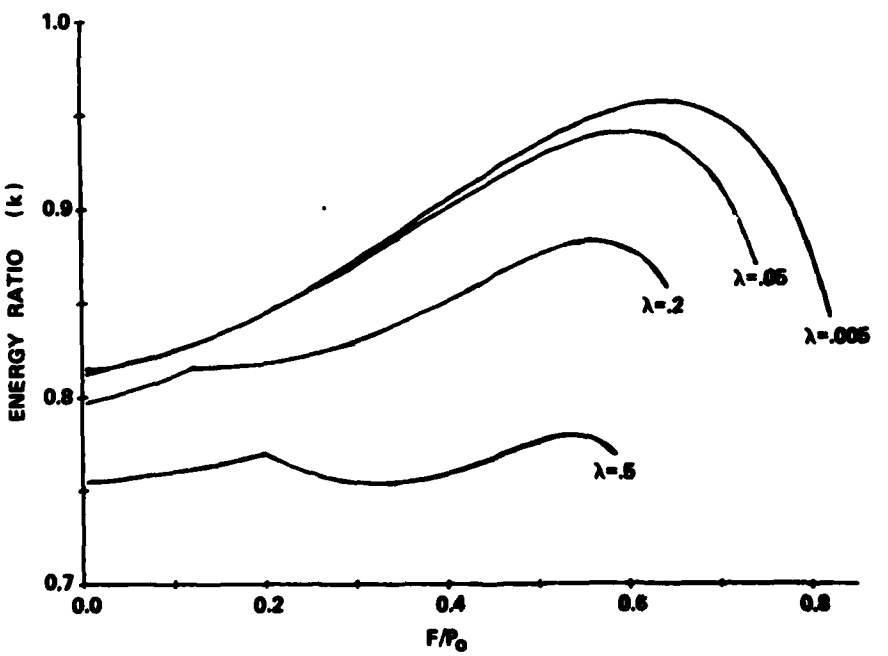

Fig. 7 - Absorbed Energy/Incident Energy Ratio Versus Restraint/Peak Pressure Ratio

SUMMARY AND CONCLUSIONS

A study of the cavitation resulting from the interaction of a shock wave with a mass having a constant restraint has been developed in support of a solution for the motion of the mass. Water is assumed to cavitate at zero absolute pressure and an exponential shock wave is assumed. Cavitation begins at a point near the mass and rushes both toward and away from the mass. Closure of this cavitated region begins when the rate of expansion becomes subsonic or when the cavitated region reaches the mass. Closure of the cavitated region imparts a secondary loading on the mass which prevents the velocity of the mass from decreasing as fast as it would without closure, thus increasing the displacement of the mass. For the case where atmospheric pressure and hydrostatic pressure are zero, the final displacement is used to determine the fraction of the incident shock wave energy which is absorbed by the restraint for various values of parameters. When mass and restraint are the only variables, energy ratio curves show that absorbed energy decreases with increasing mass but can increase with increasing restraint before falling toward zero. These results may be compared with existing analyses [4] using different assumptions and aid in making judgments of the portion or total incident energy absorbed by a yielding surface.

REFERENCES

1. Waldo, G.V., Jr., "A Bulk Cavitation Theory with a Simple Exact Solution," Naval Ship Research and Development Center Report 3010 (April 1969)

2. Kennard, E. H., "Explosive Load on Underwater Structures as Modified by Bulk Cavitation," The David W. Taylor Model Basin Report 511 (May 1943)

3. Stow, Benjamin M. and John D. Gordon, "A Solution to the One Dimensional Bulk Cavitation Problem," The Shock And Vibration Bulletin, Part 2, Fluid-Structure Dynamics And Dynamic Analysis (May 1983)

4. Driels, M.R., "The Effect of a Non-Zero Cavitation Tension on the Damage Sustained by a Target Plate Subject to an Underwater Explosion," Journal of Sound and Vibration, Vol 73, No. 4, pp. 533-545 (June 1980)

DISCUSSION

Voice: Do you have any experimental correlations with your computed one-dimensional results?

Mr. Handleton: No.

*U.S. GOVERNMENT PRINTING OFFICE: 1985-461-639:20008